

**Implementation of the ROD Crate DAQ
Software for the ATLAS Tile
Calorimeter and a Search for a MSSM
Higgs Boson Decaying into Tau Pairs**



Carlos Antonio Solans Sánchez

Departamento de Física Atómica, Molecular y Nuclear
and IFIC (Universitat de València - CSIC)

A dissertation submitted to the Universitat de València
for the degree of Doctor of Philosophy.

Declaration

This dissertation is the result of my own work, except where explicit reference is made to the work of others. It has not been submitted for another qualification to this or any other university.

Carlos Antonio Solans Sánchez

Acknowledgements

First of all I would like to thank the professors of the Departamento de Física Atómica, Molecular y Nuclear Emilio Higón, Antonio Ferrer and Victoria Castillo for the opportunity they gave me to participate in one of the biggest challenges of modern physics. I spent my first summer at CERN gazed by the activities in high energy physics, invited by the Tile Calorimeter group from IFIC. I got started at CERN with the help of Jose Castelo, Cristobal Cuenca, Esteban Fullana and Belen Salvachua, who were already involved in the project. This is when I met Juan Valls who has always been very enthusiastic about my work. It was during that first summer at the test beam I knew I had to become a part of CERN.

Back in Valencia I was welcomed to join the research group at IFIC which I accepted without really knowing what it was all about. I was actively involved in the hardware commissioning activities of the group while attending the few lectures that I had left before graduating. I spent most of the time working on the stand-alone DVS tests for the ROD motherboards.

After finishing my bachelor's degree (Licenciado en Física), I spent most of my time at CERN, learning everything I could about the TDAQ and how it should be implemented for the Tile Calorimeter from Oleg Solov'yanov. I am very grateful to him for the knowledge he shared with me, especially how to find in the source code the information that is not written in the documentation. I am thankful for Gordon Crone's code, which I read through many times to extract the full picture of the read-out software. Working on the online software I met Andrei Kazarov, Igor Soloviev and Sergei Kolos. I am very grateful for their patience every time I ran myself into implementation dilemmas. I also want to thank Sasha Solodkov for helping me out with the offline software in so

ACKNOWLEDGEMENTS

many occasions.

Suddenly I had become the Tile ROD expert, and had to work hard to get the software ready for the commissioning phase of the super-drawers. I was reporting weekly progress of the commissioning of the ROD DAQ system, which later evolved into the commissioning Team 4 and finally to the Tile DAQ development team. This had to be taken seriously because the performance of the Tile Calorimeter was a result of our work. Ana Henriques was always very supportive about the progress of the system.

The first turning point after my graduation happened when I was honoured to give a summary talk in the ATLAS overview week at CERN to talk about the status of the read-out of the Tile Calorimeter. I am in debt with Bob Stanek for that opportunity and also for the other one that came a year later in Glasgow. I recognize the fact that he was also ready to give up his banjo time before the dawn to give me some advice.

I spent my 25th birthday at CERN, on which I gave a talk at the Tile commissioning weekly meeting. But I don't regret the time I spent in meetings or working in USA15 during the commissioning of the super-drawers, because I had the chance to share my life with other people who made it worth it: David, Jalal, Ali, Bruno, Thiago, Fernando, Denis, Mike, Stan ... There was never a bad reason to organize a BBQ or even have a drink in Irakli's place, which made my Friday nights always desirable.

One of the things that I liked the most of being at CERN was the office space I shared with Irene Vichou, Nills Gollub and Gerolf Schlager. I bet it was one of the busiest offices in building 40. I am sorry for the number of times someone came into the office to talk with me interrupting their silence, and reminisce all the times a spontaneous meeting took place around Irene's desk.

The challenge of my professional skills happened during the milestone weeks, in which the knowledge of the system was not enough to determine the outcome of the exercise, and success was related to fast problem solving. Interaction in the control room with Giovanna Lehmann, Gokhan Unel and other people showed me how to control a panic situation in data taking. I cannot forget Alberto Valero, who has always been there to help me out with the DSP code and brainstorming ideas to fix an unexpected situation. Many times we up-

dated and tested the code in a few hours; many others we tried to reproduce a DAQ problem in the ROD lab in building 175 where we invited Markus Joos, Benedetto Gorini and Jorgen Petersen to help us understand it in a realistic testbench of the Tile Calorimeter read-out.

Being at CERN all the time gives you the possibility to attend short notice events like the visit of the rector of the University of Valencia to ATLAS. I followed the visit through the installation area and I am very grateful to Peter Jenni for giving me the opportunity of presenting the Tile Calorimeter Read-out Drivers to the rector.

I met Bruce Mellado when I started my physics analysis. Bruce and Juan guided my analysis towards the MSSM Higgs which was a very interesting topic. Short after that, I went to UC Davis to learn about the profiling method used by John Conway at CDF. I spent many years working on the neutral MSSM Higgs decaying to tau pairs. In the course of which I gained a profound understanding of the statistical method. I am very grateful to Bruce, Juan, Cristobal, John, Glen Cowan and Bill Quayle for their guidelines in many different aspects which lead to the current status of this analysis. A special mention to Jose Maneira, Enrique Sanchís and Vicente González for their comments, suggestions and motivation while writing this Thesis.

In the end, I have spent seven summers at CERN. In which I have passed from moving out of home to establishing a permanent base in Saint Genis Pouilly with the help of my parents. It is more than one year I am living with Sara Castells now to whom I have only words of love. Finishing the PhD was my objective when I told my family that I wanted to study physics, and it wouldn't have been possible without their caring. I am grateful for their love and consideration for me, despite a journey they didn't quite understand. To all of them I dedicate this Thesis.

ACKNOWLEDGEMENTS

Preface

The LHC is one of the most exciting challenges of our time. It will recreate the conditions moments after the Big Bang, helping us unveil one of the secrets of the universe, the origin of mass. This concept is bounded into the Standard Model of particle physics, which is in excellent agreement with observations, via Spontaneous Symmetry Breaking and the Higgs mechanism. However, the Higgs particle has not yet been discovered.

As an enthusiastic collaborator, the author has been involved in the commissioning and operation of one of the detectors of the ATLAS experiment for the LHC, the Tile Calorimeter. He has played the role of sub-detector deputy run-coordinator and been co-responsible of the DAQ team of the Tile Calorimeter. In one occasion he represented the Tile Calorimeter group at the ATLAS week in October 2006 to report on the experience with read-out, DCS, online databases, and in other occasion he represented the Tile Calorimeter group at the ATLAS week in July 2007 to report on the status of the Tile Calorimeter. As a High Energy Physics researcher, the author has devoted his time to the Higgs particle in the Minimal Supersymmetric extension of the Standard Model. The author has been working on a technique, which he learned at UC Davis in November 2007, that was used for a similar search at CDF. This technique was presented in the ATLAS Statistics Forum in July 2009, and results from this analysis were presented in the ATLAS Higgs working group in July 2010. This thesis summarizes the result of the work on the online software for the ATLAS Tile Calorimeter and the search for the neutral MSSM Higgs bosons in the di-tau decay channel.

Chapter 1 is an introduction to the LHC at CERN, followed by an extensive review on the ATLAS experiment and the Tile Calorimeter, and also on the

Trigger and Data Acquisition system.

Chapter 2 summarizes the service work contribution to the engineering requirements of the experiment. This is a review of the work done on the Trigger and Data Acquisition software, followed by an evaluation of its performance. The main purpose of the software is to control the online energy and time reconstruction of the data, which has been extensively validated. Current performance of the signal reconstruction is summarized in Chapter 3.

The second part of the thesis is devoted to Physics simulation. A brief review of the Standard Model and the Minimal Super Symmetric Extension of it is introduced in Chapter 4.

Finally, an alternative search for neutral MSSM Higgs bosons will be covered in Chapter 5. The selected channel is the di-tau decay into semileptonic modes which is enhanced a factor $\tan\beta$ over the Standard Model. This establishes a promising scenario for the discovery or exclusion of the Higgs boson.

Contents

1	CERN, LHC and the ATLAS Experiment	1
1.1	CERN	1
1.2	The Large Hadron Collider	2
1.2.1	Particle Production Rate	5
1.2.2	The LHC experiments	6
1.3	The ATLAS Experiment	8
1.3.1	Magnet System	10
1.3.2	The Muon System	12
1.3.3	The Inner Detector	14
1.3.4	Calorimeters	16
1.4	The ATLAS Trigger and Data Acquisition System	23
1.4.1	Level 1 Trigger	23
1.4.2	Level 2 Trigger	26
1.4.3	Event Filter	28
1.5	Tile Calorimeter Electronics	29
1.5.1	Front-End Electronics	30
1.5.2	Back-End Electronics	34
2	The ROD Crate DAQ for the Tile Calorimeter	41
2.1	Tile Calorimeter Read-out Chain	42
2.2	The Read-Out Driver	43
2.3	Optimal Filtering	46
2.3.1	Conditions Data	48
2.4	Online Software	49
2.4.1	The Partition	49

2.5	Tile Online Software	51
2.5.1	ROD Crate DAQ	51
2.5.2	Stopless Recovery	61
2.5.3	Detector Verification System Tests	63
2.5.4	DAQ to DCS Communication	66
2.6	Operation of the Tile Calorimeter	67
2.6.1	Transition Times	70
2.7	Online Data Quality	73
2.7.1	ROD Monitoring	74
2.7.2	ROS Monitoring	75
2.7.3	Event Filter Monitoring	77
2.8	Outlook	79
3	Performance of the Signal Reconstruction	81
3.1	Optimal Filtering Online and Offline	81
3.1.1	DSP Implementation	82
3.1.2	Iterative Optimal Filtering	83
3.2	Computing Strategy	86
3.2.1	Event Selection	88
3.3	Time Calibration	89
3.3.1	Cell Time Calibration	91
3.3.2	Time Calibration with Physics Objects	91
3.4	Signal Reconstruction Performance	96
3.4.1	Algorithm Comparison	96
3.4.2	Performance of the Non Iterative Method	99
4	Theoretical Motivation	103
4.1	The Standard Model	103
4.1.1	Quantum Electrodynamics	104
4.1.2	Quantum Chromodynamics	108
4.1.3	Electroweak interactions	111
4.1.4	Spontaneous Symmetry Breaking	115
4.1.5	The Higgs Mechanism	117
4.1.6	The Higgs Boson	119

4.1.7	Limitations of the Standard Model	123
4.2	The Minimal Supersymmetric Extension of the Standard Model .	123
4.2.1	Higgs Bosons in the MSSM	125
4.2.2	MSSM Higgs Boson Production Cross Sections	129
4.2.3	Searches for Neutral Higgs Bosons	132
5	Search for MSSM Higgs Bosons Decaying into Tau Pairs	137
5.1	Introduction	137
5.1.1	Production of MSSM Higgs Bosons	138
5.1.2	The Tau Pair Decay Mode	140
5.1.3	Background Processes	141
5.1.4	Higgs Mass Reconstruction	144
5.1.5	Visible Mass	146
5.2	Data Sets	148
5.2.1	Signal Samples	148
5.2.2	Background Samples	148
5.3	Object Reconstruction	149
5.3.1	Electrons	149
5.3.2	Muons	150
5.3.3	Taus	151
5.3.4	Fake Tau Identification	154
5.3.5	Jets	156
5.3.6	Missing Transverse Energy	157
5.3.7	Overlap Removal	157
5.4	Event Selection	160
5.4.1	Transverse Mass Cut	161
5.4.2	Cut Flow	163
5.4.3	Visible Mass Distribution	163
5.5	Statistical Analysis	167
5.5.1	Profiling	168
5.5.2	Template Morphing	170
5.5.3	Setting Limits	175
5.5.4	Discovery Significance	176
5.5.5	Software Implementation	180

CONTENTS

5.6	Results	182
5.6.1	Expected Sensitivity for Exclusion	182
5.6.2	Expected Discovery Significance	188
5.7	Outlook	193
6	Conclusions	195
7	Resumen	197
7.1	El CERN, el LHC y el Experimento ATLAS	197
7.1.1	El CERN	197
7.1.2	El LHC	197
7.1.3	El Experimento ATLAS	198
7.1.4	The Sistema de Trigger y Adquisición de Datos	198
7.2	El ROD Crate DAQ del TileCal	199
7.2.1	El software online de TileCal	201
7.2.2	Operación del TileCal	202
7.2.3	Calidad de los Datos Online	203
7.3	Rendimiento de la Reconstrucción de la Señal	205
7.3.1	Filtrado Óptimo Online y Offline	205
7.3.2	Estrategia Computacional	206
7.3.3	Calibración del Tiempo	207
7.3.4	Rendimiento de la Reconstrucción de la Señal	209
7.4	Motivación Teórica	210
7.4.1	El Modelo Estándar	210
7.4.2	El Modelo MSSM	212
7.5	Búsqueda de Bosones de Higgs MSSM decayendo a pares de Taus	213
7.5.1	Introducción	213
7.5.2	Datos de Monte Carlo	214
7.5.3	Selección de Eventos	214
7.5.4	Análisis Estadístico	217
7.5.5	Resultados	219
7.6	Conclusiones	222
	List of Acronyms	225

CONTENTS

Bibliography	229
List of Figures	237
List of Tables	248

CONTENTS

Chapter 1

CERN, LHC and the ATLAS Experiment

1.1 CERN

After the second World War, a handful of scientists encouraged by the increasing number of international organizations, proposed the creation of a european laboratory for nuclear physics allowing them to share the cost of the facilities. A provisional body was founded in 1952 under the name in french *Conseil Européen pour la Recherche Nucléaire* or CERN. The acronym was kept after the foundation of the current European Organization for Nuclear Research, the 29th of September of 1954, in the Swiss canton of Geneva, across the French-Swiss border.

CERN is run by 20 European Member States, but many non-European countries are also involved in different ways. Scientists come from around the world to use CERN's facilities. CERN employs around 2500 people, but there are around 8000 visiting scientists, half of the world's particle physicists, that come to CERN for their research. They represent 580 universities and 85 nationalities.

Many achievements can be attributed to CERN, like for instance the discovery of the weak neutral currents in 1974 by the Gargamelle experiment, the observation of W^\pm and Z particles in 1983 by the UA1 and UA2 experiments, and the accurate measurements of the Z particle in 1989 that showed that there



Figure 1.1: The Globe of Science and Innovation at CERN.

are only three families of particles in nature. In recognition, Nobel Prizes were awarded to Carlo Rubbia, Simon Van der Meer, Georges Charpak, Sam Ting, Burt Richter and Jack Steinberg.

On CERN's 50th anniversary of foundation, the Globe of science and Innovation (Figure 1.1) was built on Galileo Galilei's square, as a venue for the presentation of science, technology and industry to the general public.

1.2 The Large Hadron Collider

The Large Hadron Collider, LHC, the world's largest and most powerful particle accelerator, is the latest addition to CERN's accelerator complex (Figure 1.2). Two accelerated particle beams collide heads on with each other, with no energy wasted from the recoil of a stationary target. The LHC was built in the tunnel where the Large Electron Positron collider (LEP) operated from 1989 to the end of 2000. This tunnel has a circumference of 27 km and crosses the border of Switzerland and France.

Before being injected with an energy of 450 GeV into the LHC's 27 km ring, protons are accelerated and formed in beams in four increasingly large machines.

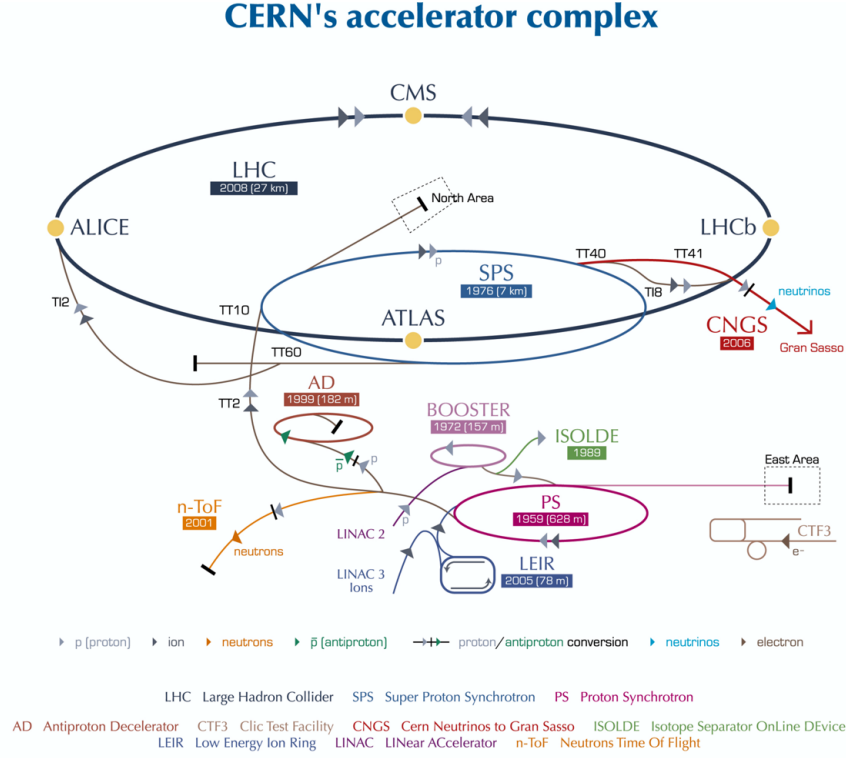


Figure 1.2: Operational CERN accelerators.

The beams are then accelerated in the ring until their energy is increased by a factor of 15, to 7000 GeV. When that energy is reached, the proton beams collide in the center of the experiments. The LHC collides beams of protons at a center of mass energy of 14 TeV and a design luminosity of $10^{34} \text{ cm}^{-2} \text{ s}^{-1}$. Beams of lead nuclei (Pb) may also be accelerated, smashing together with a collision energy of 1150 TeV in one of the experiments.

In order to achieve this, the beams of particles travel at close to the speed of light in opposite directions in separate beam pipes kept at ultrahigh vacuum. They are guided around the accelerator ring by a strong magnetic field, achieved using superconducting electromagnets. These are built from coils of Nb-Ti that operate in a superconducting state, efficiently conducting electricity without resistance or loss of energy. This requires to cool down the magnets to about 2 K (-271 °C) with superfluid helium at 1.9 K and allows an operational field of 8.4 Tesla. In total, 1232 dipole magnets of 14.2 m length are used to bend the beams, and 392 quadrupole magnets, each 5 to 7 m long, to focus the beams.

Injection energy	450 GeV
Collision energy	7000 GeV
Number of particles per bunch	1.15×10^{11}
Number of bunches per fill	2808
Nominal luminosity	$10^{34} \text{ cm}^{-2} \text{ s}^{-1}$
Inelastic cross section	60 mb
Total cross section	100 mb
Revolution frequency	11.245 kHz
Bunch frequency	40.08 MHz
Circumference length	26.66 km
Radius	4.24 km
Number of dipole magnets	1232
Number of quadrupole magnets	392
Nominal magnetic field strength	8.33 T

Table 1.1: LHC beam parameters.

Figure 1.3 shows the cross section of a dipole magnet.

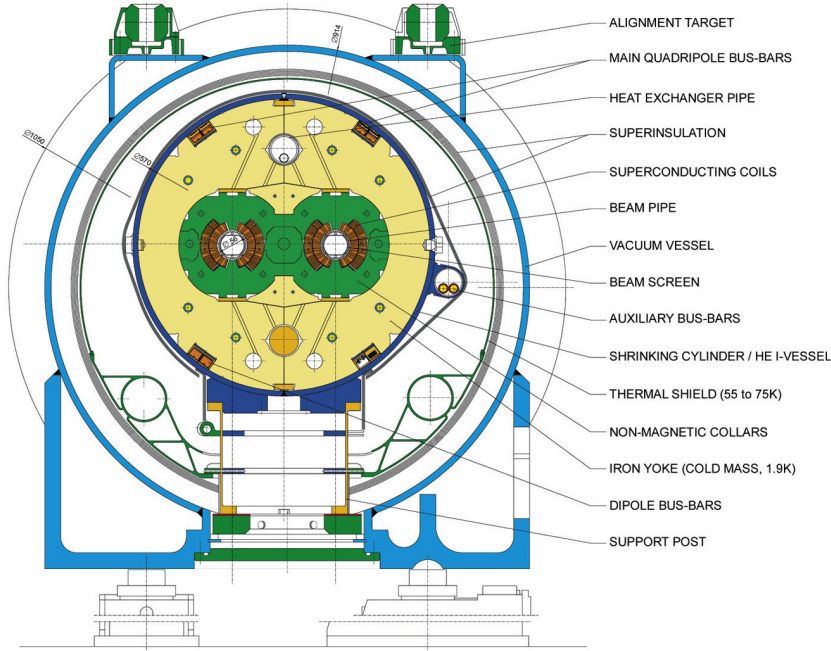


Figure 1.3: Diagram showing the cross-section of an LHC dipole magnet.

The LHC began operating on the 10th of September 2008, but only for a few days, due to an unfortunate accident. It resumed its operation in 2009 at a center of mass energy of $\sqrt{s} = 3.5 \text{ TeV}$. Collisions at half the design center of mass, $\sqrt{s} = 7 \text{ TeV}$, were accomplished in early 2010. It is expected that the

LHC will operate continuously for 18 to 24 months at this energy.

1.2.1 Particle Production Rate

The particle production rate (R) is a statistical process that depends on the type of particles to be created, represented by their cross section, σ , and the luminosity, L , by the following relation:

$$R = \sigma L$$

The luminosity is defined in terms of the beam parameters by:

$$L = \frac{1}{4\pi} \frac{N^2 f}{\sigma_x \sigma_y t}$$

where N is the number of protons per bunch, f is the fraction of bunch positions containing protons, t is the time between bunches, and σ_x and σ_y are the transverse dimensions of the Gaussian beam profiles.

All those parameters are optimized to obtain a satisfying production rate of the process of interest. The LHC is designed to work with a bunch crossing time of $t = 25$ ns with a number of protons per bunch of approximately $N = 10^{11}$. With 80% of the bunches filled ($f = 0.8$) and a bunch dimension of the order of few μm , the final luminosity of $10^{34} \text{ cm}^{-2} \text{ s}^{-1}$ can be reached.

Figure 1.4 shows the p-p cross section for different processes as a function of center-of-mass energy. Note that only inelastic scattering produces particles that cross the detectors. At the design center-of-mass energy of the LHC, the p-p inelastic scattering is ~ 70 mb. The expected rate of inelastic interactions is:

$$R = 70 \text{ mb} \times 10^{34} \text{ cm}^{-2} \text{ s}^{-1} = 700 \times 10^6 \text{ s}^{-1}$$

Hence, the expected number of interactions per bunch crossing is:

$$n = R \frac{t}{f} = 700 \times 10^6 \text{ s}^{-1} \times \frac{1}{0.8} \times 25 \text{ ns} \sim 23$$

So, there will be ~ 23 interactions per bunch crossing in the center of the detectors.

This high rate production environment sets the demands for the four ex-

periments at the LHC, in terms of radiation hardness, read-out speed and high performance of the trigger selections.

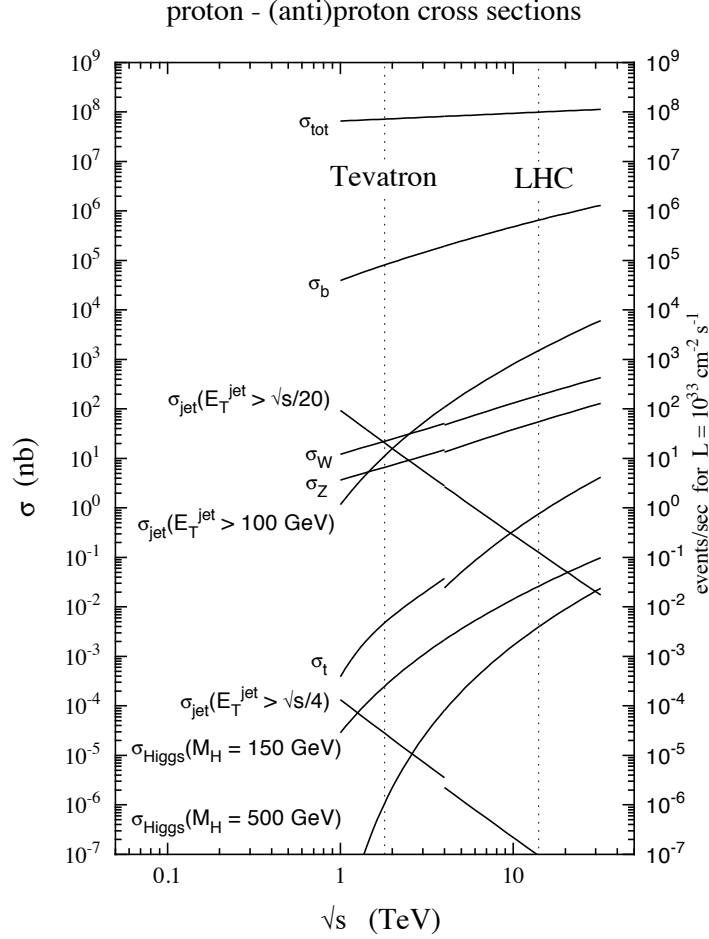


Figure 1.4: Proton-proton cross section as a function of center of mass energy for a hadron collider [1].

1.2.2 The LHC experiments

Four large experiments are installed around the ring of the LHC as shown in Figure 1.5. Two general-purpose experiments, ATLAS (A Toroidal LHC Apparatus) [2] and CMS (Compact Muon Solenoid) [3], are optimized to study new physics at the TeV scale. A detailed description of the ATLAS detector is found in Section 1.3. The other two experiments are designed to study specific phenomena, LHCb (Large Hadron Collider Beauty) [4] and ALICE (A Large

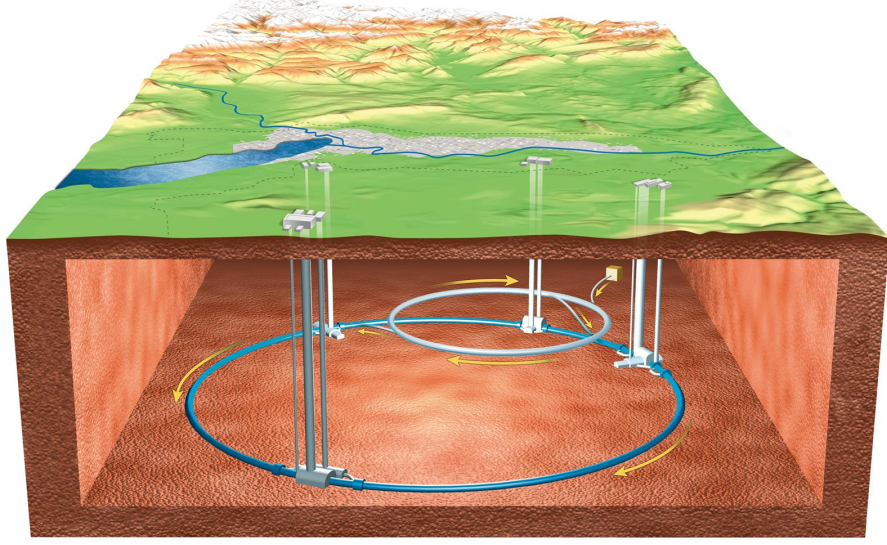


Figure 1.5: Representation of the LHC ring with its detectors.

Ion Collider Experiment) [5]. the first to investigate the CP violation in the bottom quark sector, and the other one to study quark-gluon plasma through Pb-Pb collisions.

In addition, there are three other experiments much smaller in size: TOTEM (TOTal Elastic and diffractive cross-section Measurement) [6], LHCf (LHC Forward) [7], and the recently approved MoEDAL (Monopole and Exotics Detector at the LHC) [8]. TOTEM effectively measures the size of the proton and the LHC luminosity, LHCf will study particle production and p-p cross sections in the forward region, and MoEDAL will search for the direct production of the magnetic monopole at the LHC and exotic, highly ionizing, stable (or pseudo-stable) massive particles with conventional electric charge.

The ATLAS, CMS, ALICE and LHCb detectors are installed in four large underground caverns located around the ring of the LHC. Whereas the detectors used by the LHCf experiment are positioned near the ATLAS detector, those used by TOTEM are near the CMS detector and those used by MoEDAL are attached to the walls of the cavern of the LHCb experiment.

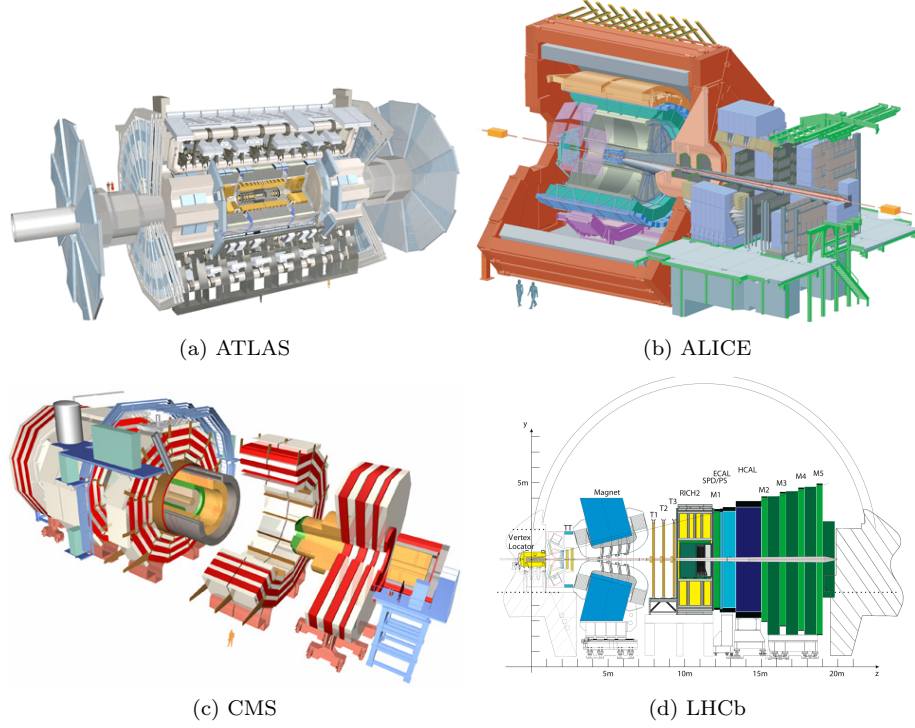


Figure 1.6: The four main LHC experiments.

1.3 The ATLAS Experiment

The ATLAS experiment is a general-purpose detector designed to exploit the full discovery potential of the LHC. ATLAS is about 45 meters long, more than 25 meters high and has an overall weight of approximately 7000 tonnes. It is divided into sub-detectors as show in Figure 1.7. The Inner Detector represents the inner most part of ATLAS, surrounded by a solenoid magnet, the Calorimeters, the Muon system and a very large air-core toroid magnet. It is designed to work at high luminosity ($10^{34} \text{ cm}^{-2} \text{ s}^{-1}$) with a bunch crossing every 25 ns. Therefore, it is built with highly sophisticated technologies and specialized materials. After the intense commissioning period, the experiment is currently running in operation mode, and the first candidates for W boson decaying into electron + neutrino have been seen at $\sqrt{s} = 7 \text{ TeV}$ (See Figure 1.8).

The detector is optimized for a long range of known and hypothetical process. The observable cross-section for most of the processes is small over a large part of mass range, hence it is an important design consideration to operate at high

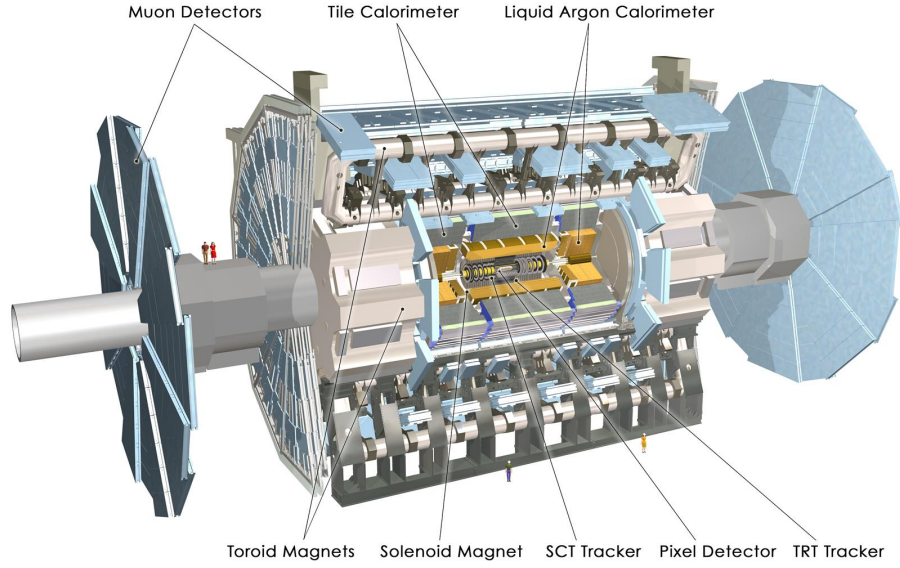


Figure 1.7: The ATLAS experiment.

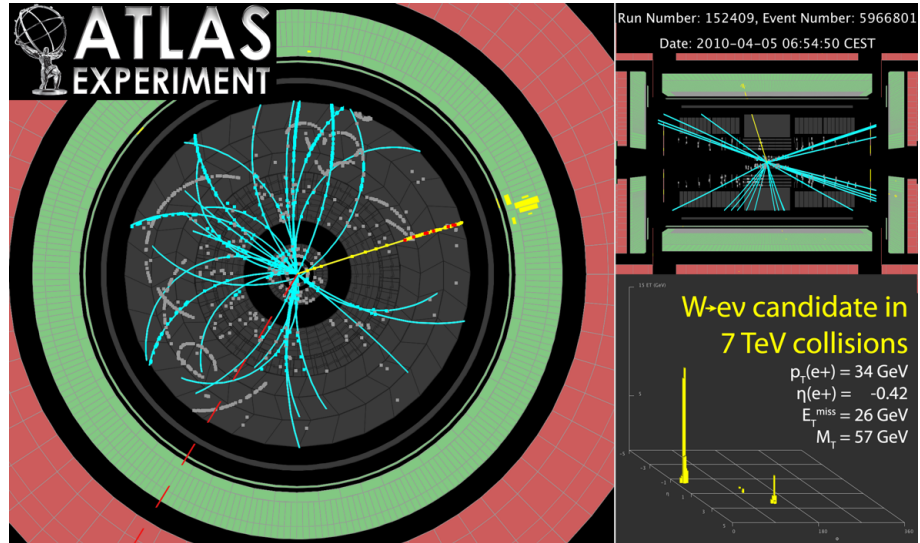


Figure 1.8: First candidate for an event with a W boson decaying to electron + neutrino seen in 7 TeV collision data.

luminosity and to maximize the detectable rates above backgrounds by high resolution measurements. The basic design criteria of the detector include the following:

- Very good electromagnetic calorimetry for electron and photon identifica-

Detector component	Required resolution	Coverage	
		Measurement	Trigger
Tracking	$\frac{\sigma_{p_T}}{p_T} = 0.05\% p_T \oplus 1\%$	$ \eta < 2.5$	
EM calorimetry	$\frac{\sigma_E}{E} = 10\%/\sqrt{E} \oplus 0.7\%$	$ \eta < 3.2$	$ \eta < 2.5$
Hadronic calorimetry			
Barrel/end cap	$\frac{\sigma_E}{E} = 50\%/\sqrt{E} \oplus 3\%$	$ \eta < 3.2$	$ \eta < 3.2$
Forward	$\frac{\sigma_E}{E} = 100\%/\sqrt{E} \oplus 10\%$	$3.1 < \eta < 4.9$	
Muon spectrometer	$\frac{\sigma_{p_T}}{p_T} = 10\%, p_T = 1 \text{ TeV}$	$ \eta < 2.7$	$ \eta < 2.4$

Table 1.2: . General performance goals of the ATLAS detector.

tion and measurements, complemented by full-coverage hadronic calorimetry for accurate jet and missing transverse energy (E_T^{miss}) measurements.

- High-precision muon measurements, with the capability to guarantee accurate measurements at the highest luminosity using the external muon spectrometer alone.
- Efficient tracking at high luminosity for high p_T lepton-momentum measurements, electron and photon identification, τ -lepton and heavy-flavour identification, and full event reconstruction capability at lower luminosity.
- Large acceptance in pseudo-rapidity η with almost full azimuthal angle ϕ coverage everywhere. The azimuthal angle θ is measured around the beam axis: $\eta = -\ln(\tan(\theta/2))$.
- Triggering and measurements of particles at low p_T thresholds, providing high efficiencies for most physics processes of interest at LHC.

The performance goals of the ATLAS detector are summarized in Table 1.2.

1.3.1 Magnet System

The ATLAS magnetic field configuration has been optimized for particle bending around the various detectors in a light and open structure which minimizes scattering effects. The experiment magnet system arrangement consists of a central solenoid servicing the inner detector trackers with an axial magnetic field of 2 T, and a barrel toroid and two end cap toroids that generate a tangential magnetic field of approximately 0.5 T and 1 T for the muon spectrometer in the

	Barrel Toroid	End Cap Toroid	Solenoid
Inner diameter [m]	9.4	1.65	2.46
Outer diameter [m]	20.1	10.7	2.63
Axial diameter [m]	25.3	5.0	5.30
Number of coils	8	2×8	1
Conductor mass [tons]	118	2×20.5	3.8
Cold mass [tons]	370	2×160	5.4
Total assembly [tons]	830	2×239	5.7
Field [T]	0.5	1	2

Table 1.3: Overview of the magnet system paramters.

barrel and end cap regions respectively. Figure 1.7 shows the position of the four superconducting magnets within the ATLAS detector.

The central solenoid is designed to provide a 2 T strong magnetic field in the central tracking volume made out of a single layer coil. It shares the cryostat with the Liquid Argon calorimeter and the flux is returned by the steel of the Hadronic calorimter.

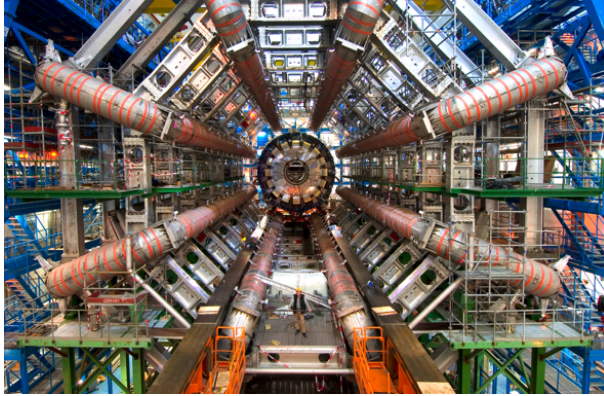


Figure 1.9: Picture of the toroid magnet.

The barrel toroid generates a magnetic field that fills the cylindrical volume surrounding the calorimeters and both end-cap toroids. It is built up of eight Nb-Ti superconductor in a copper matrix coils encased in individual racetrack-shaped, stainless-steel vacuum vessels as shown in Figure 1.9. It weighs 1300 tons and is cooled by liquid helium at 4.5 K. The air-core vessels allow to have a magnetic field in the region of the muon chambers without the return of the field with strong bending power. This technology minimizes the multiple scattering effects, hence, allowing a much easier to follow trajectory

resulting in a better precision.

The two end cap toroids are located inside the barrel toroid, one at each end of the central solenoid. They provide a magnetic field in the forward region of the detector. The eight coils of each end cap toroid are assembled as a single unit inside a large cryostat.

1.3.2 The Muon System

The ATLAS muon spectrometer has been designed to fulfill the following requirements: efficient use of the magnet bending power, pseudo-rapidity coverage of $|\eta| < 3$, and practical chamber dimensions for production, transport and installation. Figure 1.10 shows the position of the muon chambers. The spectrometer is divided into three regions, barrel region ($|\eta| < 1.05$), transition region ($1.05 < |\eta| < 1.4$) and endcap region ($|\eta| > 1.4$). Four different technologies depending on the spatial and timing resolution, resistance to radiation and engineering considerations have been used: Monitored Drift Tube chambers (MDT), Cathode Strip Chambers (CSC), Resistive Plate Chambers (RPC) and Thin Gap Chambers (TGC).

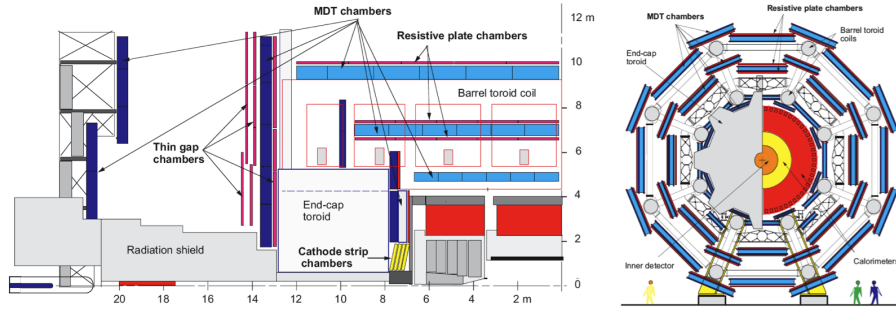


Figure 1.10: The ATLAS muon spectrometer in the rz (left) and xy view (right).

In the barrel region the chambers are situated in three concentric cylinders around the beam axis at 4.5 m, 7 m and 10 m. MDT chambers are used for high precision measurements and RPC for triggering. The low- p_T muon trigger uses two double-layer RPCs located on each side of the middle station, while the high- p_T trigger uses one triple layer chamber located at the outer barrel muon station. In the transition and end-cap region most of the chambers are

Type	Function	Chamber resolution (RMS) in			Number of	
		z/R	ϕ	time	chambers	channels
MDT	tracking	35 $\mu\text{m}(z)$	-	-	1150	354k
CSC	tracking	40 $\mu\text{m}(R)$	5 mm	7 ns	32	30.7k
RPC	trigger	10 mm(z)	10 mm	1.5 ns	606	373k
TGC	trigger	2-6 mm (R)	3-7 mm	4ns	3588	318k

Table 1.4: Muon sytem parameters.

installed perpendicular to the beam axis (see Figure 1.10). In the intermediate region ($1.05 < |\eta| < 1.4$) the muon track is measured with three vertical stations, placed inside or near the barrel magnet. In the end-cap region ($|\eta| > 1.4$), the stations are located before and after the end-cap toroid magnets and a third one near the cavern wall. The trigger is provided by TGC chambers while precision measurements are provided by MDT chambers at $|\eta| < 2$ and CSC chambers $|\eta| > 2$.

Monitored Drift Tube Chambers

The MDT chambers are composed by multilayers of high-pressure drift tubes. Each multilayer is mounted on each side of the support structure. The drift tubes are made of aluminum, 30 mm of diameter, with a central wire of W-Re. They work at 3 bar absolute pressure with a non-flammable mixture of Ar-CO₂.

Cathode Strip Chambers

The CSCs are multiwire proportional chambers operated with a mixture of Ar-CO₂-CF₄. The distance between anode wires (2.5 mm) equals the distance to the cathode. The cathode readout is segmented into strips (5.08 mm) orthogonal to the anode wires. The precision coordinate is obtained by measuring the induced avalanche in the segmented cathode, achieving space resolutions better than 60 μm .

Resistive Plate Chambers

The RPC is a gaseous parallel-plate detector with a typical space-time resolution of 1 cm \times 1 ns with digital readout. It is composed by two parallel resistive plates made of Bakelite. The plates are separated by spacers that define the

size of the gas gaps. The gas is a mixture of $\text{C}_2\text{H}_2\text{F}_4$. A uniform electric field of a few kV/mm produces the avalanche multiplication of ionization electrons. The signal is readout via capacitive coupling to metal strips placed at both sides of the detector and grounded.

Thin Gap Chambers

A TGC is built with $50\text{ }\mu\text{m}$ wires separated 2 mm. The wires are placed between two graphite cathodes at a distance of 1.6 mm. Behind the graphite cathodes, strips or pads are located to perform a capacitive readout in any desired geometry. Some advantages of these chambers are a fast signal, typical rise time 10 ns and low sensitivity to mechanical deformations.

1.3.3 The Inner Detector

The Inner Detector is designed to reconstruct tracks and decay vertices in any event with high efficiency. Using additional information from the calorimeter and muon systems, the inner detector also contributes to electron, photon, and muon identification, and supplies extra signatures for short-lived particle decay vertices. Important physics considerations for the design of the inner detector are:

- excellent momentum and impact parameter resolution for tracks with $p_T > 0.5\text{ GeV}$ up to very high momentum,
- tracking coverage over the range $|\eta| < 2.5$,
- high efficiency keeping high noise rejection,
- identification of the charge of high- p_T tracks,
- tagging of b-jets originating from b-quarks,
- reconstruction of soft electrons and secondary vertices from b and τ decays,
- identification of the primary vertex,
- electron identification capability,

- identification of a high p_T track to reduce the level-1 electromagnetic cluster trigger rate from jet events.

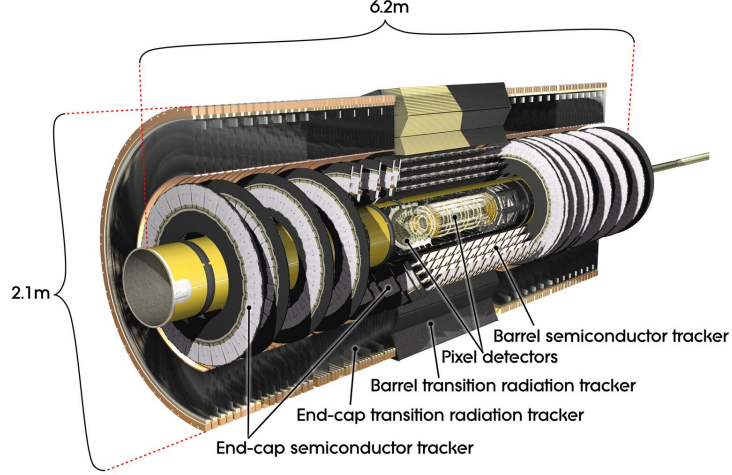


Figure 1.11: The Inner detector.

The magnetic field configuration of the Inner Detector is based on an inner thin super-conducting solenoid surrounding the inner detector cavity with a radius of 1.2 m and a length of 5.3 m. It provides an axial magnetic field of 2 T in the centre of the tracking volume. The momentum and vertex resolution requirements from physics call for high-precision measurements to be made with fine granularity detectors, given the very large track density expected at the LHC. The layout of the Inner Detector is shown in Figure 1.11. The outer radius of the Inner Detector cavity is 115 cm. It consists of three units: a barrel section extending over 80 cm, and two identical end-caps covering the rest of the cylindrical part. In the barrel region, high-precision detector layers are arranged on concentric cylinders around the beam axis, while the end-cap detectors are mounted on disks perpendicular to the beam axis. The main parameters of the Inner Detector are summarized in Table 1.5.

The highest granularity around the vertex region is provided by semi-conductor pixel and strip detectors, the latter employed in the SemiConductor Tracker (SCT). The basic principle of the semiconductor detectors is that the passage of ionizing radiation creates electron-hole pairs in the semiconductor which are collected by an electrical field. The difference between strips and pixels is mainly

System	Position	Area (m ²)	Resolution σ (μm)		Channels ($\times 10^6$)	Coverage ($ \eta $)
			$R\phi$	z		
Pixels	Removable layer	0.2	12	66	16	2.5
	Barrel layers	1.4	12	66	81	1.7
	End cap disks	0.7	12	77	43	1.7 - 2.5
SCT	Barrel layers	34.4	16	580	3.2	1.4
	End cap wheels	26.7	16	580	3.0	1.4 - 2.5
TRT	Barrel straws		170 (per straw)		0.1	2.5
	End cap straws		170 (per straw)		0.32	0.7 - 2.5

Table 1.5: Parameters of the Inner Detector.

geometry, pixels being closely spaced pads capable of good two dimensional reconstruction while strips give a better spacial resolution in one coordinate than the other.

The pixel layers are segmented in $R\phi$ and z , while the SCT detector uses small angle (40 mrad) stereo strips to measure both coordinates, with one set of strips in each layer measuring ϕ . The pixel detector is much more radiation tolerant than the silicon strip tracker. The number of layers of the semiconductor detectors must be limited due to the amount of material they introduce and their high cost. A larger number of tracking points is provided by the straw tube tracker also called Transition Radiation Tracker (TRT), which provides tracking with much less material per point and a lower cost. The barrel TRT tubes are parallel to the beam direction.

1.3.4 Calorimeters

At the LHC about twenty soft collisions per bunch crossing will be produced when operating at design luminosity. Therefore, fast detector response and fine granularity are required to minimize the impact of the pile-up on the physics performance. The calorimetry part of the ATLAS detector covers the range $|\eta| < 4.9$, using a wide variety of techniques suited for the different requirements of physics processes. A scheme with all the calorimeters for ATLAS can be seen in Figure 1.12.

The EM calorimeter is a lead Liquid-Argon (LAr) detector with accordion geometry. The Hadronic Barrel calorimeter (Tile Calorimeter) is based on a sampling technique with plastic scintillator plates (tiles) embedded in a steel

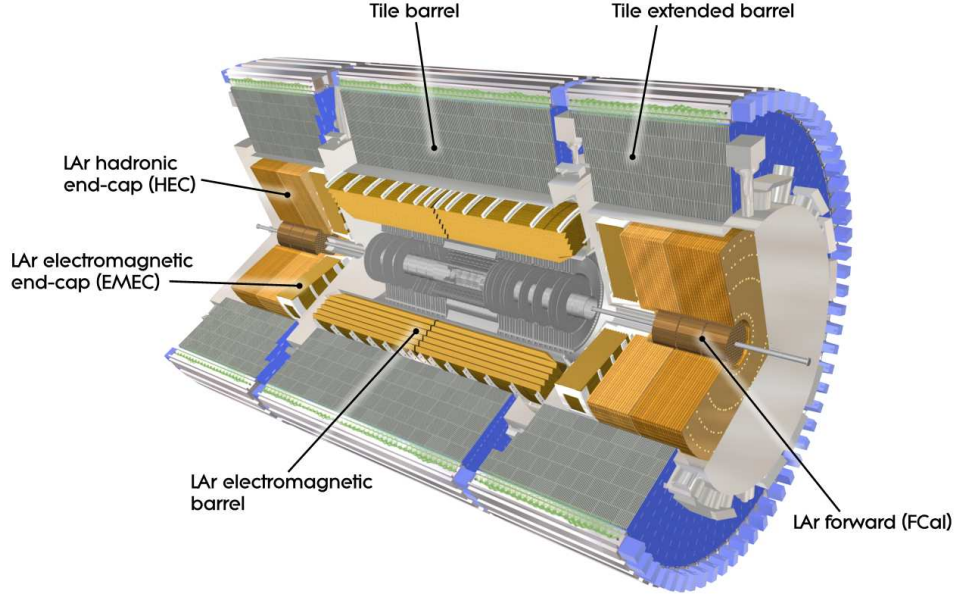


Figure 1.12: Layout of the ATLAS calorimeters.

absorber. At larger rapidities, where higher radiation resistance is needed, the radiation-hard LAr technology is used for the Hadronic Endcap Calorimeter (HEC) and the Forward CALorimeter (FCAL). In the region of $|\eta| < 1.8$, a pre-sampler detector is used to correct for the energy lost by electrons and photons upstream of the calorimeter. The presampler consists of an active LAr layer of thickness 1.1 cm (0.5 cm) in the barrel (end cap) region. Main parameters of the different calorimeter systems is shown in Table 1.6.

Hadronic calorimetry at the LHC is mainly designed to identify jets and measure their energy and direction, and to measure the total missing transverse energy (E_T^{miss}). Fragmentation, gluon radiation and the presence of magnetic fields are intrinsic effects that limit the resolution of these measurements. Moreover, at LHC designed luminosity, the pile-up energy from minimum-bias events also becomes important. In order to be sensitive to interesting physics, the central region is required to have a fine segmentation of $\Delta\eta \times \Delta\phi = 0.1 \times 0.1$, good hermiticity for E_T^{miss} , and a good energy resolution of:

$$\frac{\Delta E}{E} = \frac{50\%}{\sqrt{E}} \oplus 3\%$$

For the forward region, a segmentation of $\Delta\eta \times \Delta\phi = 0.2 \times 0.2$ is sufficient a resolution of:

$$\frac{\Delta E}{E} = \frac{100\%}{\sqrt{E}} \oplus 10\%$$

Figure 1.13 shows the cumulative amount of material, in units of interaction length, as a function of absolute pseudorapidity in the calorimeter system.

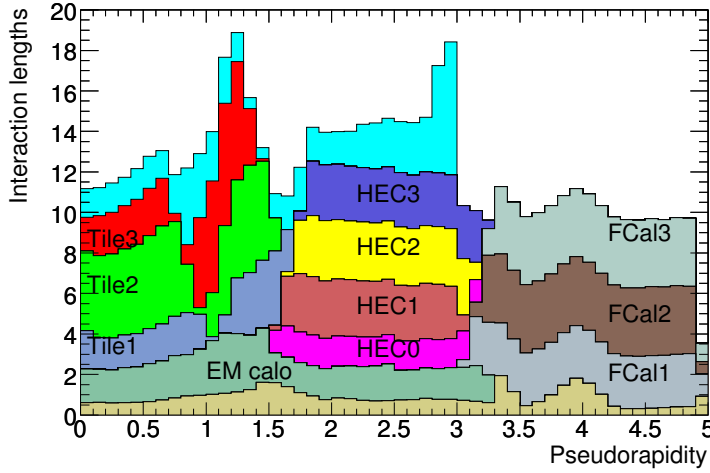


Figure 1.13: Cumulative amount of material, in units of interaction length, as a function of absolute pseudorapidity, in front of the calorimeters and across them.

Liquid Argon Calorimeters

The Liquid Argon sampling calorimeter technique with accordion-shaped electrodes and lead absorber is used for all electromagnetic calorimetry covering the pseudorapidity interval $|\eta| < 3.2$, and for part of the hadronic calorimetry in the range $1.4 < |\eta| < 4.8$.

The EM calorimeter is divided into a barrel part $|\eta| < 1.4$ and into two end cap parts $1.375 < |\eta| < 3.2$, each one housed in its own cryostat. The EM Barrel Calorimeter consists of two identical half-barrels separated by a 4 mm gap at $z = 0$. Each half-barrel is divided into 16 modules. The calorimeter is made out of 1024 accordion-shaped absorbers alternating with 1024 read-out electrodes, arranged with a complete ϕ symmetry around the beam axis. Between each pair of absorbers, there are two Liquid Argon gaps, separated by a read-out

Coverage	Samplings	Granularity ($\Delta\eta \times \Delta\phi$)	
Presampler			
$ \eta < 1.52$	1	0.25×0.1	
$1.50 < \eta < 1.7$	1	0.25×0.1	
EM Calorimeter			
$ \eta < 1.475$	3	0.003×0.1	(Sampling 1)
$1.375 < \eta < 3.2$	3	0.025×0.025	(Sampling 2)
		0.05×0.025	(Sampling 3)
		0.025×0.1	($1.375 < \eta < 1.5$, Sampling 1)
		0.003×0.1	($1.5 < \eta < 1.8$, Sampling 1)
		0.004×0.1	($1.8 < \eta < 2.0$, Sampling 1)
		0.006×0.1	($2.0 < \eta < 2.5$, Sampling 1)
		0.1×0.1	($2.5 < \eta < 3.2$, Sampling 1)
		0.025×0.025	($1.375 < \eta < 2.5$, Sampling 2)
		0.1×0.1	($2.5 < \eta < 3.2$, Sampling 2)
		0.05×0.025	($1.5 < \eta < 2.5$, Sampling 3)
Tile Calorimeter			
$ \eta < 1$	3	0.1×0.1	(Samplings 1 and 2)
$0.8 < \eta < 1.7$	3	0.2×0.1	(Sampling 3)
		0.1×0.1	(Samplings 1 and 2)
		0.2×0.1	(Sampling 3)
HEC			
$1.5 < \eta < 3.2$	3	1.1×0.1	($1.5 < \eta < 2.5$)
		0.2×0.2	($2.5 < \eta < 3.2$)
FCAL			
$3.1 < \eta < 4.9$	3	$\sim 0.2 \times 0.2$	

Table 1.6: Main parameters of the ATLAS calorimeters.

electrode. The EM Endcap Calorimeter (EMEC) is placed inside the endcap cryostat. The EMEC, which covers the range uses the same technique as in the barrel part. In the EMEC, the absorber plates are separated by 8.5 mm gaps filled with liquid-argon and a structure of three electrodes that divide the gap into four drift spaces of ~ 1.8 mm. The EM calorimeter is segmented in three longitudinal samplings in the $|\eta| < 2.5$ region and in two samples in the $|\eta| > 2.5$ region, as shown in Figure 1.14. The total thickness of the EM calorimeter is above 22 radiation lengths for the barrel and above 24 for the endcaps.

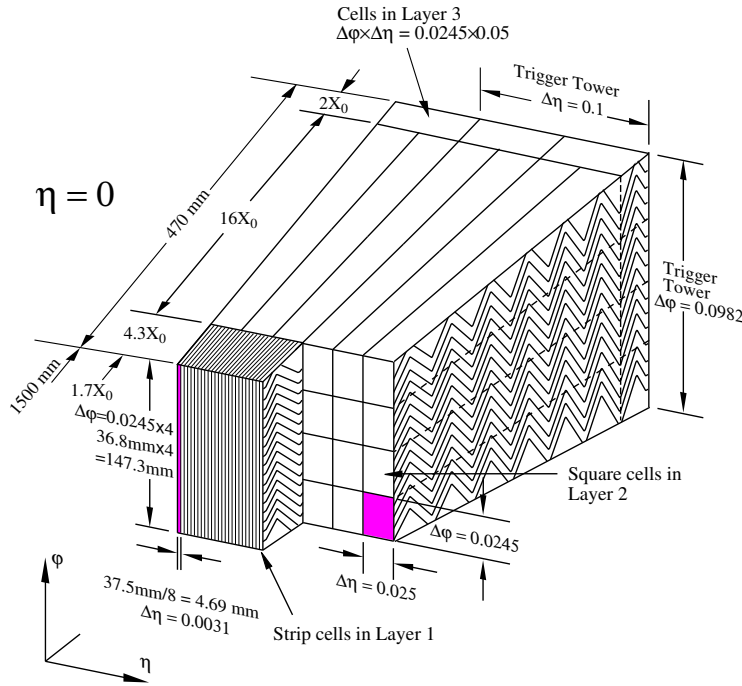


Figure 1.14: Diagram of a LAr EM calorimeter barrel module. It is shown the longitudinal segmentation, cell size is shown and the accordion structure.

The Hadronic Endcap Calorimeter (HEC) covers the range $(1.5 < |\eta| < 3.2)$. It has the same size in volume as the EMEC but it uses 50 mm copper plates as the absorber. Compared to iron, copper has a shorter interaction length and allows to increase the size of liquid-argon gaps between plates, thereby reducing the electronic noise, the integration time and pile-up noise.

The Forward CALorimeter (FCAL) covers the range $(3.2 < |\eta| < 4.9)$. It is a high density detector in order to accommodate at least 9 interaction lengths of active material in a short longitudinal space. Each forward calorimeter is

divided into three longitudinal sections. In the first section the absorber is copper while in the second and third sections tungsten is used. The calorimeter consists of a metal matrix (the absorber) filled with rods (electrodes). The liquid-argon is the active medium and fills the gaps between the matrix and the rods.

Tile Calorimeter

The Hadronic Tile Calorimeter covers the range $|\eta| < 1.7$. It is based on a sampling technique where plastic scintillator plates (tiles) are embedded in an steel absorber structure as shown in Figure 1.15. The innovative feature of this calorimeter is that the plates are disposed perpendicularly to the beam axis. Each tile is read-out on both sides by wavelength shifting (WLS) fibers. Groups of tiles are bundled together into cells, each of them is read-out by two photomultiplier tubes (PMTs). Figure 1.12 shows the layout of the Tile Calorimeter within the rest of calorimeters.

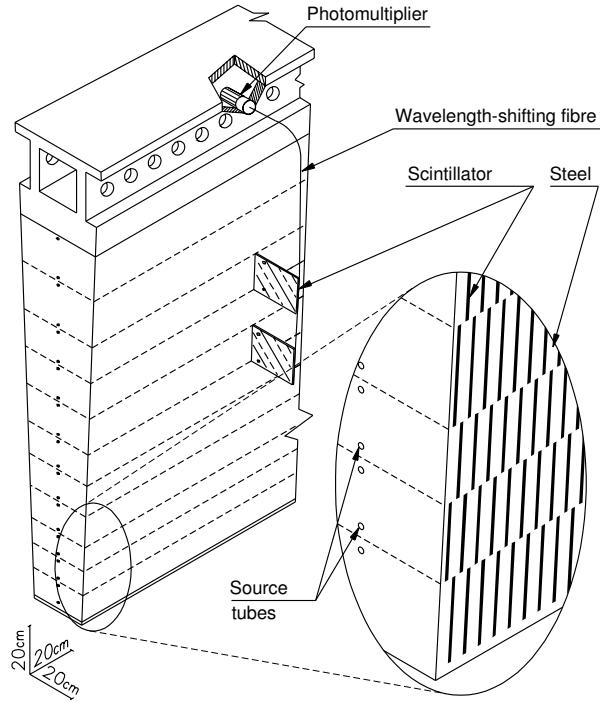


Figure 1.15: TileCal module components and structure.

The Tile Calorimeter is a hollow cylinder with an inner radius of 2.28 m

and an outer radius of 4.23 m. The length of the central Long Barrel is 5.56 m covering the range $|\eta| < 1$, and the length of the Extended Barrels is 2.91 m each covering the range $0.8 < |\eta| < 1$. Each barrel is assembled out of 64 wedge-shaped modules, staggered in the ϕ direction. There is a gap between the Long Barrel and the Extended Barrels of 0.6 m, which is needed for the Inner Detector and Liquid Argon Calorimeter services. A stepped calorimeter structure is placed in the gap region, the Intermediate Tile Calorimeter (ITC), which tries to maximize the active material in this region while leaving enough space for cables and services. The ITC consists of a plug calorimeter between $0.8 < |\eta| < 1$, and scintillators between $1 < |\eta| < 1.6$, divided into Gap scintillators, between $1 < |\eta| < 1.2$ and Crack scintillators, between $1.2 < |\eta| < 1.6$.

The Tile Calorimeter is radially divided into three layers (A, BC and D going outwards). The cell segmentation in $\Delta\eta \times \Delta\phi$ is 0.1×0.1 for A and BC type cells and 0.2×0.1 for D type cells as shown in Figure 1.16.

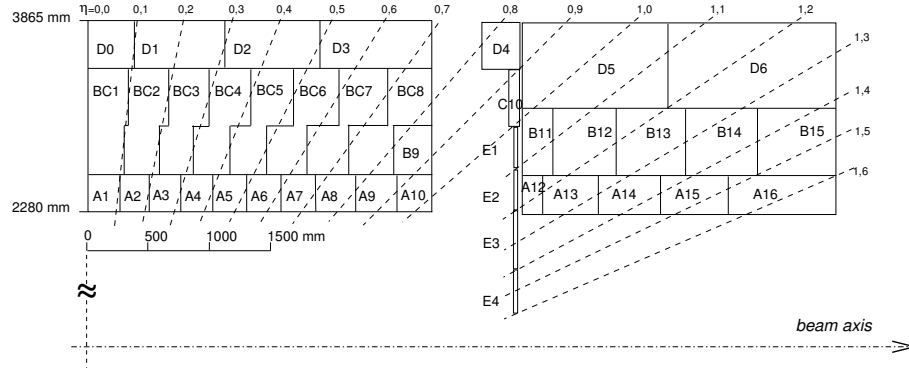


Figure 1.16: Scheme of the TileCal cell distribution for half of a long barrel module (on the left) and an extended barrel module (on the right) with lines that show the pseudorapidity projective distribution.

The PMTs and front-end electronics are located in the outer radius back-beam region of the calorimeter, placed in moveable drawers. Two drawers of 1.5 m long, which are combined together to form a super-drawer, are sequentially inserted from the two sides of the Long Barrel and from one side of the Extended Barrels. This gives name to the four front-end electronics partitions, LBA and LBC for the Long Barrel and EBA and EBC for the Extended Barrels. A total of 512 identical drawers are needed for the whole calorimeter. Each super-drawer can hold up to 48 PMTs, 45 are needed for each of the sides of the Long Barrel

and 38 for the Extended Barrels. It contains approximately 10000 read-out channels and it weighs around 2300 tons.

1.4 The ATLAS Trigger and Data Acquisition System

The ATLAS Trigger and Data Acquisition (TDAQ) system [1] is divided into two tightly coupled parts: The Trigger and the Data Acquisition (DAQ). The Trigger system selects events at three different stages of the DAQ: Level 1, Level 2 and Event Filter. This strategy allows the ATLAS Trigger to select interesting events from the very large background of QCD and minimum bias events produced by the LHC. For instance W production cross section is ~ 6 orders of magnitude smaller than the total p-p cross section. The Trigger selection as a whole is designed to reduce the event rate from 10^9 Hz (40 MHz times 20 collisions per bunch crossing) to 10^2 Hz.

The Level 2 trigger and the Event Filter form the so called High Level Trigger or HLT. The Level 1 trigger is implemented using custom-made electronics, while the HLT is software based and uses almost entirely commercially available computing and networking hardware. The DAQ is responsible for the data flow from the sub-detector to the Level 2 trigger and to the Event Filter. A simplified block diagram of the TDAQ is shown in Figure 1.17.

1.4.1 Level 1 Trigger

The core of the Level 1 Trigger is the Central Trigger Processor (CTP). It performs the Level 1 Trigger selection based on information from calorimeters and muon detectors. The Trigger menu can be programmed with up to 256 distinct items, each of them being a combination of requirements on the input data. The Trigger decision, together with the 40.08 MHz clock and other signals, is distributed to the detector front-end and read-out systems via the Timing, Trigger and Control (TTC) system, using an optical-broadcast network. The design rate of the Level 1 Trigger acceptance is 75 kHz (upgradeable to 100 kHz). The latency of the Level 1 Trigger, time between the detection of the particle and the decision Trigger, is less than 2.5 ms. During that time, the events

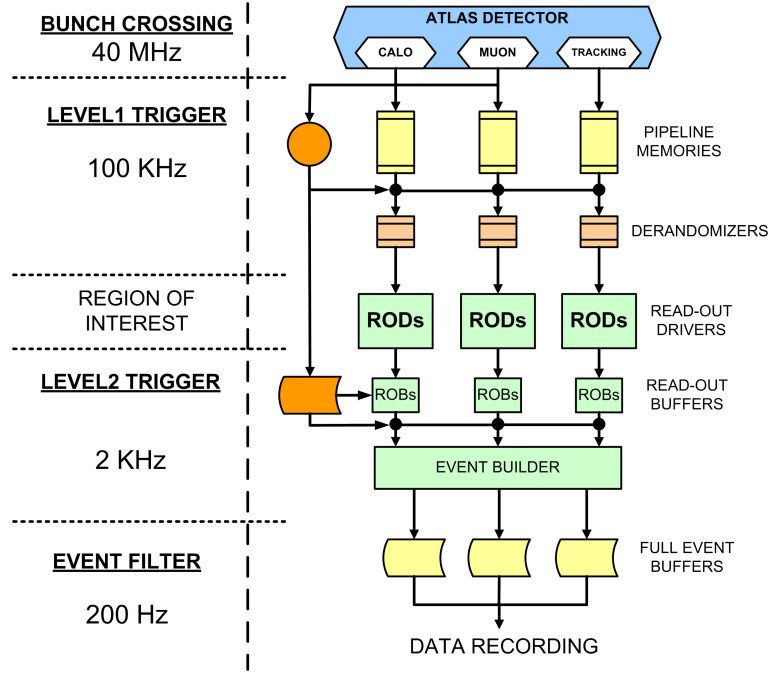


Figure 1.17: ATLAS data acquisition system and trigger levels.

are buffered in the front-end electronics in pipeline memories. Almost 1 ms of this time is accounted for cable propagation delays. Due to this constraint, the Level 1 Trigger is implemented in state-of-the-art hardware processors. For each Level 1 Trigger acceptance, the geometrical Region of Interest (ROI) associated to the event is propagated to the Level 2 Trigger, where it is used as seed for the following Trigger algorithms. The flow of the L1 trigger is shown in Figure 1.18.

Calorimeter Trigger

The Level 1 Calorimeter Trigger (L1Calo) is a pipelined digital system designed to work with the trigger towers from the calorimeters, electromagnetic and hadronic. A trigger tower corresponds to a summation of the trigger signals in a projective cone from the interaction point. Trigger towers are of reduced granularity, $\Delta\eta \times \Delta\phi = 0.1 \times 0.1$ in most regions, but larger for high values of $|\eta|$.

L1Calo searches for electrons/photons with high momentum in the transverse plane to the beam axis (transverse momentum, p_T) and tau leptons with high transverse energy computed with a look-up-table, above a programmable

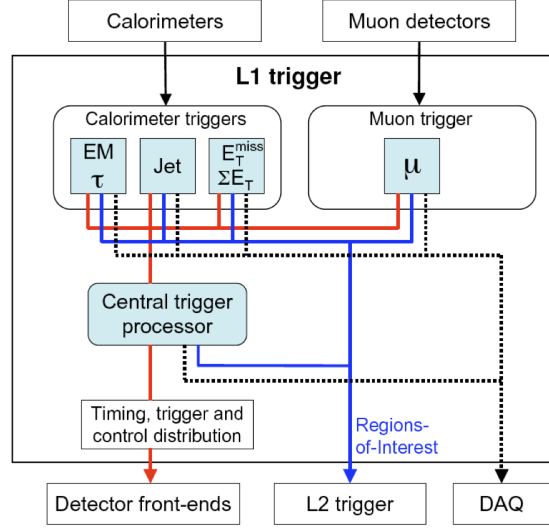


Figure 1.18: Block diagram of the Level 1 Trigger.

threshold and satisfying certain isolation criteria. Isolation implies that the energy deposition must have a minimum angular separation from any other significant deposition.

It also searches for jets given the same transverse energy computation, with an angular resolution of $\Delta\eta \times \Delta\phi = 0.2 \times 0.2$, and produces global sums of scalar and missing transverse energy.

All this information is fed into the CTP every bunch crossing. Upon the Level 1 Trigger acceptance, the L1Calo transfers a fragment containing trigger information into the Read-out System and into the application in charge of creating the Regions Of Interest (ROI) for the HLT, the ROI builder.

Muon Trigger

The Level 1 muon Trigger is based on signals in the muon trigger chambers: RPCs in the barrel and TGCs in the end-caps. The trigger searches for patterns of hits consistent with high p_T muons originating from the interaction region. The logic provides six independently programmable p_T thresholds for each trigger chamber.

The information for each bunch-crossing used in the Level 1 Trigger decision is the multiplicity of muons for each of the p_T thresholds (muons within different

thresholds are not double-counted). The trigger signals from the barrel and the muon end-cap trigger are combined into one set of six threshold multiplicities for each bunch crossing in the muon to CTP interface (MuCTPi), before being passed on to the CTP itself.

Read-Out System

The Read-out System (ROS) receives event data from the detector RODs via 1574 Read-out Links (ROL). All of the ROLs have the same design and implementation, based on CERN's S-Link interface [9]. The ROS is a server class PC which houses up to twelve Read-out Buffers (ROB). Each ROB buffers the data from a specific (η, ϕ) region at the Level 1 Trigger rate.

A special type of ROS that collects summary data from the Trigger and not data from the detector, is called a pseudo-ROS. It acts as any other ROS application in the data-flow.

The data per event can receive three types of request. Upon a Level 2 request, data is copied from the ROB and transferred to the Level 2. Upon an Event Building request, the data is transferred to the Event Builder and erased from the memory. Upon a clear request, the data is erased from the memory.

1.4.2 Level 2 Trigger

The Level 2 Trigger bases its decision on a subset of data from the event defined by the ROI. The ROI builder, that is operating at Level 1 Trigger rate, collects the information from the Level 1 Trigger sources and builds a ROI. This ROI is used as a seed for the Level 2 Trigger. The Level 2 Supervisor (L2SV) distributes the ROIs accross the Level 2 Processing Units (L2PUs).

At a first stage, the L2PUs request the data only from the Read-out Buffers (ROB) that contain the data for the given ROI. If the Trigger algorithm confirms the request, it can increase the data request up to 12% of the whole event. The summary information of the L2PU result is packed as data fragment and transmitted to a pseudo-ROS of the Read-out System, which makes it available for the Event Building. The Level 2 Trigger decision is transmitted back to the L2SV. After all Level 2 Trigger algorithms have finished, the L2SV sends the Level 2 decision to the Data Flow Manager (DFM).

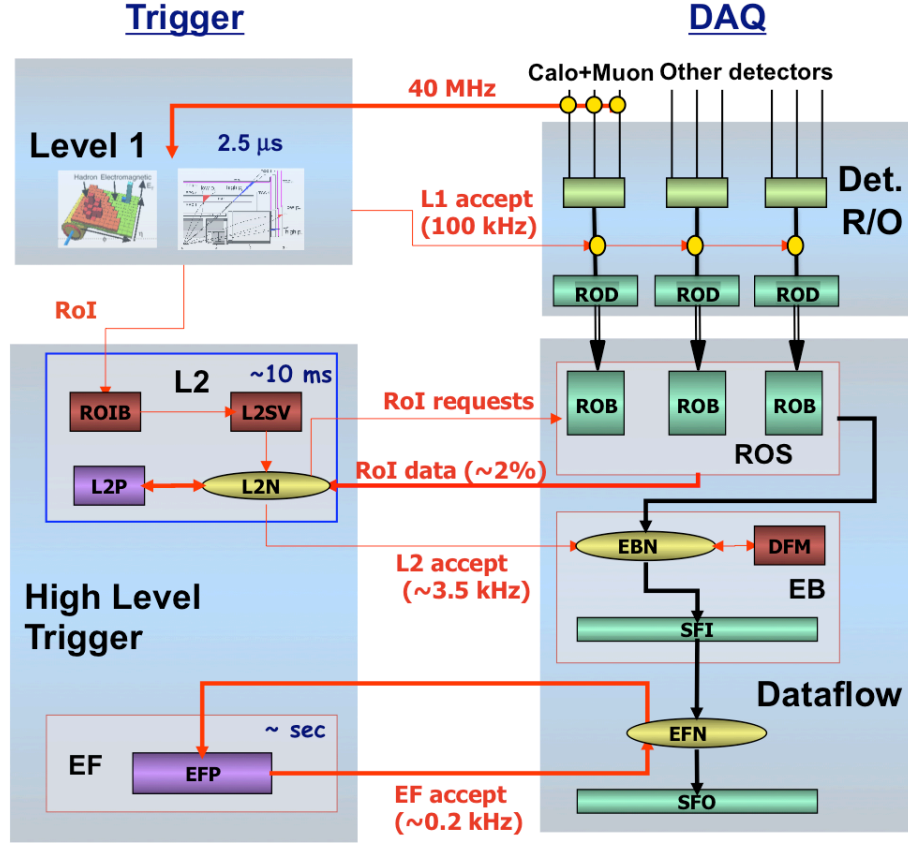


Figure 1.19: Block diagram of the DAQ HLT architecture.

The Level 2 Trigger reduces the event rate to below 3.5 kHz, with an average event processing time of approximately 40 ms. The failure of one or more L2PUs during run time does not incur in system down time. The system continues to operate at a reduced rate while the L2PU is restarted.

Event Building

The Event Building (EB) facility is divided into Sub-Farm Input (SFI) applications that build the event with the full information and Sub-Farm Output (SFO) applications that store the events locally. They are inter-connected by a network switch together with the Event Filter which makes the event selection on whole events. The number of events built does not have to match the number of events recorded, as they might not pass the Event Filter cut. The DFM receives the Level 2 Trigger decision and sends an EB request to a given SFI. Each SFI

requests the data from all the ROSs and builds a whole event. Each SFI informs the DFM of its readiness to receive data to ensure the load balance across all SFIs.

1.4.3 Event Filter

The Event Filter is implemented as a processing farm. Each node of the farm has a configurable number of independent Processing Tasks (PT) executing an HLT algorithm, which is looking for physics signatures like di-jet candidates or high p_T leptons.

Each node polls the SFIs for whole events to search for those worth keeping in a given stream. The Event Filter reduces the event rate to approximately 200 Hz, with an average event processing time of order of three seconds. According to the physics stream, the events are transferred to the SFO application storing that particular stream. As for the other Trigger levels, the result of the Event Filter is stored with the data, allowing sub-sequent offline analysis to rely on the decisions of the online Trigger system.

Event Output

The main functionality of the Event Filter output nodes (SFOs) is to receive events which have passed the event filter selection criteria, interface the DAQ/HLT to CERNs central data-recording facility, and de-couple the data-taking process from possible variations in the central data-recording service. The SFO maintains, locally, a set of files into which it records events at a peak event rate of up to 400 Hz. In the eventuality of a prolonged failure in the transmission of data to CERNs central data recording service, there is sufficient local storage capacity to buffer all events locally for up to 24 hours. Under normal operating conditions, this storage capacity is only partially used. The set of files maps to the ATLAS-defined data streams: electrons, muons, jets, photons, E_T^{miss} and τ -leptons, and B-physics. Each event is recorded in one or more files according to the stream classification made by the Event Filter configuration.

In addition to the data streams mentioned above, a subset of the events is also written to calibration streams and an express stream. The express stream is a subset of the events selected by the event filter and fulfils additional criteria

which select the events as being useful for monitoring the quality of the data and the detector. The calibration stream provides the minimum amount of information needed for detector calibration, possibly at a rate higher than the data streams provide. These events will only contain a subset of the event data.

1.5 Tile Calorimeter Electronics

This section is an overview of the electronics for the Tile Calorimeter, which are referenced in Chapter 2 to describe the software. It is divided into the front-end electronics which are those installed on the detector, and back-end electronics, which are installed in the counting rooms of the ATLAS cavern, in a low radiation environment. The communication between the front-end and the back-end electronics is done via redundant optical links, which are of two types: Write only, used for Trigger Timing and Control, and read only, which are used for Read-out. Figure 1.20 shows a block diagram of the Tile Calorimeter electronics.

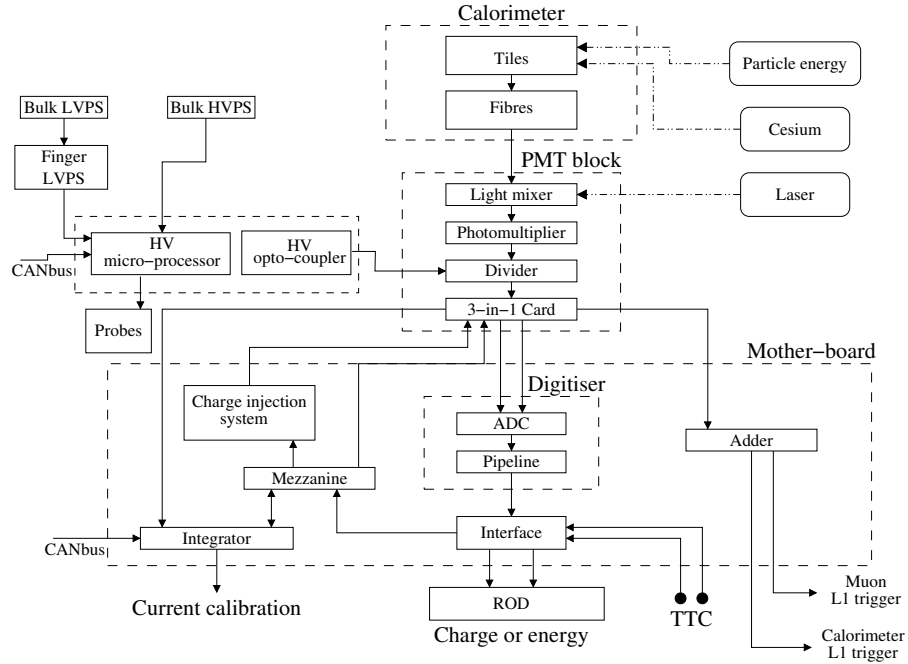


Figure 1.20: Block diagram of Tile Calorimeter electronics.

The Tile Calorimeter counts on three calibration systems which aim for the

calibration of the cell energy to the electromagnetic scale. Each calibration system acts on a specific element inside the read-out chain as shown in Figure 1.20. The derived calibration factors are combined together to obtain the ulterior calibration for each read-out channel.

The Charge Injection System (CIS), injects a known charge in the 3-in-1 cards prior to the signal digitization. This allows the calibration of the signal from ADC counts to pC in two gains that cover the full expected dynamic range. The Laser System sends a LASER pulse with known intensity to the PMTs. It provides a correction for the gain linearity and stability over time. The Cesium System acts on the optics elements by means of a ^{137}Cs radioactive source which is circulated through the calorimeter. It is used to correct for non-uniformity of the optics response. These corrections are computed from the response of the PMTs to the source photons after the equalization via the high voltage settings from their nominal value.

1.5.1 Front-End Electronics

The front-end electronics is contained in moveable drawers located in the outer radius beam back region of the calorimeter. Two drawers form a super-drawer which is inside each of the two sides of the Long Barrel and on one side in each of the two Extended Barrels. The super-drawer consists of several subsystems: the PMT blocks, the motherboards, the digitizer boards, and the optical interface board.

The PMT block

The function of a PMT block is to convert the light from the scintillating tiles into analog signals. Each PMT block is composed of four parts: a light mixer, a photomultiplier tube, a high voltage divider and a 3-in-1 card as shown in Figure 1.21.

The PMT blocks are located in holes inside the rigid aluminium structure of the drawers and are inserted in a μ -metal cylinder to provide magnetic shielding of up to 200 G in any direction. A light mixer is placed between the fiber bundle and the photocathode to mix the light coming from the fibers, so that there is no correlation between the position of a fiber and the area of the photocathode

which receives the light. The photomultiplier employed is a Hamamatsu R5900, which is very compact ($28 \times 28 \times 28 \text{ mm}^3$) and its dinode structure incorporates between 8 and 10 amplification stages. The rise time is around 1.4 ns, which provides a fast response to the excitation. The operation voltage of the photomultiplier is around 800 V, which is below the limit of ATLAS requirements (1000 V), and its sensitivity to magnetic fields and non-linearity ($\sim 1\%$) are very low.

The high voltage divider is a printed circuit with surface mounted device components which is attached to the 3-in-1 card. The high voltage is distributed in two steps, in the first step, a high voltage power supply provides a single source of 1 kV with a current of 10 mA to each super-drawer, in the second step, optocontroller boards mounted on the drawer distribute the power to each PMT with an adjustable voltage of 400 V.

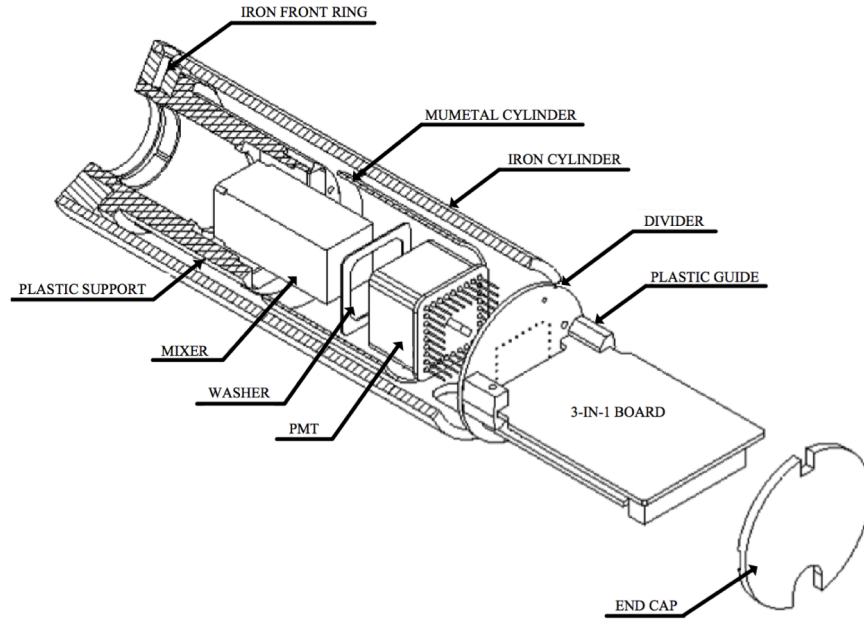


Figure 1.21: Scheme of a TileCal PMT block.

The 3-in-1 card [10] is a 7 cm by 4.7 cm printed circuit board, which implements most of the analog functions of the front-end electronics, and it is also located inside the steel shield of the PMT block. A shaping functionality of the PMT pulse removes the pulse to pulse signal shape fluctuation in the raw

PMT pulse producing a standard signal shape for all channels. The shaped signal is passed to two operational amplifiers that produce two signals with a relative gain ratio of 64, corresponding to a low and a high gain range. The amplified signals are then passed to differential drivers which send them to digitizer boards. In addition to the low and high gain outputs a differential fast trigger signal, derived from the low gain output is sent to the trigger sum boards mounted on the motherboards in order to produce trigger tower sums.

The 3-in-1 card provides a Charge Injection System (CIS) which allows the injection of a known charge into the input of the shaper that covers the full dynamical range. Two capacitors (5.1 pF and 100 pF) are controlled by fast switches. When the switch is closed, a fast pulse is sent through the shaping network. The 100 pF capacitor produces a signal that can cover the full 800 pC range, while the small 5.1 pF capacitor provides a up to 40 pC, suitable for the high gain channel.

The 3-in-1 card also provides a slow integrator amplifier, which averages over a time period of 10 ms the DC level of the PMT signal. This signal is multiplexed onto a bus on the motherboard and sent to the Integrator card which contains a microprocessor, an ADC, and a CANBUS interface. It digitizes the integrator signal level and transmits the data to the counting room via CANBUS. These signals are used in the radioactive source calibration of the PMT signals and Minimum Bias monitoring.

The Motherboard

The motherboard is the basic element that holds together all the electronics in a drawer. There are two motherboards in a super-drawer. It provides power and Timing Trigger and Control commands to the 3-in-1 cards, and hosts up to 4 digitizer boards and one interface board.

The Digitizers

Each digitizer board reads out data from up to six PMT blocks. The digitizer receives the high and low gain signals from six 3-in-1 cards, which are digitized every 25 ns by 10-bit ADCs, using a clock that can be adjusted in units of 106 ps. The digitizer is equipped with two Tile Data Management Units (DMU), which

1.5. TILE CALORIMETER ELECTRONICS

are a custom ASIC chips which temporarily store the data in pipeline memories. The digitized samples from three PMTs are processed by one TileDMU. The pipeline length is programmable up to 256 samples giving a pipeline latency of up to $6.4 \mu\text{s}$, which is considerably longer than the $2.5 \mu\text{s}$ ATLAS requirement. The latency is needed to allow the Level 1 Trigger system receive the Trigger information, make a decision and return Level 1 accept trigger signal to the digitizer system.

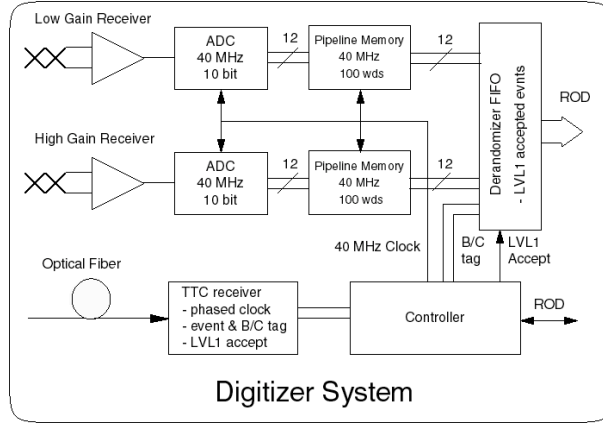


Figure 1.22: Block diagram of the digitizer system.

Each digitizer board is also equipped with one TTCrx chip responsible for system timing and programming. There are 8 digitizer boards in each Long Barrel super-drawer, that read-out 45 PMT blocks, and 6 digitizer boards in each Extended Barrel super-drawer, that read-out 32 PMT blocks.

The Interface Board

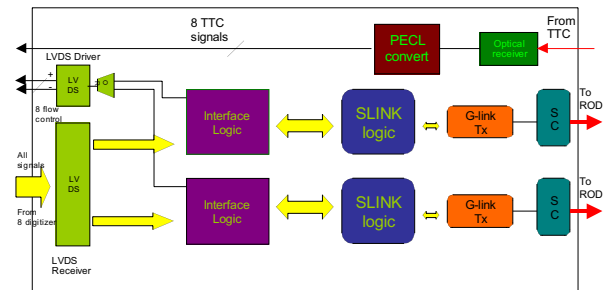


Figure 1.23: Block diagram of the Interface board.

The optical interface board [11], which is placed in the middle of the super-drawer, receives the TTC optical signals and distributes them to the rest of components inside the drawer. It collects the serial data streams from the 16 TileDMU chips in the super-drawer through an LVDS bus that uses a 2-bit stream of each TileDMU. Data is realigned to a common clock, packed into 32-bit words, and temporarily stored in an event frame which is sent via G-link transmitters (HDMP-1032 from Agilent Technologies) to the back-end electronics through two redundant optical links at 640 Mbit/s. Figure 1.23 shows the block diagram of the Interface board.

Cyclic Redundancy Checks (CRC) are performed on the data link between the digitizers and the interface board. A global CRC is computed on the event frame before transmission. The interface board memory holds a maximum of 16 physics event frames.

1.5.2 Back-End Electronics

The back-end electronics is organized in four partitions, two servicing the read-out of the Long Barrel and two servicing the read-out of the Extended Barrels. Each back-end partition is equipped with its own Trigger Timing and Control (TTC) and Read-Out Driver (ROD) units. These units are physically split into a 6U VME ancilliary crate, so called TTC crate, and an 9U VME and read-out crate, so called ROD crate.

Figure 1.24 shows a picture of the Tile Calorimeter back-end electronics racks. Left rack contains the TTC and ROD crates for side A of the detector, LBA (top) and EBA (bottom), the rack on the right contains the TTC and ROD crates for side C of the detector, EBC (top) and LBC (bottom). The center rack hosts the TTC optical couplers (TTCoc) which split the TTC optical signals from 1 to 32 links. It also houses the patch panel for the front-end optical links, all TTC and read-out links from the detector are connected to the back of the patch panel. Short optical fibers are routed from the front of the patch panel to the back-end electronics.

ATLAS standard VME modules are placed in the ancilliary crate, along with specific modules for the Tile Calorimeter. VME modules that are common to all calorimeters are placed in the read-out crate. The modules in the crate



Figure 1.24: Picture of the back-end electronic crates.

are controlled by a Single Board Computer (SBC) 6U VME module. This SBC is a VP-110 model from Concurrent Technologies [12] which is standard for all ATLAS. Each of the VME modules is briefly described in the following paragraphs.

Trigger Timing and Control Modules

The ATLAS Local Trigger Processor (LTP) receives timing and trigger signals from the CTP and injects them into the TTC system of the sub-detector. The LTP allows also stand-alone running by using local timing and trigger signal sources or by internal signal generation. The LTP can pass on signals to a

sub-sequent LTP in a daisy-chained manner.

The ATLAS Local Trigger Processor interface (LTPI) is a VME module that interfaces multiple LTP modules with the CTP. The LTPI allows communication with other sub-detectors.

The ATLAS Trigger Timing and Control VME bus interface (TTCvi) is a VME module that interfaces the local TTC system to the global TTC system. It delivers A and B Channel signals to the TTC transmitters for multiplexing, encoding, optical conversion and distribution to the TTCrx chips associated with the front-end electronics controllers. The TTC channel A is used to transmit the Level 1 Accept (L1A) signal. The TTCvi incorporates a programmable L1A source selector and an internal trigger emulator for test purposes. The TTC channel B is used to transmit framed and formatted commands and data, which can be synchronous or asynchronous with respect to the LHC clock.

The ATLAS Trigger Timing and Control emitter (TTCex) module is a laser transmitter module. Converts the TTCvi commands into optical TTC signals that arrive to the front-end electronics. It provides 10 optical outputs at a level ~ 0 dBm. The optical outputs of the TTCex are fanned out by a 1:32 optical coupler (TTCoc) to broadcast to a total of 320 destinations.

The ATLAS ROD Busy module monitors the busy, measures it in Bunch Crossing units, and produces the sum of each of its 16 busy input lines, which can be conveniently masked. The ROD Busy module generates a VME interrupt after a programmed time-out. In the Tile Calorimeter specifications, it receives the busy signal from the Trigger and Busy Module and the TTCpr card. The busy output is sent to the LTP busy input.

Shaft Module

The Shaft module is a 6U VME module which controls the different calibration trigger requests foreseen in the Tile Calorimeter. It is a specific VME board to share the calibration requests during physics runs. Each calibration request can be enabled and its firing timed with respect to the TTC signal that clocks the turn of the LHC beam.

Trigger Timing and Control Receiver in PMC Form Factor

The Trigger Timing and Control PMC form factor Receiver (TTCpr) [13] is a Tile Calorimeter specific card. It is plugged in to the Single Board Computer (SBC) of the TTC crate, which is used to make available the TTC information in the TDAQ framework for calibration runs. It was designed to provide Event ID, Bunch Crossing ID, and Trigger Type for each event in the data records. It provides a busy signal which is connected to the ROD Busy module.

Trigger and Busy Module

The Trigger and Busy Module [14] is a 9U VME module for the ROD crate. It receives TTC signals from an optical link from the local TTC system. The signal is propagated to each ROD module through the P3/J3 connector, using the CP3 plane in the ROD crate. The TBM also gathers the busy signals through the CP3 from the eight RODs in the crate, and provides a busy signal to the ROD Busy module.

Laser Read-Out Driver

The Laser Read-out Driver is a 6U VME module that provides information from the Laser calibration system into the data-flow, and furnishes TTC signals to the Laser system. It is equipped with a HOLA [15] card which provides data fragments to a Read-out Buffer of the Read-Out System of LBC through a Read-Out Link.

Read-Out Driver

The Read-Out Driver is a 9U VME module that receives data from the super-drawers, through eight front-end links, each corresponding to one super-drawer. It is equipped with two Processing Units which compute the energy and time of each read-out channel, and it is coupled to a Transition Module [16], placed behind the Read-Out Driver, which receives data fragments through the P2 and P3 connectors of the crate. The Transition Module is equipped with two HOLA cards which transmit data fragments to the Read-Out System through Read-out Links.

Eight Read-Out Drivers are installed in the ROD crate. Front and rear views of the ROD crate are shown in Figure 1.25. A picture of a ROD motherboard is shown in Figure 1.26.

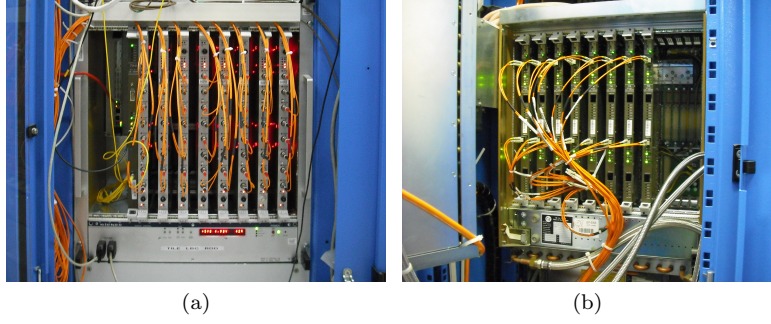


Figure 1.25: Pictures of the front (a) and rear (b) views of the ROD crate.

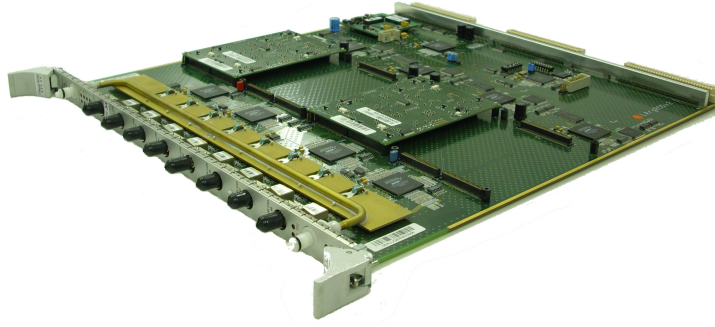


Figure 1.26: TileCal ROD motherboard picture.

The components of the ROD are described in the following paragraphs. A review of the operation of the ROD is done in Section 2.2.

Optical Receivers The data coming from the front-end links are received in the Optical Receivers located in the front panel of the ROD. There are 8 Optical Receivers mounted on each ROD and each one receives data from one super-drawer.

HDMP-1024 deserializers The signal coming from the Optical Receivers is deserialized with 8 G-Links. The G-Link used in the ROD is the HDMP-1024 device from Agilent Technologies. The G-link clock is 40 MHz, providing a ROD input data bandwidth of 5.12 Gbps.

Staging FPGA The Staging FPGA distributes the data from the deserializers to the Processing Units. There are four Staging FPGAs on each ROD, each one manages the data from two front-end links. It is possible to route the data from two Staging FPGAs to the other two. In the Tile Calorimeter specifications, the data from four front-end links is routed to one Processing Unit.

Processing Units The ROD Processing Unit (PU) is a mezzanine card equipped with two Input FPGAs, two DSPs and one Output FPGA. The Output FPGA provides interface with the rest of the ROD. The Input FPGA receives data from two front-end links, which is checked and formatted for DSP processing. The data is processed by the DSP and stored in an external FIFO. The DSP has an input buffer where it is possible to store up to 16 events. The busy is raised when the input buffer has more than 8 events and is freed when it has less. The busy signal is set by the DSP, transmitted to the Trigger and Busy Module, which propagates it to the ROD Busy module.

Output Controllers The Output Controller (OC) FPGA is the ROD output distributor. There are four OC mounted in the ROD but only two are used in the Tile Calorimeter specifications. Each OC reads out the data from one PU and builds a ROD data fragment. This fragment is sent to the HOLA S-Link LSC card located in the Transition Module.

TTC FPGA The TTC information distributed by the TBM to the ROD is decoded by a TTCrx chip and managed by the TTC FPGA which sends this information to the PUs. The TTC FPGA has different trigger operation modes.

VME FPGA The VME FPGA of the ROD provides communication between the ROD crate controller and the rest of the devices in the ROD. This communication allows configuration tasks, such as configuration of the PUs or remote access to the Joint Test Action Group (JTAG) chain. The busy logic and monitoring system is also implemented in the VME FPGA.

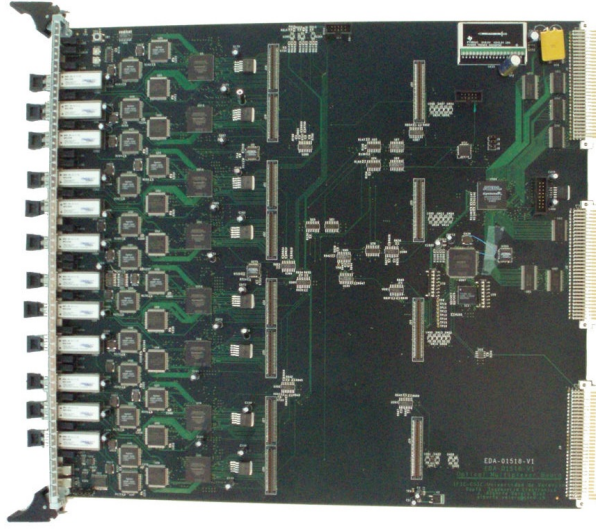


Figure 1.27: TileCal Optical Multiplexer Board picture.

Optical Multiplexer Board

The data from the front-end is transmitted to the back-end through two redundant read-out optical fibers. Such a redundancy is mandatory in a long lived experiment as ATLAS, in order to prevent data corruption due to single bit upset caused by radiation. To exploit this redundancy, the Optical Multiplexer Board [17] has been produced by the TileCal-Valencia group in collaboration with the DSDC group of the *Dpto. Ingeniería Electrónica, Universitat de València*. This 9U VME module will select data from one of the two front-end links and transfer it to the ROD. It can also be used to inject data to the ROD for test purposes. The installation of this board is scheduled for the long shutdown of 2012.

Chapter 2

The ROD Crate DAQ for the Tile Calorimeter

In the previous Chapter we briefly introduced the Tile Calorimeter, starting with the detector segmentation, tiles, wavelength shifting fibers and photomultiplier blocks, followed by a description of super-drawers, front-end electronics and finally back-end electronics.

As an introduction to this Chapter, we will first describe the read-out chain, from the operational point of view, simplifying the complexity into concepts easier to understand. There are many concepts which are coupled between hardware, electronics, trigger and data acquisition, which can be reviewed in [1]. The attention is focused on the Read-Out Drivers, for which the author has been responsible for installation, commissioning and operation under physics running conditions. These were also used for the commissioning and refurbishment campaigns of the front-end electronics.

The aim of the first part of this Chapter is to present the Tile Calorimeter online software used in the operation of the detector which is built on top of the TDAQ software, without overwhelming the reader. Details can be found in [18]. This work has been almost entirely developed by the author during the past five years. During this time, the author has been co-responsible of the DAQ development team for the Tile Calorimeter at CERN. He has been in charge of organizing regular meetings and participating in the combined data

taking efforts, where he has played the role of the ROD DAQ expert for the Tile Calorimeter.

The second part of the Chapter will cover the performance of the Tile Calorimeter online software during the initial operation of the LHC, and the results achieved on the online energy and time reconstruction with real data controlled and monitored by this software. These results are part of the outcome of the Tile Signal Reconstruction Validation task force, in which the author has been actively involved.

2.1 Tile Calorimeter Read-out Chain

Multiple particles produced in the interaction point travel through the Tile Calorimeter. These produce light in the scintillating tiles as they deposit their energy. Light is turned into visible blue by wavelength shifting fibers and guided to photomultiplier tubes. The photomultiplier generates analog pulses which, after a process of amplification and shaping in the 3-in-1 cards, are summed in groups of five. The analog sums sent to the Level 1 Calorimeter Trigger (L1Calo), through trigger cables. The analog pulses were received by the digitizers where the signal is converted into digital samples every 25 ns, which are finally stored in the front-end pipeline memory, the so called Data Management Units (DMU). The Central Trigger Processor (CTP) of the Level 1 Trigger processes the trigger information and selects the Bunch Cross Identifiers (BCID) that are worth keeping at a mean rate value of 75 kHz. It sends a request for the given BCID and a Level 1 accept (L1A) signal to the front-end electronics in the form of Trigger Timing and Control (TTC) signals.

The detector back-end electronics, which is split into four independent replicas, each one with its own TTC and read-out crates, receives the TTC signals from the CTP via the Local Trigger Processor (LTP) and distributes them to the front-end through optical links. Yet another TTC link is used as a feedback and re-connected to the back-end electronics. The TTC signals are distributed inside the super-drawer to the DMUs as shown in Figure 2.1. Each time a DMU receives a L1A the samples for the given BCID are sent to the interface board. The interface board builds up a data fragment containing the samples from all

channels (PMTs) in the super-drawer and transfers it through optical links to the back-end electronics.

The data flow rate is dynamically regulated via the busy feedback from the back-end electronics. The busy signal, generated in the read-out is combined together in the ROD Busy module and trasfered through the LTP to the CTP. This introduces dead time in which the CTP cannot request new events.

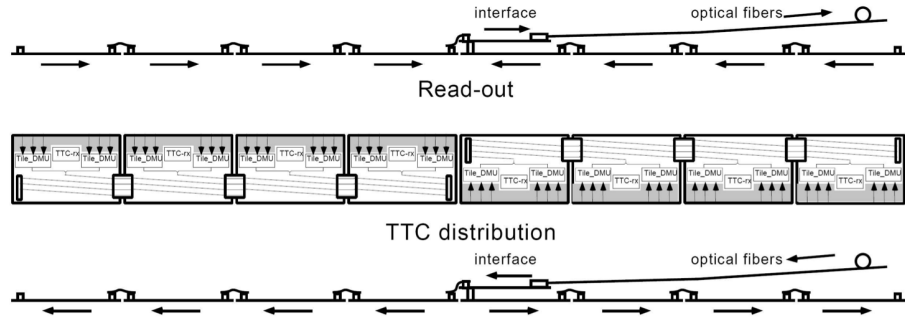


Figure 2.1: Schematic diagram of the TTC distribution and Read-out of a super-drawer.

2.2 The Read-Out Driver

The Read-Out Driver (ROD) is the central element of the back-end electronics. It has a sub-detector specific design, but it interfaces with the Read-Out System (ROS) through the ATLAS wide standard protocol, S-Link. The main goals of the ROD are:

- Data processing: gathering of raw data from the front-end pipeline memories at nominal Level 1 Trigger rate of 100 kHz. Computation of energy, time and quality factor, and packing and transmission of the data within 10 μ s.
- Error detection: reception of TTC signals and matching of the received Bunch Crossing Identifier (BCID) with the one from the raw data.
- Busy generation: generation of busy signals when the ROD buffers are half full.

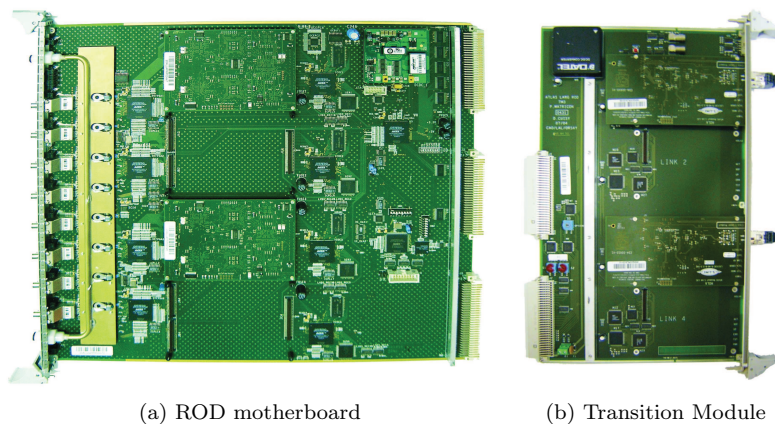


Figure 2.3: TileCal ROD motherboard and Transition Module pictures.

The Optimal Filtering algorithm [20], reviewed in Section 2.3, reconstructs the energy and time from the samples received for each read-out channel. The ROD is equipped with two Processing Unit daughterboards which implement two Digital Signal Processors (DSPs) for online reconstruction.

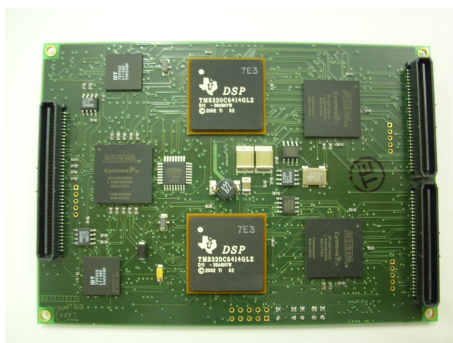


Figure 2.4: Tile Calorimeter Processing Unit daughter board picture.

The processing time for each read-out channel cannot exceed $10 \mu s$. Otherwise, it would raise the busy signal that would limit the maximum Level 1 Trigger rate. Thus, the performance of the reconstruction algorithms is an important factor. A full description of algorithms available in the DSP can be found in [21] and [22]. High performance tests were conducted on each ROD prior to their installation in the experimental cavern [23]. A picture of a ROD motherboard is shown in Figure 2.3.

2.3 Optimal Filtering

The Optimal Filtering algorithm reconstructs the amplitude and phase of a digitized signal by linear combination of its digital samples using weights calculated by the method of Lagrange multipliers. Details of the Optimal Filtering method can be found in [24]. The procedure to compute the amplitude and phase with the Optimal Filtering algorithm is given by the equations:

$$A = \sum_{i=1}^7 a_i S_i \quad (2.1)$$

$$\tau = \frac{1}{A} \sum_{i=1}^7 b_i S_i \quad (2.2)$$

where S_i represents the i -th digital sample. The pedestal, which is the baseline of the signal, can be either estimated as the average of the first and last samples, or calculated in a similar linear combination of the samples given by the equation:

$$p = \sum_{i=1}^7 c_i S_i \quad (2.3)$$

The amplitude, A , is the distance from the pedestal to the maximum of the reconstructed peak. The energy is proportional to A , and a calibration constant per channel must be applied to get the energy. The phase, τ , is defined as the time between the peak of the pulse (Figure 2.5) and the expected time of the pulse. This reference time is calculated for each channel with calibration systems and beam data, taking into account the time of flight of the particles from the interaction point and the length of the wavelength shifting optical fibers.

The weights, a_i and b_i are obtained from the signal pulse shape of the photomultipliers and the correlation of noise between the digital samples. The process to calculate them minimizes the effect of the noise in the amplitude and time reconstruction [25]. The linear combination constants are calculated in such a way that pedestal subtraction is not necessary. This is known as Optimal Filtering 2, as opposed to Optimal Filtering 1 where the pedestal, computed as the mean of the first and last sample, is subtracted to the samples.

The reconstructed energy as used by the High Level Trigger and the ATLAS

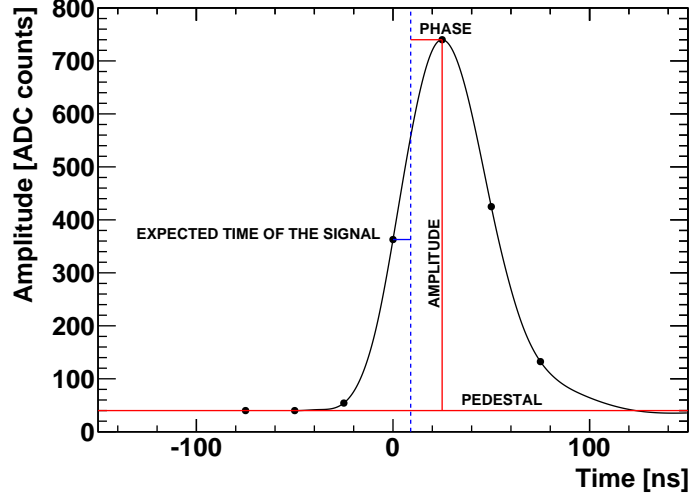


Figure 2.5: Optimal Filtering magnitudes.

offline software is given by:

$$E_{channel} = A \times C_{ADC \rightarrow pC} \times C_{pC \rightarrow GeV} \times C_{Cs} \times C_{Laser} \quad (2.4)$$

The signal amplitude A , described in more detail above, represents the measured energy in ADC counts as in equation (2.1). The $C_{ADC \rightarrow pC}$ is the conversion factor of ADC to charge and it is determined using a well defined injected charge with the CIS (Charge Injection System) calibration system. The $C_{pC \rightarrow GeV}$ is the conversion factor of charge to energy in GeV and it has been defined at testbeam for a subset of modules via the response to electron beams of known momentum. This is a global factor and has a layer dependence. The C_{Cs} corrects for residual non-uniformities after the gain equalisation of all channels has been performed by the Cs radioactive source system. The C_{Laser} , not currently implemented, corrects for non-linearities of the PMT response measured by the Laser calibration system. The derived time dependence of the last two factors will be applied to preserve the energy scale of TileCal

Moreover, Optimal Filtering allows one to calculate a Quality Factor (QF) defined as :

$$QF = \sum_{i=1}^7 (S_i - (Ag_i + A\tau g'_i + p))^2 \quad (2.5)$$

where g_i are weights obtained from the functional form of the pulse shape centered at the expected time of the pulse, g'_i are the weights obtained from the derivative of the same functional form of the pulse shape, and p is the pedestal of the signal.

The QF provides information about the goodness of the reconstruction. This information can be used online to decide to send raw data for single channels, that will allow a more refined offline reconstruction.

The Optimal Filtering explained here, is extended to an iterative version, that is used when the expected time of the signal is not fixed. The so-called Optimal Filtering with iterations is explained in Section 3.1.2.

2.3.1 Conditions Data

The several sets of weights (a_i, b_i, g_i, g'_i) required by the Optimal Filtering algorithm are different for different values of the expected time of the pulse. These are computed for different phases in steps of 0.1 ns inside the read-out window, from -75 to 75 ns. This step size is chosen so that the resolution of the time required in the Tile Calorimeter, which is 1 ns, is not dominated by the step size of the weights. As the pulse shape is different for physics, Laser or CIS events, up to three versions of the weights have to be computed. These weights are stored in the ATLAS COOL conditions database [26]. In order to download these weights for a given channel to the DSPs at configuration time, the expected time for the pulse is also required. This is the so called Best Phase in COOL.

The conditions database also hosts the calibration constants per channel, shown in equation (2.4), and other information like the channel status, which represents the goodness of each channel for physics, calibration or timing. It also contains the thresholds for the low p_T muon identification algorithm executed in the DSPs and the set of thresholds for the conditional dumping of the samples in physics runs.

The total payload per instance of the conditions data is around 50 MB. This increases proportionally with the number of copies needed for different reprocessing efforts.

2.4 Online Software

The Online Software is a part of the TDAQ system. It encompasses the software to configure, control and monitor the TDAQ, but excludes the processing and transportation of physics data. It is essentially the glue that holds the various sub-systems together. It does not contain any elements that are detector specific as it is to be used by all possible configurations of the DAQ and detector instrumentation. It coexists and cooperates with the other sub-systems; in particular, interfaces are required to the data flow, triggers, processor farm, event builder, detector read-out crate controllers and Detector Control System (DCS). The various components of the Online Software include:

- Inter Process Communication (IPC): The core communication service. It relies on the underlying TCP/IP message passing.
- Information Services (IS): The service that allows sharing of any kind of user defined information between applications.
- Configuration databases: The implementation of the database system used to describe the configuration.
- Process Manager: The service responsible for the execution of applications on the nodes.
- Access Manager: The service responsible for the access to resources and nodes for a given user.
- Resource Manager: The bookkeeping of allocated resources.
- Run control: The core Finite State Machine (FSM) service responsible for the structure of controlled applications.
- Monitoring: The online monitoring infrastructure.
- Integrated Graphical User Interface (IGUI): The friendly user interface with the run control.
- Expert System: The service that supervises the recovery actions.

2.4.1 The Partition

The TDAQ system has a modular architecture which may be subdivided in different ways, with each definition corresponding to a specific function [27].

- **TTC Partition:** A TTC partition comprises a part of the TTC system and the corresponding part of the busy feedback chain. A TTC partition corresponds to a single TTCvi module. There are four TTC partitions in the Tile Calorimeter, two in the Long Barrel (LBA and LBC) and one in each Extended Barrel (EBA and EBC). A detailed description of the ATLAS TTC partitions can be found in [28].
- **Resource:** A resource is a part of the TDAQ system which can be individually disabled (masked), and possibly enabled, without stopping the data taking process. A single Read-out Link in the Tile Calorimeter is an example of a resource (explained in detail in Section 2.5.2).
- **Segment:** A segment is defined as a set of TDAQ system elements that can be configured and controlled independently from the rest of the TDAQ system. A segment can be dynamically removed from / inserted into an active TDAQ partition without stopping the run. Each of the four TTC partitions of the Tile Calorimeter is represented as a TDAQ segment.
- **TDAQ partition:** This is a sub-set of the TDAQ system for the purpose of data taking. The full TDAQ functionality is available to a sub-set of the detector. A TDAQ partition corresponds to one or more TTC partitions.

TDAQ partitions can usually be operated simultaneously, depending on the maximum number of instances allowed for the used resources. Some resources are designed to have a unique instance across all partitions. This is the case of the detector instrumentation resources. A super-drawer cannot be in two contradictory states of the Finite State Machine (FSM) at the same time (i.e. powered and not powered). But, two super-drawers from two different TTC partitions could be in two contradictory states. There is one TDAQ partition that describes each TTC partition of the Tile Calorimeter in the configuration database. Yet another TDAQ partition includes the four TTC partitions, each one described in a different segment. This way, easy swapping between configurations may be achieved.

In ATLAS data-taking, each sub-detector is included into the ATLAS TDAQ partition as a different segment. These top level segments are organized into

further segments which describe the different TTC partitions and other over-all sub-detector segments, such as monitoring segments.

2.5 Tile Online Software

The Tile online software is the software used in the operation of the Tile Calorimeter, which is not provided by the TDAQ online software. It provides detector specific software for the back-end electronic crates, the steering mechanism for calibration runs and infrastructure to handle calibration events during physics runs, monitoring software at hardware level, so called verification system tests, and monitoring at the level of the read-out system.

The Tile online software does not make provision for Cesium calibration scans, which is handled by dedicated software extended from the Tile online software.

One of the central pieces of the Tile online software is the ROD Crate DAQ, which is supported by the Data Flow software, for which the Tile online software provides plug-ins. This keeps the programming efforts focussed on specific hardware handling, as the core software is centrally maintained.

The author contributed in the current production version of the ROD Crate DAQ, and design and implementation of most of its plug-ins for the Tile Calorimeter.

2.5.1 ROD Crate DAQ

The ROD Crate DAQ (RCD) framework is an extension of the ROS software that offers the possibility to integrate the handmade hardware into the general TDAQ software. The RCD is based on a multi-threaded read-out application core (See reference [29]) which loads specific plug-ins at runtime to adapt its behaviour to the detector specific needs. There are different plug-ins for different purposes. A schematic overview of the read-out application is shown in Figure 2.6.

- The Configuration plug-in loads the information from the configuration database and passes it to the RCD core application.

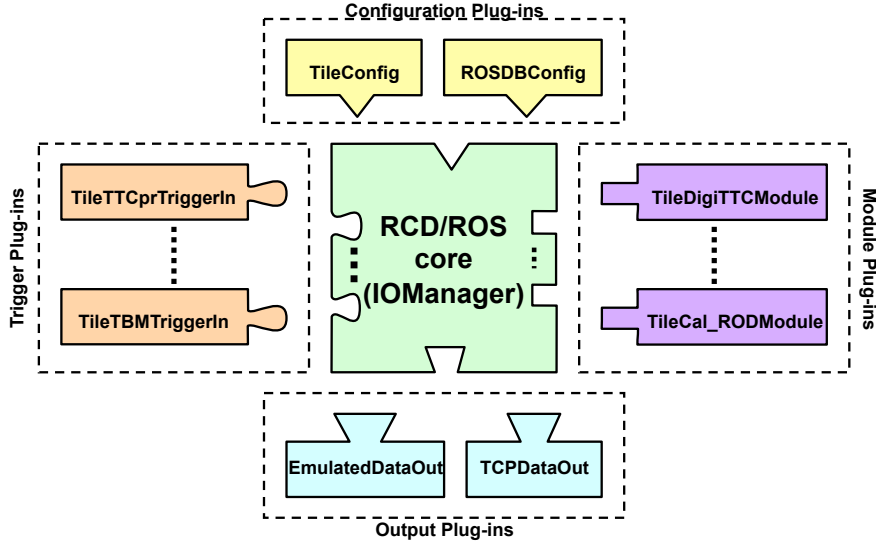


Figure 2.6: ROD Crate DAQ schematic diagram.

- The Trigger plug-in handles the trigger requests for data fragments. It runs as a separate thread that queues requests on a request list. A number of request handlers from the RCD dequeues them by executing the data requests that push the output information to the output plug-in.
- The Module plug-in is a controlled resource which receives transition commands from the RCD. In ATLAS operation mode it does not send data out to the output plug-in.
- The Output plug-in manages the output of the data which can be sent elsewhere through ethernet or written down to a file.

The RCD application is commanded by the run control service. When a run control transition command is sent by the user through the IGUI, a request for a state transition is sent to the RCD. The RCD reacts to the request and operates the controlled hardware according to the detector specific code. The relationships between the TDAQ run control FSM transition commands and RCD methods have been detailed before in [30].

The configuration required by the RCD is stored in the configuration database, which is an object oriented database which allows relationships between objects. To add an object in the configuration database, it must belong to a class

	RCD	Tile
Segments	4	9
Applications	9	29
Classes	15	18
Objects	30	50

Table 2.1: Details of the ROD Crate DAQ configuration. The RCD are a subset of the Tile which includes other applications for monitoring.

defined in the schema. The base schema is extended to describe the specific Tile Calorimeter classes. All hardware objects are described in the configuration database. Figure 2.7 shows a view of the classes used for the configuration of the RCD for the Tile Calorimeter. Boxes represent each class type, lines between classes indicate relationships between classes. Lines ended in arrows indicate the pointed class has been extended. Names beside a line indicate the name of the relationship. Pairs of numbers separated by dots indicate the minimum and maximum number of instances. Lines ended with a diamond indicate exclusive relationships. Once an object is linked to another via an exclusive relationship, it cannot be linked to any other object of the same type. Most of the RCD schema objects inherit from ReadoutModule.

The payload of the RCD configuration is listed in Table 2.1. The number of instances is quoted just for the Tile RCD configuration and for the entire Tile configuration.

An RCD application is represented in the configuration database by the RCD object. It loads the different plug-ins based on its attributes and relationships. The RCD retrieves the class name of the objects linked to it and dynamically loads the plug-in library with the same name. To access the objects stored in the configuration database, a programming interface is auto-generated from the schema classes. This is known as Data Access Libraries or DAL.

Configuration

A generic configuration plug-in called ROSDBConfig is available for its use with the RCD. In addition, there is a Tile Calorimeter specific configuration plug-in, TileConfig, exceptionally the TileDigiTTCModule plug-in uses TileConfig to retrieve the configuration of the super-drawers, instead of the generic one.

In particular, the trigger and module RCD plugins for the Tile Calorime-

Trigger

Specific trigger plug-ins are available for both TTC and ROD crates. These make use of sub-detector hardware such as the TTC PMC format receiver (TTCpr) [13] and the Trigger and Busy Module (TBM) [14].

TileTTCprTriggerIn

The TileTTCprTriggerIn is a trigger plug-in used in calibration runs. It waits for a L1A in the TTCpr input link and reacts to it. The TTCpr buffers the EventID, BCID, and trigger type associated to the L1A. When a L1A is received, the TileTTCprTriggerIn creates a data request and schedules it on the requested data fragments queue. The request handlers in the RCD retrieve the request from the queue and execute it. The executed request builds the data fragment which contains calibration information and pushes it to the data output plug-in. The busy is raised at the first event in and it is removed once the data has been moved out from the request queue.

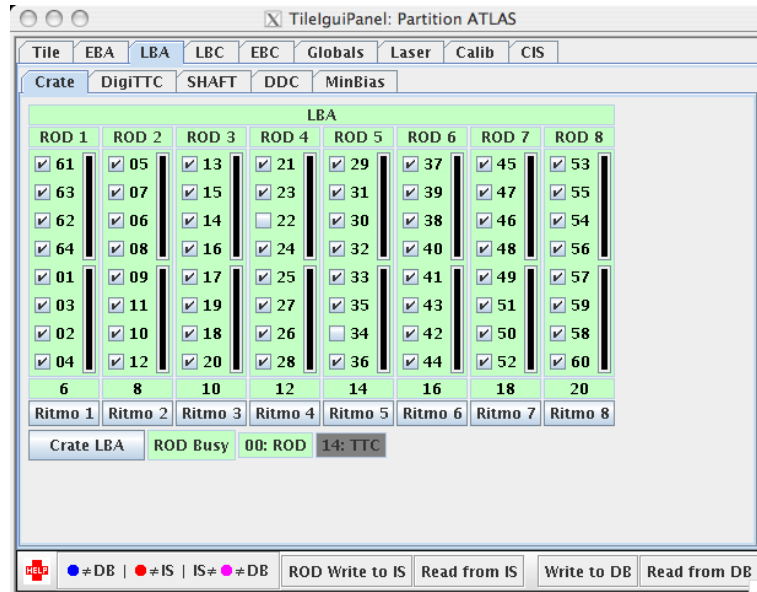


Figure 2.8: Crate sub-panel in the Tile IGUI panel.

The RODBusy module retrieves the busy status of the TTCpr, publishes it to the IS and it is displayed in the Crate panel of the Tile Calorimeter specific IGUI panel, as shown in Figure 2.8.

TileTBMTriggerIn

The functionality of the Trigger and Busy Module (TBM) is to distribute the TTC signals through the VME backplane of the crate and handle the busy from the eight RODs. The TBM trigger plug-in is a trigger plug-in to the RCD that does not queue data requests. It gathers the active RODs for the run at configuration time and configures the busy mask accordingly. On every probe command, every 5 s, the busy information is published into the IS and displayed as the colour of each ROD in the Crate panel of the Tile Calorimeter specific IGUI panel, as shown in Figure 2.8.

Modules

A module plug-in describes a hardware or software component that is controlled by the RCD. It can extend any of the methods of the ReadoutModule class which represent a run control transition command. The RCD module plug-in can be used in ROD emulation or ROD hardware manipulation.

TileCal specific module plug-ins for their use in the RCD framework are TileDigiTTCModule, TileVMEReadoutModule, TileCal RODModule, TileOfcShameModule, TileShaftModule and TileLaserModule.

TileDigiTTCModule

The TileDigiTTCModule is a double purpose module. It controls the front-end electronics through 3-in-1 TTC commands and the back-end electronics needed for TTC.

It is the steering wheel of the calibration run. It provides the charge injection settings to the front-end and, coupled with the TileVMEReadoutModule, provides data fragments containing the same settings to the data flow.

The configuration of the TileDigiTTCModule may be done through the TTC sub-panel of the Tile IGUI panel, shown in Figure 2.9.

TileVMEReadoutModule

The TileVMEReadoutModule is a general purpose module. In calibration runs it is configured to read-out data from the shared memory region of the crate controller and provide data fragments to the output plug-in.

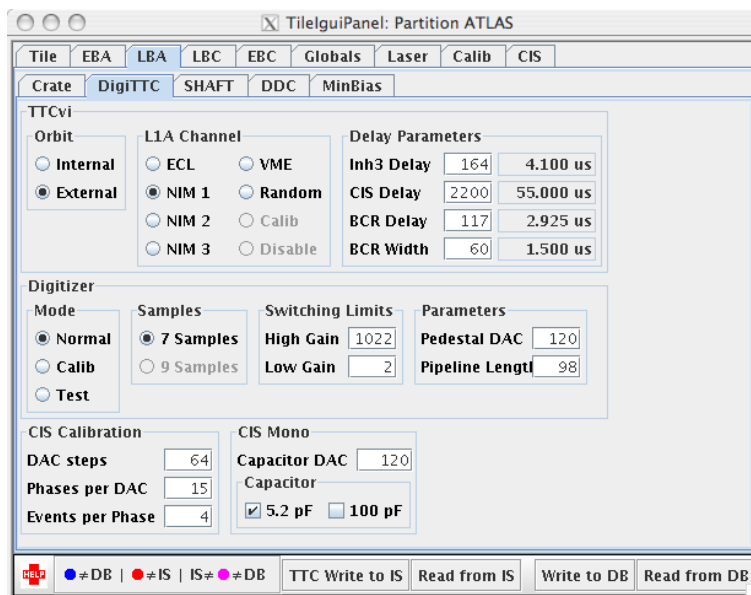


Figure 2.9: TTC sub-panel in the Tile IGUI panel.

TileCal_RODModule

The TileCal_RODModule controls the ROD motherboard. It configures the motherboard and the processing units according to the run type. For physics runs, ROD is configured as a data-flow element between the front-end electronics and the read-out system. Figure 2.10 shows the schematic overview of the operation of the ROD crate. It takes data in from the front-end links and sends data out through the Read-out Links. Monitoring quantities computed inside the boards are accesses from the Single Board Computer and made available to the TDAQ monitoring service from it.

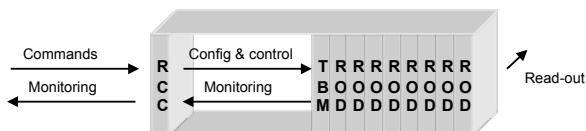


Figure 2.10: Schematic view of the ROD crate operation in S-link read-out mode. Commands are issued by the user to the ROD Crate Controller (RCC), and monitoring quantities are returned from it. The configuration and control of the boards is done through the VME bus. Monitoring quantities are read-out from the boards. Data is transmitted to the Read-out System through S-Link.

Eight instances of the TileCal_RODModule are needed by the RCD applica-

tion in the ROD crate. Each one controls a different motherboard independently. Masking of individual input links to the motherboard may be done through the Crate panel of the Tile Calorimeter specific IGUI panel, as shown in Figure 2.8.

The online processing algorithm may be configured through the Globals sub-panel of the Tile IGUI panel, shown in Figure 2.11. The conditions settings are retrieved accordingly at configuration time, in the "prepare-for-run" transition, from the shared memory region of the crate controller.

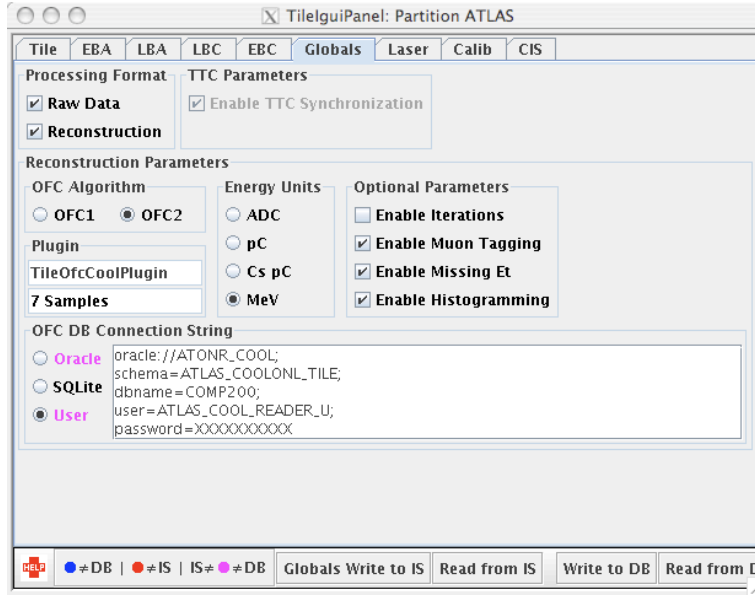


Figure 2.11: Globals sub-panel in the Tile IGUI panel.

TileOfcShameModule

The TileOfcShameModule is a module plug-in that doesn't control any hardware module. It is used as the conditions data cache for the whole crate. In order to avoid eight connections to the conditions database, one per ROD module, this module is used to gather conditions settings and store it in the shared memory ("shame") region of the crate controller. In order to avoid unnecessary time consumption, this module checks the input link status of the RODs. If an input link is set to be masked, the corresponding conditions data will not be retrieved for it. The same will occur for pedestal calibration runs, where conditions settings are not necessary.

The connection to the database takes up to 20 s to establish. The payload of the data is stored in the shared memory region of the crate controller and retrieved by the TileCal_RODModule using the same technique.

The payload data for one super-drawer is 48 channels \times 5 weights \times 7 samples \times 2 gains 32-bit words for the OFC settings, plus 48 channels 32-bit words for the channel status, plus 48 channels \times 2 gains \times 15 32-bit words for the muon identification thresholds and 48 channels \times 4 32-bit words for the conditional dumping of the raw data. This sums up to 2.4 MB of conditions data for the whole crate per run.

Calibration in Empty Bunches

In the bunch train structure of the LHC there are certain bunches which are empty by design. This allows the different experiments to perform calibration tasks in these empty bunches within a physics run. One LHC fill cycle is segmented into 3564 parts of 25 ns, or Bunch Cross IDs (BCIDs), of which 2808 are full for design Luminosity as shown in Figure 2.12. Technical limitations impose a 3 μ s gap for the beam dump kicker rise time at the end of each fill, which means that at the end of each cycle, the LHC has a long extraction gap of 119 bunches, BCIDs from 3445 to 3563.

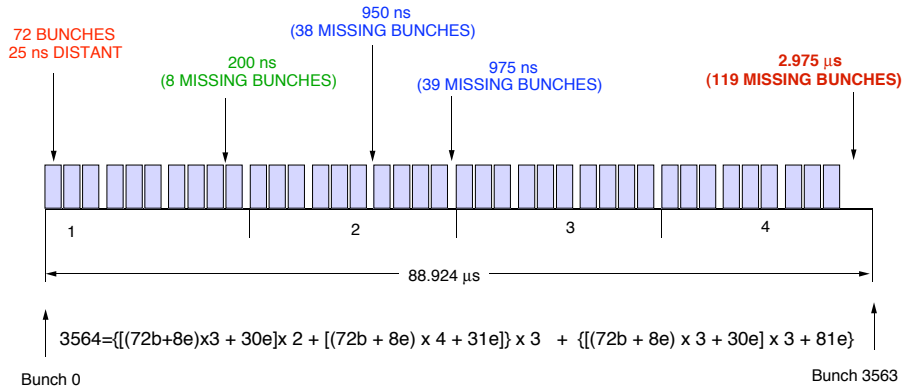


Figure 2.12: Bunch structure of an LHC fill.

Within the ATLAS experiment there are several triggers foreseen in these LHC gaps:

- Pedestal/noise triggers: Random trigger in some bunch group of the long

gap, with low frequency rate ~ 1 Hz. These will end up in the pedestal stream.

- Cosmic trigger: High p_T muon trigger in most of the empty bunches of the short gaps. These will end up in the cosmic stream.
- Physics triggers: Searches for long lived particles. These will end up in the corresponding particle stream.
- Sub-detector calibration triggers: In some bunch group of the long gaps, each sub-detector can ask for a calibration trigger for 1 out of 16 cycles, called turn, via LTP calibration request lines. These events will end up in the sub-detector calibration stream.

The Tile Calorimeter plan is to have CIS, laser and minimum bias monitoring in the long extraction gap. In order to share the gap, the Shaft VME board was introduced. The foreseen frequency of calibration events is ~ 2 Hz.

TileShaftModule

The TileShaftModule is a module plug-in to control the Shaft board, which is a specific VME board to share the calibration requests in empty bunches, as mentioned above. This module controls the different calibration trigger requests foreseen in the Tile Calorimeter. Each calibration request can be enabled and its firing timed with respect to the TTC signal that clocks the turn of the LHC beam.

There is one shaft board per partition. The information about the calibration requests is placed in IS for the Laser ROD to retrieve. The configuration of the Shaft board may be done through the Shaft sub-panel of the Tile IGUI panel, shown in Figure 2.13.

TileLaserModule

The TileLaserModule is a module plug-in that controls the Laser ROD. This is a ROD which does not read-out data from the front-end but from the back-end, it is used in physics runs to insert calibration information into the data-flow. Its read-out link is connected to the LBC partition read-out system. It receives TTC information from the shafts and the calibration information of the current event is read-out from IS.

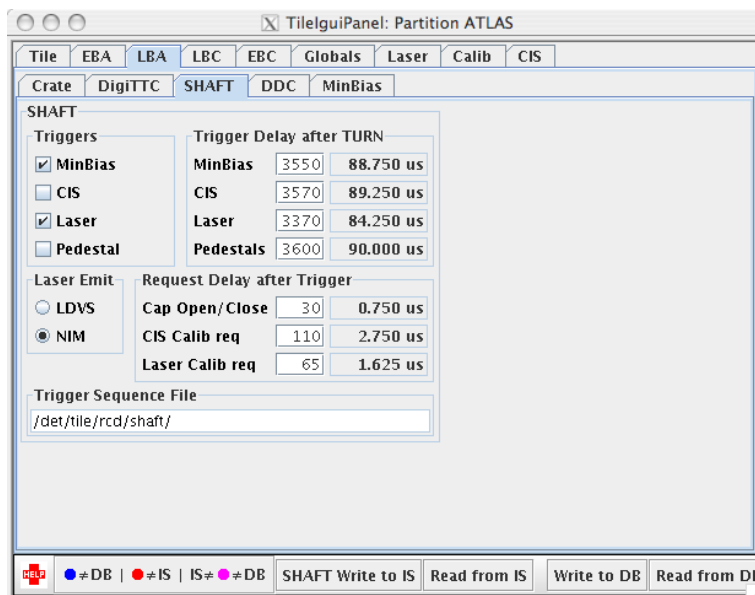


Figure 2.13: Shaft sub-panel in the Tile IGUI panel.

The Laser calibration system provides a Laser pulse to all the PMTs. The intensity of the pulse can be regulated via a Digital to Analog Converter (DAC) and an attenuation filter which is placed in front of the source. The response of the detector PMTs is compared to the response of an internal PMT of the system. This PMT is calibrated via an internal α -source run. The configuration of the Laser run parameters can be done through the Laser panel in the Tile specific IGUI panel, shown in Figure 2.14

2.5.2 Stopless Recovery

During the combined data-taking periods of 2008, one of the cutting edge problems was the un-recoverable busy produced by a part of a sud-detector read-out. The only way to recover the data flow was to reconfigure the run, which introduced an important loss of data-taking time. The ROD is the only element which can raise the busy signal, within the busy chain of the ATLAS detector. Hence it should incorporate a mechanism to continue the data-taking with reduced granularity.

The ATLAS wide automatic stopless recovery mechanism, supervised by the expert system, is the automatic procedure through which a hardware resource

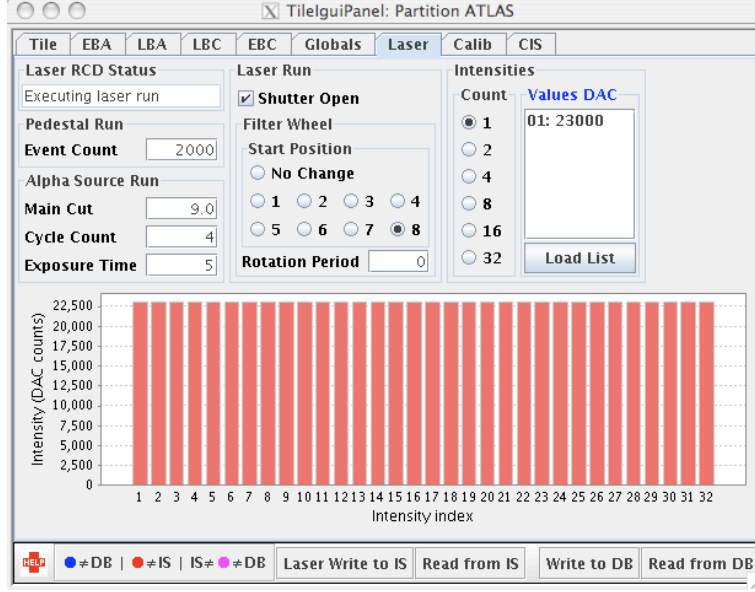


Figure 2.14: Laser sub-panel in the Tile IGUI panel.

which is raising the busy signal for a fixed amount of time is disabled and possibly re-enabled without stopping the data-taking process. The Tile Calorimeter has implemented the stoless recovery mechanism up to the read-out link granularity, which is four consecutive super-drawers in (η, ϕ) that cover a range of $\Delta\eta \times \Delta\phi = 0.7 \times 0.4$. If a read-out link goes busy, the Tile ROD RCD will react by sending a command to the expert system to disable the faulty hardware. The hardware can be resynchronized with the rest of the detector by a shifter operation. Removal takes 5 seconds to be issued and some delay from the run control. Recovery is immediate after the shifter has issued the command.

Bookkeeping of the stopless recovery actions takes place in the conditions database for future analysis. The stopless recovery aims for full data taking efficiency, although with reduced granularity, and the recovery of special cases in which the reconfiguration of the run would normally be necessary. After the run has stopped, there is no trace of the stopless recovery mechanism. In special cases, it is also possible to force the disabling of a Read-out Link (ROL) by setting it manually to busy.

Stopless Removal

On each RCD probe, approximately every 5 s, each ROD performs a check to see whether they are busy. If there is a busy inside a PU that lasted 100% of the time, a hardware failure message is issued on a ROL. The expert system reacts on this message and suggests that run control removes the faulty hardware. If run control accepts the removal, ROD and ROS are notified and the hardware is disabled.

Recovery After Removal

Once the faulty hardware has been removed, there is a run control command that can be issued to re-synchronize the hardware. The recovered hardware issues a message that is processed by the expert system and the hardware at both sides of the ROL is enabled back.

Front-end Re-configuration

In the event that a super-drawer power supply fails but can be powered back again, the front-end configuration is lost. To reconfigure the front-end electronics would require stopping and reconfiguring the run to recover the read-out of the affected part of the detector. There is a mechanism implemented in the RCD to allow single super-drawer electronics reconfiguration during the run. This way, once the power has been restored to the front-end, a user command can be issued to the TTC RCD application that will go through the configuration transition for the selected super-drawer.

Currently this is an important action for the Tile Calorimeter given the failure rate of the power supplies and the LHC fill structure. Reconfiguring the run for a small fraction of the Tile Calorimeter ($\Delta\eta \times \Delta\phi = (0.7 \times 0.1)$) is not desirable, and the stopless recovery allows to fix these problems on the fly, which is a synonym for excellence.

2.5.3 Detector Verification System Tests

The Detector Verification System (DVS) is a part of the online software. High precision DVS measurements are available for the Tile Calorimeter. In these

tests, the data is read-out through the VME bus into the memory of the crate controller as shown in Figure 2.15. The data is decoded and analyzed and results are returned to the user.

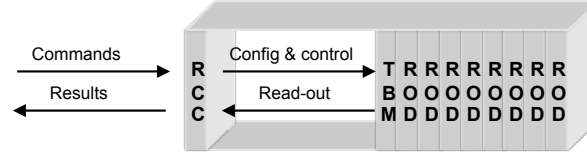


Figure 2.15: VME read-out mode of the ROD crate. Commands and results are issued by the user to the ROD Crate Controller (RCC). The configuration and control of the boards and the read-out of the data is done through the VME bus.

The tests are the following:

- **ROD motherboard functionality:** These tests check the reading and writing from all possible registers of the ROD motherboard. They are referred to as static tests.
- **Charge Injection System:** A defined charge is injected through the Charge Injection System to the super-drawers in two sensible ranges, one for high gain and one for low gain. The tests check that the response of each channel corresponds to the injected charge within 5% and the time of the pulse is within the read-out window.
- **Pedestal:** Data is read-out with a random trigger. Test looks for high and low frequency noise in the samples not above 5 ADC counts.
- **Stress:** A 100 kHz random trigger and a full busy logic is used to veto the acquisition. Data is processed inside the DSP. The number of Cyclic Redundancy Check (CRC) errors found in the data is reported.
- **Memory:** A bitwise pattern is written into the memory of the DMU. Pattern data is read-out and checked for mistakes.

Tests are integrated into the DVS graphical user interface as shown in Figure 2.16. A result of a high gain Charge Injection System test is shown in Figure 2.17. A gaussian function is fit through the samples to ease the recognition of the pulse. Note, the uninstrumented channels are marked as such.

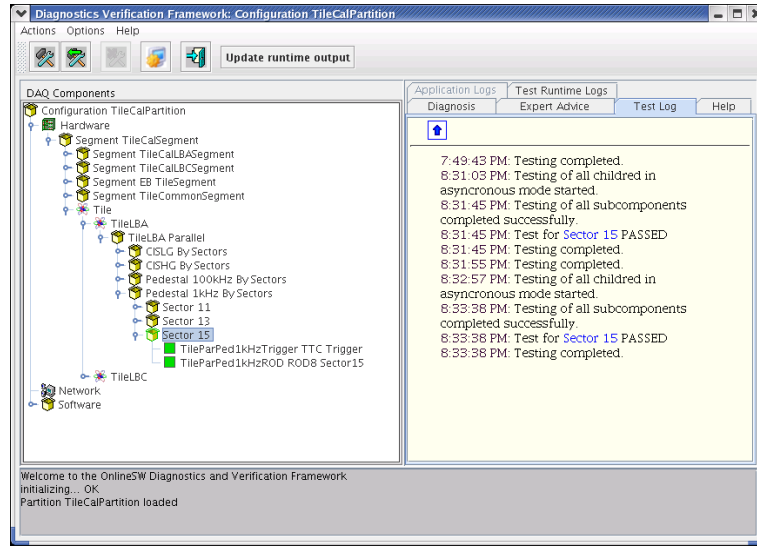


Figure 2.16: DVS application view.

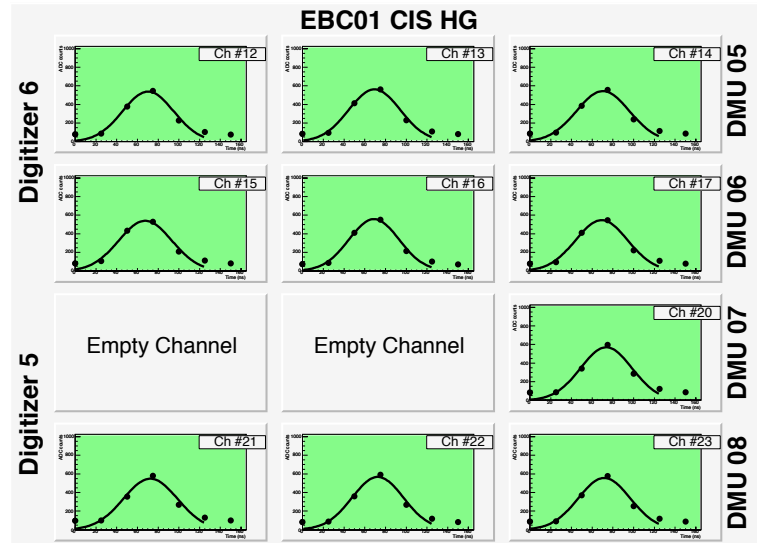


Figure 2.17: High gain Charge Injection System DVS test results.

In recent times since the stability of the detector has improved and there are more functionalities in the monitoring systems, the DVS tests are less used with respect to the intensive usage during the commissioning phase of the detector.

2.5.4 DAQ to DCS Communication

The Detector Control System (DCS) is a part of the TDAQ project that manages the control of:

- Sub-detectors
- Shared infrastructure with CERN and the LHC (cooling, ventilation, electricity distribution, safety, etc)

The exchange of information between DAQ and DCS during the run, provides better understanding of the each system when looking only at one source of data. As an example, the power status of the front-end electronics controlled by DCS is relevant for the DAQ data, and the DAQ status of the run is relevant for DCS analysis.

The Tile online software provides a mechanism to exchange information with DCS through DAQ to DCS Communication (DDC), which can be reviewed in [31]. One application provides DAQ activity information to DCS including run number, run type and partition being executed; another application provides DCS summary information per super-drawer to the DAQ, which is presented to the user in a Tile Calorimeter specific IGUI panel. Figure 2.18 shows a screenshot of the DDC display for LBA partition. The information is displayed by super-drawer, in each of the 64 wedges. A legend shows the meaning of each box and colour.

Each of the four TTC partitions defines the DAQ operation granularity of the front-end super-drawers. The minimum control of the front-end is done in groups defined by TTC partition. This means that the number of information elements that need to be sent from the DAQ to the DCS is one per TTC partition. From the DCS point of view, each super-drawer is an independent element that can be operated individually. Therefore, the number of information elements that need to be sent from the DCS to the DAQ is 64 per TTC partition.

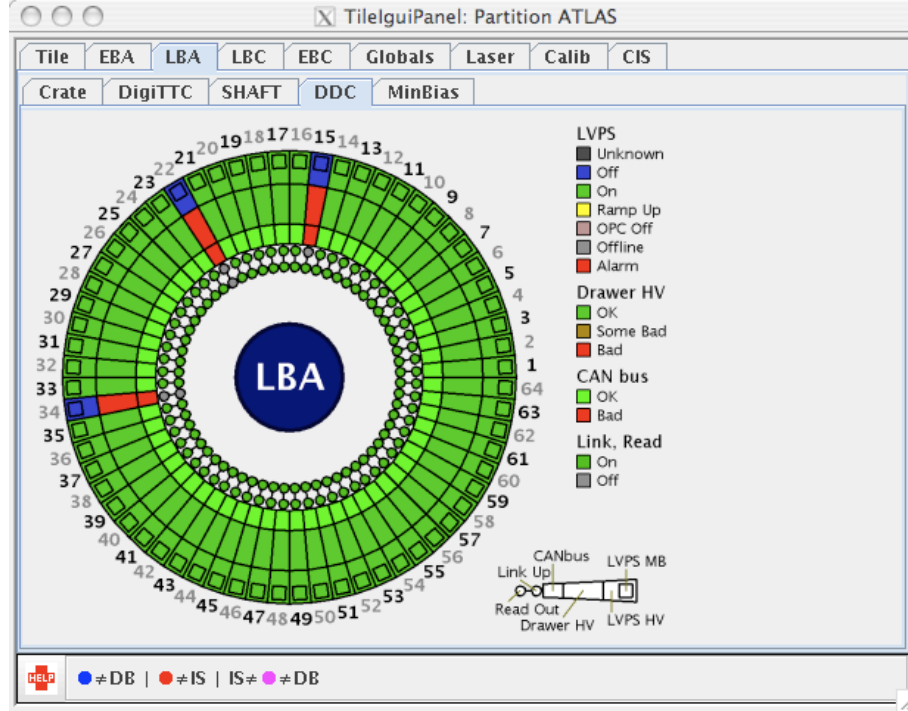


Figure 2.18: DAQ to DCS display in the Tile Calorimeter specific IGUI panel for one Tile Calorimeter partition (LBA). Each partition is divided into 64 modules.

2.6 Operation of the Tile Calorimeter

The ATLAS experiment started operation in 2010 at $\sqrt{s} = 7$ TeV. Figure 2.20 shows the integrated luminosity as a function of time for the first months of running in 2010. During this time, the Tile Calorimeter has been running within ATLAS as shown in Figure 2.19, where the Tile Calorimeter segment is highlighted inside the IGUI panel running the ATLAS partition.

Table 2.2 shows the Luminosity weighted relative fraction of detector uptime and good quality data delivery of the different sub-detectors. The DAQ inefficiency (3.4%) during stable beams is not included in the numbers. The Tile Calorimeter has delivered 100% of good quality data ($\sim 97\%$ of the modules are powered). Most of the inefficiencies seen in the Inner Detector and Muon Systems is related to the so-called "warm start", which includes a ramp of the high-voltage when the stable beam flag is raised.

Period	Pixel	SCT	TRT	LAr	Tile	MDT	RPC	TGC	CSC
a	80.9	86.2	100	99.0	100	87.4	88.6	84.4	
b	88.8	92.8	100	100	100	94.0	94.6	92.2	
c	97.5	98.3	100	92.2	100	97.1	98.4	98.2	98.4
d	91.9	98.2	100	91.9	100	97.8	97.9	97.4	97.8
e	95.0	99.6	100	96.6	100	99.6	99.6	97.7	100

Table 2.2: Luminosity weighted relative fraction of detector uptime and good quality data during 2009 and 2010 beam periods a) All stable beams 2009, b) Until 12/12/2009, c) 30/03/2010 - 17/05/10 d) 18/05/2010 - 27/05/2010 e) From 01/06/2010 (preliminary).

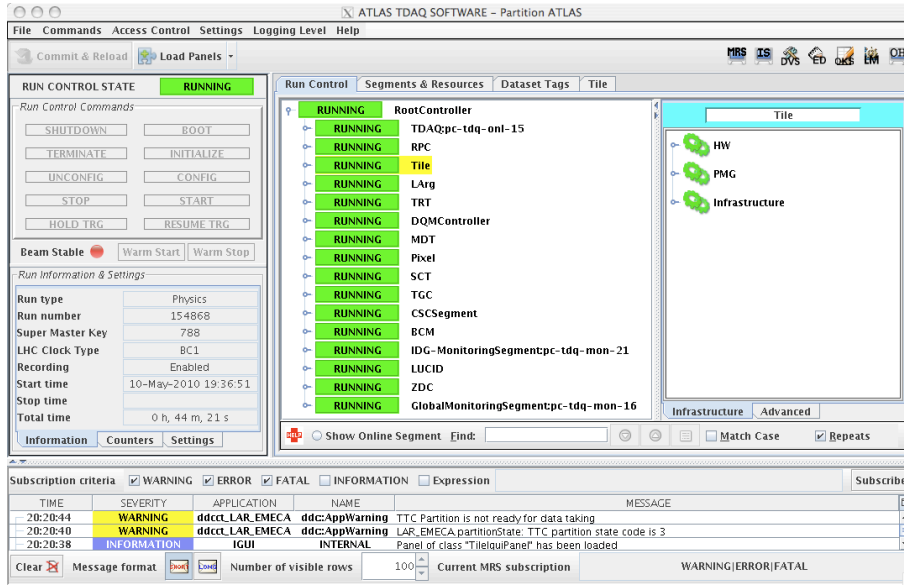


Figure 2.19: Screenshot of the Igui for ATLAS partition in state running.

The Data Taking Efficiency, defined as the ratio of the running time during beam time to beam time, is shown in Figure 2.21. The running time incorporates the dead time fraction during each Luminosity Block reported by the Central Trigger Processor. The beam time is defined by the presence of two circulating stable beams. The width of each bar is a measure of the stable beam (shown in gray) availability during 24 hours. Each green bar corresponds to an average efficiency calculated for a period of 24 hours. The absence of filled bars indicates a period of no stable beams. Reasons for lower efficiency are stop of the run during beam time to work on a subsystem and possible trigger holds due to a sub-system issuing busy for a brief period of time. Average efficiency, calculated every 24 hours for the last 24 hours, over the whole period is 96.5

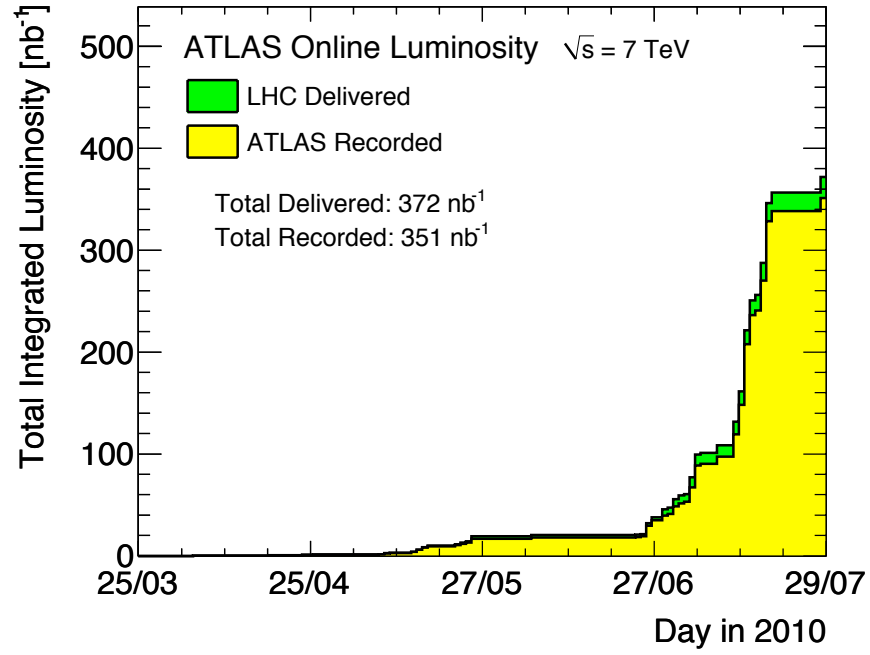


Figure 2.20: Integrated Luminosity as a function of days.

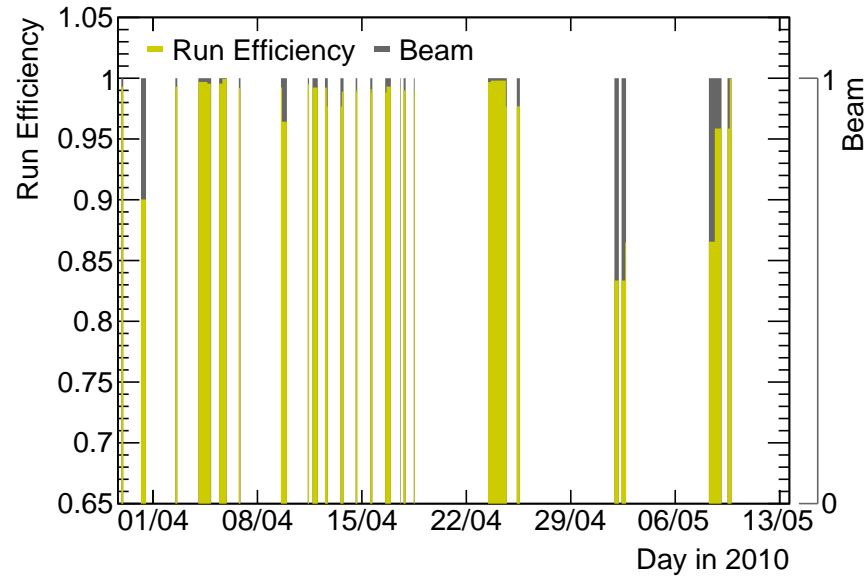


Figure 2.21: Data taking efficiency during stable beams in 2010.

2.6.1 Transition Times

One of the factors that directly affects the data taking efficiency is the time it takes to perform a run control state transition. The run control tree is organized into sub-detectors segments. This simplifies the task of including or excluding sub-detectors from the partition. The Tile Calorimeter is one of the fastest sub-detectors in changing state as shown in Figure 2.22. Notice both Tile and LAr are the slowest in the “prepare-for-run” transition. This is because they both access the conditions database to retrieve the coefficients for energy reconstruction per channel.

The Tile segment is organized in four TTC partition segments (EBA, LBA, LBC, EBC) and overall monitoring segments, Minimum Bias Monitoring (MBM), Data Quality Monitoring (DQM) and Monitoring Data Archiving (MDA). Figure 2.23 shows the times for the configuration transitions for the Tile segment. TTC partition segments are more than two times slower than monitoring segments. The slowest transitions are configure and “prepare-for-run” which are more than three times slower than the rest. It is indeed where the configuration of the front-end and back-end electronics takes place. The rest of the transitions don’t rely on hardware communication and are mostly software related.

Each TTC partition segment is organized in detector electronics applications (RCD), read-out system applications (ROS) and monitoring applications (GNAM, Minimum Bias Monitoring). Particularly, the LBC segment has another RCD application to control the Laser calibration during physics runs, where laser pulses are sent to the front-end in the empty bunches of the long gap region of the LHC fill.

Figure 2.24 shows the mean values of the most critical transition states for the LBC TTC partition segment over the course of 30 days of operation at $\sqrt{s} = 7$ TeV. ROD RCD applications take around 30 s to configure, already a considerable amount of time. All the DSPs in the crate are booted in this transition. Due to technical limitations of the VME bus, this action is performed sequentially in the ROD modules. It would be reasonable to think that there is no need to boot the DSPs from one run to another. This is the aim for the maturity state of the ROD RCD code. The ROD and Laser RCD applications load the conditions data on prepare for run transition, which results in a con-

siderable time of more than 30 s for the ROD RCD and 10 s for the Laser RCD. Minimum Bias Monitoring applications take double the time to configure required by the ROD RCD. They perform the configuration of the super-drawers for slow read-out (CAN bus) during a physics run. TTC RCD applications perform a similar action in one sixth of the time. It would be reasonable to think the configuration time for Minimum Bias could be optimized at about 10 s.

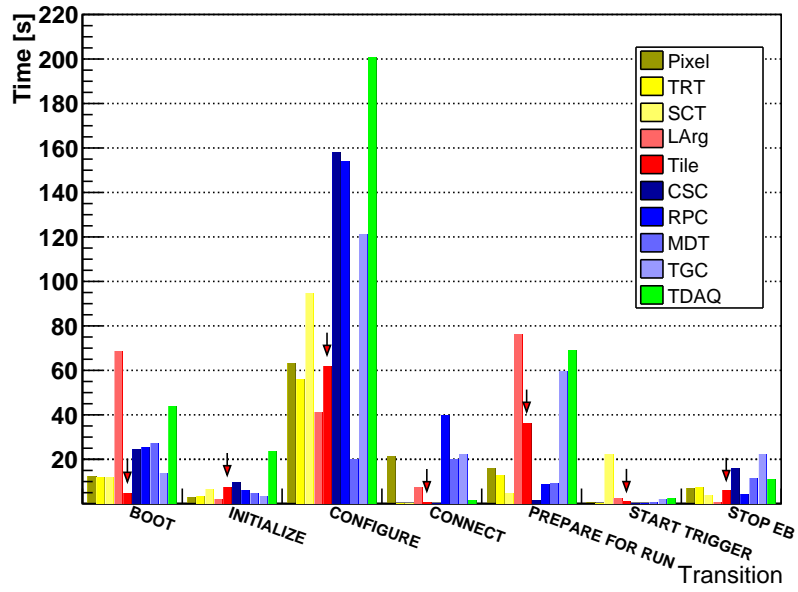


Figure 2.22: Mean values of longest transition times per sub-detector. The arrows indicate the Tile Calorimeter.

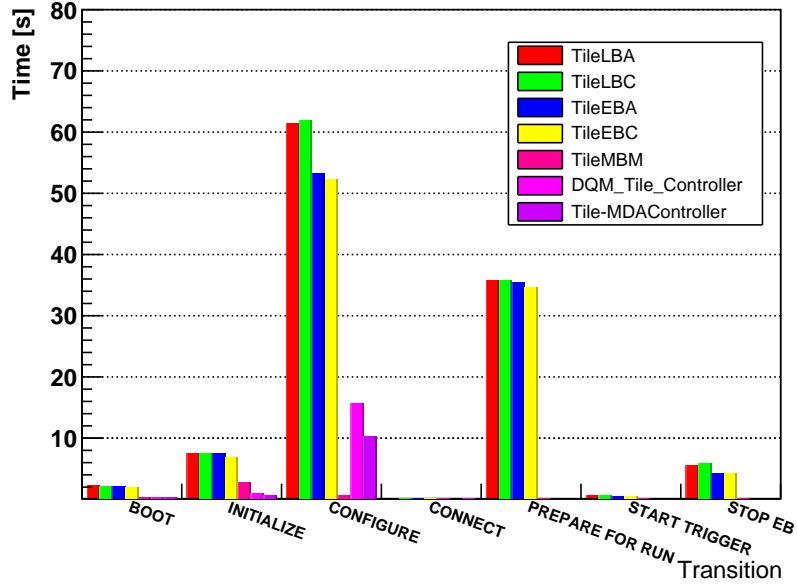


Figure 2.23: Mean values of Tile interesting transition times in the Tile Calorimeter.

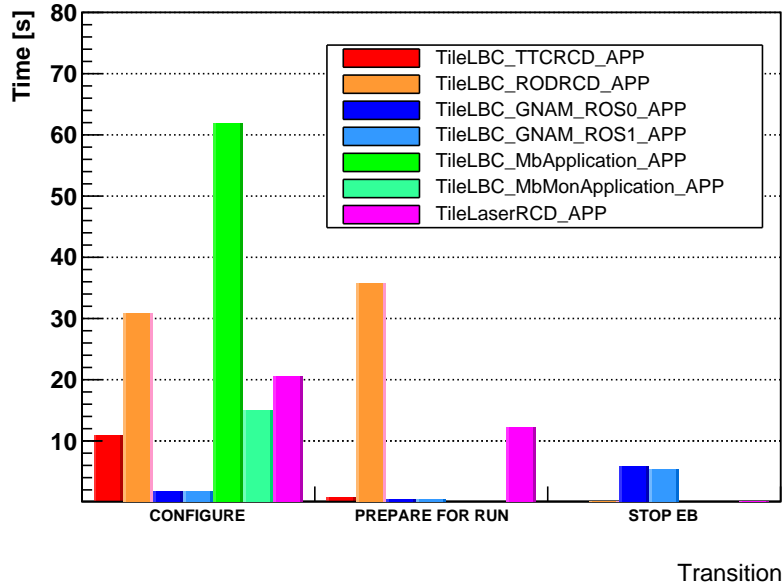


Figure 2.24: Mean values of Tile interesting transition times in LBC TTC partition.

2.7 Online Data Quality

The ATLAS online monitoring infrastructure, called GNAM, allows monitoring at all levels of the data flow: ROD, ROS and Event Filter. At each level a sampler intercepts the data fragments and the Event Monitoring Service sends them to the corresponding Monitoring Process that is asking for them. This process unpacks and decodes the data, fills histograms and sends them to the Online Histogram service. A presenter receives them from the Online Histogramming service and displays them on a graphical user interface for use by shifters and DQ experts to monitor the performance of the detector.

Within the Tile Calorimeter, three monitoring levels are implemented in order to assess data quality. Note that only the first two monitoring levels (ROD, ROS) are embedded in the online software, whereas the Event Filter monitoring is incorporated in the offline software. Figure 2.25 summarizes the different Tile Calorimeter monitoring levels and rates.

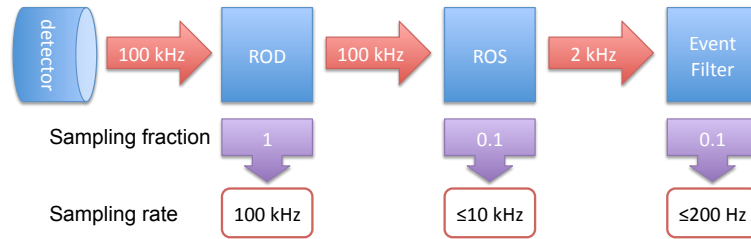


Figure 2.25: Summary of the different Tile Calorimeter monitoring levels and rates.

Tile Decoder

In the online software, there is no sub-detector specific description of the data fragments. This is why the TileDecoder library was provided within the Tile online software. This library decodes Tile specific data fragments and provides a friendly programming structure for its access, following the electronics layout of the detector: Super-drawers, DMUs, channels and gains. This library is also used in the Tile specific DVS tests described in Section 2.5.3 to decode the data from the front-end.

2.7.1 ROD Monitoring

ROD monitoring is a hardware monitoring that reads information from every event that passes the Level 1 Trigger selection. It aims to spot problems related to the data acquisition.

The publishing of the results is implemented within the RCD ROD module plug-in in the probe run transition issued every 5 s, which is meant to publish fast statistics. When a probe transition occurs, the `TileCal RODModule` receives the results of the monitoring that takes place inside the ROD, but it does not receive data for decoding and histogramming. It doesn't handle data fragments themselves but just gets the results of the underlayin monitoring process.

There are two types of results, the simple counters and the histograms. The simple counters that are available provide the number of events into the ROD motherboard from the input links. The histograms are produced inside the DSP, these are the Optimal Filtering quality factor and first sample distributions for all events.

RITMO

The ROD Information for Tile Monitoring (RITMO), is a selection of counters from the DSPs that are published on every probe. These counters, like the rest of the ROD monitoring, take into account all events that passed the Level 1 Trigger selection.

Each DSP handles data from two super-drawers, there are three types of counters (*in*, *out*, *discarded*) that count the number of events per super-drawer. The number of events *in* is incremented each time a data fragment from the super-drawer arrives to the DSP input memory buffer. The number of events *out* counts the number of events that have been procesed from the input buffer and sent to the output buffer. The number of events *discarded* counts the number of trials to process data from the input buffer and the data was not successfully processed, either because the data was missing or the BCID of the data didn't match the BCID of the TTC event for the matching.

The number of TTC events in counts the number of TTC events received by the DSP through the backplane of the ROD crate from the TTC system. These events drive the processing of the DSP, no event is processed if no TTC events

are received. The number of total events out is the number of processed events given by the number of TTC events received. The number of TTC events out counts the number of TTC events that have been sent to the output.

The busy of the DSP is defined by the difference between the number of TTC events in and TTC events out. If the difference is greater than eight, the busy is set; if the difference is less than eight the busy is cleared. This difference is checked upon the reception of a TTC event by the DSP and on the transmission of a processed event to the output. It can happen that the DSP is in busy state during the processing of a single event, if a TTC event is received while event number eight is being processed, the busy will be set, and cleared just after the event has been transferred. The busy of the DSP is monitored by the instantaneous busy counter, which can only take values 0 or 1, and the number of busy counts, which counts the number of times the DSP has been busy.

The conditions that could cause the DSP to assert the busy are related to burst of data in the input buffer or output data bandwidth limitations. The second condition can be met when the DSP is required to transfer the raw data from the front-end along with the reconstructed data fragments, the output data bandwidth is not enough to cope with the $10\ \mu\text{s}$ upper limit to transfer an event. Hence, the DSP will set the busy in order to reach a balance between input and output. In everyday data taking conditions, there is no busy introduced by the DSPs.

There are also three counters that are overwritten with every TTC event, the aim of which is to sample the last TTC event processed in the case the trigger is paused. These counters are the Extended L1ID, BCID and Trigger type.

2.7.2 ROS Monitoring

The ROS monitoring aims for hardware checks at the level of the super-drawer. It is implemented to take full advantage of the online monitoring infrastructure. Each ROS has a dedicated monitoring application that is configured to sample a maximum of 10% of the events. The application receives the data and uses the TileDecoder library to decode it.

To keep the complexity low, and the number of sampled events high, advanced computing techniques like Optimal Filtering are not implemented at the ROS level. However, comparisons between online Optimal Filtering and another basic filtering, called flat filtering, are used instead. Flat filtering provides a coarse estimation of the energy, time and pedestal. Energy is computed as the value of the maximum sample minus the pedestal; the pedestal is the value of the mean of the first and last sample; and the time is computed as the time of the maximum sample.

The basic histograms produced at the ROS level are:

- PMT level histograms: Energy, time and quality factor from online Optimal Filtering reconstruction; energy and pedestal for flat filtering reconstruction; and high frequency noise.
- Super-drawer summary histograms: Flat filtering pedestal and pedestal RMS, online Optimal Filtering time, time RMS, quality factor and quality factor RMS.
- Digital error histograms: BCID, CRC, single and double strobe errors, memory parity, header parity and format, sample parity and format and global CRC errors

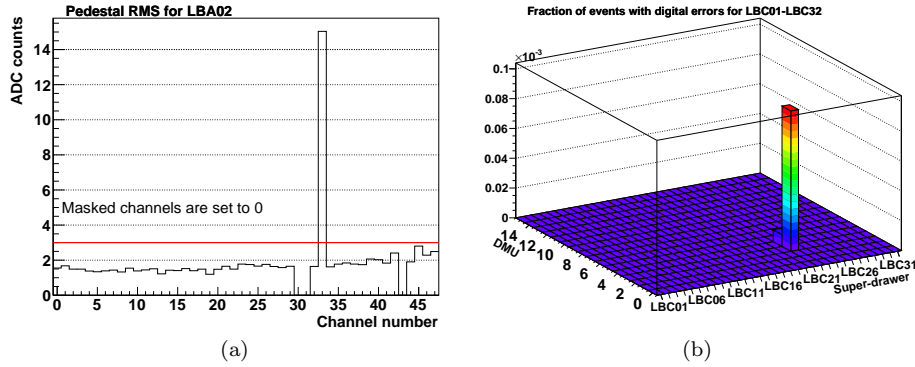


Figure 2.26: Distribution of the RMS of the pedestal for LBA02 (left) and distribution of the fraction of events with digital errors as a function of super-module and DMU (right) as seen by the ROS monitoring for beam data at $\sqrt{s} = 7$ TeV.

Figure 2.26 (a) shows the distribution of the RMS of the pedestal in LBA02. The red line indicates the threshold value, above which it constitutes a warn-

ing, of 3 ADC counts, already twice the expected RMS of 1.5 ADC counts. Figure 2.26 (b) shows the distribution of the fraction of events with digital errors as a function of super-module and DMU. The super-drawer LBC22 shown in this plot, has $9 \cdot 10^{-2}$ % of the events with digital errors. The percentage of digital errors at which the super-drawer is masked for offline analysis is 1%.

2.7.3 Event Filter Monitoring

The Event Filter monitoring is an advanced and complex monitoring performed over a full event. It provides results that are not possible with other monitorings. The maximum sampling fraction is 0.1, thus only a small fraction of the events are sampled. The ATLAS offline software is used to decode and analyze the data, but the online monitoring infrastructure is used to retrieve and publish the results. The monitoring applications, called processing tasks, run on a node connected to the Event Filter network. The applications request events from a Sub Farm Input (SFI) application.

If the data samples are available, it is possible to execute the Optimal Filtering algorithm within the Event Filter monitoring. Figure 2.27 shows the time difference between online and offline reconstruction versus offline reconstructed energy as seen by the Event Filter monitoring in the four TTC partitions for beam data at $\sqrt{s} = 7$ TeV. Red lines indicate the threshold for the Time differences. The green frame indicates the test is OK. The results from the Optimal Filtering algorithm online and offline should be the same except for small differences due to numerical precision.

Physics in beam periods has no privileged direction, therefore the energy deposition in the (η, ϕ) plane should be flat for beam data. Figure 2.28 shows the position of cells with depositions above 300 MeV in the (η, ϕ) plane, for any physics triggered event using beam data at $\sqrt{s} = 7$ TeV. This energy has been computed with the Optimal Filtering algorithm with iterations that is explained in Section 3.1.2. This is only possible when the samples are also transmitted with the data.

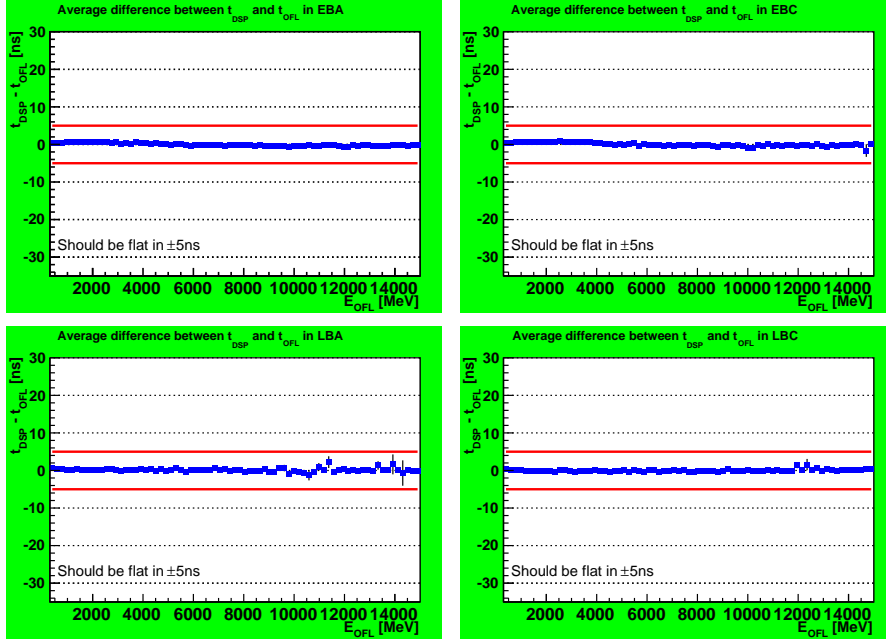


Figure 2.27: Time difference between online and offline reconstruction versus offline reconstructed time as seen by the Event Filter monitoring in the four TTC partitions for beam data at $\sqrt{s} = 7$ TeV.

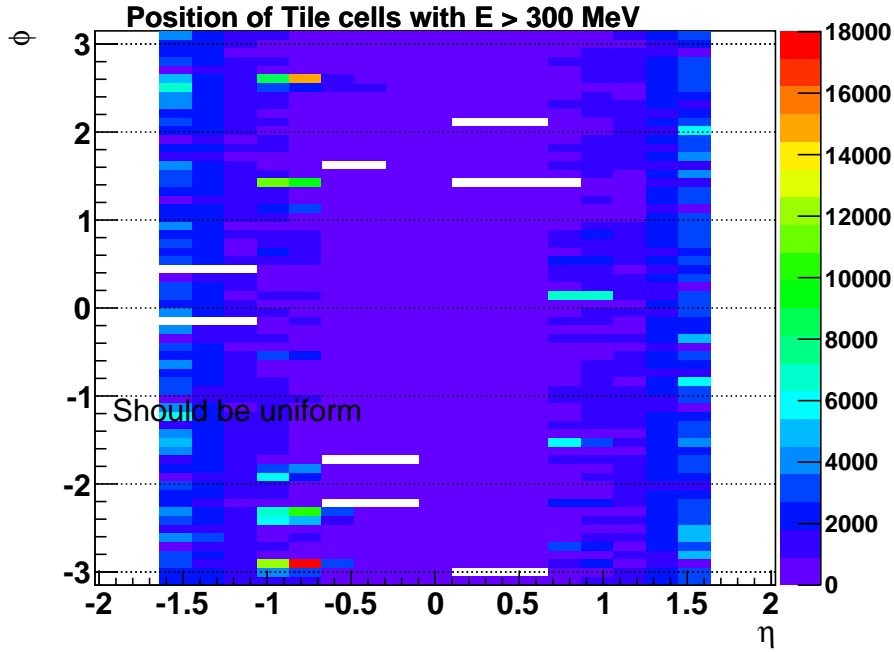


Figure 2.28: Position (ϕ vs η) of cells with depositions above 300 MeV for any physics triggered event as seen by the Event Filter monitoring for beam data at $\sqrt{s} = 7$ TeV. Masked channels are left blank.

2.8 Outlook

The implementation of the online software for the Tile Calorimeter has presented many challenges. The ROD had to be fully operational for the commissioning period of 2006, for which, the RCD and DVS tests had to be implemented. DVS tests were intensively developed for the commissioning of the super-drawers. The choice of using the RCD as opposed to a sub-detector specific read-out application was based on the cost of code development. The RCD provided a core infrastructure which was already working and actively maintained in a highly demanding computing environment. The points of failure in the software architecture are minimized while profiting from the detailed knowledge of the Tile Calorimeter hardware. Dedicated effort was put into understanding the RCD framework and interacting with the developers to make sure the framework possibilities met our demands.

The Tile Calorimeter was one of the first sub-systems to participate in a Milestone week in December 2006. During this time, it was realized that another of the challenges of the implementation was to combine everything together. The modular framework offers high flexibility in the implementation of plug-ins, which are entirely written in C++, but as in any other software project, the RCD code had to go major refactoring to be ready for physics.

One of the latest developments in the RCD has been the implementation of the stopless recovery mechanism. This mechanism was required while the author was deputy run coordinator for the Tile Calorimeter. The Tile Calorimeter was one of the first sub-detectors to implement such mechanism, which aimed for continuous running for the whole time of the LHC fill.

Currently, the RCD for the Tile Calorimeter is ready for physics, and also prepared to run at 75 kHz Level 1 Trigger rate. The stopless recovery mechanism has been implemented for front-end and back-end electronics and the advanced state of the monitoring tools guarantee the quality of the data at all times.

One of the outlooks for the future is to make an effort in reducing the transition times, that would minimize the dead time of the data acquisition. The object oriented approach is an advantage for any possible upgrade scenario, in which the adopted technology could be easily plugged into the current design.

Chapter 3

Performance of the Signal Reconstruction

In this Chapter we will overview the performance of the Optimal Filtering algorithm executed in the ROD DSPs. The aim is to evaluate its results for physics analysis.

3.1 Optimal Filtering Online and Offline

The Optimal Filtering used for online signal reconstruction is implemented in the ROD DSPs. Several aspects of its implementation determine its performance, and are highlighted in Section 3.1.1.

The Optimal Filtering algorithm exists in different flavours. The one explained in Section 2.3 and implemented in the DSPs is commonly known as Optimal Filtering without iterations, as opposed to the Optimal Filtering with iterations, which is mostly used in the ATLAS offline software, explained in Section 3.1.2.

One of the key points impacting the performance of the Optimal Filtering is the fact that the weights are computed for a given time phase difference between the signal peak and the LHC clock. The amplitude reconstruction bias due to this difference is a well known parabolic function. It is reasonable to think on a correction for the reconstructed energy based on the phase difference. This is

explained in Section 3.4.2.

3.1.1 DSP Implementation

The Optimal Filtering reconstruction is performed in the DSP using fixed point arithmetic which is a limitation in the computation of magnitudes. However, the magnitudes are computed in 32-bit logic operations and the results are rounded and packed according to the Tile calorimeter data format (Table 3.1). Hence, the precision of the DSP is limited by the number of bits available in the data format to pack the result.

31	30.....16	15.....5	4	3.....0
Gain	Energy	Phase	HLT	QF

Table 3.1: Data format of the reconstruction word for a read-out channel in the Tile Calorimeter.

Moreover, the amplitude of the pulse is computed in ADC counts and multiplied by the corresponding calibration constants, as explained in Section 2.3. The Optimal Filtering weights and calibration constants are retrieved from the Conditions database at configuration time and are copied into the internal DSP memory using a 16-bit integer, which is the product of the floating point value times two to the power of a scale:

$$\text{value} = \text{floating point value} \times 2^{\text{scale}} \quad (3.1)$$

The scale is derived from a maximum value for the set of constants being loaded; in the case of Optimal Filtering weights is their highest absolute value; in the case of the calibration constants is the product of the calibration factors. The scale is given by the following:

$$\text{scale} = \text{truncf} \left(\frac{\log 2^{15} - 1}{\frac{\max}{\log 2}} \right) \quad (3.2)$$

The energy has a different output range depending on the gain. Thus, the precision of the DSP reconstruction depends both on the gain and the units. The different energy ranges and the precision of the DSP result are shown in Table 3.2 for the Low Gain (LG) and in Table 3.3 for the High Gain (HG). If the

energy result exceeds these ranges it is saturated, and the maximum/minimum values are packed in the data.

Energy Units	Min	Max	Precision
ADC	−32	2016	0.0625
pC	−16	1008	0.03125
MeV	−16384	1032160	32

Table 3.2: Online reconstruction range and precision of the energy for the different energy units in low gain

Energy Units	Min	Max	Precision
ADC	−128	1920	0.0625
pC	−1	15	0.00048828125
MeV	−1024	15360	0.5

Table 3.3: Online reconstruction range and precision of the energy for the different energy units in high gain.

Concerning the phase, one bit corresponds to 0.0625 ns, and the range of phases varies from −64 ns to 64 ns. The DSP phase result is saturated if it exceeds this range. However, in order to optimize the phase computation in the DSP the division by the amplitude (Equation 2.2) has been implemented as a look-up-table. There are 2048 entries in the look-up-table with a 16-bit precision. There is a corresponding value of $1/A$ for each value of A (from 0 to 1023 ADCs) in steps of 0.5 ADC counts. The look-up-table values are scaled by a power of 2 in order to optimize the precision within the memory constraints. This scale establishes the precision. Since the highest value is $1/0.5$ the scale used is 2^{15} . Then, the precision of the look-up-table is 3×10^{-3} , which corresponds to value of the least significant bit. Since values in the look-up-table are scaled and rounded the actual precision of the look-up-table is $\pm 1.5 \cdot 10^{-5}$ (Figure 3.1).

3.1.2 Iterative Optimal Filtering

The Optimal Filtering results rely on having a fixed and known time phase between the signal peak and the LHC clock for all channels. This is not the case for signals caused by cosmic rays which are completely asynchronous with respect to the LHC clock, or even from energy deposits caused by collision events

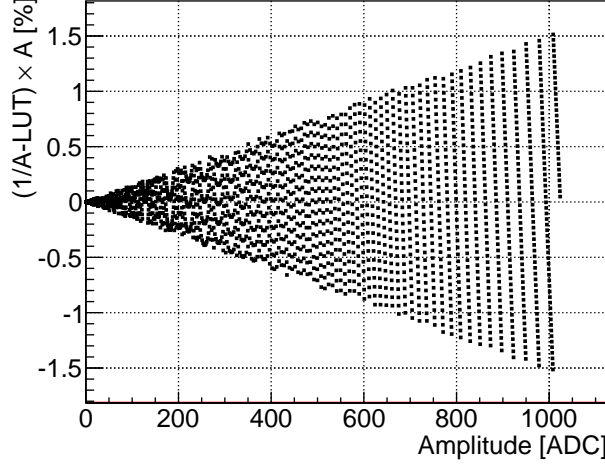


Figure 3.1: Relative difference between $1/A$ and the corresponding value in the look-up-table (LUT) of the DSP implementation as a function of the amplitude.

where the interaction point is shifted slightly from the nominal position.

Nevertheless, the Optimal Filtering can still be applied and accurate reconstruction may be obtained by applying proper weights for each event according to the time position of the signal. This is achieved by an implementation of the Optimal Filtering with iterations, in which the signal phase is obtained by the iterative execution of the Optimal Filtering algorithm up to three times. The computed time after each iteration is used as the input to select the proper weights for the next one, starting from weights computed at time equal to zero. The iterative Optimal Filtering is given by the following equations:

$$A_k = \sum_{i=1}^7 a_i \Big|_{\tau_{k-1}} S_i$$

$$\tau_k = \frac{1}{A_k} \sum_{i=1}^7 b_i \Big|_{\tau_{k-1}} S_i$$

$$p_k = \sum_{i=1}^7 c_i \Big|_{\tau_{k-1}} S_i$$

where S_i represents the i -th digital sample, k is the iteration index starting from 1 and a_i , b_i , c_i are the Optimal Filtering weights which have been previously computed and stored in the Conditions database as explained in

Section 2.3.1.

One of the differences of this algorithm compared to the non-iterative one is the definition of the reconstructed time. The iterative procedure returns the time phase between the maximum of the peak of the received signal and the center of the read-out window, as shown in Figure 3.2. It doesn't take into account the expected time of the pulse explained in Section 2.3, or in other words, the expected time of the pulse when the algorithm is applied is zero. Therefore, the reconstructed time by the Optimal Filtering with iterations can be used to compute the expected time of the pulse when the signals show fixed time phases.

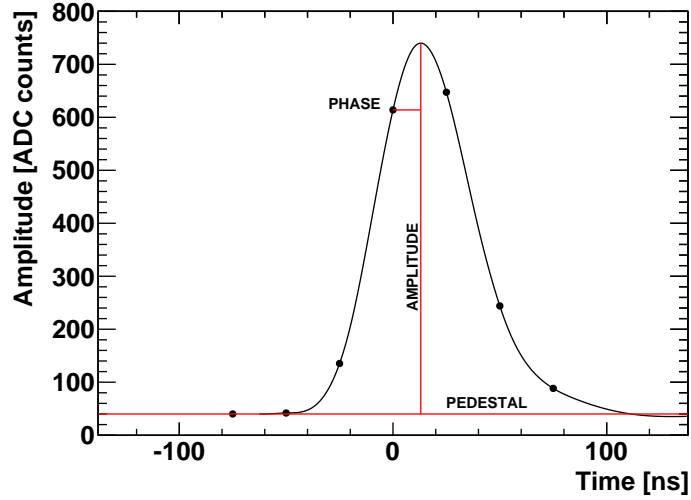


Figure 3.2: Iterative Optimal Filtering magnitudes.

The iterative Optimal Filtering is implemented in the ATLAS offline software and it is the default reconstruction algorithm of the signal when the digital samples are available in the data. This is the case for calibration runs and any other data taking mode in which there are no bandwidth constraints, such as commissioning periods and low Level 1 Trigger rate data taking. The Optimal Filtering with iterations is also implemented online in the ROD DSPs. It was used during the commissioning period of the detector [32], and good reconstruction was achieved although with reduced time granularity due to DSP memory limitations [33]. The Optimal Filtering without iterations has been used by de-

fault in the DSP during all 2010 data taking, due to the time constraint in the processing of a single event. Furthermore, the non-iterative Optimal Filtering provides better results for pedestal and pile-up events.

3.2 Computing Strategy

The storage of the data happens at the Event Filter level. The Sub-Farm Output applications locally store separate data files organized in streams, each of them listed and described briefly in Table 3.4. The data is transferred to permanent storage at Tier 0 within a maximum latency of 24 h. Each of these is briefly described:

Stream	Description
L1Calo	Events triggered by the Level 1 Calorimeter Trigger
MinBias	Events triggered by the Level 1 Minimum Bias Trigger input
Cosmics	Cosmic triggered events
Random	Random triggered events.

Table 3.4: Table of the different data streams as of 2010.

Once the data is available at Tier 0, it makes use of the ATLAS offline software to make a first processing of the data. The raw data streams are reconstructed into Event Summary Data (ESD) files which contain Trigger, tracking and calorimetry information as well as Physics objects containers. Each of them is briefly described below:

- Trigger information: Level 1, Level 2 and Event Filter details.
- Tracking information: inner detector tracks and muon chamber tracks and segments.
- Calorimeter information: electromagnetic and hadronic calorimetric cell details.
- Physics objects containers: electron/photon, muon, tau and jet candidate containers and missing energy information.

Until the Level 1 Trigger rate does not reach 50 kHz the digital samples of the Tile Calorimeter are stored with the data. These are used by the processing

at Tier 0 to perform an Optimal Filtering reconstruction of the data with full floating point precision as opposed to the limited computing power of the DSPs. Results from offline Optimal Filtering are used to populate the cell information for the Tile Calorimeter.

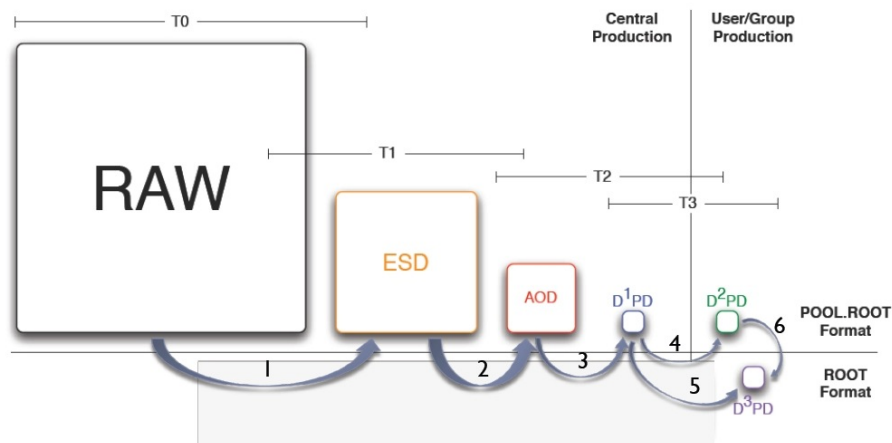


Figure 3.3: ATLAS Event Data Model representation. The square areas are proportional to the event size.

The different data formats in the ATLAS Event Data Model are shown in Figure 3.3. The Raw data is the output data from the Event Filter, the event size is ~ 1.6 MB. The ESD data already explained before has an event size of ~ 0.5 MB. The Analysis Object Data (AOD) is a compact dataset for general physics analysis which has an event size of ~ 0.1 MB. The Derived Physics Data (DPD) is reduced dataset oriented to a specific physics analysis, with an event size of ~ 0.05 MB.

Within the ATLAS analysis model [34], ESD files are generated at Tier 0 and distributed around the Tier 1 computing sites localized around the world. The Grid infrastructure is used to access the ESD files and run processing tasks on them using ATLAS offline software. This consists of sending the task where the data files are, rather than bringing the data to the user.

Among the available data streams, the Level 1 Calorimeter Trigger (L1Calo) stream is chosen to evaluate the performance of the signal reconstruction, This stream has a greater number of high p_T events in the Tile Calorimeter than other streams. ESD files are chosen as opposed to data formats that have

been slimmed since these contain PMT level information. ESD files for L1Calo stream are processed and a ROOT analysis framework [35] file is derived from it. Output files are smaller than 1% of the size of the ESD and accessible for the user to download through Grid applications.

3.2.1 Event Selection

The online Optimal Filtering performance is evaluated in terms of time and energy reconstruction. Since the algorithm relies on the expected time of the signals, its performance can only be considered once the phases for all channels have been correctly determined. The reconstruction performance and the timing of the detector are closely related. Thus, the performance of the Optimal Filtering will be considered after the timing of the detector.

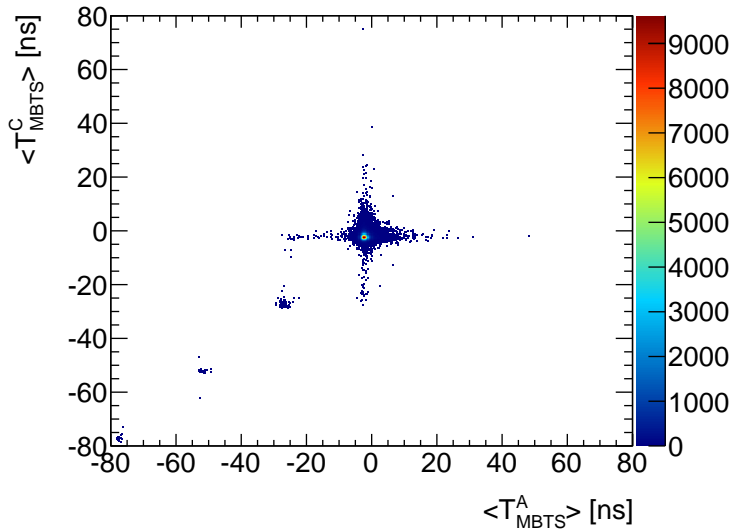


Figure 3.4: Mean value of time for side A MBTS cells versus mean value of time for side C MBTS cells from $\sqrt{s} = 7$ TeV data.

In the following we will use collision data from 2010 at $\sqrt{s} = 7$ TeV. In order to select events from the interaction point, we set some timing criteria on every event. We use the signal from the Minimum Bias Trigger Scintillator (MBTS) cells which are part of the Tile Calorimeter. We compute the mean time of the MBTS cells for the A and C side, T_{MBTS}^A and T_{MBTS}^C respectively, and require an absolute difference smaller than 10 ns, $(|T_{MBTS}^A - T_{MBTS}^C|)$. This

requirement alone does not reject particles originated in the interaction point 1 or 2 bunch crossings in the past. Therefore, it is also required that the absolute mean time of MBTS cells of both sides is smaller than 10 ns. Figure 3.4 shows the distribution of T_{MBTS}^A versus T_{MBTS}^C without the event selection criteria. Figure 3.5 shows the same distribution after the event selection criteria.

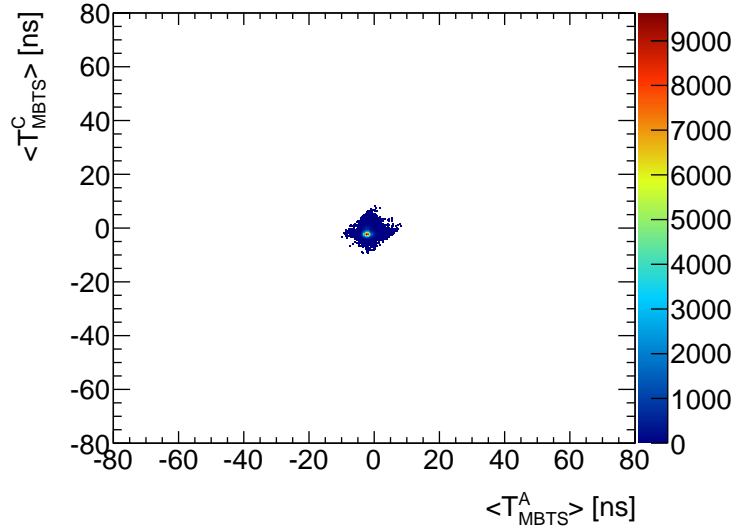


Figure 3.5: Mean value of time for side A MBTS cells versus mean value of time for side C MBTS cells from $\sqrt{s} = 7$ TeV data.

3.3 Time Calibration

The aim of the time calibration is to obtain the reconstructed time by the DSP equal to zero, $T_{DSP} = 0$, for particles coming from the interaction point, in all the channels of the calorimeter. Once this objective is met, particles not originated in the interaction point, such as those originated by cosmic ray deposits, could be removed by a selection cut.

Sources of timing spread are the propagation of clock signals into a large detector, time of flight from the interaction point, the length of WLS fibers, gain dependence and different physics sources (long lived particles). The detector hardware time can be adjusted per digitizer (groups of 6 nearby PMTs) through programmable delays of fine (104 ps) and coarse (25 ns) step which are stored

in the Configuration database. The residual time per channel that cannot be adjusted by these steps is stored in the Conditions database and it is defined as the expected time of the signal.

The mechanisms to achieve the time calibration of the detector include Laser calibration runs, beam data and cosmic ray data. In Laser calibration runs, a Laser pulse is fed to all the PMTs of the calorimeter with a known time shift with respect to the LHC clock. In this way, the time corrections are computed for all channels up to the 5 ns level, which is the current precision of the Laser system. Single beam data is used to compute the fine step corrections for all PMTs and cross checking is done with cosmic ray data. However, the aim of the time calibration should be to provide the expected time of the signal for each channel only from collision data. In the following we argument how time calibration can be achieved from collision data.

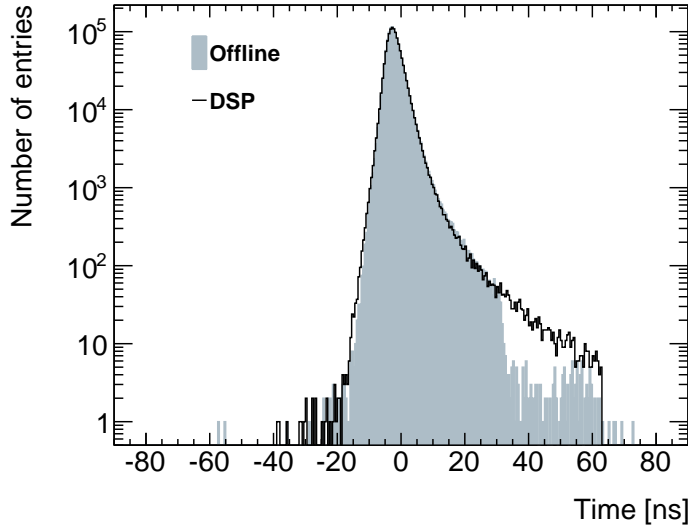


Figure 3.6: Channel time distributions computed by the Optimal Filtering online with no iterations (DSP) and Optimal Filtering offline with iterations (Offline) from $\sqrt{s} = 7$ TeV data.

The algorithm used for the signal reconstruction for timing studies is the offline version of the Optimal Filtering algorithm, the Optimal Filtering with iterations. As mentioned in Section 3.1.2, the reconstructed time by the iterative Optimal Filtering is corrected by the expected time of the signal to obtain the

proper time. The distributions of the time of the channels as reconstructed by the DSP and offline are superimposed in Figure 3.6. In order to eliminate noise, only channels with energy depositions above 300 MeV are selected. The offline reconstruction provides very similar results to the DSP. Both distributions are close to zero with some spread and outliers. The maximum time provided by the DSP is 65 ns as explained in Section 3.1.1. The asymmetry to positive time values is due to the slow cascade in the hadronic interaction. Offline reconstruction shows a sharp edge around 25 ns because of the iterative method.

3.3.1 Cell Time Calibration

Each cell of the Tile Calorimeter is read-out by two PMTs, one on each side. The energy and time of the cell are given respectively by the sum and the mean of the energy and time of both read-out channels, like the following:

$$E_{cell} = E_{chan1} + E_{chan2}$$

$$T_{cell} = \frac{T_{chan1} + T_{chan2}}{2}$$

Figure 3.7 shows the distributions of the cell time using offline reconstruction (T_{OFF-I}) to compute the time per channel. In order to eliminate noise, only cells with energy depositions above 300 MeV per channel are selected. There is a clear peak at -12.5 ns caused by 25 ns difference between channels. There is a bump at 25 ns which could indicate out of time signals. These are the channels that should be further analysed. However, it is impossible to tell whether the signal on these cells was originated by a particle from the interaction point or some other out of time particle based only on the time of the cell.

3.3.2 Time Calibration with Physics Objects

One step further has to be taken in order to properly select signal depositions from the interaction point. For this reason we consider the time of the cells which are included in physics objects such as topological clusters and jets.

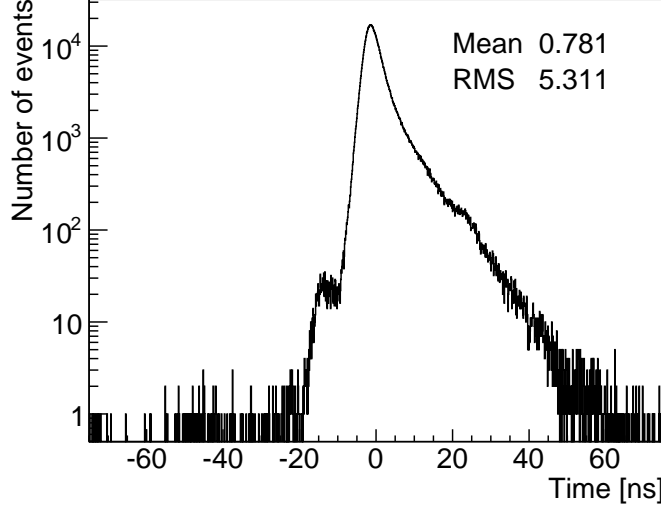


Figure 3.7: Time distribution for Tile Calorimeter cells with energy deposit above 300 MeV per channel for Level 1 Calorimeter Trigger stream from $\sqrt{s} = 7$ TeV data.

Time Calibration with Topological Clusters

Topological clusters are built per event from the cells based on energy thresholds. One of the main advantages of the topological clusters is the noise suppression. The time of the cluster is the weighted mean of the cell time by the square of the cell energy, as the following:

$$T_{cluster} = \frac{\sum_{cells}^{cluster} T_{cell} E_{cell}^2}{\sum_{cells}^{cluster} E_{cell}^2}$$

Only a part of the cells from the Tile Calorimeter are embedded in topological clusters. Figure 3.8 shows the topological cluster time reconstructed offline (using T_{OFF-I} and E_{OFF-I}) considering only Tile Calorimeter cells within a cluster. The few outliers indicate out of time energy signals, probably caused by cosmic rays. Wider spread at the bottom of the peak could be caused by energy depositions in the out of time cells identified in Figure 3.7. However, the time mean value is within the time resolution required for the Tile Calorimeter.

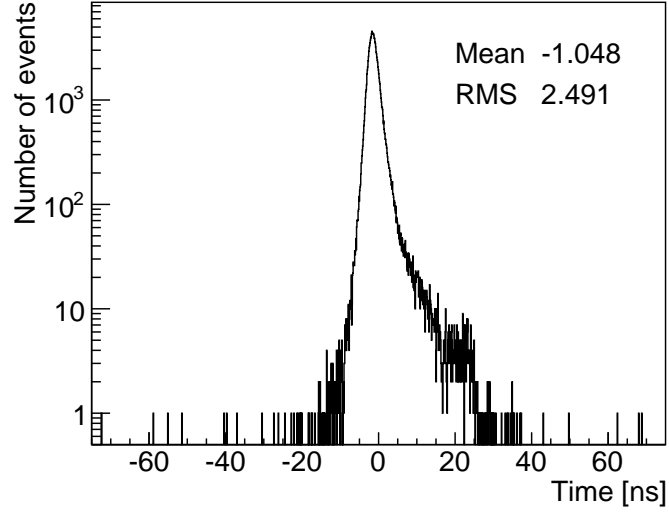


Figure 3.8: Topological cluster time for Tile Calorimeter cells for Level 1 Calorimeter Trigger stream from $\sqrt{s} = 7$ TeV data.

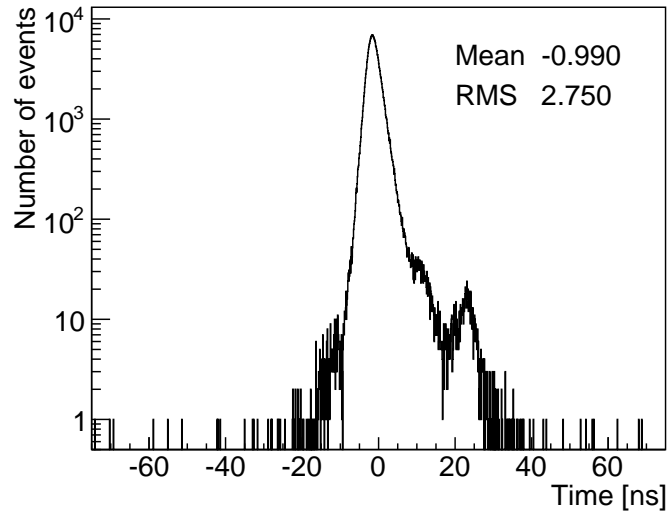


Figure 3.9: Time distribution for Tile Calorimeter cells within a topological cluster for Level 1 Calorimeter Trigger stream from $\sqrt{s} = 7$ TeV data.

Figure 3.9 shows the cell time distribution of cells within a topological cluster, reconstructed offline. This reduces significantly the negative reconstructed time which has no physical meaning. The same outliers of Figure 3.8 are

present from which we can draw the same conclusion. The bump at 12.5 ns and the peak at 25 ns are visible when not weighted by the cell energy. This implies low energy depositions in these cells.

Time Calibration with Jets

Jets are built from selected tracks per event using the anti- k_t algorithm [36]; this is the default jet reconstruction algorithm for ATLAS. One of the main advantages of jets is the interaction point projection. The time of the jet is the weighted mean of the cell time by the square of the cell energy, as the following:

$$T_{jet} = \frac{\sum_{cells}^{jet} T_{cell} E_{cell}^2}{\sum_{cells}^{jet} E_{cell}^2}$$

The jet time distribution for Tile Calorimeter cells (using T_{OFF-I} and E_{OFF-I}) within a jet is shown in Figure 3.10. Most of the outliers of previous Figures are not present anymore. The bump at -12.5 ns and peak at 25 ns clearly indicates out of time cells for which new expected time of the signal should be computed. However, the jet time mean value is within the time resolution required for the Tile Calorimeter.

Figure 3.11 shows the offline cell time distribution of cells within a jet. This distribution is very similar to Figure 3.10. Note out of time cells are easier to identify as they are not weighted by the cell energy. These cells should be identified and new expected time of the signal computed for them.

The Tile Calorimeter time is well calibrated. Most of the signal deposits are within the expected resolution. Out of time cells don't represent a significant contribution to the time as they are three orders of magnitude below the peak. Nevertheless, one of the most important outcomes of the time calibration is the existence of a tool that can allow identification of out of time deposits. Such a technique should be implemented within the data quality assessment tools.

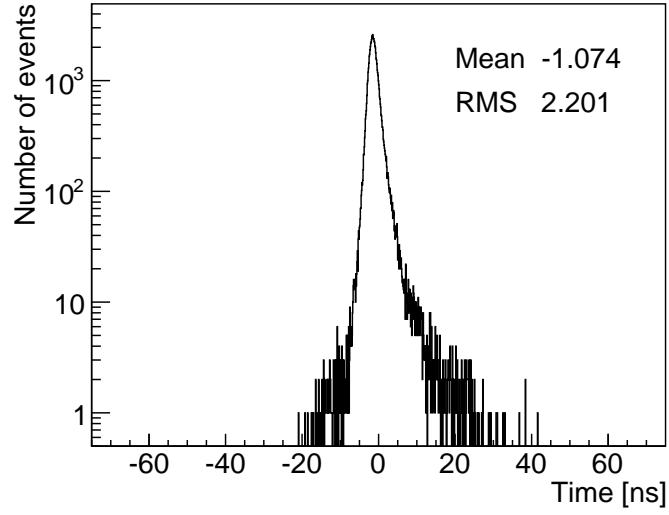


Figure 3.10: Jet time distribution for Tile Calorimeter cells for Level 1 Calorimeter Trigger stream from $\sqrt{s} = 7$ TeV data.

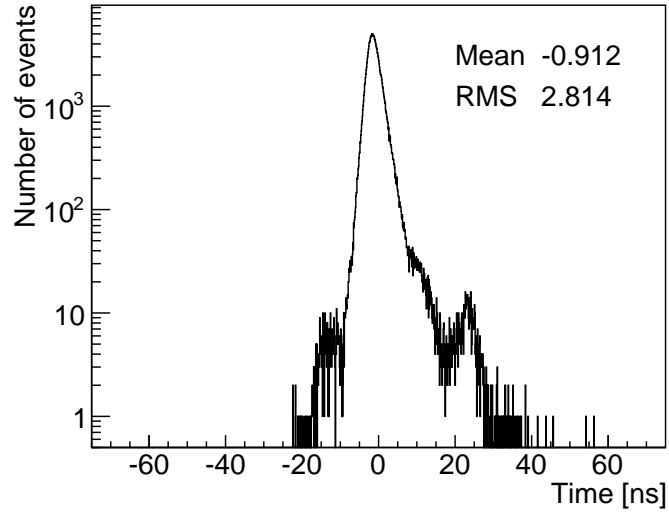


Figure 3.11: Time distribution for Tile Calorimeter cells within a jet for Level 1 Calorimeter Trigger stream from $\sqrt{s} = 7$ TeV data.

3.4 Signal Reconstruction Performance

3.4.1 Algorithm Comparison

The aim of this Section is to evaluate the non iterative Optimal Filtering reconstruction algorithm in terms of the comparison of the implementation online and offline. The results merely differ due to the higher precision of the offline computing and calibration constants.

The calibration constants are computed for each channel by means of the Tile Calorimeter calibration systems: Charge Injection System, Laser and Cesium. Each value of the calibration constants is packed with the highest precision possible, as explained in Section 3.1.

Figure 3.12 shows the relative energy difference between online Optimal Filtering without iterations (E_{DSP}) and offline Optimal Filtering without iterations (E_{OFF-NI}) as a function of E_{OFF-NI} for High and Low gains. Figure 3.13 shows the relative time difference between online (T_{DSP}) and offline (T_{OFF-NI}) as a function of E_{OFF-NI} for High and Low gains. Collision data is used to populate these distributions, with event selection based on collision candidates and 500 MeV cut on the cell energy.

Both results show that the DSP implementation of the Optimal Filtering without iterations is compatible with the offline implementation. There is a maximum uncertainty, due to the implementation reconstruction, of 1 MeV in HG and 40 MeV in LG which is far below the typical 500 MeV cut for noise. It is also true for the time reconstruction, where the error is smaller than 0.3 ns which is better than the time resolution of 1 ns for both gains.

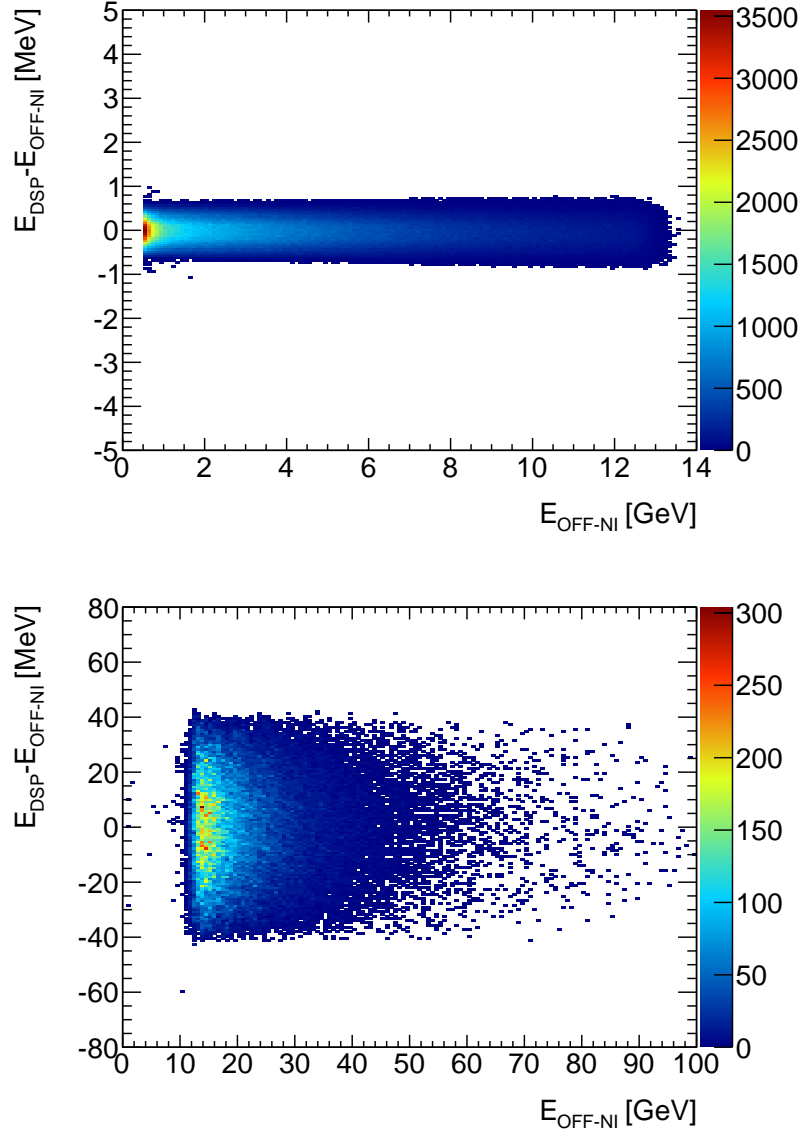


Figure 3.12: Relative energy difference between online and offline Optimal Filtering without iterations (E_{DSP} , E_{OFF-NI}) as a function of the E_{OFF-NI} for high (top) and low (bottom) gains for collision data at $\sqrt{s} = 7$ TeV.

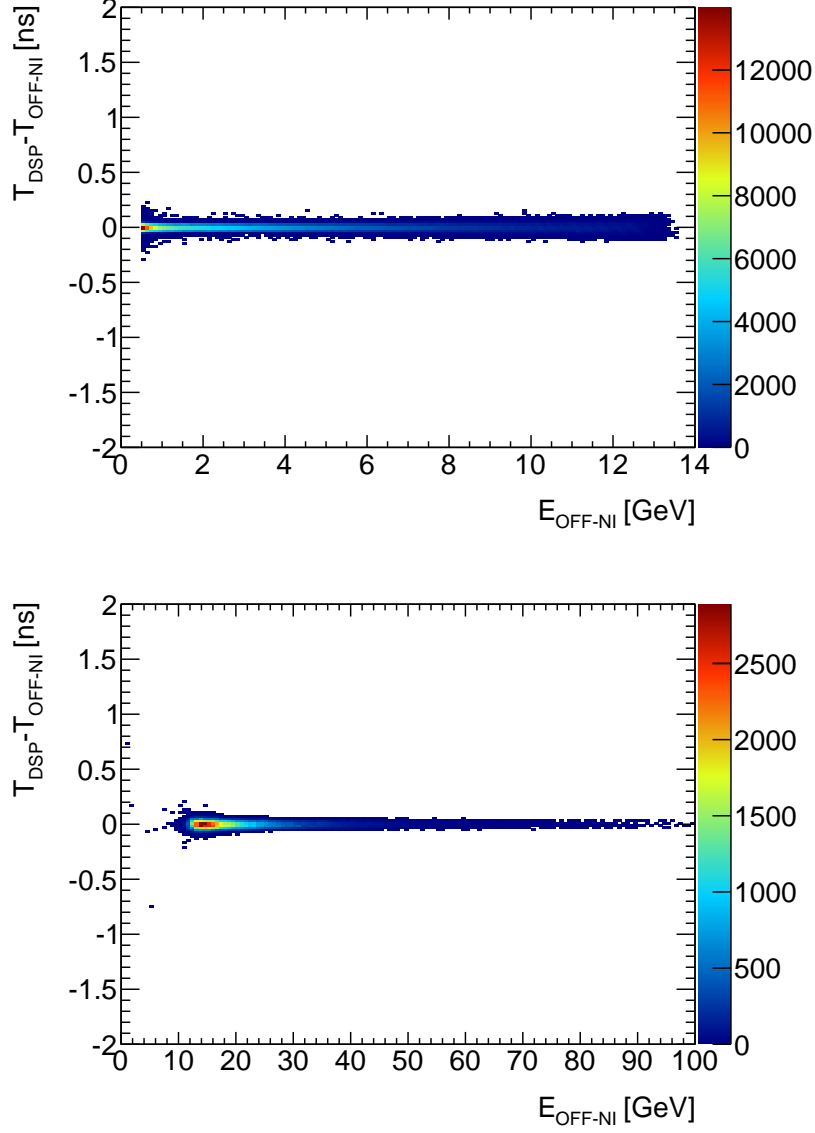


Figure 3.13: Relative time difference between online and offline Optimal Filtering without iterations (T_{DSP}, T_{OFF-NI}) as a function of the energy of the offline Optimal Filtering without iterations (E_{OFF-NI}) for high (top) and low (bottom) gains for collision data at $\sqrt{s} = 7$ TeV.

3.4.2 Performance of the Non Iterative Method

The performance of the Optimal Filtering reconstruction data can be evaluated by the correlation of offline versus online Optimal Filtering time as shown in Figure 3.14. Collision events as well as out of time events, such as cosmics and single beam events, populate the distribution, in order to evaluate the DSP reconstruction performance on a wide time window. Nevertheless, 90% of the pulses are in the time range $[-5,5]$ ns. The distribution shows that the online algorithm reconstructs the time of the signal with a linearity of a few percent in the time range $[-10,10]$ ns. At higher time values the performance deteriorates as expected.

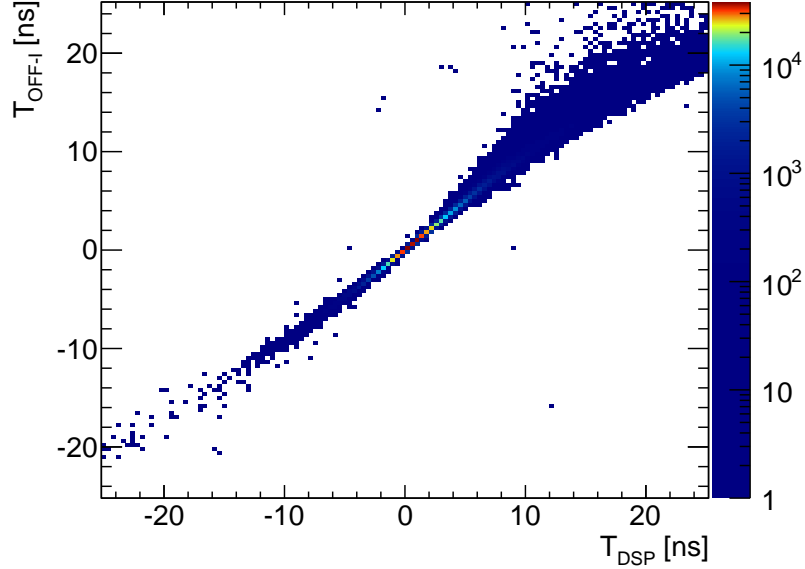


Figure 3.14: Reconstructed time of the offline Optimal Filtering with iterations (T_{OFF-I}) as a function of the time of the online Optimal Filtering without iterations (T_{DSP}) from collision data at $\sqrt{s} = 7$ TeV.

The energy reconstructed by the DSP is affected by the difference between the expected and actual phase of the received pulse. The difference is approximately a parabolic function of the time as reconstructed by the DSP. A parabolic correction can be defined as a function of T_{DSP} . For phases between ± 10 ns there is a maximum deviation of 12%, which can be reduced to 2% after the correction, as shown in Figure 3.15.

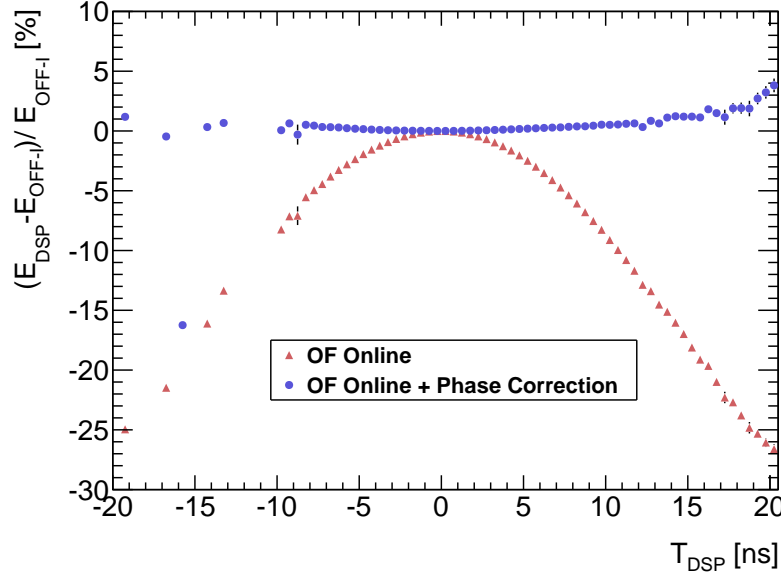


Figure 3.15: Relative difference of the energy of the online Optimal Filtering without iterations (E_{DSP}) with respect to the offline Optimal Filtering with iterations (E_{OFF-I}) as a function of the time of the online Optimal Filtering without iterations (T_{DSP}) with and without parabolic correction from collision data at $\sqrt{s} = 7$ TeV.

The parabolic correction improves the energy reconstruction in the DSP. Figure 3.16 (a) shows the relative energy difference between offline and online before the parabolic correction and Figure 3.16 (b) shows the same distribution after its application. The low energy region of Figure 3.16 is the most affected by the parabolic correction. This indicates that the out of time energy deposits are small, from which we can infer that the time calibration of the Tile Calorimeter is good for energetic signals. The 5-10% discrepancy for small energies implies out of time signals beyond ± 10 ns.

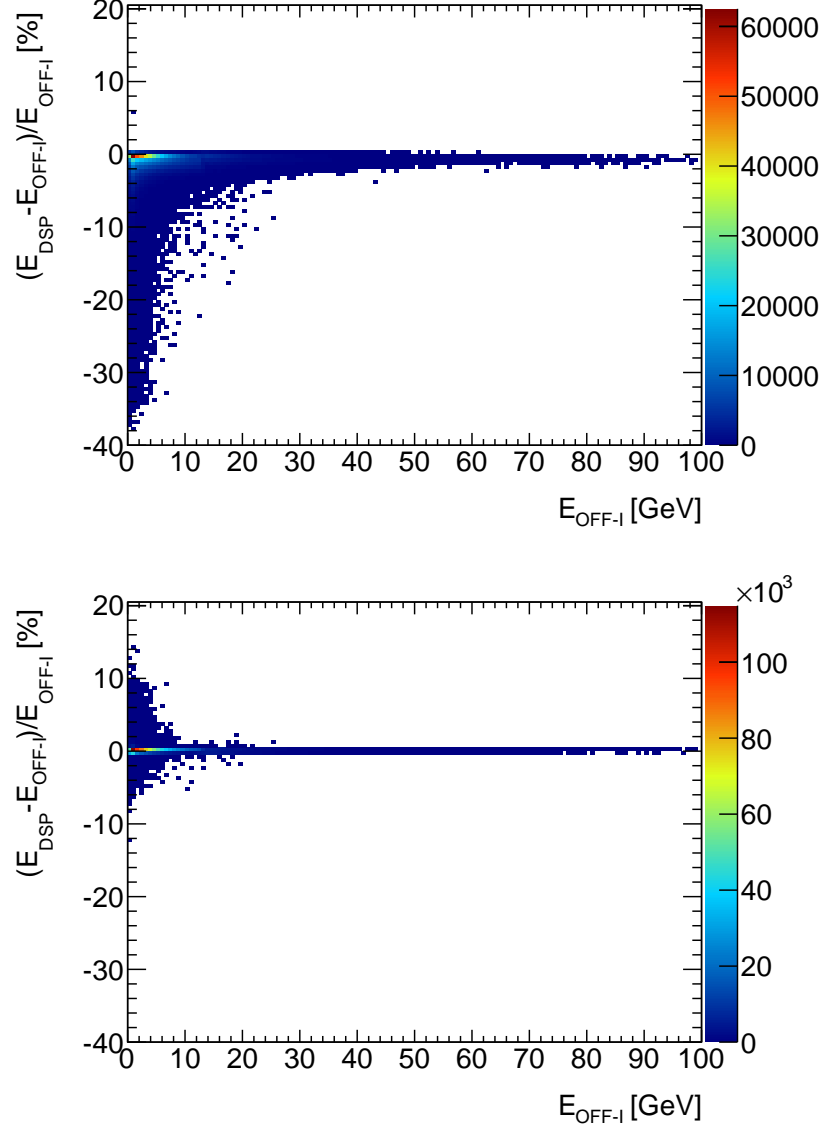


Figure 3.16: Relative difference of the energy of the online Optimal Filtering without iterations (E_{DSP}) with respect to the offline Optimal Filtering with iterations (E_{OFF-I}) as a function of E_{OFF-I} without (top) and with (bottom) parabolic correction from collision data at $\sqrt{s} = 7$ TeV.

Chapter 4

Theoretical Motivation

4.1 The Standard Model

The Standard Model is the most accurate quantum field theory of fundamental particles and their interactions. It unifies three of the four forces of nature, electromagnetic, strong and weak forces, into a single one. It describes the building blocks of matter by means of fermion particles and the forces between them by means of boson particles which are the carriers of those interacting forces. When a force mediating particle is exchanged, at a macro level the effect is equivalent to a force influencing both of them, and the particle is therefore said to have mediated that force.

Fermions are particles of spin $\frac{1}{2}$ that respect the Pauli exclusion principle. Each fermion has a corresponding anti particle with opposite quantum numbers. Fermions are classified into those that feel the strong interaction, quarks, and those that don't, leptons. There are six lepton particles, electron (e), muon (μ) and tau (τ), which have electric charge equal to the charge of the electron, together with their corresponding neutral partners, electron neutrino (ν_e), muon neutrino (ν_μ) and tau neutrino (ν_τ). They are classified into three generations, as shown in Figure 4.1. Each generation has the same properties except for their mass. Quarks are also arranged in doublets as the leptons, their names are up and down (u,d), charm and strange (c,s) and top and bottom (t,b). They have fractional electric charge with respect to the charge of the electron $+\frac{2}{3}$ for

the up-type quarks (u, c, t) and $-\frac{1}{3}$ for down-type quarks (d, s, b) . Quarks also carry a color charge, which makes results in being perpetually bounded to one another in colourless particles (hadrons). There is mixing between the three generations of quarks, which in the Standard Model is parametrized (but not explained) by the Cabibbo-Kobayashi-Maskawa (CKM) matrix.

Bosons are particles of spin 1 that do not follow the Pauli exclusion principle. These arise when a local gauge invariance is applied to the fermionic fields, and are a manifestation of the symmetry group of the theory, which for the Standard Model is $SU(3) \times SU(2) \times U(1)$. Massless photons mediate the electromagnetic force between electrically charged particles. Quantum Electrodynamics (QED) describes this interaction in terms of the underlying $U(1)$ symmetry. Massive W^\pm and Z gauge bosons mediate the weak interactions between particles of different flavours (all quarks and leptons). The W^\pm carry an electric charge and couple to electrically charged particles through the electromagnetic interaction. These three gauge bosons along with the photons are grouped together which collectively mediate the electroweak interactions described in terms of the $SU(2) \times U(1)$ symmetry. Finally, eight massless gluons mediate the strong interactions between color charged particles (quarks). The eightfold multiplicity of gluons is labeled by a combination of color and an anticolor charge. Because the gluon has an effective color charge, they can interact among themselves. The gluons and their interactions are described by the theory of Quantum Chromodynamics (QCD) guided by the $SU(3)$ symmetry.

4.1.1 Quantum Electrodynamics

Quantum Electrodynamics (QED) was developed in 1940s by Feynman, Dyson, Schwinger and Tomonaga [37]. It was the first satisfactory quantum field theory. It describes the interaction of electrons and positrons with the electromagnetic field, and the creation and annihilation of quantum particles. To understand QED and the other quantum field theories that will follow, a basic concept in physics has to be introduced, which is the notion of symmetry.

We say there is a symmetry under a certain transformation, when the equation representing the physical process is invariant under the application of the operator representing such transformation. Following Noether's theorem [38],

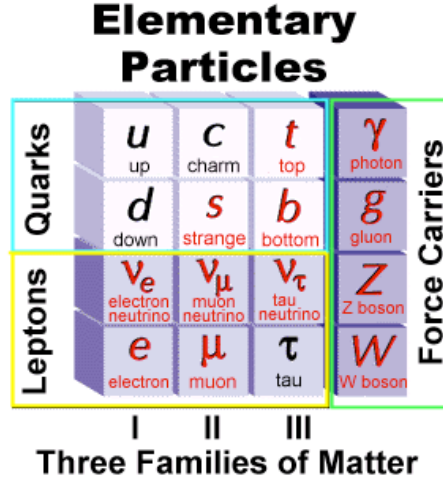


Figure 4.1: The Standard Model.

to every differentiable symmetry generated by local actions, there corresponds a conserved current, which results in the conservation of a physical quantity. But there is a caveat to this great procedure in science, that is experimental "verification". Although there can be a mathematical proof for a conservation law, experimental data may refute this conservation. Only when there is no evidence of the contrarary, the conservation law can be assumed to be true, but it has to be accompanied by the upper limit given by the experiment.

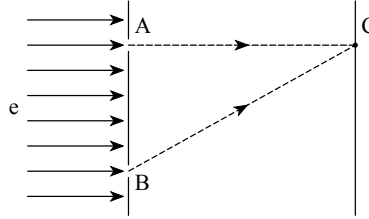


Figure 4.2: Diagram of a low energy electron beam colliding against a double slit.

We will derive the QED Lagrangian from basic principles. For simplicity we will use natural units, where $\hbar = c = 1$. Let us take a low energy electron beam (Figure 4.2) colliding against a double slit AB. The electron beam is described by a plane wave function $\psi = e^{ipx}$. The interference pattern at C will depend on the difference of phases at A and B, therefore depend of the global phase difference. We can choose to measure this phase at points A and B

independently but the result in C has to be independent of local phase selections in each point.

So the wave function has a phase θ , which can be arbitrarily measured in each point $\theta = \theta(x)$. For convenience we will write $\theta(x) \equiv q\Lambda$, so the transformation of the wave function is the following:

$$\psi \rightarrow \psi' = e^{i\theta(x)}\psi = e^{iq\Lambda}\psi$$

The Dirac Lagrangian density for a free particle is given by:

$$\mathcal{L}_D = \bar{\psi}(i\gamma^\mu\partial_\mu - m)\psi \quad (4.1)$$

If we try to transform blindly the Lagrangian we will obtain the following non-invariant expression:

$$\mathcal{L} \rightarrow \mathcal{L}' = \bar{\psi}'(i\gamma^\mu\partial_\mu - m)\psi' = \bar{\psi}(i\gamma^\mu\partial_\mu - m - q\gamma^\mu\partial_\mu\Lambda)\psi = \mathcal{L} - \bar{\psi}(q\gamma^\mu\partial_\mu\Lambda)\psi$$

But we have to remember that we are talking about the electromagnetic field known since Maxwell's time [39]. If we intend to move an electron in empty space, there will be a four-potential $A_\mu = (E, \phi)$ creating a field around it.

To restore the invariance of the Lagrangian we introduce the *Covariant Derivative* which uses the four-potential as the *connection* in differential geometry [40]:

$$D_\mu \equiv \partial_\mu + iqA_\mu$$

If the four-potential transforms under phase rotations as:

$$A_\mu \rightarrow A'_\mu \equiv A_\mu - \frac{1}{q}\partial_\mu\Lambda$$

the Covariant Derivative transforms like the following:

$$D_\mu \rightarrow D'_\mu = \partial_\mu + iA'_\mu = D_\mu - i\partial_\mu\Lambda$$

We can re-write the Lagrangian in terms of the Covariant Derivative and prove

it is invariant under gauge transformations:

$$\begin{aligned}\mathcal{L}' &= \bar{\psi}'(i\gamma^\mu D'_\mu - m)\psi' = e^{-iq\Lambda}\bar{\psi}(i\gamma^\mu D_\mu - m + q\gamma^\mu\partial_\mu\Lambda)e^{iq\Lambda}\psi = \\ &= \bar{\psi}(i\gamma^\mu D_\mu - q\gamma^\mu\partial_\mu\Lambda - m + q\gamma^\mu\partial_\mu\Lambda)\psi = \bar{\psi}(i\gamma^\mu D_\mu - m)\psi = \mathcal{L}\end{aligned}$$

But before we claim the QED Lagrangian we should recall the contribution of a free term of this vector field A_μ for massless particles (photons) given by the tensor field $F^{\mu\nu} \equiv \partial^\mu A^\nu - \partial^\nu A^\mu$, that represents the potential kinetic energy:

$$\mathcal{L} = -\frac{1}{4}F^{\mu\nu}F_{\mu\nu}$$

Therefore, starting from the Dirac Lagrangian and imposing local phase invariance, we obtain the QED Lagrangian:

$$\mathcal{L}_{QED} = i\bar{\psi}\gamma^\mu\partial_\mu\psi - m\bar{\psi}\psi - q\bar{\psi}\gamma^\mu A_\mu\psi - \frac{1}{4}F^{\mu\nu}F_{\mu\nu} \quad (4.2)$$

or in covariant notation:

$$\mathcal{L}_{QED} = \bar{\psi}(i\gamma^\mu D_\mu - m)\psi - \frac{1}{4}F^{\mu\nu}F_{\mu\nu}$$

that describes the interaction of charged particles and photons in terms of quantum fields. Any field theory in which the Lagrangian is invariant under a continuous group of local transformations is known as a gauge theory. We have applied a phase transformation which in group theory corresponds to the simplest form of a unitary group transformation, $U(1)$. This is the circle group, all complex numbers with absolute value 1 under multiplication ($U^\dagger U = 1$).

The charge of the electron is the conserved magnitude derived from the gauge invariance. The strength of the interaction is usually described by the coupling constant α_{em} which can be computed from the charge of the electron. Its value depends on the momentum transfer q^2 in an interaction. At low energies ($q^2 \rightarrow 0$) the coupling constant value is that of the fine structure constant, $\alpha_{em} = \frac{e^2}{4\pi\hbar c} = \frac{1}{137}$. At the scale of the Z-boson mass (short distances), its value increases: $\alpha_{em}(m_Z) \approx \frac{1}{128}$.

4.1.2 Quantum Chromodynamics

The principle of Quantum Chromodynamics (QCD) is that hadronic matter is made of quarks. Quarks were introduced in 1963 [41] to explain the increasing number of hadrons discovered by particle physics experiments. It seemed that such a large number of particles could not be all fundamental and to gain deeper insight they were sorted into groups having similar properties and masses. Gell-Mann [42] and Zweig [43, 44] proposed that this group structure could be explained by the existence of a flavoured particle inside the hadrons: The quark.

But the existence of quarks on it's own was not enough to explain the apparent violation of the Pauli exclusion principle observed by some of these bound states. Half integer spin hadrons, called baryons, are believed to be a bound state of three ¹ quarks. The observation of the Δ^{++} baryon, with ($J = \frac{3}{2}$), that was described as a bound state of three *up* type quarks, should have a symmetric wave function in spin ($u^\uparrow u^\uparrow u^\uparrow$), which would be contrary to Fermi-Dirac statistics. So, in order to make the wave function anti-symmetric, an additional quantum number was introduced [45]. It was called the colour quantum number, with three possible values, often called red, green and blue. In this way, the wave function of the Δ^{++} could be described by an anti-symmetric wave function as the result of three up quarks with aligned spins and different colour ($u_r^\uparrow u_g^\uparrow u_b^\uparrow$). Of course the introduction of the coulour degree of freedom should lead to a proliferation of states, that is not observed, and so it had to be complemented by another ad-hoc hypothesis that only colour singlet states can exist in nature. This property is known as confinement.

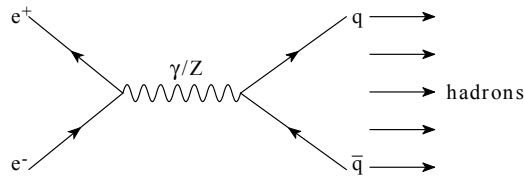


Figure 4.3: Feynman diagram of the $e^+e^- \rightarrow \text{hadrons}$ mediated by a photon (γ) or a Z boson.

The experimental evidence for the number of colours came from the descrip-

¹Any odd number of quark constituents will also give a half-integer spin state.

Quark	Mass [GeV/c ²]	Q	Generation
u	0.004	+2/3	1
d	0.008	-1/3	1
c	1.2	+2/3	2
s	0.15	-1/3	2
t	175	+2/3	3
b	4.7	-1/3	3

Table 4.1: List of quarks in the Standard Model.

tion of the process $e^+e^- \rightarrow \text{hadrons}$, where the following ratio can be measured:

$$R_{e^+e^-} \equiv \frac{\sigma(e^+e^- \rightarrow \text{hadrons})}{\sigma(e^+e^- \rightarrow \mu^+\mu^-)}$$

At energies well below the mass of the Z, the dominant process is photon exchange (Figure 4.3) and the approximate value of the ratio is:

$$R_{e^+e^-} \approx N_C \sum_{f=1}^{N_f} Q_f^2$$

This ratio was found to be consistent with N_C equal to three. Therefore, each quark exists in three different states of colour.

Within the SM, the QCD sector describes the strong interaction between quarks. It was developed in 1973 [46] following the way opened by QED and the Yang-Mills theories [47].

We can think of a quark as being a triplet of colour, represented by a three component vector of wave functions $\psi^T = (\psi_r, \psi_g, \psi_b)$. So each of the known six quarks is represented by a colour triplet ψ_i , $i=1, \dots, 6$. If we want to build a gauge invariant theory for quarks we should replace the U(1) symmetry group that we used in QED by the U(3) symmetry group as we now have three component wave functions. U(3) can be split into $U(1) \otimes SU(3)$ where U(1) is a phase transformation as in QED. U(1) could be associated with the conservation of the baryon number. However it is evident that it is a broken symmetry because the matter we see is made out of baryons and not anti-baryons. So the local gauge invariance will be restricted to the SU(3) symmetry group. SU(3) is a matrix of the Lie group of dimension n^2-1 . Where the group generators T_a ($a=1, \dots, 8$), frequently represented by the Gell-Mann matrices (Figure 4.4) ($T_a = \lambda_a/2$), are

traceless and anti-hermitian which obey the following commutation relation:

$$[T_a, T_b] = i \sum_{c=1}^8 f_{abc} T_c$$

Where f_{abc} are the structure constants for SU(3) and the non-zero values are:

$$\begin{aligned} f_{123} &= 1 \\ f_{147} &= -f_{156} = f_{246} = f_{257} = f_{345} = -f_{367} = \frac{1}{2} \\ f_{458} &= f_{678} = \frac{\sqrt{3}}{2} \end{aligned}$$

We can generalize the gauge transformation on the wave function:

$$\psi_i \rightarrow \psi'_i = \psi_i e^{ig_s T_a \Lambda_a}$$

Where g_s is a constant, analogous to the electric charge in QED that will set the interaction strength. It is related to the strong coupling constant α_s and it is not predicted by the theory. The eight Λ_a functions are the eight degrees of freedom of the gauge symmetry and T_a are the generators of the transformation presented above. Thus we now expect QCD to have eight vector fields A_μ^a instead of one, which will count for the eight coloured gluons that mediate the quark interaction. We generalize the covariant derivative expression to:

$$D_\mu = \partial_\mu - ig_s A_\mu^a T_a$$

and the field strength is generalized by the expression:

$$F_{\mu\nu}^a = \partial_\mu A_\nu^a - \partial_\nu A_\mu^a + g_s f^{abc} A_\mu^b A_\nu^c$$

The Lagrangian, that describes the strong interaction of coloured quarks and gluons, can be written in covariant notation like:

$$\mathcal{L}_{QCD} = \sum_i^{flavours} \bar{\psi}_i (\gamma^\mu D_\mu - m_i) \psi_i - \frac{1}{4} F_{\mu\nu}^a F_a^{\mu\nu}$$

The main difference of QCD with respect to QED lies on the additional term in the field tensor $F_{\mu\nu}^a$. It is a consequence of the non-abelian property of

$$\begin{aligned}
\lambda_1 &= \begin{pmatrix} 0 & 1 & 0 \\ 1 & 0 & 0 \\ 0 & 0 & 0 \end{pmatrix} & \lambda_2 &= \begin{pmatrix} 0 & -i & 0 \\ i & 0 & 0 \\ 0 & 0 & 0 \end{pmatrix} & \lambda_3 &= \begin{pmatrix} 1 & 0 & 0 \\ 0 & -1 & 0 \\ 0 & 0 & 0 \end{pmatrix} \\
\lambda_4 &= \begin{pmatrix} 0 & 0 & 1 \\ 0 & 0 & 0 \\ 1 & 0 & 0 \end{pmatrix} & \lambda_5 &= \begin{pmatrix} 0 & 0 & -i \\ 0 & 0 & 0 \\ i & 0 & 0 \end{pmatrix} & \lambda_6 &= \begin{pmatrix} 0 & 0 & 0 \\ 0 & 0 & 1 \\ 0 & 1 & 0 \end{pmatrix} \\
\lambda_7 &= \begin{pmatrix} 0 & 0 & -i \\ 0 & i & 0 \\ 0 & 0 & 0 \end{pmatrix} & \lambda_8 &= \frac{1}{\sqrt{3}} \begin{pmatrix} 1 & 0 & 0 \\ 0 & 1 & 0 \\ 0 & 0 & -2 \end{pmatrix}
\end{aligned}$$

Figure 4.4: Gell-Man's matrix representation of the infinitesimal generators of the $SU(3)$ symmetry group.

the theory and represents the self-interaction of the gauge fields, which leads to a QCD coupling constant g_s small at large momentum transfers but large for soft processes. This creates a completely different phenomenology with respect to QED. Quarks inside hadrons behave almost as free particles in high energy interactions, allowing perturbative calculations (Feynman rules). This property is called asymptotic freedom. On the contrary, at distances larger than 10^{-15} m, the strong force becomes so intense that new quark-antiquark pairs can be created from the vacuum. As a result, quarks only appear in colourless states inside baryons and mesons. This property is called confinement, which was one of the requirements of the theory.

In some sense, the strong interaction acts much like an elastic band being hold by two fingers. It is loose as you approach the fingers, but it increases its strength as the fingers move apart. Needless to say that the principle of maximum entropy and minimum energy will favour the creation of pairs of quark anti-quark from the QCD vacuum, rather than letting us observe a free quark in space. Which is in agreement with the observations.

4.1.3 Electroweak interactions

The search for the description of the weak interactions started already in the XIX century, when Becquerel accidentally discovered the nuclear β decay (${}^AZ \rightarrow {}^AZ + \beta^-$) in 1896. This decay showed a continuous spectrum indicating

Lepton			H	Q	I	Y
I	II	III				
ν_e	ν_μ	ν_τ	-1	0	$+\frac{1}{2}$	-1
e^-	μ^-	τ^-	-1 +1	-1 -1	$-\frac{1}{2}$ 0	-1 -2

Table 4.2: Listing of Standard Model Leptons and their quantum numbers relevant for the Electroweak interaction. Helicity (H), Charge (Q), Weak Isospin (I) and Weak Hypercharge ($Y=2(Q-I_3)$).

3-body kinematics, which lead to the hypothesis of a new elementary particle approximately massless, neutral and penetrating, named as neutrino in the 1930's. This process was described by Fermi's contact interaction perfectly well at tree level. It can be expressed in current terms as:

$$n \rightarrow p + e^- + \bar{\nu}_e$$

Another step forward was taken in 1932 with the discovery of the neutron by Chadwick [48], from which the concept of isospin was later derived by Heisenberg. Isospin describes protons and neutrons as components of the same doublet or different states of the same particle, undistinguishable without electromagnetic interaction (and gravitation). But it was most probably the discovery of parity violation in weak decays in 1956, a turning point in the development of the current theory. The spin of the neutrino, inferred by measurements of other particles, was always emitted with the spin contrary to the direction of movement. It is therefore called left handed (it has left handed helicity). This discovery implied also maximal parity violation in weak interactions. After all, low energy weak interaction processes were characterized by Fermi coupling constant G_F which was experimentally measured.

$$G_F \approx 10^{-5} \text{ GeV}^{-2}$$

The current theory was developed by Glashow [49], Weinberg [50] and Salam [51] by the end of the 1960s. It unifies electromagnetic and weak interactions into the Electroweak interaction. We shall derive the Lagrangian of this theory by recognising the symmetries of nature, although they don't appear so evident as in QED or QCD cases.

$$\sigma_1 = \begin{pmatrix} 0 & 1 \\ 1 & 0 \end{pmatrix} \quad \sigma_2 = \begin{pmatrix} 0 & -i \\ i & 0 \end{pmatrix} \quad \sigma_3 = \begin{pmatrix} 1 & 0 \\ 0 & -1 \end{pmatrix}$$

Figure 4.5: Pauli's matrix representation of the infinitesimal generators of the SU(2) symmetry group.

Left handed leptons are organized in doublets of weak isospin (Figure 4.2). For each of the three generations of the SM, we can describe the doublet as a two component vector of wave functions $\psi_L^T = (\psi(\nu_e), \psi(e_L^-))$. Right handed leptons are weak isospin singlets and only one wave function is needed: $\psi_R = \psi(e_R^-)$.

Like for the QCD case, we can build a gauge invariant QFT for left handed leptons based on weak isospin conservation. We first consider the U(2) symmetry group, breaking it down into unimodular transformations and phase transformations, SU(2)xU(1), we identify SU(2) as the symmetry group that fits for weak isospin representation, named SU(2)_L. SU(2) is a real matrix Lie group of dimension n²-1. In this case, the group generators τ_a (a=1,2,3) are frequently represented by the Pauli matrices (Figure 4.5) ($\tau_a = \sigma_a/2$), which are traceless, anti-hermitian and obey the following commutation relation:

$$[\tau_a, \tau_b] = i\varepsilon_{abc}\tau_c$$

where ε_{abc} is the Levi-Civita symbol.

However, we still have to include somehow the electromagnetic interaction between charged leptons. This description has to be invariant under SU(2) and it must represent QED under some certain limits. A weak hypercharge defined using the Gell-Man - Nishijima connection ($Y=2(Q-I_3)$), classifies the left handed leptons and right handed leptons by hypercharge, where both components of the SU(2) doublets have the same value:

$$Y(\psi_L) = -1$$

$$Y(\psi_R) = +1$$

Therefore, we recall the U(1) symmetry similar to QED based on a hypercharge, named U(1)_Y. Summarising, SU(2) symmetry group is applied to left handed

leptons and U(1) to both lepton helicities. The wave functions are transformed like the following:

$$\psi_{i,L} \rightarrow \psi'_{i,L} = \psi_{i,L} e^{ig\tau_a \Lambda_a} e^{ig'y}$$

$$\psi_{i,R} \rightarrow \psi'_{i,R} = \psi_{i,R} e^{ig'y}$$

Where i is the generation number ($i = 1, 2, 3$), g the interaction strength for SU(2), the three Λ_a functions are the degrees of freedom of SU(2), g' the interaction strength for U(1) and the y function the degree of freedom for U(1). We define the covariant derivatives as:

$$D_\mu \psi_{i,L} \equiv (\partial_\mu - ig\tau_a W_\mu^a - ig'B_\mu) \psi_{i,L}$$

$$D_\mu \psi_{i,R} \equiv (\partial_\mu - ig'B_\mu) \psi_{i,R}$$

Where we introduce the W_μ^a and B_μ vector fields. Their field strength tensor is given by:

$$B_{\mu\nu} = \partial_\mu B_\nu - \partial_\nu B_\mu$$

$$W_{\mu\nu}^a = \partial_\mu W_\nu^a - \partial_\nu W_\mu^a + g\varepsilon^{abc} W_\mu^b W_\nu^c$$

The three, $W_\mu^a = (W_\mu^1, W_\mu^2, W_\mu^3)$, and the B_μ fields are associated with W^\pm , Z and γ bosons in the following way:

$$W_\mu^\pm \equiv \frac{1}{\sqrt{2}}(W_\mu^1 \mp iW_\mu^2)$$

$$\begin{pmatrix} Z_\mu \\ A_\mu \end{pmatrix} \equiv \begin{pmatrix} \cos\theta_W & -\sin\theta_W \\ \sin\theta_W & \cos\theta_W \end{pmatrix} \begin{pmatrix} W_\mu^3 \\ B_\mu \end{pmatrix}$$

The free Lagrangian for massless leptons is like the following:

$$\mathcal{L} = \sum_{i=1}^3 i\bar{\psi}_{i,L} \gamma^\mu D_\mu \psi_{i,L} + i\bar{\psi}_{i,R} \gamma^\mu D_\mu \psi_{i,R}$$

Where we add the contribution of the gauge fields:

$$\mathcal{L}_{EW} = \sum_{i=1}^3 i\bar{\psi}_{i,L} \gamma^\mu D_\mu \psi_{i,L} + i\bar{\psi}_{i,R} \gamma^\mu D_\mu \psi_{i,R} - \frac{1}{4} B_{\mu\nu} B^{\mu\nu} - \frac{1}{4} W_{\mu\nu}^a W_a^{\mu\nu}$$

This model explains in an accurate way the electroweak interaction, but is incomplete since it only allows massless fermions and bosons. The photon is certainly massless but the other three bosons, W^\pm and Z^0 , discovered in 1983 at the CERN SPS collider [52] have non-zero masses. The addition of mass terms violates local gauge invariance and spoils the renormalizability of the theory. Therefore, it is necessary to introduce a new mechanism to give mass to bosons and fermions. This mechanism is called the Higgs mechanism.

4.1.4 Spontaneous Symmetry Breaking

One of the breakthroughs in modern particle physics has been the mechanism of spontaneous symmetry breaking. It is used in the Higgs mechanism to give mass to the gauge bosons. Philosophically it is a subtle but very deep idea. The Lagrangian that governs the dynamics of a physical system is invariant under the transformation of the symmetry group but the ground state of the system does not exhibit the same invariance. Like a ball sitting on top of a hill, which is in a completely symmetric but unstable state as it is not at its lowest energy state, the slightest perturbation force will cause it to roll down the hill in some particular direction, implying a new distinguishable direction for the system. This concept explains how from a symmetric description of nature, massive particles can exist but does not explain what forces caused the observed non-symmetry. Examples of spontaneous symmetry breaking are found in nature. The following macroscopic example is attributed to Salam. Let's imagine N diners at a banquet seated symmetrically around a circular table, with N pieces of bread placed equidistantly between adjacent diners. Any diner will find a piece of bread on his left and on his right. Someone has to break the symmetry by taking a bread, say that on his left, then all diners will be compelled to follow this choice.

Now let us consider the model of a scalar field ϕ affected by the following potential:

$$V(\phi) = \frac{1}{2}\mu^2\phi^2 + \frac{1}{4}\lambda\phi^4$$

The Lagrangian of the system is given by:

$$\mathcal{L} = \frac{1}{2}(\partial_\mu \phi)^2 - \frac{1}{2}\mu^2 \phi^2 - \frac{1}{4}\lambda \phi^4 \quad (4.3)$$

which is invariant under the transformation $\phi \rightarrow -\phi$. The vacuum state of the system ϕ_0 must satisfy the condition:

$$\left. \frac{\partial \mathcal{L}}{\partial \phi} \right|_{\phi=\phi_0} = \phi_0(\mu^2 + \lambda \phi_0^2) = 0$$

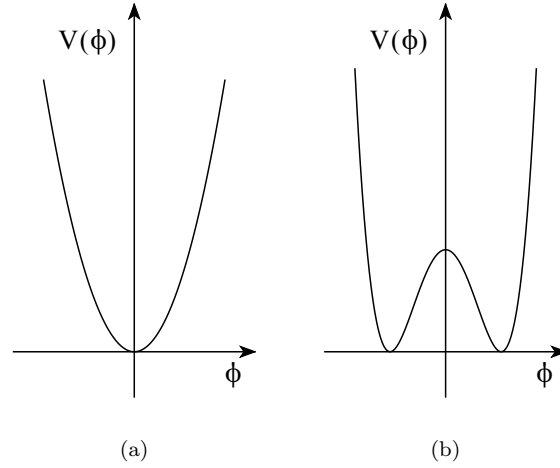


Figure 4.6: Spontaneous symmetry breaking potentials.

This condition has two possibilities, the first one is when both μ^2 (mass²) and λ (signal strength) are positive, which implies that there is only one solution ($\phi_0 = 0$) as shown in Figure 4.6 (a). Any attempt of moving the particle away from ϕ_0 will result in a resistance which one can identify with inertia against movement.

The second solution is given when μ^2 is negative while λ remains positive. In which case we get the form of the potential represented in Figure 4.6 (b). Note that λ cannot be negative as the potential must have a lower bound. In this case, the ground state solution is the following:

$$\phi_0^2 = \frac{-\mu^2}{\lambda}$$

This solution appears to represent a particle with imaginary mass ($\mu^2 < 0$). It gives a negative resistance to any attempts of moving it from the origin, where the field is zero. The potential decreases in both directions, so it is energetically favorable for our field to roll down to one of the two ground states.

The vacuum should correspond to the minimum energy state of the system as there cannot be less energy than in the vacuum. But in the case $\mu^2 < 0$, the vacuum does not correspond to zero value of the field. On the contrary, the field takes the Vacuum Expectation Value (VEV):

$$v = \pm \sqrt{\frac{-\mu^2}{\lambda}}$$

Physics cannot depend on the shift of a scalar field. We will try to redefine the vacuum state as the minimum energy state by shifting the field to one of the solutions for the VEV. We define $\phi = \eta + v$ (or $-v$). The Lagrangian rewritten in terms of the new field η is like the following:

$$\mathcal{L} = \frac{1}{2}(\partial_\mu \eta)^2 - \lambda v^2 \eta^2 - \lambda v \eta^3 - \frac{1}{4} \lambda \eta^4 \quad (4.4)$$

The Lagrangian in equation (4.4) is equivalent to the Lagrangian in equation (4.3) but now the mass term of the field η is positive:

$$m = \sqrt{2\lambda v^2} = \sqrt{-2\mu^2}$$

It is important to point out in equation (4.4), that the symmetry $\eta \rightarrow -\eta$ is not preserved, but the physics described by it cannot have changed as a result of a simple constant shift of the field. The conclusion is that the symmetry is still there, but *hidden* because of our choice of the VEV for the original field.

4.1.5 The Higgs Mechanism

The real scalar field discussed up to now and described in equation (4.3) has only discrete symmetry, whereas we are concerned about continuous gauge symmetry. The spontaneous breaking in the continuous symmetry exhibits novel features that do not appear in the discrete case. Let ϕ be now a scalar complex field.

The Lagrangian is given by:

$$\mathcal{L} = (\partial^\mu \phi^*)(\partial_\mu \phi) - V(\phi^*, \phi) \quad (4.5)$$

where

$$V(\phi^*, \phi) = \frac{1}{2}\mu^2(\phi^*\phi) + \frac{1}{4}\lambda(\phi^*\phi)^2$$

When we add U(1) gauge invariance to 4.5 we obtain the following form

$$\mathcal{L} = (\partial^\mu + iqA^\mu)\phi^*(\partial_\mu - iqA_\mu)\phi - \frac{1}{4}F_{\mu\nu}F^{\mu\nu} - \frac{1}{2}\mu^2(\phi^*\phi) - \frac{1}{4}\lambda(\phi^*\phi)^2$$

and we describe the field ϕ in terms of two real fields ϕ_1 and ϕ_2 , that represent the radial and tangential fields to the degenerate minimum respectively, as shown in Figure 4.7:

$$\phi \equiv \phi_1 + i\phi_2 \quad \phi^*\phi = \phi_1^2 + \phi_2^2$$

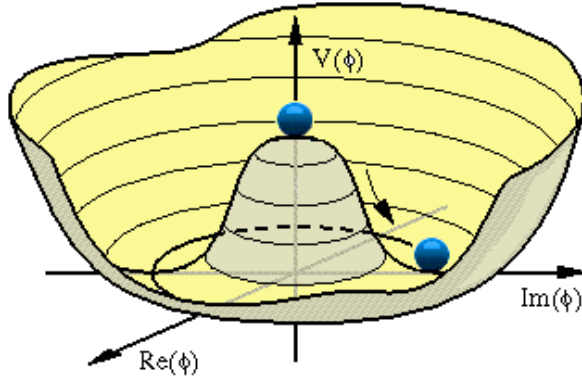


Figure 4.7: Gauge invariant potential in terms of real and imaginary fields.

It follows that only ϕ_1 has non-zero VEV. We can obtain the mass terms from the Lagrangian by the following:

$$\left. \frac{\partial^2 V}{\partial \phi_1^2} \right|_{(\phi_1, \phi_2)=(v, 0)} = -2\mu^2$$

The novel feature is that the field ϕ_2 is massless.

$$\left. \frac{\partial^2 V}{\partial \phi_2^2} \right|_{(\phi_1, \phi_2)=(v, 0)} = 0$$

The symmetry is spontaneously broken because V has a true minimum at P in the plane $\phi_2=0$. Such massless modes, which arise from the degeneracy of the ground state after spontaneous symmetry breaking, are called Goldstone bosons.

The Higgs mechanism [53] posits a self-interacting complex doublet of scalar fields, and renormalizable interactions are arranged such that the neutral component of the scalar doublet acquires a vacuum expectation value fixed by the Fermi coupling constant, G_F , which sets the scale of the Electroweak symmetry breaking:

$$v = \left(\sqrt{2} G_F \right)^{-1/2} = 246 \text{ GeV} \quad (4.6)$$

Three massless Goldstone bosons are generated, which are absorbed to give masses to the W^\pm and Z gauge bosons. The masses of all fermions are also a consequence of the electroweak symmetry breaking since the Higgs doublet is postulated to couple to the fermions through Yukawa interactions.

$$\begin{aligned} M_{W^\pm} &= v \frac{g}{2} \\ M_{Z^0} &= v \frac{\sqrt{g^2 + g'^2}}{2} \\ M_f &= v \frac{\lambda_f}{\sqrt{2}} \\ M_\gamma &= 0 \end{aligned}$$

The remaining component of the complex doublet becomes the Higgs boson, a new fundamental scalar particle. The mass of which is given by the following:

$$M_H = v \sqrt{2\lambda} \quad (4.7)$$

4.1.6 The Higgs Boson

The Higgs boson is introduced into the electroweak Lagrangian as a new scalar field. This provides mass terms for all fermions and bosons. Unfortunately,

the SM Higgs boson has not been discovered yet and its mass (equation (4.7)) depends on a parameter of the theory, the signal strength, λ . Since λ is presently unknown, the value of the SM Higgs boson mass m_H cannot be predicted. However, upper and lower bounds can be set to its mass based on theoretical arguments and unitarity constraints [54].

There is an upper bound based on the perturbativity of the theory up to the scale Λ at which the SM breaks down, and a lower bound derived from the stability of the Higgs potential. If m_H is too large, then the Higgs self-coupling diverges at some scale λ below the Planck scale. If m_H is too small, then the Higgs potential develops a second minimum at a large value of the scalar field of order Λ . New physics must enter at a scale Λ or below, so that the global minimum of the theory corresponds to the observed broken symmetry group for the electroweak theory, $SU(2)_L \times U(1)_Y$ with the VEV given by equation (4.6). Given a value of Λ , one can compute the minimum and maximum allowed Higgs boson mass. The current accepted value for Λ is:

$$\Lambda \equiv \Lambda_{GUT} \approx 10^{15} \text{ GeV}$$

In particular, a Higgs boson with mass in the range $130 \text{ GeV} < m_H < 180 \text{ GeV}$ is consistent with an effective SM description that survives all the way to the Planck scale.

The SM Higgs couplings to fundamental fermions are proportional to the fermion masses, and the couplings to bosons are proportional to the squares of the boson masses. In particular, the SM Higgs boson is a CP-even scalar, and its couplings to gauge bosons, Higgs bosons and fermions are given by:

$$g_{Hf\bar{f}} = \frac{m_f}{v}, \quad g_{HVV} = \frac{2m_V^2}{v}, \quad g_{HHVV} = \frac{2m_V^2}{v^2}$$

$$g_{HHH} = \frac{3m_H^2}{v}, \quad g_{HHHH} = \frac{3m_H^2}{v^2}$$

where $V = W^\pm$ or Z^0 . In Higgs boson production and decay processes, the dominant mechanisms involve the coupling of the H to the W^\pm , Z^0 and/or the third generation of quarks and leptons.

The cross sections for the production of SM Higgs bosons for pp collisions at

the LHC [55] are summarized in Figure 4.9. The cross section for the dominant gluon fusion process ($gg \rightarrow H + X$) is known at next-to-next-to-leading order (NNLO) QCD. NLO electroweak corrections are also available for Higgs boson masses below $2M_W$. The electroweak corrections are not included in the figure. The second most important Higgs production channel at the LHC is the vector boson fusion mechanism ($qq \rightarrow qqH$). The cross sections for the associated production processes, Higgs-strahlung, ($q\bar{q} \rightarrow VH + X$ with $V = W^\pm, Z$) are known at NNLO for the QCD corrections and at NLO for the electroweak corrections. The cross section for the associated production process with t quarks ($q\bar{q}/gg \rightarrow t\bar{t}H$) has been calculated at NLO in QCD, while the bottom fusion Higgs boson production cross section ($b\bar{b} \rightarrow H$) is known at NNLO. Feynman diagrams for the SM Higgs production mechanisms are shown in Figure 4.8.

The branching ratios for the most relevant decay modes of the SM Higgs boson are shown in Figure 4.10 as a function of m_H . For masses below 135 GeV, decays to fermion pairs dominate, of which the decay $H \rightarrow b\bar{b}$ has the largest branching ratio. Decays to $\tau^+\tau^-$, $c\bar{c}$ and gluon pairs together contribute less than 15%. For Higgs boson masses above 135 GeV, the W^+W^- decay dominates (below the W^+W^- threshold, one of the W bosons is virtual) with an important contribution from $H \rightarrow ZZ$. Above the $t\bar{t}$ threshold, the branching ratio into top-quark pairs increases rapidly as a function of the Higgs boson mass.

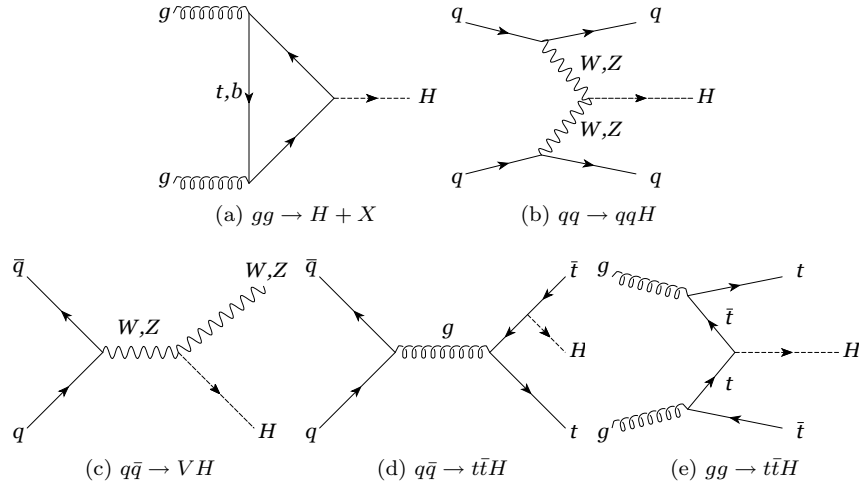


Figure 4.8: Feynman diagrams for the SM Higgs production mechanisms at the LHC.

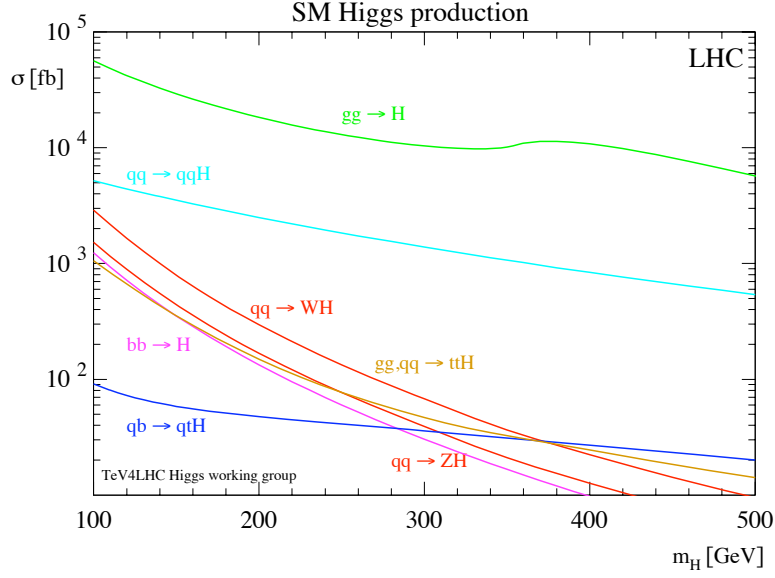


Figure 4.9: SM Higgs boson production cross-section for $\sqrt{s}=14$ TeV at the LHC as a function of the Higgs boson mass [55].

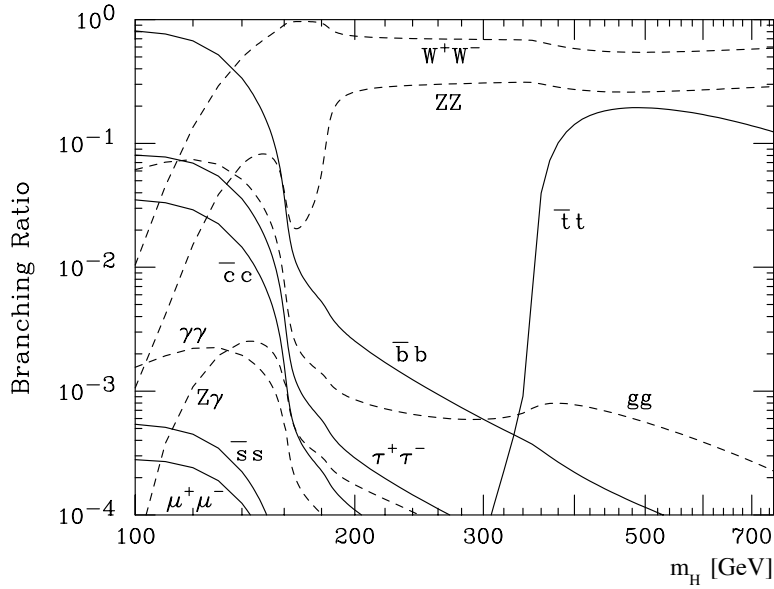


Figure 4.10: SM Higgs branching ratios $\sqrt{s}=14$ TeV at the LHC as a function of the Higgs boson mass [56].

4.1.7 Limitations of the Standard Model

Despite its unprecedented success, the SM is not an elegant theory. At least 19 free parameters are required by the theory that have to be measured in the experiment, involving quark and lepton masses, mixing angles and coupling constants. Many other parameters are required if one takes into account observable events from recent experiments like neutrino oscillations. But what if everything is true?

The SM does not deal with the problem of mass. What is the origin of all particle masses? Are they due to a Higgs boson, and, if so, why are the masses so small compared to M_{Planck} ? What about the problem of **unification**? Is there any simple group framework for unifying all the particle interactions, a so-called Grand Unified Theory (GUT)? Would it predict baryon decay? What about the **flavour** problem: why are there so many different types of quarks and leptons and why do their weak interactions mix in the peculiar way observed? Finally, what about the **hierarchy** problem?

We know that in the Higgs mass, there are correction terms due to virtual loops of scalar and fermionic particles. These terms can add up to be divergent in case there are heavy particles yet to discover. Does it mean, that if the mass of the Higgs is not affected by this divergence, it is assumed the non-existence of heavy particles? Or on the contrary, is it the proof of a symmetry that will cancel it out? Supersymmetry was built exactly with the purpose of cancelling out the divergences in the corrections for scalar particles.

4.2 The Minimal Supersymmetric Extension of the Standard Model

Supersymmetry (SUSY) [57] [58] is a symmetry which transforms bosons into fermions. This is a symmetry not yet discovered, but alike other surprising hypothesis in the past, might lead to unprecedented discoveries. In SUSY, particles are combined into superfields and an operator Q generates the transformation of converting fermions to bosons and vice versa:

$$Q|Boson\rangle = |Fermion\rangle \quad Q^\dagger|Fermion\rangle = |Boson\rangle$$

Therefore Q is a complex anticommuting spinor and its hermitian conjugate, Q^\dagger , is also a symmetry generator. Both generators are fermionic in nature ($S = \frac{1}{2}$) and form a Lie algebra together with the four-momentum and the Lorentz transformation generators. In fact, SUSY is a generalization of the space-time symmetries of quantum field theory and seems to be the last possible extension of the Lorentz group [59]. In this situation, each chiral fermion $f_{L,R}$ has a scalar partner $\tilde{f}_{L,R}$ and for each massless gauge boson A_μ , with the helicity states ± 1 , there is a massless spin $\frac{1}{2}$ gaugino partner, with helicity states $\pm \frac{1}{2}$. SUSY is by definition a broken symmetry, as the masses of the fields and their super-partners are different. The most studied SUSY breaking mechanisms are Gravity, Gauge and Anomaly mediated SUSY breakings.

The agreement with a general SUSY theory is unrealistic at this time. However, similarly to the concept of the standard model, which is the minimal viable group to explain the electroweak sector, the Minimal Supersymmetric extension of the Standard Model (MSSM) [60] can be introduced. MSSM associates a supersymmetric partner to each gauge boson and chiral fermion of the SM, and provides a realistic model of physics at the weak scale. However, even in this minimal model with the most general set of soft supersymmetry-breaking terms, more than 100 new parameters are introduced.

Particle	Spin	Superpartner	Spin
Quark (q)	$\frac{1}{2}$	Squark (\tilde{q})	0
Lepton (l)	$\frac{1}{2}$	Slepton (\tilde{l})	0
W (W^\pm)	1	Wino (\tilde{W}^\pm)	$\frac{1}{2}$
Z (Z^0)	1	Zino (\tilde{Z}^0)	$\frac{1}{2}$
Gluon (g)	1	Gluino (\tilde{g})	$\frac{1}{2}$
Photon (γ)	1	Photino ($\tilde{\gamma}$)	$\frac{1}{2}$

Table 4.3: MSSM particle listing.

The MSSM Lagrangian is constructed using the already defined particle content and following an analogy with the SM. Following a similar notation as in the SM, the kinetic term of the Lagrangian can be written as:

$$\begin{aligned} \mathcal{L}_K = & \sum_i \{ ((D_\mu S_i)^\dagger (D^\mu S_i) + \frac{i}{2} \bar{\psi}_i \gamma^\mu D_\mu \psi_i) \\ & + \sum_A \{ -\frac{1}{4} F_{\mu\nu}^A F^{A\mu\nu} + \frac{i}{2} \bar{\lambda}_A D \lambda_A \} \end{aligned}$$

4.2. THE MINIMAL SUPERSYMMETRIC EXTENSION OF THE STANDARD MODEL

Here, S_i (ψ_i) is the scalar (fermion) component of the i^{th} chiral superfield, D is the $SU(3) \times SU(2)_L \times U(1)$ gauge invariant derivative, $F_{\mu\nu}^A$ is the Yang-Mills gauge field and λ^A is the gaugino super-partner of the corresponding gauge boson. It is worth noticing that \sum_i is a sum over all the fermion fields of the SM, the scalar partners and the two Higgs doublets with their fermion partners. On the other hand, \sum_A is a sum over the $SU(3)_c$, $SU(2)_L$ and $U(1)_Y$ gauge fields with their fermion partners, the gauginos.

The interactions between fermions are completely determined by the gauge symmetries and SUSY:

$$\begin{aligned} \mathcal{L}_{int} = & -\sqrt{2} \sum_{i,A} g_A [S_i^* T^A \bar{\psi}_{i,L} \lambda_A + \text{h.c.}] \\ & - \frac{1}{2} \sum_A \left(\sum_i g_A S_i^* T^A S_i \right)^2 \end{aligned}$$

where $\psi_L \equiv \frac{1}{2}(1 - \gamma_5)\psi$, T^A are the group generators and g_A are the gauge coupling constants. It can be seen that there are no adjustable parameters, hence all interaction strengths are completely fixed in terms of the SM coupling constants.

The MSSM introduces a new quantum number, R-parity, associated to the conservation of the baryon and lepton number:

$$R_P = (-1)^{3B+L+2S}$$

where B is the baryon number, L the lepton number and S the spin. The SM particles have $R_P = 1$, whereas their supersymmetric partners have $R_P = -1$. The conservation of the R-parity implies that SUSY particles have to be created in pairs and that the Lightest Supersymmetric Partner (LSP) is stable, hence a good candidate for dark matter.

4.2.1 Higgs Bosons in the MSSM

In the MSSM, the doubling of all SM particles is straightforward, except for the Higgs boson, which is more complicated. A single Higgsino, the fermionic superpartner of the Higgs boson, would lead to a gauge anomaly and would cause the theory to be inconsistent. However, if two Higgsinos are added, there is no

gauge anomaly. The simplest theory is one with two Higgsinos and therefore two scalar Higgs doublets. Another reason for having two scalar Higgs doublets rather than one, is to be able to provide mass to up-type and down-type quarks separately.

Two Higgs doublets, called, H_u and H_d , ensure an anomaly free MSSM and generate mass for both up-type and down-type quarks and charged leptons (Figure 4.1). After the spontaneous breaking of the electroweak symmetry, five physical Higgs particles appear: one charged Higgs pair, H^\pm , one CP-odd scalar, A , and two CP-even states, H and h . The supersymmetric structure of the theory imposes constraints on the Higgs sector of the model. In particular, the parameters of the Higgs self interaction are not independent of the gauge coupling constants. As a result, all Higgs sector parameters at tree level are determined by only two free parameters taken to be: the ratio of the H_u and H_d vacuum expectation values,

$$\tan\beta = \frac{v_u}{v_d}$$

where $v_u^2 + v_d^2 = (246 \text{ GeV})^2$, and a Higgs mass, conventionally chosen as m_A .

The other tree-level Higgs masses are then given in terms of these parameters:

$$m_{H^\pm}^2 = m_A^2 + M_W^2$$

$$m_{H,h}^2 = \frac{1}{2} \left[m_A^2 + M_Z^2 \pm \sqrt{(m_A^2 + M_Z^2)^2 - 4(m_A M_Z \cos 2\beta)^2} \right]$$

where the \pm sign corresponds to the H and h respectively.

An important consequence of these mass formulae is that the mass of the lightest CP-even Higgs boson is bounded from above:

$$m_H \leq M_Z |\cos 2\beta|$$

This contrasts sharply with the SM, in which this Higgs mass is only constrained by perturbativity and unitarity bounds. In the large m_A limit, one finds that $m_h \simeq M_Z \cos 2\beta$ and $m_A \simeq m_H \simeq m_{H^\pm}$ up to corrections of order $\mathcal{O}(M_Z^2/m_A)$. Below the m_A scale, the effective Higgs sector consists only of h , which behaves very similarly to the SM Higgs boson. The different values of

4.2. THE MINIMAL SUPERSYMMETRIC EXTENSION OF THE STANDARD MODEL

m_h , m_H and m_{H^\pm} are shown as a function of m_A for two different values of $\tan\beta$ in Figure 4.11.

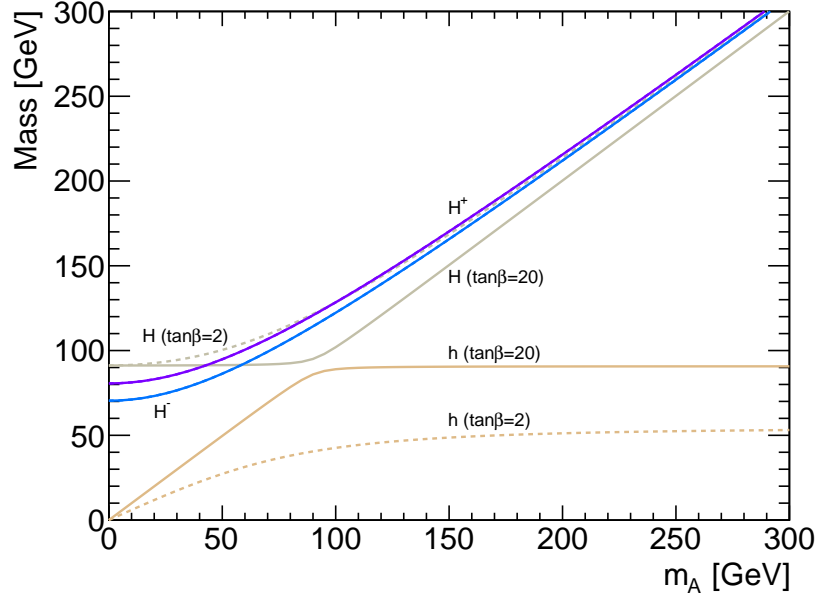


Figure 4.11: Masses of the Higgs bosons in the MSSM m_h -max scenario as a function of m_A for two values of $\tan\beta$.

The phenomenology of the Higgs sector depends on the couplings of the Higgs bosons to gauge bosons and fermions. The couplings of the two CP-even Higgs bosons (h and H) to W^\pm and Z bosons (V) are given in terms of the angles α and β by:

$$g_{hVV} = 2\frac{m_V^2}{v}\sin(\beta - \alpha)$$

$$g_{HVV} = 2\frac{m_V^2}{v}\cos(\beta - \alpha)$$

where α is the angle that diagonalizes the CP-even Higgs squared-mass matrix.

There are no tree-level couplings of A or H^\pm to W^\pm and Z bosons. The couplings of the Z boson to two neutral Higgs bosons, which must have opposite CP-quantum numbers, are given by:

$$g_{hAZ} = \frac{m_Z}{v}\cos(\beta - \alpha)$$

$$g_{HAZ} = \frac{m_Z}{v}\sin(\beta - \alpha)$$

The tree-level Higgs couplings to fermions obey the following property: the neutral components of one Higgs doublet couples exclusively to down-type fermion pairs while the neutral components of the other couples exclusively to up-type fermion pairs [61]. Fermions acquire mass when the neutral Higgs components acquire vacuum expectation values. The relations between Yukawa couplings and fermion masses are (in third-generation notation):

$$\begin{aligned} h_b &= \sqrt{2}m_b/v_d = \sqrt{2}m_b/(v \cos\beta) \\ h_t &= \sqrt{2}m_t/v_u = \sqrt{2}m_t/(v \sin\beta) \end{aligned}$$

Similarly, one can define the Yukawa coupling of the Higgs boson to τ -leptons (the latter is a down-type fermion). The couplings of the neutral Higgs bosons to fermion pairs relative to the SM value are given by:

$$\begin{aligned} h\bar{b}b &: -\sin\alpha/\cos\beta = \sin(\beta - \alpha) - \tan\beta \cos(\beta - \alpha), \\ h\bar{t}t &: \cos\alpha/\sin\beta = \sin(\beta - \alpha) + \cot\beta \cos(\beta - \alpha), \\ H\bar{b}b &: \cos\alpha/\cos\beta = \cos(\beta - \alpha) + \tan\beta \sin(\beta - \alpha), \\ H\bar{t}t &: \sin\alpha/\sin\beta = \cos(\beta - \alpha) - \cot\beta \sin(\beta - \alpha), \\ A\bar{b}b &: \gamma_5 \tan\beta, \\ A\bar{t}t &: \gamma_5 \cot\beta, \end{aligned}$$

where the γ_5 indicates a pseudoscalar coupling. In each relation above, the factor listed for $\bar{b}b$ also pertains to $\tau^+\tau^-$. The charged Higgs boson couplings to fermion pairs are given by:

$$\begin{aligned} g_{H^-\bar{t}b} &= \frac{g}{\sqrt{2}M_W} [m_t \cot\beta P_R + m_b \tan\beta P_L], \\ g_{H^-\tau^+\nu} &= \frac{g}{\sqrt{2}M_W} [m_\tau \tan\beta P_L], \end{aligned}$$

with $P_{L,R} = (1 \mp \gamma_5)/2$.

The total production rate of bottom quarks and tau pairs mediated by the production of a CP-odd Higgs boson (A) in the large $\tan\beta$ regime is approxi-

mately given by:

$$\sigma(b\bar{b}A) \times \text{BR}(A \rightarrow b\bar{b}) \simeq \sigma(b\bar{b}A)_{SM} \frac{\tan^2\beta}{(1+\Delta_b)^2} \frac{9}{(1+\Delta_b)^2+9}$$

and:

$$\sigma(gg \rightarrow A, b\bar{b}A) \times \text{BR}(A \rightarrow \tau^+\tau^-) \simeq \sigma(gg \rightarrow A, b\bar{b}A)_{SM} \frac{\tan^2\beta}{(1+\Delta_b)^2+9}$$

where $\sigma(b\bar{b}A)_{SM}$ and $\sigma(gg \Rightarrow A, b\bar{b}A)_{SM}$ denote the values of the corresponding SM Higgs boson cross sections for a SM Higgs boson mass equal to m_A . The function Δ_b includes the dominant effects of SUSY radiative corrections for large $\tan\beta$. The main radiative contributions in Δ_b depend strongly on $\tan\beta$ and on the SUSY mass parameters. The $b\bar{b}A$ channel is more sensitive to the value of Δ_b through the factor $1/(1+\Delta_b)^2$ than the inclusive $\tau^+\tau^-$ channel, for which this leading dependence on Δ_b cancels out. As a consequence, the limits derived from the inclusive $\tau^+\tau^-$ channel depend less on the precise MSSM scenario chosen than those of the $b\bar{b}A$ channel.

4.2.2 MSSM Higgs Boson Production Cross Sections

In the MSSM there are a total of 105 new parameters. Theoretical assumptions are required in order to provide self-consistent frameworks in which to test the ability of the experiments to study supersymmetry. One of these assumptions is that the sfermion and gaugino masses, and the trilinear Higgs-fermion couplings must unify at the Grand Unification Theory (GUT) scale. This leads to a constrained MSSM model in which the parameters are:

- $\tan\beta$: ratio of the vacuum expectation values of the two Higgs fields.
- m_A : mass of the CP-odd Higgs boson.
- M_{SUSY} : common mass for all sfermions at the electroweak scale.
- M_2 : common $SU(2)_L$ gaugino mass at the electroweak scale.
- μ : strength of the supersymmetric Higgs mixing.
- $A = A_t = A_b$: common trilinear Higgs-squarks coupling at the electroweak scale.
- $m_{\tilde{g}}$: gluino mass.

Within this MSSM model, different benchmark scenarios have been proposed [62]. One of the most discussed is the m_h -max scenario, which has been designed to obtain conservative $\tan\beta$ exclusion bounds. The parameters are chosen such that the maximum possible Higgs-boson mass as a function of $\tan\beta$ is obtained. Another scenario is the so called no mixing, which is associated with vanishing mixing in the $t\tilde{t}p$ sector and with a higher SUSY mass scale as compared to the m_h -max scenario to increase the parameter space that avoids the LEP Higgs bounds. The parameters for these scenarios are shown in Table 4.4.

Parameter	m_h -max	No mixing
M_{SUSY} [TeV]	1	2
μ [GeV]	200	200
M_2 [GeV]	200	200
X_t	$2M_{SUSY}$	0
$m_{\tilde{g}}$	$0.8M_{SUSY}$	$0.8M_{SUSY}$

Table 4.4: MSSM parameters for the m_h -max and no mixing benchmark scenarios.

Production cross sections for neutral MSSM Higgs bosons in the m_h -max and no mixing benchmark scenarios are shown in Figure 4.12. These have been obtained by rescaling the corresponding SM cross sections either with ratio of the corresponding MSSM decay width (of the inverse process) over the SM decay width, or with the square of the ratio of the corresponding couplings [55]. Where the following production mechanisms have been considered (ϕ denotes all neutral MSSM Higgs bosons, $\phi = h, H, A$):

$$\begin{aligned}
 gg &\rightarrow \phi + X , \\
 qq &\rightarrow qq\phi + X , \\
 q\bar{q} &\rightarrow W/Z\phi + X , \\
 b\bar{b} &\rightarrow \phi + X , \\
 gg, qq &\rightarrow t\bar{t}\phi .
 \end{aligned}$$

4.2. THE MINIMAL SUPERSYMMETRIC EXTENSION OF THE STANDARD MODEL

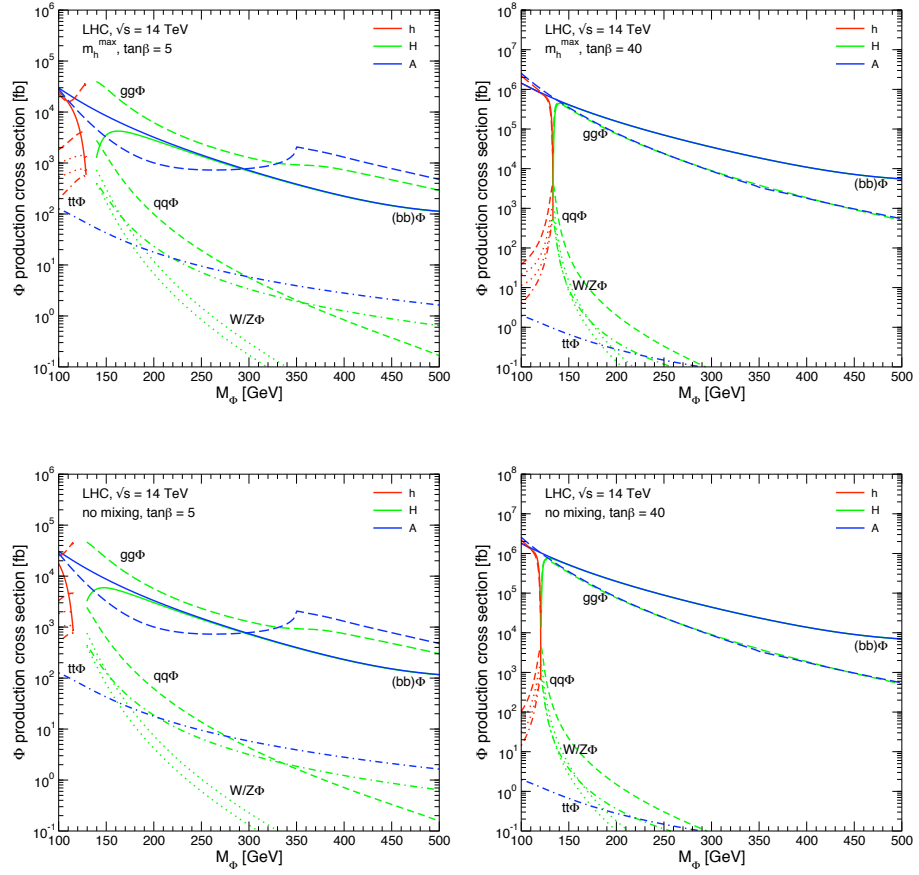


Figure 4.12: Neutral MSSM Higgs bosons production cross sections [fb] at the LHC, $\sqrt{s}=14$ TeV, for the most relevant production mechanisms as a function of the Higgs boson mass for $\tan\beta = 5, 40$ in the m_h -max and no mixing scenarios [55].

4.2.3 Searches for Neutral Higgs Bosons

In the search for neutral Higgs bosons, the experimental results are often compared with several benchmark scenarios. One of the most common scenarios is the m_h -max model described above, which given a value of $\tan\beta$, M_{SUSY} and m_t leads to relative conservative exclusion limits.

The first important searches for neutral MSSM Higgs bosons were carried out at LEP, at electroweak scale energies in e^+e^- collisions. The main production mechanisms of the neutral MSSM Higgs bosons were Higgs-strahlung ($e^+e^- \rightarrow hZ, HZ$) and the pair production ($e^+e^- \rightarrow hA, HA$) while the fusion processes played a marginal role. Results from LEP [56] are shown in Figure 4.13.

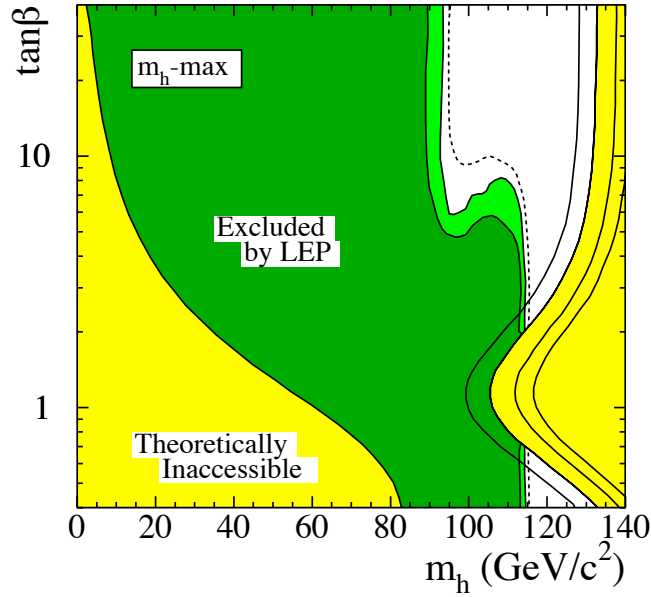


Figure 4.13: The MSSM exclusion contours at 95%C.L. (light-green) and 99.7%CL (dark-green) in the $\tan\beta$ - m_A plane, obtained by LEP for the CP conserving m_h -max benchmark scenario, with $m_t = 174.3$ GeV [56].

Searches for MSSM Higgs bosons are also feasible in hadron colliders. These take advantage of the enhanced or suppressed couplings with respect to those of the SM, since these can significantly modify the production cross-sections of neutral Higgs bosons.

Scenarios with enhanced Higgs boson production cross sections are still being studied at the Tevatron. The best sensitivity is in the regime with low to moderate m_A and with large $\tan\beta$, which enhances the couplings of the Higgs bosons to down-type fermions. The most promising channels at the Tevatron are $b\bar{b}\varphi$, with φ being either A or H , the decay modes being $\varphi \rightarrow b\bar{b}$ or $\varphi \rightarrow \tau^+\tau^-$, with three tagged b-jets or $b\tau\tau$ in the final state, respectively, and the inclusive $p\bar{p} \rightarrow \varphi \rightarrow \tau^+\tau^-$ process, with contributions from both gluon fusion ($gg \rightarrow \varphi$) and bottom fusion ($b\bar{b} \rightarrow \varphi$) production [63], [64].

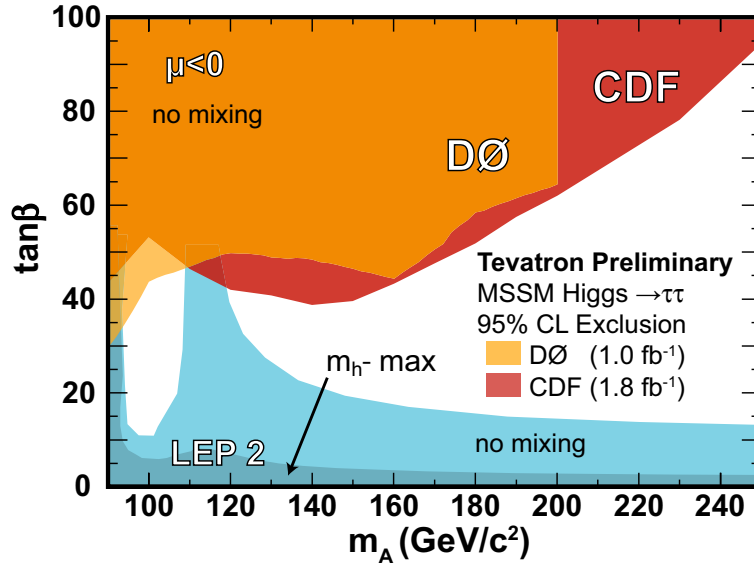


Figure 4.14: The 95% C.L. MSSM exclusion contours obtained by CDF and DØ in the $H \rightarrow \tau^+\tau^-$ searches in the no-mixing benchmark scenario with $\mu = 200$ GeV, projected on to the $(m_A, \tan\beta)$ plane. The Tevatron limits for the m_h -max scenario are nearly the same as in the no-mixing scenario. Also shown are the regions excluded by LEP searches, separately for the m_h -max scenario (darker shading) and the no-mixing scenario, (lighter shading). The LEP limits are shown for a top quark mass of 174.3 GeV (the Tevatron results are not sensitive to the precise value of the top mass) [56].

The production and decay rates of the CP-even Higgs bosons with $\tan\beta$ enhanced couplings to down-type fermions H (or h) for m_A larger (or smaller) than m_h^{max} , respectively are governed by formulae similar to the ones presented above. At high $\tan\beta$, one of the CP-even and the CP-odd Higgs bosons are nearly degenerate in mass enhancing the signal cross section by roughly a factor of two, without complicating the experimental signature except in a small mass

region in which the three neutral MSSM Higgs boson masses are close together and each boson contributes to the total production rate. The excluded domains for the inclusive $\varphi \rightarrow \tau^+ \tau^-$ channels are shown in Figure 4.14, in the $(m_A, \tan\beta)$ projection, considering the contribution of both the CP-odd and CP-even neutral Higgs bosons with enhanced couplings to bottom quarks [56].

Also shown in Figure 4.14 are the LEP limits, for the no-mixing and the m_h -max scenarios. The limits from the Tevatron are shown only for the no-mixing scenario, but, as discussed above, due to the tiny dependence of this channel under variations of the SUSY parameter space, the Tevatron limits are nearly identical in the m_h -max scenario. Even though $\text{BR}(\varphi \rightarrow b\bar{b})$ exceeds $\text{BR}(\varphi \rightarrow \tau^+ \tau^-)$ by an order of magnitude for the models considered, the $bbb(b)$ channel limits are weaker due to the much larger background, and the $\tau^+ \tau^-$ channels exclude the domain tested by the $bbb(b)$ channels.

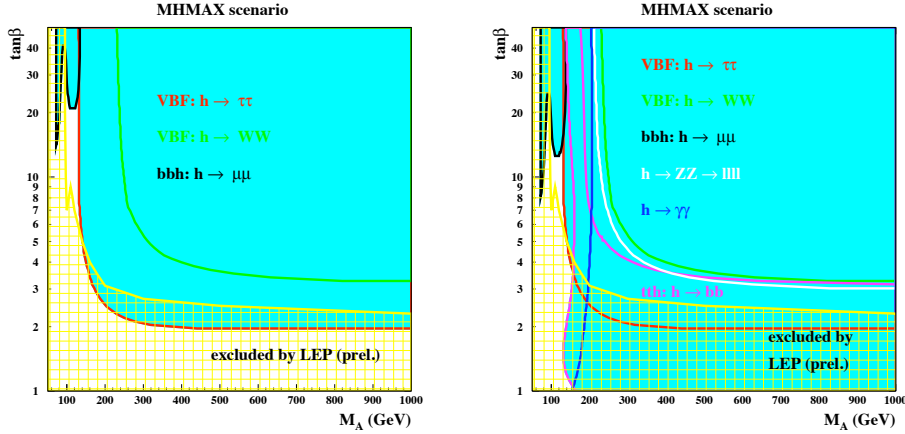


Figure 4.15: Discovery potential for light CP-even Higgs boson in the m_h -max CP-conserving scenario after collecting 30 fb^{-1} (left) and 300 fb^{-1} (right) from the ATLAS TDR physics performance. The cross hatched area is excluded by LEP at 95% C.L. from [65].

Prospects for discovering the MSSM Higgs bosons at the LHC have been explored in detail, as shown in Figure 4.15, and reviewed in [66]. They predict that the reach of the LHC experiments would be sufficient to discover MSSM Higgs bosons in many different channels. The main channels for the SM-like Higgs boson are expected to be vector boson fusion production ($qq \rightarrow qq\varphi$) with $\varphi \rightarrow \tau^+ \tau^-$ and $\varphi \rightarrow \gamma\gamma$, where $\varphi = h$ or H , depending on m_A . The discovery

of a light SM-like Higgs boson with $m_h < 130$ GeV would require a few years of running. With an integrated luminosity larger than 30 fb^{-1} , the $t\bar{t}\varphi$ production process may also become effective.

For MSSM Higgs bosons, the most relevant channels are expected to be $pp \rightarrow H/A + X$, with $H/A \rightarrow \tau^+\tau^-$ and $pp \rightarrow tH^\pm + X$, with $H^\pm \rightarrow \tau\nu_\tau$. After the inclusion of supersymmetric radiative corrections to the production cross sections and decay widths, the prospective discovery reach in these channels is robust, with mild dependence on the specific MSSM parameters. The particular channel for this thesis is $pp \rightarrow H/A + X$ with $H/A \rightarrow \tau^+\tau^-$.

Chapter 5

Search for MSSM Higgs Bosons Decaying into Tau Pairs

5.1 Introduction

While the Standard Model of electroweak and strong interactions, briefly explained in Chapter 4, is in excellent agreement with the numerous experimental measurements, the dynamics responsible for the electroweak symmetry breaking are still unknown. Within the Standard Model, the Higgs mechanism is invoked to break the electroweak symmetry. A doublet of complex scalar fields is introduced, of which a single neutral scalar particle, the Higgs boson, remains after symmetry breaking. Many extensions of this minimal version of the Higgs sector have been proposed. Mostly discussed is a scenario with two complex Higgs doublets as realized in the Minimal Supersymmetric Standard Model (MSSM). The Higgs sector in the MSSM consists of two charged (H^+, H^-) and three neutral bosons (a CP-even light Higgs h , a CP-even heavy Higgs H and a CP-odd pseudoscalar A).

The MSSM benchmark considered here is the maximal-mixing scenario, represented by m_h -max, where the stop mixing parameter is arbitrarily set to

$X_t = 2M_{SUSY}$. This maximizes the allowed values of m_h , for a given $\tan\beta$, M_{SUSY} , and m_t . The values used for M_{SUSY} and m_t are set to 1 TeV and 172.4 GeV respectively.

We shall aim for the discovery of neutral MSSM Higgs bosons, both the CP-odd A and CP-even states H , that we shall conveniently describe as ϕ , decaying into tau pairs, which have been already searched for at Tevatron [67]. The Yukawa couplings of ϕ to down-type fermions (such as the b quark and τ) are enhanced by a factor of $\tan\beta$ relative to the SM. Moreover, this channel will consider the di-tau state where one tau decays leptonically and the other one decays hadronically. Other discovery channels for neutral MSSM Higgs bosons include the di-muon decay, which is suppressed with respect to the one proposed here, and has already been extensively discussed elsewhere [68].

The LHC restarted its operation in March 2010 at $\sqrt{s} = 7$ TeV aiming for an integrated luminosity of 1 fb^{-1} by the end of 2011, with 10 pb^{-1} by the end of 2010. The present analysis addresses the discovery potential of $\phi \rightarrow \tau^+\tau^- \rightarrow \ell h$ for the MSSM m_h -max benchmark scenario at 1 fb^{-1} . Results are based on studies conducted at $\sqrt{s} = 14$ TeV which should be appropriately scaled to the current center-of-mass energy. No pile-up or cavern background has been considered. These are compared to those obtained at 30 fb^{-1} in the recently published analysis [69], [70].

This Chapter presents the statistical technique implemented by the author in ATLAS, based on the Bayesian paradigm, which incorporates systematic uncertainties on known parameters and energy scales.

5.1.1 Production of MSSM Higgs Bosons

This analysis relies in an inclusive Higgs search where no bottom quark jets are tagged. In this case, the main production mechanisms of neutral MSSM Higgs bosons at the LHC are gluon fusion ($gg \rightarrow \phi$) through a triangular virtual loop of top and bottom quarks shown in Figure 5.1 (a), and associated production with bottom quarks ($gg \rightarrow b\bar{b}\phi$) which becomes enhanced in the MSSM and dominates over all other production modes in the large $\tan\beta$ regime shown in Figures 5.1 (b) and (c). If one would rely instead on exclusive Higgs searches with b-tagged jets, other diagrams would become relevant induced by $bg(\bar{b}g)$ and

$b\bar{b}$ initial states, shown in Figures 5.1 (d) and (e). These enhanced Higgs boson production scenario can be studied at the LHC, in which the best sensitivity is in the low to moderate m_A and large $\tan\beta$ regime.

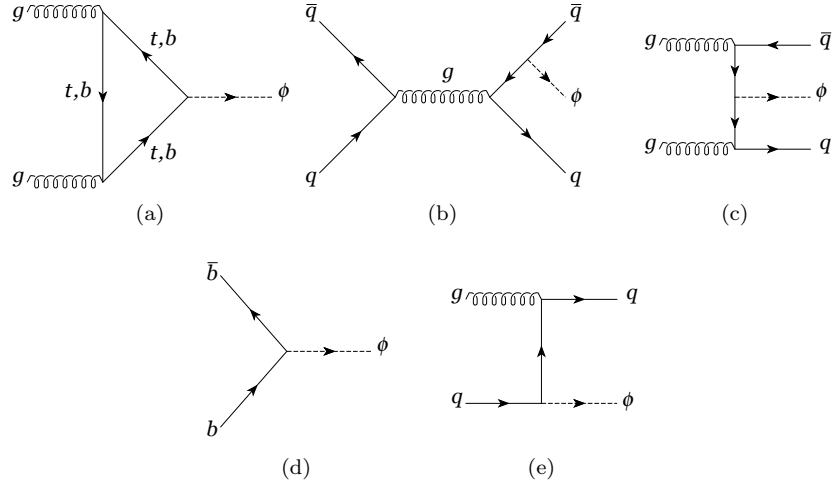


Figure 5.1: Feynman diagrams contributing to the MSSM Higgs boson production.

The cross-sections are calculated using FeynHiggs [71] and HIGLU [72] yielding the cross-section for a Standard Model Higgs boson. The cross-sections in the MSSM are then obtained by scaling them by the ratio of partial widths into:

$$\sigma_{MSSM}(m_A, \tan\beta) = \sigma_{SM}(m_\phi) \frac{\Gamma_{MSSM}(m_A, \tan\beta)}{\Gamma_{SM}(m_\phi)}$$

Mass [GeV]			Direct [fb]			Associated [fb]		
A	H	h	A	H	h	A	H	h
150	151.1	127.7	120371	111094	11790	37200	40569	27508
300	300.4	128.6	10312	10253	979	811	1252	31131
450	449.8	128.6	2019	2035	723	165	136	31445
600	600.0	128.6	578	585	654	0	1768	31577

Table 5.1: Listing of mass of Higgs bosons and direct and associated production cross sections in the m_h -max scenario for $\tan\beta = 20$.

Table 5.1 shows the total MSSM Higgs bosons production cross section as a function of m_A for $\tan\beta = 20$.

5.1.2 The Tau Pair Decay Mode

The leading decay modes of neutral MSSM Higgs bosons are $\phi \rightarrow b\bar{b}$ ($\sim 90\%$) and $\phi \rightarrow \tau^+\tau^-$ ($\sim 10\%$). Table 5.2 lists the branching ratios for MSSM Higgs bosons to tau and muon pairs. The decay to muon pairs is suppressed with respect to the Standard Model.

m_A [GeV]	BR($\phi \rightarrow \tau^+\tau^-$) [%]			BR($\phi \rightarrow \mu^+\mu^-$) [%]		
	A	H	h	A	H	h
150	9.32	9.37	8.65	0.033	0.033	0.031
300	8.22	9.51	6.27	0.029	0.034	0.022
450	6.07	6.24	5.68	0.021	0.022	0.020
600	4.76	4.53	5.47	0.017	0.016	0.019

Table 5.2: Branching ratios for MSSM Higgs Bosons to tau and muon pairs in the m_h -max scenario for $\tan\beta = 20$.

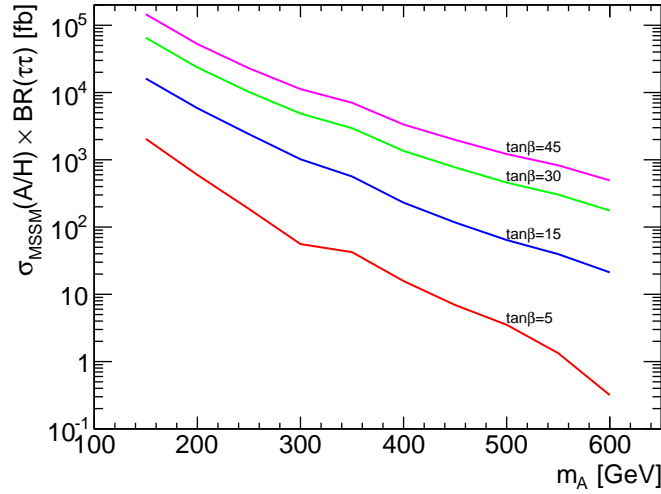


Figure 5.2: Total MSSM Higgs bosons production cross section times branching ratios as a function of m_A for different values of $\tan\beta$ calculated with FeynHiggs at $\sqrt{s} = 14$ TeV.

Single tau decay modes are listed in Table 5.3. Leptonic modes have a total branching ratio of 35.2%, whereas leading hadronic decay modes with one prong or three prongs sum up to 65.5%. Tau pair decay modes are listed in Table 5.4. Purely leptonic modes ($\ell\ell$) represent 12%, purely hadronic modes (hh) have a branching ratio of 42%, whereas semi-leptonic modes (ℓh) have a branching ratio of 46%.

Final State	BR [%]	
$e\nu_e\nu_\tau$	17.8	Leptonic
$\mu\nu_\mu\nu_\tau$	17.4	
$\pi^\pm\nu_\tau$	11.1	Hadronic (one-prong)
$\pi^0\pi^\pm\nu_\tau$	25.1	
$\pi^0\pi^0\pi^\pm\nu_\tau$	10.3	
$\pi^\pm\pi^\pm\pi^\pm\nu_\tau$	9.5	Hadronic (three prong)
$n\pi^0\pi^\pm\pi^\pm\pi^\pm\nu_\tau$	4.5	

Table 5.3: Branching ratios of single tau decay modes for $\tan\beta = 20$.

Final state	BR [%]	
$\ell\ell\nu$	12	leptonic
$\ell h\nu$	46	semi-leptonic
$hh\nu$	42	hadronic

Table 5.4: Branching ratios of tau pair decay modes.

Figure 5.2 shows the cross section times branching ratios for tau pairs and lepton hadron decays for A and H MSSM Higgs bosons as a function of m_A for different values of $\tan\beta$ at $\sqrt{s} = 14$ TeV.

In this analysis we select semi leptonic decay modes, where only one tau decays leptonically while the other decays hadronically to one or three prongs. We require one high p_T light lepton trigger and no b-tagging as it is not foreseen to be available for early data. This analysis can be regarded as a proposal for an inclusive $pp \rightarrow b\bar{b}\phi$ search with $\phi = A$ or H in the $\phi \rightarrow \tau^+\tau^- \rightarrow \ell h$ channel. The expected acceptance for semi leptonic modes is $2 \times BR(\phi \rightarrow \tau^+\tau^-) \times BR(\tau\tau \rightarrow \ell h) \approx 4.6\%$ of the total Higgs production cross-section. Where the factor 2 takes into account the two Higgs mass states A and H .

5.1.3 Background Processes

A summary of the relevant background cross sections is listed in Table 5.5.

Process	Cross section [pb]
$\sigma_{Z \rightarrow \ell\ell}$	2051
$\sigma_{t\bar{t}}$	833
$\sigma_{Wq \rightarrow \ell\nu}$	20510

Table 5.5: Cross section values for background processes as recommended by ATLAS. Values are quoted for one lepton family.

The dominant background process for this channel is the Drell-Yan Z/γ

production, with subsequent gauge boson decay into tau pairs, $Z/\gamma \rightarrow \tau^+\tau^-$. The feynman diagram of this process is shown in Figure 5.3. The cross section of this process is larger than for the signal, thus, one has to pay attention in understanding it. The final states are identical to those from the Higgs production, where the difference in the diagram is the kind of boson produced. This background sets a constraint in the search, as the invariant di-tau mass peaks at the Z resonance, thus, the search becomes unfeasible for Higgs masses below 100 GeV. The cross section for this process is given by:

$$\sigma(Z/\gamma) \times \text{BR}(Z/\gamma \rightarrow \tau^+\tau^-)$$

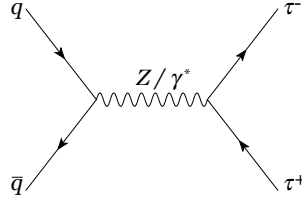


Figure 5.3: Tree level Feynman diagram for the Drell-Yan Z/γ production decaying into tau pairs.

The W +jets background plays an important role in this analysis. This background contributes due to the mis-identification of particles. The final state is identical to the one from the signal. Electron, muon or tau leptons are produced together with quarks. Mis-identification of jets as tau leptons lead to an important background source. The cross section of the W +jets background is given by:

$$\sigma(Wq) \times \text{BR}(W \rightarrow \ell\nu)$$

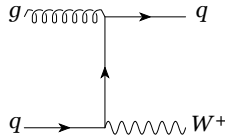


Figure 5.4: Tree level Feynman diagram for the production of W^\pm associated with jets.

Another background that contributes to the same final state is the top quark

production with two W^\pm and two b quark jets in the final state. The Feynman diagram of this process is shown in Figure 5.5. The main cut for this background is the number of jet candidates present in the event. This background could be further reduced by means of b-tagging. However, this is not the case for this analysis, and the background still plays an important role for energies above the Z boson mass. The $t\bar{t}$ background cross section is given by:

$$\sigma(t\bar{t}) \times 2 \times \text{BR}(t \rightarrow bW^\pm) \times \text{BR}(W^\pm \rightarrow \tau^\pm \nu)$$

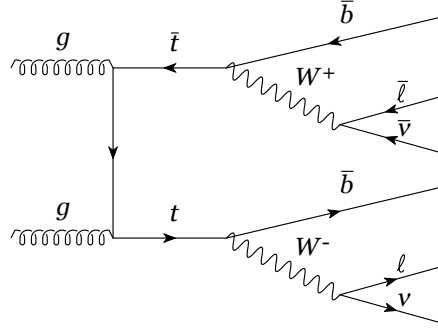


Figure 5.5: Tree level Feynman diagram for the top quark production with two W^\pm and two b quark jets in the final state.

The QCD background from gg and qq processes is one of the main backgrounds in a hadron collider. It is an irreducible source of background for most of the physics channels. In our case, this background constitutes a major source of jet mis-identification from the main interaction. It can be easily addressed with b-tagging in the associated Higgs production, as it would be easy to cut out all non b-flavoured jets reducing the QCD background. However, this is not the case for first data analysis, when no b-tagging is foreseen, and the QCD background jets cannot be separated from the b-jets. Thus the QCD background has to be addressed differently. This background is reduced through means of the missing transverse energy (E_T^{miss}), since a QCD multi-jet spectrum would have little E_T^{miss} . A cut on E_T^{miss} separates background-only events from signal events. Still, in a signal plus background sample, the QCD multijet background contributes to the mis-identification of hadronic taus. This contamination of tau-jets is considered as a systematic uncertainty associated

to the tau reconstruction and is covered in Section 5.3.4. Figure 5.6 shows the Feynman diagrams corresponding to the main processes which contribute to the QCD background.

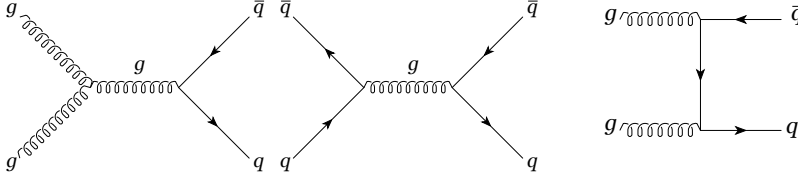


Figure 5.6: Feynman diagrams for QCD background processes.

5.1.4 Higgs Mass Reconstruction

The invariant mass reconstruction is limited by the number of weakly interacting particles present in the interaction. The total contribution of missing energy due to neutrinos cannot be separated.

There are three neutrinos present in the considered channel decays:

$$\phi \rightarrow \tau^+ \tau^- \rightarrow (\ell^\pm \nu_\ell \nu_\tau)(h^\mp \nu_\tau)$$

This makes the precision of the invariant mass reconstruction limited by the E_T^{miss} reconstruction. A typical assumption in the reconstruction of the Higgs mass is that the tau decay products are collinear with the direction of the tau. This collinear approximation is thus very accurate for associated Higgs production, where the decay products acquire a strong boost. Therefore, the τ decay products carry a fraction of the τ momentum ($P_\ell = x_\ell P_\tau$).

The invariant mass of the Higgs can be computed as the invariant mass of the τ pair.

$$M_\phi = M_{\tau^+ \tau^-} = \sqrt{(P_{\tau_\ell} + P_{\tau_h})^2} = \sqrt{P_{\tau_\ell}^2 + P_{\tau_h}^2 + 2P_{\tau_\ell} P_{\tau_h}}$$

Where applying the collinear approximation ($m_\tau \sim 0 \rightarrow P_\tau^2 \sim 0$, $P_\tau = P_\ell/x_\ell$), it can be written in terms of the invariant mass of the visible products

of the τ decay and their momentum fraction.

$$M_\phi \approx \sqrt{2P_{\tau_\ell}P_{\tau_h}} = \sqrt{2\frac{P_\ell}{x_\ell}\frac{P_h}{x_h}} = \frac{M_{\ell h}}{\sqrt{x_\ell x_h}}$$

The momentum fraction carried by the τ decay products can be computed. Starting from the momentum conservation expresion. We introduce the missing momentum ($\vec{P}_{miss} = \vec{P}_{miss_\ell} + \vec{P}_{miss_h}$)

$$\vec{P}_{\tau_h} + \vec{P}_{\tau_\ell} = \vec{P}_h + \vec{P}_\ell + \vec{P}_{miss} = \vec{P}_h + \vec{P}_{miss_h} + \vec{P}_\ell + \vec{P}_{miss_\ell}$$

Thus, we can define both momentum fractions and the missing momentum contributions.

$$x_\ell = \frac{\vec{P}_\ell}{\vec{P}_{\tau_\ell}} = \frac{\vec{P}_\ell}{\vec{P}_\ell + \vec{P}_{miss_\ell}} \rightarrow \vec{P}_{miss_\ell} = \vec{P}_\ell \frac{1-x_\ell}{x_\ell}$$

$$x_h = \frac{\vec{P}_h}{\vec{P}_{\tau_h}} = \frac{\vec{P}_h}{\vec{P}_h + \vec{P}_{miss_h}} \rightarrow \vec{P}_{miss_h} = \vec{P}_h \frac{1-x_h}{x_h}$$

The missing momentum can be defined as a function of momentum fractions.

$$\vec{P}_{miss} = \vec{P}_\ell \frac{1-x_\ell}{x_\ell} + \vec{P}_h \frac{1-x_h}{x_h}$$

$$P_{miss}^x = P_\ell^x \frac{1-x_\ell}{x_\ell} + P_h^x \frac{1-x_h}{x_h}$$

$$P_{miss}^y = P_\ell^y \frac{1-x_\ell}{x_\ell} + P_h^y \frac{1-x_h}{x_h}$$

Furthermore, the momentum fraction can be computed as a function of the previous

$$x_\ell = \frac{P_h^y P_\ell^x - P_h^x P_\ell^y}{P_h^y P_\ell^x - P_h^x P_\ell^y + P_h^y P_{miss}^x - P_h^x P_{miss}^y}$$

$$x_h = \frac{P_h^y P_\ell^x - P_h^x P_\ell^y}{P_h^y P_\ell^x - P_h^x P_\ell^y + P_\ell^y P_{miss}^x - P_\ell^x P_{miss}^y}$$

5.1.5 Visible Mass

The conventional approach to the Higgs mass reconstruction is through means of the collinear approximation. This cannot be applied to back-to-back events due to the limitation in its formulation (i.e. when $x_\ell = x_h = 0$). Other analysis [73] apply a cut on $\Delta\phi$ of the reconstructed taus ($\Delta\phi < 2.9$) in order to apply the collinear approximation. This eliminates from the all events which are fully back-to-back, including a considerable amount of signal events in the channel, as shown in Figure 5.7.

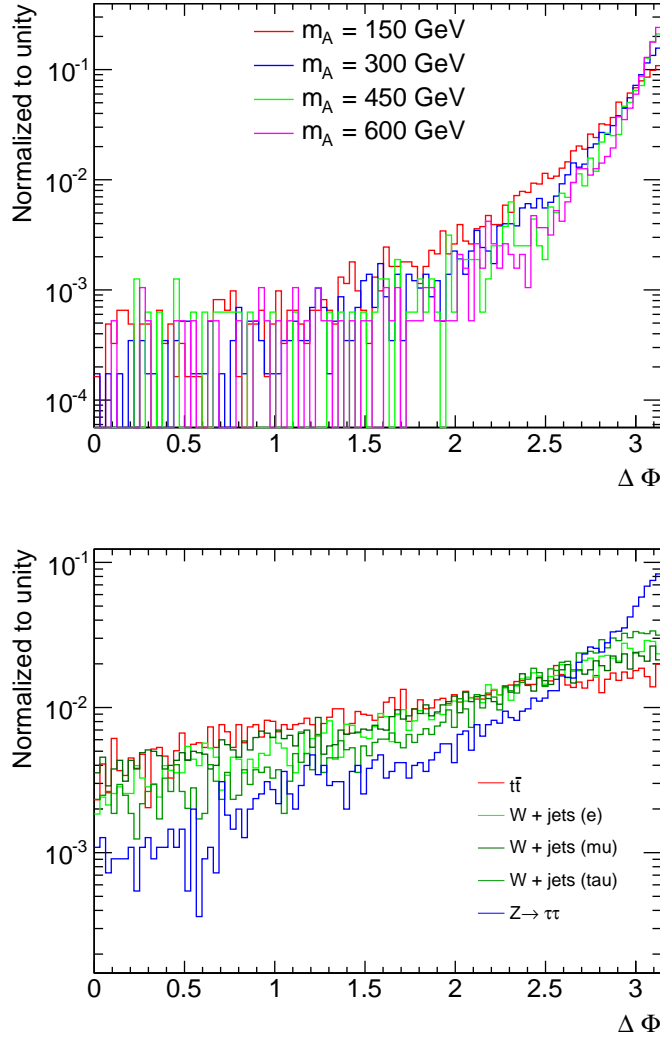


Figure 5.7: Delta ϕ distributions for signal and background data.

In order to recover these signal events we use the visible mass, M_{vis} , which is the invariant mass of the visible decay products plus the E_T^{miss} , given by the following:

$$M_{vis} = |P_\ell^\alpha + P_h^\alpha + P_{Miss}^\alpha|$$

where P_{Miss}^α is the four vector of the E_T^{miss} defined as:

$$P_{Miss}^\alpha = \{p_{xMiss}, p_{yMiss}, 0, \sqrt{p_{xMiss}^2 + p_{yMiss}^2}\}$$

The visible mass has already been used as the observable in Higgs boson searches at Tevatron [74], Figure 5.8 shows both M_{vis} and M_{inv} distributions for $m_A = 150$ GeV and $\tan\beta = 15$. The M_{vis} distribution is not peaked at the Higgs mass due to the non-contribution of the neutrinos. The tail of the M_{vis} distribution spreads out to higher energies because of the collinear neutrinos. The tighter requirements for the collinear approximation imply less statistics but a peak centered at the Higgs mass.

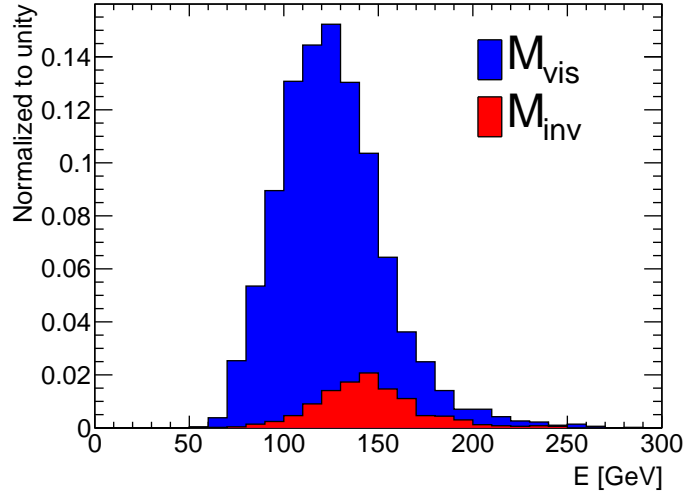


Figure 5.8: M_{vis} and M_{inv} distributions for $m_A = 150$ GeV and $\tan\beta = 45$.

5.2 Data Sets

In this analysis we use Monte Carlo simulated events for $\sqrt{s} = 14$ TeV, previously used in the ATLAS performance paper [75], using version 12 of the ATLAS offline software [76].

5.2.1 Signal Samples

The signal datasets have been generated with PYTHIA [77]. The generator process is $gg, q\bar{q} \rightarrow b\bar{b}h$. Table 5.6 contains the list of the datasets.

Dataset	m_A [GeV]	$\tan\beta$	σ_{NLO} [fb]	Generator	Events
6571	150	45	24.5	Pythia 6.4	47250
6828	150	45	24.5	Pythia 6.4	8000
6536	300	15	219	Pythia 6.4	50000
6575	450	20	70.1	Pythia 6.4	13500
6576	600	30	44.4	Pythia 6.4	17950
6573	800	35	15.1	Pythia 6.4	5750

Table 5.6: Signal datasets.

Signal Dependence with SUSY Parameters

Due to the limited number of datasets available to cover a reasonable range in the $(m_A, \tan\beta)$ plane, the visible mass distributions for different values of $\tan\beta$ are obtained by scaling the available distributions by the cross section ratio between the desired and available $\tan\beta$. This is a first order approximation, as we know the width of the reconstructed higgs mass distribution is dependent on $\tan\beta$. Other methods could be recalled, like the scaling in amplitude and width of a widthless signal computed for a SM Higgs. However, as the aim of this analysis is not to unveil the characterization of the visible mass distribution as a function of $\tan\beta$, in the following the suggested first order approximation will be used.

5.2.2 Background Samples

A set of background samples have been considered that cover the most important backgrounds of the channel. These datasets were simulated with ATLAS full

simulation software with release 12 except the W+jets datasets which were generated with release 14.

Dataset	Process	σ_{NLO} [pb]	Generator	Events
6052	$Z \rightarrow \tau^+ \tau^- \rightarrow \ell h$	684	Pythia	288425
5200	$gg \rightarrow t\bar{t} \rightarrow \ell h$	461	Jimmy	537800
209530	$gq \rightarrow Wq \rightarrow e\nu$	2051	Sherpa	4250000
209531	$gq \rightarrow Wq \rightarrow \mu\nu$	2051	Sherpa	4250000
209532	$gq \rightarrow Wq \rightarrow \tau\nu$	2051	Sherpa	4021603
5010	J1 di-jets $\hat{p}_T = [17-35]$ GeV	1380000000	Pythia	373350
5011	J2 di-jets $\hat{p}_T = [35-70]$ GeV	96900000	Pythia	371010
5012	J3 di-jets $\hat{p}_T = [70-140]$ GeV	5880000	Pythia	365800
5013	J4 di-jets $\hat{p}_T = [140-280]$ GeV	308000	Pythia	387372

Table 5.7: Background datasets.

5.3 Object Reconstruction

The signature for the di-tau channel decaying into semi-leptonic modes is one high p_T lepton plus a hadronically reconstructed tau and missing E_T . These physics objects are reconstructed by standard ATLAS algorithms. Identification requirements are applied to the object candidates based on kinematic variables (p_T, η), and other parameters relative to the reconstruction of each object type. A common variable used in object identification is $\Delta R \equiv \sqrt{\Delta\eta^2 + \Delta\phi^2}$, which represents the distance between two objects in the (η, ϕ) plane. In the following, we present the reconstruction algorithms used for each type of object, and the identification criteria, which can be found in [69].

5.3.1 Electrons

The electron identification algorithm used in this analysis is the egamma algorithm [78]. Electrons and photons are reconstructed using information from the electromagnetic calorimeter and the inner detector tracking systems. Electron and photon clusters can be identified in the calorimeter by means of the transverse shower shape and the leakage into the hadronic calorimeters. Tracks associated to the cluster in a cone of ΔR are used to distinguish electrons from photons. The isolation of the electron is measured by the sum of the transverse energy of all the tracks matching the electron track in a cone of $\Delta R < 0.2$ over

the electron p_T , $E_T^{\Delta R < 0.2}/p_T$. The electron identification cuts are the following:

- High p_T : $p_T \geq 25$ GeV
- Falls inside the EM calorimeter: $|\eta| < 2.5$
- Is well isolated: $E_T^{\Delta R < 0.2}/p_T < 0.1$
- Electron reconstruction quality: is good

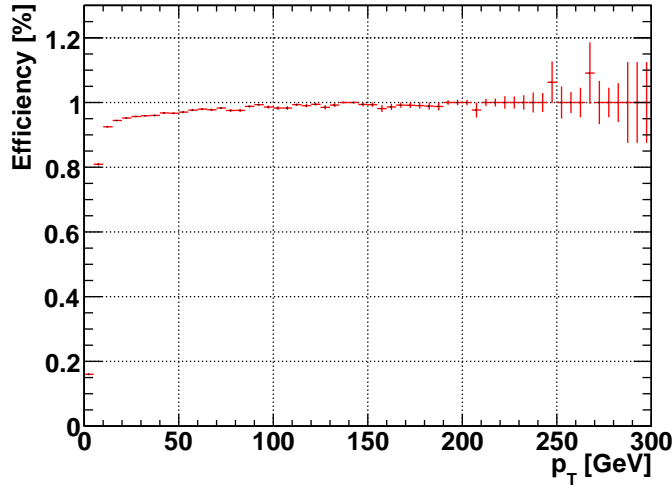


Figure 5.9: Electron identification efficiency as a function of transverse momentum, p_T .

The electron identification efficiency is computed as the ratio of the number of reconstructed objects after the identification cuts over the total number of true electrons in every event for each p_T range. Figure 5.9 shows the electron identification efficiency for a signal sample. Efficiency increases rapidly from zero to 20 GeV and is close to 100% for $p_T > 50$ GeV.

5.3.2 Muons

The muon identification algorithm used in this analysis is the Staco algorithm [79], where a track is built starting from the parameters of a segment in the outer muon chambers, then iteratively adding segments in the middle and inner layers until the full track is obtained. The track parameters are fitted and expressed at muon spectrometer entrance, at calorimeter entrance, as well as at the interaction point. Back extrapolation through the calorimeters uses parameterized

energy loss. The muon reconstruction quality factor is expressed in terms of a χ^2 , which is used in the muon candidate selection. The isolation of the muon is measured by the sum of the transverse energy of all the tracks matching the muon track in a cone of $\Delta R < 0.2$ over the muon p_T , $E_T^{\Delta R < 0.2}/p_T$. The muon identification cuts are the following:

- High p_T : $p_T \geq 20$ GeV
- Falls inside LAr: $|\eta| < 2.5$
- Is well isolated: $E_T^{\Delta R < 0.2}/p_T < 0.1$
- χ^2 cut: $0 < \chi^2 < 20$

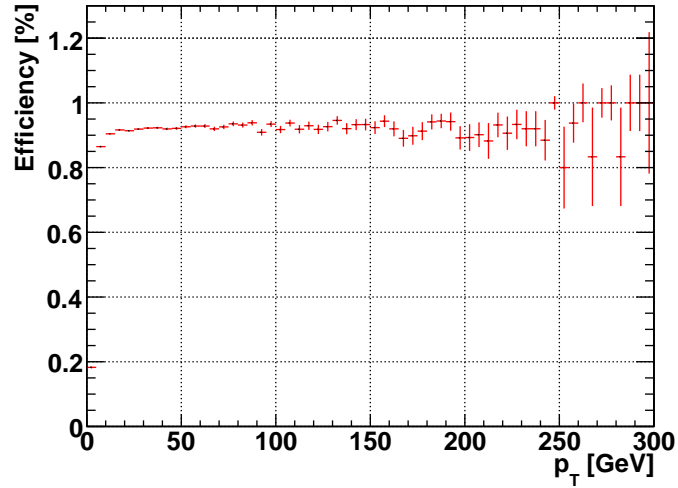


Figure 5.10: Muon identification efficiency as a function of transverse momentum, p_T .

The muon identification efficiency is computed as the ratio of the number of reconstructed objects after the identification cuts over the total number of true muons in every event for each p_T range. Figure 5.10 shows the muon identification efficiency for a signal sample. Efficiency increases rapidly from zero to 20 GeV reaching a maximum of 90% for the rest of the p_T range.

5.3.3 Taus

For leptonic tau decays, since they produce standard leptons (electrons and muons), identification is done through the final lepton. For hadronic tau decay

identification, one has to consider the different hadronic tau decay modes:

- Single-prong decays (with one charged pion and neutral pions) which are easier to identify.
- Three-prong decays (with three charged pions and neutral pions) which have a higher rate of fakes from QCD jets.

Hadronic tau decays produce tracks and hadronic showers due to the charged particles, and electromagnetic clusters due to the neutral particles. Thus, there is hadronic and electromagnetic energy deposition.

A high tau momentum implies collimated decay products (up to 90% of the energy contained in a cone of radius $\Delta R = 0.2$ around the jet direction for $E_T > 50$ GeV) as shown in Figure 5.11. The main backgrounds for hadronic taus are QCD jets faking tau jets, electrons with late showering or with strong bremsstrahlung and muons interacting in the calorimeter (always faking tau jets).

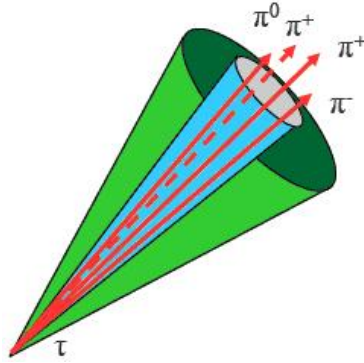


Figure 5.11: Tau signal cone and isolation annulus for tracks and pions. The inner cone contains the hadronic tau track.

ATLAS provides two hadronic tau reconstruction algorithms which both require a hadronic cluster matched to an inner detector track:

- The TauRec algorithm is a likelihood based algorithm to identify hadronically decaying taus from QCD jets. The algorithm is seeded by calorimeter clusters with $E_T > 10$ GeV and $|\eta| < 2.5$. Tracks from tau decays are selected within a $\Delta R < 0.3$ cone. The likelihood variables are the number of associated tracks, the radius of the cluster in the electromagnetic

calorimeter, the isolation, the number of hits in the eta-strip with $E_T < 200$ MeV, the width of the profile in the eta-strip, the electric charge, the lifetime signed impact parameter of the leading track and the ratio of the E_T to the transverse momentum of the leading track ($E_T/p_T(1)$).

- The Tau1p3p algorithm starts with a seed track with $p_T > 9$ GeV and associates other tracks with $p_T > 2$ GeV within a cone radius of $\Delta R < 0.2$. If no other track was found the track is labelled as single-prong, if two and only two tracks are found the track is labelled as three-prong. The (η, ϕ) coordinates for the three-prong decay are the barycentre of the (η, ϕ) positions of all three tracks weighted by their respective momenta. The Tau1p3p reconstruction result is stored in a `discriCut` variable. The E_T energy is reconstructed using the energy flow method [80].

$$E_T = E_T^{EM} + p_T^{track} + E_T^{neuEM} + resE_T^{EM} + resE_T^{neuEM}$$

where E_T^{EM} represents the total transverse energy summed over the electromagnetic cells of the cluster, p_T^{track} is the transverse momentum of the tracks as measured in the Inner Detector, E_T^{neuEM} represents the scalar sum of transverse energies of all remaining electromagnetic cells within a cone $\Delta R = 0.2$, and $resE_T^{EM}$ and $resE_T^{neuEM}$ take into account leakage of photon showers and the double-counting of electromagnetic leakage. The reference calorimetric energy E_T^{calo} is calculated at the electromagnetic scale from energy deposits in the hadronic and electromagnetic calorimeter in a cone $\Delta R = 0.2$ around the leading track.

Another selection criteria is proposed to suppress contamination from QCD jets by exploring isolation from tracks in the extended region around the reconstructed tau. We re-calculate the multiplicity of tracks for a given candidate counting not only tracks inside the core-cone of the tau candidate but adding also tracks inside a searching cone. We define a distance parameter from a track in the searching cone to a given tau candidate as the following:

$$D^i = \frac{p_T^i}{p_T^\tau \Delta R}$$

where p_T^τ is a transverse momentum of the tau candidate track, ΔR is the distance in the (η, ϕ) plane from the candidate track to the target track, and p_T^i is the transverse momentum of the target track in the searching cone. If the minimum value of the D^i is larger than a given threshold, this track is counted into track multiplicity of the tau candidate. The searching cone is chosen to be 0.7.

In this analysis we use Tau1p3p algorithm due to its better performance in the range from 20 to 80 GeV [81]. The tau identification cuts applied are the following:

- High p_T : $p_T \geq 30$ GeV
- Falls inside EM calorimeter: $|\eta| < 2.5$
- Number of tracks: 1 or 3
- Reconstructed charge: $|Q| = 1$
- Track recounting: $\sum_i D^i > 0.4$
- Tau1p3p discriminant: $discrCut = 1$
- High E_T^{calo} : $E_T^{calo} \geq 10$ GeV

The tau identification efficiency is computed as the ratio of the number of reconstructed objects after the identification cuts over the total number of true taus in every event for each p_T range. Figure 5.12 shows the tau identification efficiency for a signal sample. Efficiency increases rapidly from zero to 50 GeV reaching a maximum of 70% for the rest of the p_T range.

5.3.4 Fake Tau Identification

The QCD background, introduced in Section 5.1.3, can be reduced through a set of predefined cuts, $E_T^{miss} > 30$ GeV, that separates background only from signal plus background events, and b-jet requirement, which separates the jets from the main interaction from all other jets. However, due to the tau lepton decay properties, the hadronic tau reconstruction can wrongly identify a jet as a tau. Several QCD di-jet samples have been used to compute the fake rate of tau identification, defined as:

$$R(p_T) = \frac{\#_{\text{tau candidates}}(p_T)}{\#_{\text{jets}}(p_T)}$$

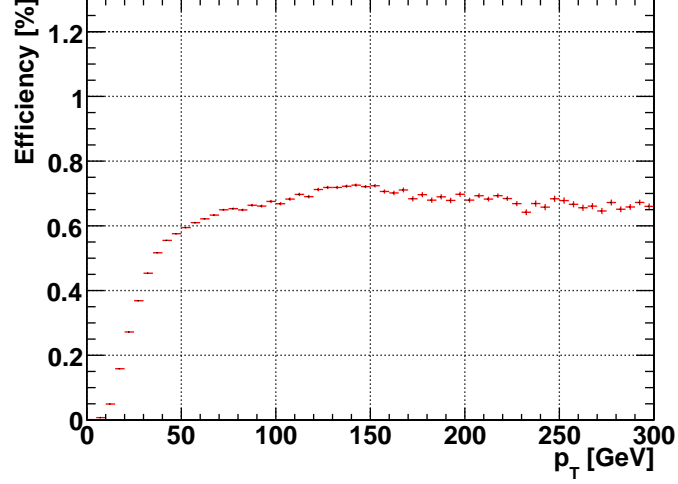


Figure 5.12: Tau identification efficiency as a function of transverse momentum, p_T .

Figure 5.13 shows the rate of fake identified taus as a function of p_T for a set of loose and tight tau identification cuts. The loose identification requires no discrimination cut in the tau reconstruction. As shown in Figure 5.13, the value of the $R(p_T)^{tight}$ distribution varies from 10^{-2} to 10^{-3} in the energy range covered. This implies a small systematic error in the identification of taus, but not negligible. The effect of this error would be a change in the M_{vis} distribution used for the statistical analysis. The template morphing technique explained in Section 5.5.2 could be used to take into account the tau identification efficiency. Unfortunately, this is not the case in this analysis, but should be considered in the future.

Di-jet Visible Mass

The QCD di-jet M_{vis} distribution for the statistical analysis cannot be directly obtained applying the standard event selection, because no event passes the event selection cuts. A common approach to obtain the distribution of interest is through means of the fake tau identification rate for a set of loose and tight cuts, under the assumption that the loose cuts don't modify the shape but only the integral of the distribution. The distribution of interest, M_{vis} in this case, is computed for the tight cuts, M_{vis}^{tight} , by scaling the distribution obtained for

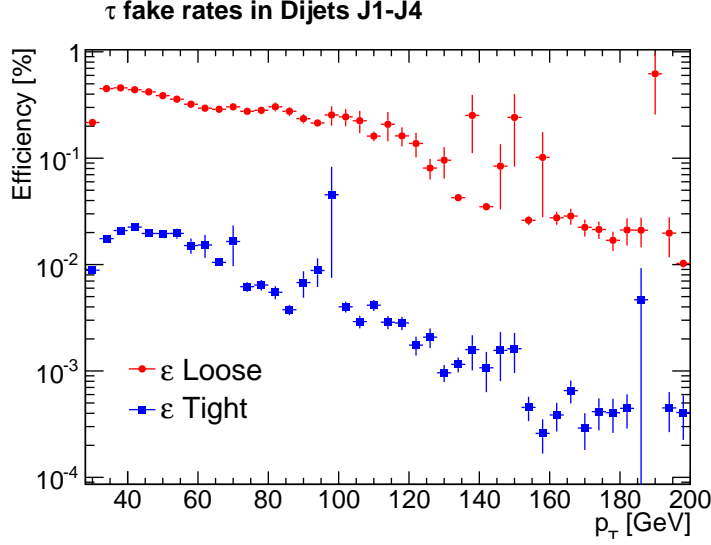


Figure 5.13: Rate of fake tau identification as a function of P_T for a set of tight and loose cuts.

the loose cuts, M_{vis}^{loose} , by the ratio of fake identification rate, like the following:

$$M_{vis}^{tight} = \frac{R(P_T)^{tight}}{R(P_T)^{loose}} M_{vis}^{loose}$$

Unfortunately only one event for the loose set of cuts survives the event selection process. Thus, the application of this technique is impossible in this case. The contribution of the QCD di-jet background to any physics analysis is undeniable but the effect of this background in this analysis will be neglected, as the CPU time required for its correct estimation would be very high, and other important background source (W +jets) is already considered. In the following QCD di-jet will not be added to the background sources for the statistical analysis.

5.3.5 Jets

Jets are reconstructed with the C4TopoJet algorithm which builds Jets from Topological clusters [82] in a cone of $\Delta R = 0.4$. The topological clusters are built from the calorimeter cells by grouping neighbours with three different signal to noise ratios (E/σ):

- Seed threshold: $|E/\sigma| > 4$.

- Neighbour threshold: $|E/\sigma| > 3$.
- Cell threshold: $|E/\sigma| > 0$.

The requirements on the reconstructed jets are the following:

- High p_T : $p_T \geq 20$ GeV
- Falls inside calorimetric region: $|\eta| < 4.8$

Figure 5.14 shows the jet multiplicity in signal and background samples. We select events with more than two jets.

5.3.6 Missing Transverse Energy

The Missing Transverse Energy, E_T^{miss} , algorithm used in this analysis is the object based algorithm for the reconstruction of Missing Transverse Momentum [83]. Figure 5.15 shows the E_T^{miss} distributions for signal and background events. We select events with $E_T^{miss} > 30$ GeV.

5.3.7 Overlap Removal

Sometimes the same physical object might be reconstructed by various particle identification algorithms. These multiple reconstructed objects have to be removed from the particle candidates. This is called *overlap removal*. There is no general method to address this matter, there are general guidelines but the technique is analysis dependent [84].

The overlap removal technique used in this analysis is based on correct light lepton identification. No overlap removal is applied to electron or muon candidates. After the tau identification, tau candidates are removed from the container, if they match a well identified electron or muon inside a cone of $\Delta R < 0.4$.

After the jet identification, jet candidates are removed from the container when they match a well identified electron, muon or tau applying the same algorithm as before.

For the previous we rely on the fact that if two reconstructed objects represent the same physical object in the detector, their η and ϕ coordinates will be equal except for rounding corrections.

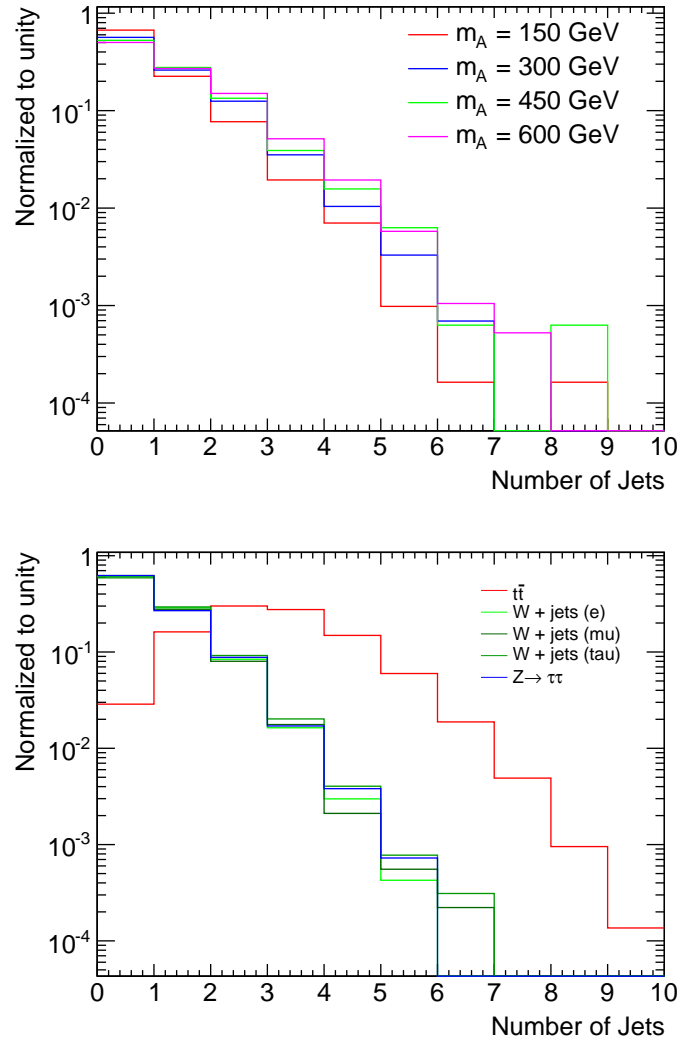


Figure 5.14: Jet multiplicity per event in Signal (top) and Background (bottom) samples.

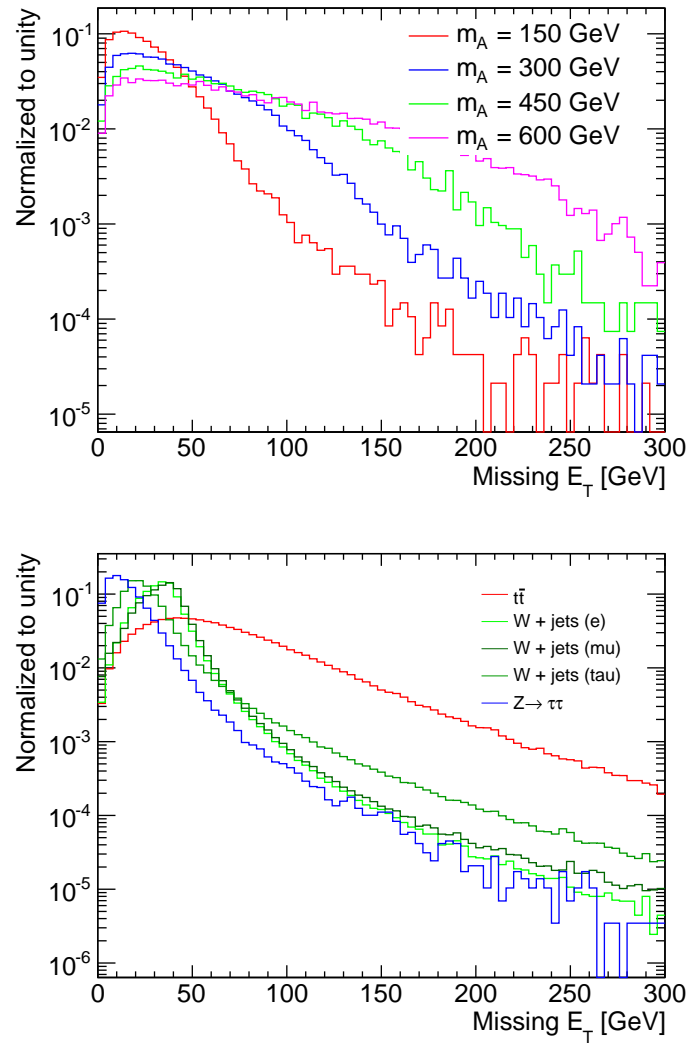


Figure 5.15: Missing transverse energy distributions for signal (top) and background (bottom) samples.

5.4 Event Selection

The event selection criteria described in the following paragraphs is based on the selection criteria used in [69], except for the transverse mass cut. These are the following:

1. One light lepton flavour is required with $p_T > 25$ GeV for electrons and $p_T > 20$ GeV for muons, along with the identification criteria detailed in Section 5.3. Lepton flavour is given by the Event Filter Trigger information. If the Event Filter triggers an electron, an electron candidate is chosen. If it triggers a muon, a muon candidate is chosen. If it triggers both electron and muon, the lepton with highest p_T is chosen. This provides separation of electron-hadron from muon-hadron channels.
2. A tightly identified tau is required as explained in Section 5.3.3. After this cut, events are considered to be lepton-hadron.
3. Events with $E_T^{miss} > 30$ GeV are selected as explained in Section 5.3.6 to remove most of the QCD di-jet background.
4. Opposite charges are required on the lepton-hadron pair, in order to select pairs that have been produced in a neutral Higgs decay.
5. In order to remove tau fakes, a high cut on the transverse momentum of the tau is required, $p_T > 30$ GeV.
6. Events with a number of jets less than two are required. This reduces most of the $t\bar{t}$ background.
7. The last step of the event selection requires the anticorrelation in the transverse mass plane of the lepton plus E_T^{miss} vs hadron plus E_T^{miss} . This cut is explained in the following Section. It is applied to remove most of the W +jets background.

5.4.1 Transverse Mass Cut

Consider a single heavy particle of mass M , produced in association with visible particles which decay into two particles where one is invisible. The mass of the parent particle can be constrained by the quantity M_T , so called the hadron collider experimentalist's Transverse Mass [85], defined by:

$$M_T^2 \equiv E_T^2 - \vec{p}_T^2$$

where $E_T = E_{T1} + E_{T2}$ and $\vec{p}_T = \vec{p}_{T1} + \vec{p}_{T2}$. The maximum value of the Transverse Mass is $M_T^{max} = M$.

For massless particles it becomes:

$$M_T^2 = 2E_{T1}E_{T2}(1 - \cos\Delta\phi_{12}))$$

Figure 5.16, shows the Transverse Mass for the lepton plus missing E_T versus the Transverse mass for the hadron plus missing E_T , for signal and background samples. The signal sample shows an anti-correlation whereas the background sample distribution shows a correlation. We optimize the cut to remove as much background as possible keeping the signal. We obtain a cut efficiency of 20% for signal and to 90% for background.

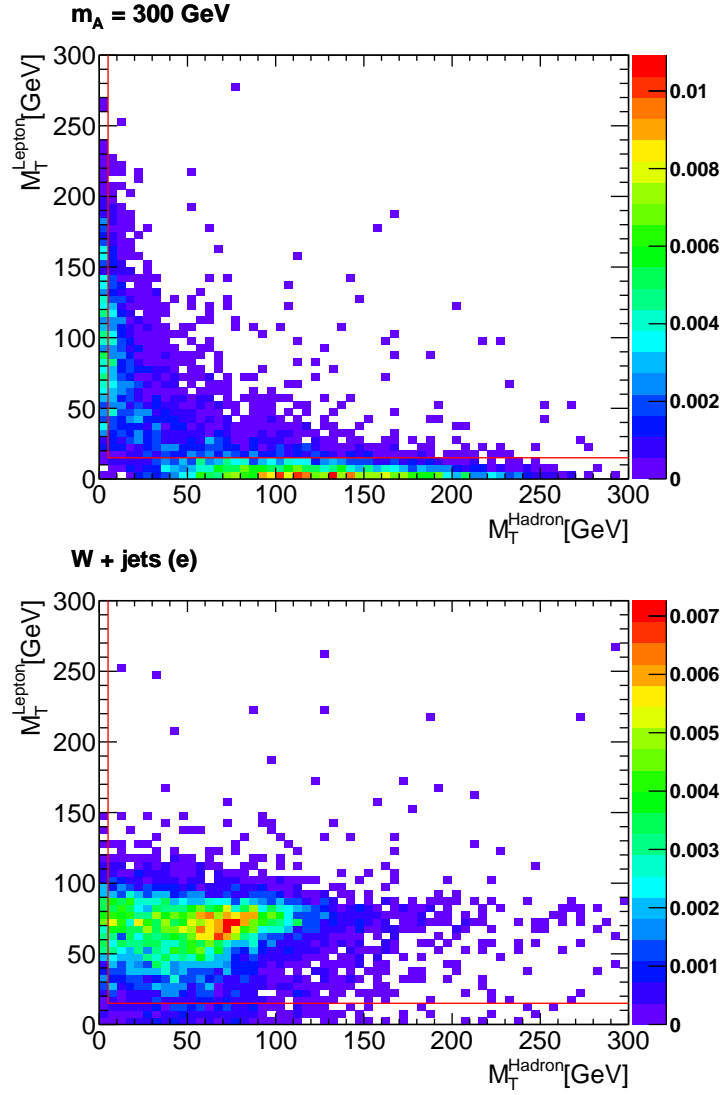


Figure 5.16: Lepton versus Hadron Transverse mass distributions for signal (top) and background (bottom) samples normalized to unity.

5.4.2 Cut Flow

Tables 5.8 and 5.9 shows the contribution of each dataset in fb after each cut for signal and background datasets respectively. The cut that reduces the most background is the missing Et cut.

Cut [fb]	A150	A300	A450	A600
Total	67041	1020	269	176
Lepton ID	34745	489	142	95
Tau ID	8684	122	31	18
$E_T^{miss} > 20$ GeV	4181	89	26	16
Opposite sign	4121	85	25	15
$E_T^\tau > 40$ GeV	3227	77	23	15
$\#jets < 2$	2880	67	20	12
M_T cut	2389	48	13	8

Table 5.8: Cut flow in fb for signal datasets.

Cut [fb]	$t\bar{t}$	$Wq \rightarrow e\nu$	$Wq \rightarrow \mu\nu$	$Wq \rightarrow \tau\nu$	$Z \rightarrow \tau\tau$
Total	461000	12420856	12416754	1374170	451440
Lepton ID	233573	7188633	8097155	485075	66622
Tau ID	6284	19493	21876	2203	8633
$E_T^{miss} > 20$ GeV	5696	15755	18159	1630	2817
Opposite sign	4514	11576	12794	1203	2518
$E_T^\tau > 40$ GeV	3025	7143	7623	870	1227
$\#jets < 2$	817	6646	6922	790	984
M_T cut	67	383	371	208	663

Table 5.9: Cut flow in fb for background datasets.

5.4.3 Visible Mass Distribution

Figure 5.17 shows the expected visible mass distribution, M_{vis} , as the stack of all background channels, together with the M_{vis} of the neutral MSSM Higgs boson, A/H , for $\tan\beta = 15$ and integrated luminosity of 1 fb^{-1} . Figure 5.18 shows the same distributions for $\tan\beta = 45$.

These distributions shall be called templates. In the following we present the statistical mechanism to obtain the expected exclusion limits and discovery significances based on these templates and the pseudo-experimental data generated from them. This analysis is independent of the ATLAS software version used to compute the shapes and could be reproduced with up-to-date shapes from simulation or real data.

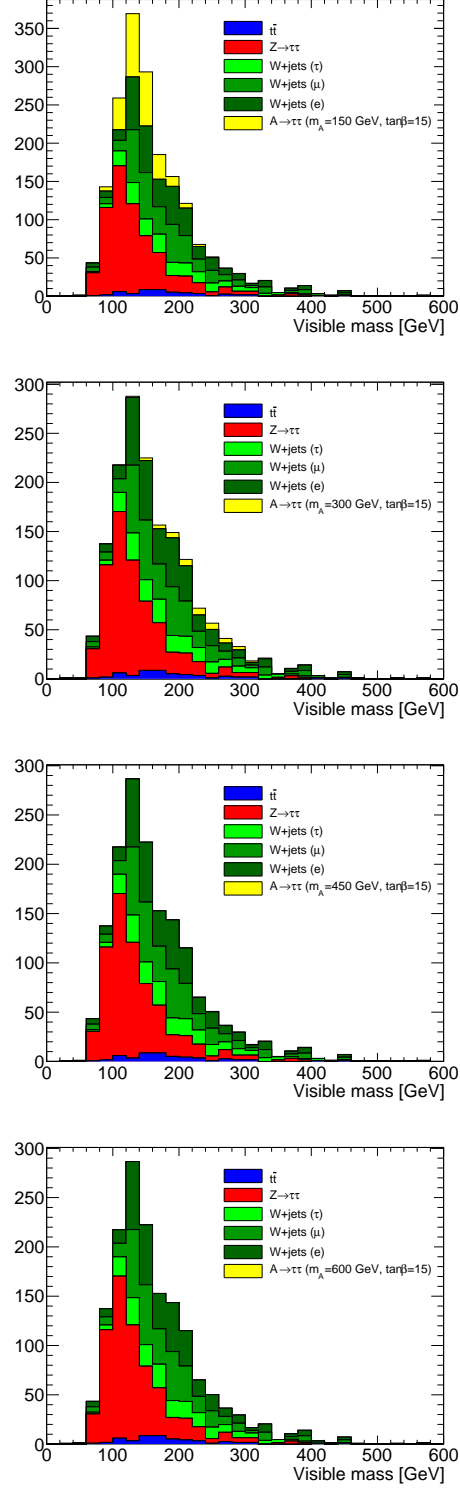


Figure 5.17: Typical M_{vis} distribution of the background and signal processes at $\tan\beta = 15$ for different values of m_A (150, 300, 450 and 600 GeV from top to bottom) for 1 fb^{-1} .

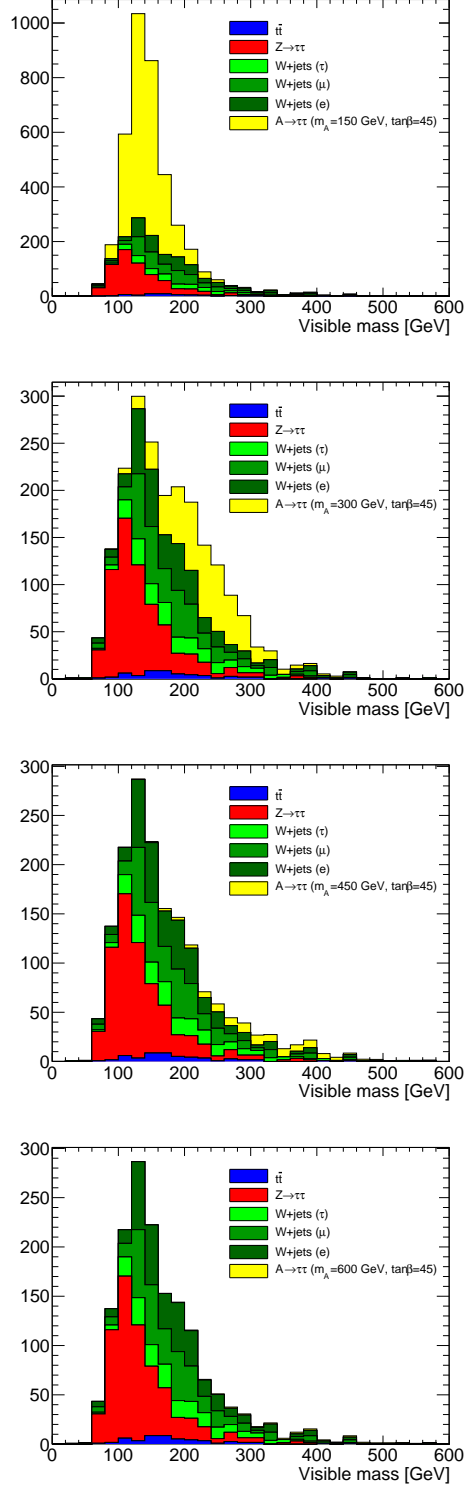


Figure 5.18: Typical M_{vis} distribution of the background and signal processes at $\tan\beta = 45$ for different values of m_A (150, 300, 450 and 600 GeV from top to bottom) for 1 fb^{-1} .

Pseudo-experimental Data

Pseudo-experimental data generated from the M_{vis} distributions is used to evaluate expected results. For each distribution we consider that the value in each bin is the mean of a Poisson distribution, and using a random generator we obtain a new value for the bin. The value in each bin of the pseudo-data is the sum of the generated random values in each bin for all contributing distributions.

For a background-only pseudo-experiment, the outcome contains in each bin the sum of the Poisson fluctuation for the same bin over all backgrounds. An example of a background-only pseudo-experiment is shown in Figure 5.19, represented as a dot in each bin. Note the pseudo-data does not have an error band. The error bars quoted represent the error in the mean value of each bin, which represents the $\pm 1\sigma$ probability of the outcome of the pseudo-experiments.

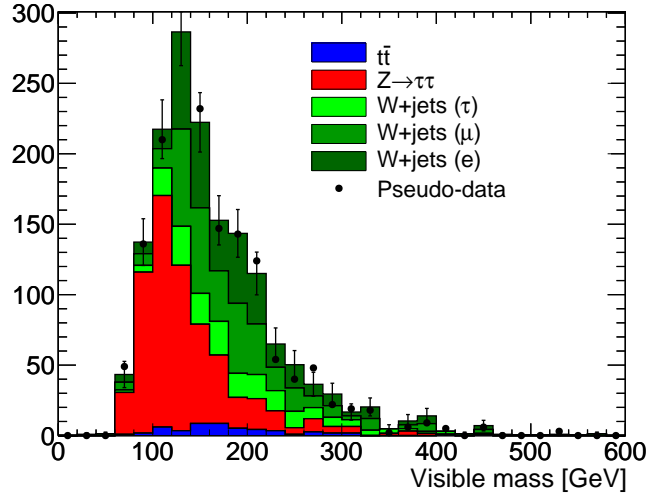


Figure 5.19: Pseudo-experimental data generated from M_{vis} distribution of the background.

5.5 Statistical Analysis

Bayesian techniques to set confidence intervals have been extensively used at CDF [86]. They describe a convenient way to combine sensitivities from more than one channel and incorporate systematic uncertainties which might be correlated among channels. These techniques may also be used to characterize an eventual excess by setting discovery significance thresholds.

Bayes' theorem states that the conditional probability of a hypothesis given the data (posterior probability) is proportional to the product of the conditional probability of seeing the data when the hypothesis is true (likelihood) times the prior probability that the hypothesis is true (prior). The posterior probability density is, thus, given by:

$$\mathcal{P}(\theta, \nu|x) = \frac{\mathcal{P}(x|\theta, \nu) \pi(\theta, \nu)}{\pi(x)} \quad (5.1)$$

where x represents the data, (θ, ν) the parameters of the hypothesis and $\pi(\theta, \nu)$ the prior probability of the parameters. The denominator in equation (5.1) is the prior probability of the data, which can be written as an integral over all the parameter space, and regarded as a normalization factor:

$$\pi(x) = \int_0^\infty \mathcal{P}(x|\theta', \nu') \pi(\theta', \nu') d\theta' d\nu'$$

The probability $\mathcal{P}(x|\theta, \nu)$ represents the likelihood function for the data given the model, i.e., the likelihood for observing x events given the expected θ and ν . Thus equation (5.1) can be expressed as:

$$\mathcal{P}(\theta, \nu|x) = \frac{\mathcal{L}(\theta, \nu|x) \pi(\theta, \nu)}{\pi(x)} \quad (5.2)$$

Note that θ represents the parameter of interest, the neutral MSSM Higgs production cross section, while ν represents the nuisance parameters, of no particular interest in the measurement. Nevertheless they must be specified in order to extract physics information from the data, such as the integrated luminosity, the background cross sections, jet and electromagnetic energy scales, parton distribution functions, etc. Uncertainties on nuisance parameters are usually referred to as *systematic uncertainties*.

The prior probability density for the (unknown) parameters, $\pi(\theta, \nu)$, expresses our knowledge about θ and ν prior to the measurement. Bayes' theorem as shown in equation (5.5), specifies how the prior information about θ, ν is updated by the measurement of x to yield the posterior density of θ, ν . In general the prior contains correlations between the parameters.

The posterior probability depends, of course, on the choice of the prior. In the following, we consider the prior on (θ, ν) to be factorizable into a product of independent priors:

$$\pi(\theta, \nu) = \pi(\theta) \times \pi(\nu)$$

Since θ is the parameter of interest, our intention is not to favour any particular value of the parameter. We use an uninformative prior probability density function from zero up to a maximum cutoff.

$$\pi(\theta) = \text{constant} ; \theta \in [0, \Lambda_{\text{cutoff}}]$$

Concerning the nuisance parameters, there is often an estimate of both the value and uncertainty. For example, in the background production cross-section where the estimates are obtained from subsidiary studies. This results, then, in treating these parameters as having Gaussian probability distribution functions which is a convenient way to incorporate systematics. We choose Gaussian truncated distributions, not allowing the expected values to be negative, although any other reasonable description for the priors would be also correct. Therefore, the Gaussian probability on that parameter will depend on a central value and a standard deviation. In this case, a typical parametrization for the priors associated to nuisance parameters may be expressed as:

$$\pi(\nu) = G(\nu, \hat{\nu}, \varepsilon(\nu)) = \frac{1}{\sqrt{2\pi\varepsilon(\nu)^2}} \exp\left(-\frac{(\nu - \hat{\nu})^2}{2\varepsilon(\nu)^2}\right)$$

5.5.1 Profiling

In the case of counting experiments, a conventionally accepted likelihood function is the Poisson distribution with expectation value (mean) μ , given by:

$$\mathcal{L}(\theta, \nu|x) = P(\mu = f(\theta, \nu), x) = \frac{\mu^x \exp(-\mu)}{x!} \quad (5.3)$$

where $\mu = s + b$ with s the expected signal and b the expected background. In the present analysis we consider a binned likelihood. If we call x_{ij} the observed number of events in bin i , for channel j (where $j = 1$ corresponds to the eh channel and $j = 2$ to the μh channel), and μ_{ij} the expected number of events in that bin, then the likelihood function given by equation (5.3) may be written as:

$$\mathcal{L}(\theta, \nu | x) = \prod_{ij} \frac{\mu_{ij}^{x_{ij}} \exp(-\mu_{ij})}{x_{ij}!}$$

Note that the expected number of events in a particular bin, μ_{ij} , are the sum of the expected number of events for signal and all background sources. In general terms, this results from the product of the integrated luminosity (L) times the cross sections times branching ratio of the signal (σ_s) and the backgrounds (σ_k) and the efficiency for each bin and channel (ϵ_{ij} for the signal and ϵ_{ijk} for the backgrounds) which is given by the visible mass distribution. For k background sources the expected number of events is written as:

$$\mu_{ij} = s_{ij} + \sum_k b_{kij} = L\sigma_s\epsilon_{ij} + \sum_k L\sigma_k\epsilon_{kij} \quad (5.4)$$

In our case, the parameter of interest is the signal cross section (σ_s) and the nuisance parameters are the background cross sections (σ_k) and the luminosity (L). Thus, the posterior probability now takes the form:

$$\mathcal{P}(\theta, \nu | x) = \mathcal{C} \prod_{ij} \frac{\mu_{ij}^{x_{ij}} \exp(-\mu_{ij})}{x_{ij}!} \times \prod_k G(\nu_k, \hat{\nu}_k, \varepsilon(\nu_k))$$

To obtain the posterior density in the parameters of interest (i.e., the signal cross section σ_s) one needs to eliminate the nuisance parameters (i.e., the background cross sections σ_k). In other words, to eliminate the dependence of \mathcal{L} on ν without ignoring the effect that uncertainties on ν have on inferences about θ . This is generally achieved by integrating the likelihood times the priors over the nuisance parameters (*marginalization method*) which results in averaging the likelihood with respect to the nuisance parameters.

It is of course tempting to maximize the likelihood times the prior with respect to the nuisance parameters instead of marginalizing. This method is called *profiling*. It is an iterative procedure that finds the Maximum Likelihood

Estimator (MLE) for the nuisance parameters. Hence, the posterior probability is now independent of the nuisance parameters, and equation (5.5) becomes the following:

$$\mathcal{P}(\theta|x) = \mathcal{C} \mathcal{L}(\theta, \nu_{MLE}|x) \pi(\nu_{MLE}) \quad (5.5)$$

The normalization factor of the posterior probability (\mathcal{C}) is the ratio of the prior probability for the parameter of interest over the prior probability for the data ($\pi(\theta)/\pi(x)$). It can be regarded as the integral of the posterior probability over the full parameter space.

$$\mathcal{C} = \int_0^\infty \mathcal{P}(\theta'|x) d\theta'$$

The profiling method described here provides a way to compute the posterior probability through means of maximization of the likelihood times the priors of the nuisance parameters. Note, there is no reason to prevent the likelihood function to be a convolution of a core likelihood function times the constraint functions for the nuisance parameters, leaving space for other prior definitions. However, we consider that the prior functions on our nuisance parameters are really prior to the experiment. Thus, contain information that has been obtained through different measurements and have associated error distributions which, alike our interpretation, are commonly described by gaussian distributions. This is the case of the cross section of the Z boson production, which is not directly measured by our experiment but, its value is a crucial nuisance parameter in this analysis.

5.5.2 Template Morphing

Systematic uncertainties due to uncertainty on the energy scale can introduce shape and normalization errors. These are treated using a *template morphing* [86] technique developed at CDF. To incorporate the effect of a single energy scale uncertainty of value α on a template (ϵ_{ij}), which is the visible mass distribution of the electron or muon channel, we recall on auxiliary templates which take into account the $+1\alpha$ and -1α shift on the energy scale. We consider that the morphed template is the value of the nominal template plus a first order

perturbation correction ($\delta\epsilon_{ij}$), which is defined as the difference of the shifted templates, like the following:

$$\delta\epsilon_{ij}(m) = f_m \frac{\epsilon_{ij}^{m+} - \epsilon_{ij}^{m-}}{2}$$

where ϵ_{ij}^{m+} and ϵ_{ij}^{m-} represent the content of bin i of the $+1\alpha$ and -1α shifted templates, and f_m is the parameter that represents the strength of the morphing of the nominal template for an energy scale m . The nominal value of the morphing parameter is $\hat{f}_m = 0$, which is assumed to follow a Gaussian distribution with $\sigma = \varepsilon(f_m) = 1$.

The morphed template taking into account multiple energy scale shifts is given by:

$$\epsilon'_{ij} = \epsilon_{ij} + \sum_m f_m \frac{\epsilon_{ij}^{m+} - \epsilon_{ij}^{m-}}{2} \quad (5.6)$$

The profiling method described in the Section 5.5.1 is extended to take into account the template morphing. The efficiency distributions (ϵ_{ij}) used to compute μ_{ij} , are replaced by morphing capable templates (ϵ'_{ij}) given by equation (5.6). Thus, equation (5.4) becomes the following:

$$\mu_{ij} = L\sigma_s \left(\epsilon_{ij} + \sum_m f_m \frac{\epsilon_{ij}^{m+} - \epsilon_{ij}^{m-}}{2} \right) + \sum_k L\sigma_k \left(\epsilon_{kij} + \sum_m f_m \frac{\epsilon_{kij}^{m+} - \epsilon_{kij}^{m-}}{2} \right) \quad (5.7)$$

This introduces new nuisance parameters in the posterior probability, one for each energy scale shift, which also have a gaussian prior. The posterior probability is now given by:

$$\mathcal{P}(\theta, \nu, f|x) = \mathcal{C} \prod_{ij} \frac{\mu_{ij}^{x_{ij}} \exp(-\mu_{ij})}{x_{ij}!} \times \prod_k G(\nu_k, \hat{\nu}_k, \varepsilon(\nu_k)) \times \prod_m G(f_m, \hat{f}_m, \varepsilon(f_m))$$

where f represents the morphing parameters. Note, there is really no difference between ν and f (both are nuisance parameters) and are handled in the same way.

The morphing parameters are correlated across templates. Each trial of a morphing parameter value will result on slightly a different template for all signal and background sources.

Computation of Shifted Templates

At the particle identification stage, the energy of a given particle is shifted by a factor α which is given by the uncertainty on the energy scale, resulting in the production of shifted templates. The electromagnetic energy scale is shifted by 1% and the jet energy scale is shifted by 10%. The particle energy shift also implies the correction of the E_T^{miss} by a factor α . The particle energy shifts are given by:

$$p_i(\text{particle}) = (1 + \alpha)p_i(\text{particle})$$

$$E_T^{miss} = E_T^{miss} + \alpha E_T^{miss}(\text{particle})$$

where index i corresponds to each of the three space coordinates (x,y,z).

Figure 5.20 shows the nominal and the $+1\alpha$, -1α shifted p_T and M_{vis} distributions for a shift of the Jet energy scale on a $Z \rightarrow \tau^+\tau^-$ dataset. Both, p_T and M_{vis} distributions are shifted with the same magnitude. The differences between shifted and nominal M_{vis} distributions are smaller than those between the shifted and nominal p_T distributions.

Figure 5.21 shows the difference between the positive and negative shifted p_T and M_{vis} distributions shown in Figure 5.20. In the case of M_{vis} , this difference depicts the contribution of the shifted templates to the nominal template is the morphing technique.

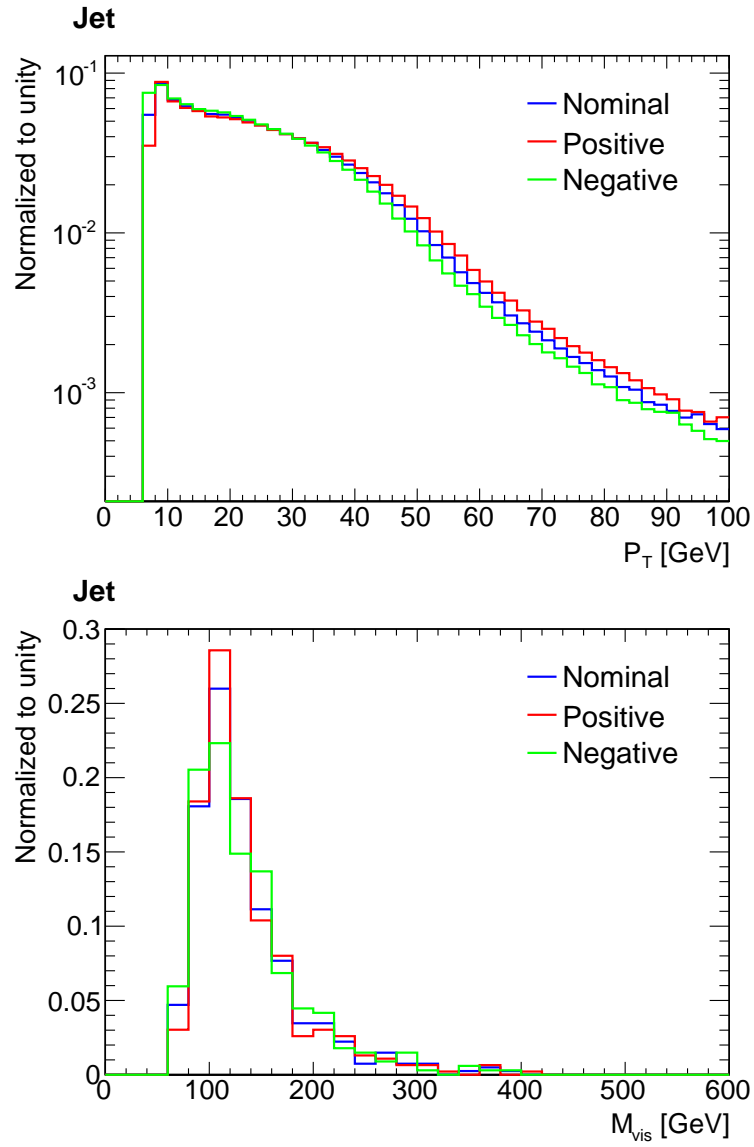


Figure 5.20: Nominal and shifted p_T (top) and M_{vis} (bottom) distributions for $Z \rightarrow \tau^+\tau^-$ dataset with jet energy scale shift.

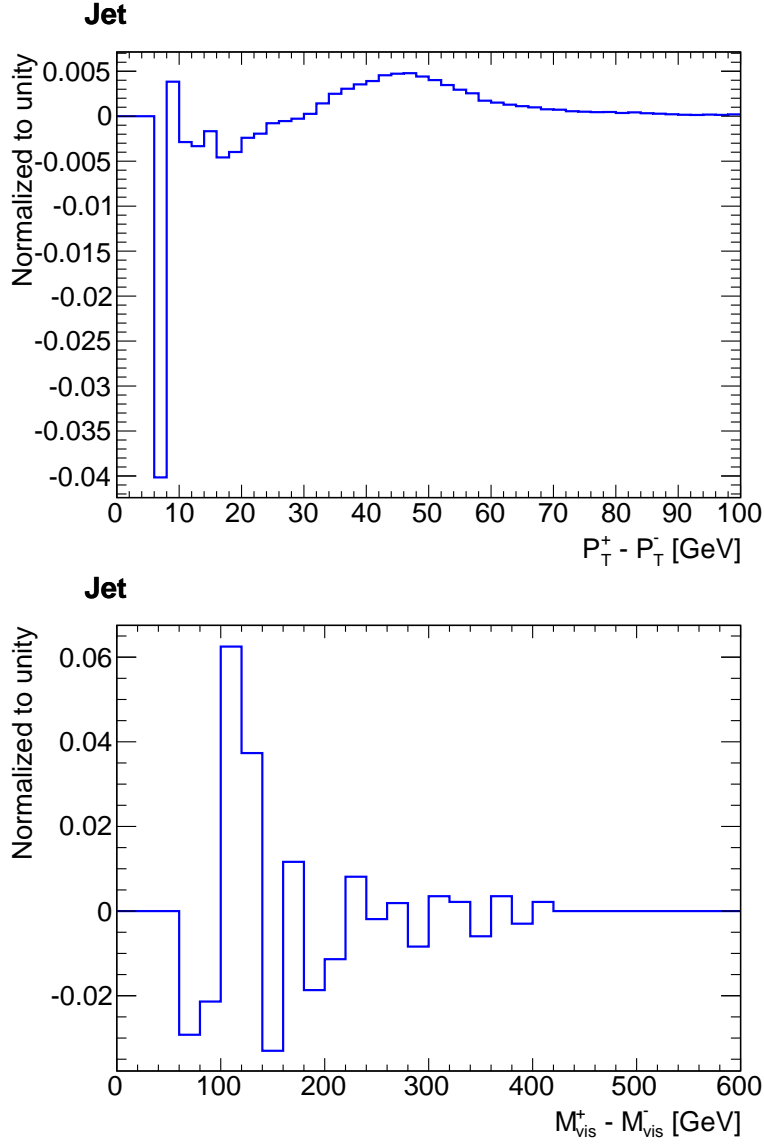


Figure 5.21: Difference between positive and negative shifted p_T (top) and M_{vis} (bottom) distributions for $Z \rightarrow \tau^+\tau^-$ dataset with jet energy scale shift.

5.5.3 Setting Limits

The full information for a Bayesian analysis is contained in the posterior density function, $\mathcal{P}(\theta|x)$, which may be used to calculate the confidence intervals¹ for the parameter of interest by integrating it [87] so as to include the desired probability at Confidence Level (CL) $1 - \alpha$, given by the following:

$$1 - \alpha = \int_{-\infty}^{\theta^{UP}} \mathcal{P}(\theta|x) d\theta \quad (5.8)$$

In this case the parameter of interest (signal cross section) is known to be non-negative, thus the prior and the posterior are zero for $\theta < 0$, and the integral effectively starts at value zero. We are interested in computing the upper exclusion limit cross section, θ^{UEL} , for a new phenomena, below which the new phenomena would be un-observable. In other words, if the new phenomena had a cross section greater than θ^{UEL} , it should be observed with a posterior probability of $1 - \alpha$. Hence equation (5.8) becomes the following:

$$1 - \alpha = \int_0^{\theta^{UEL}} \mathcal{P}(\theta|x) d\theta \quad (5.9)$$

For example, to set a 95% CL upper limit on the signal, one finds the value of θ , beyond which the 5% of the total integral lies, θ^{UEL} . If there is equal *a priori* probability that the signal could have any normalization from zero to infinity, then it is less than 5% probable that the true value is bigger than θ^{UEL} .

To ease numerical implementation, the confidence interval expression is arbitrarily normalized to the value of the posterior density at zero cross section. Thus, equation (5.9) becomes the following:

$$1 - \alpha = \int_0^{\theta^{UEL}} \frac{\mathcal{P}(\theta|x)}{\mathcal{P}(0|x)} d\theta = \int_0^{\theta^{UEL}} \frac{\mathcal{L}(\theta, \nu_{MLE}|x) \pi(\nu_{MLE})}{\mathcal{L}(0, \nu_{MLE}|x) \pi(\nu_{MLE})} d\theta \quad (5.10)$$

This expression does not vary the definition of the θ^{UEL} . Further details of the implementation are given in Section 5.5.5.

To evaluate the expected exclusion sensitivities we rely on pseudo-experimental data, assuming null-signal hypothesis. We generate many pseudo-

¹Note Bayesian confidence intervals are sometimes called credible ranges.

experiments with no signal. For each pseudo-experiment we numerically integrate equation (5.10). The value of $\mathcal{P}(\theta|x)$ at each cross section value (θ) is obtained via the *profiling* technique. Figure 5.22 shows an example of the normalized posterior probability as a function of signal cross section for a single background only pseudo-experiment and a particular value of m_A . The θ^{UEL} value at 95% CL for each pseudo-experiment is obtained as the value of θ below which the 95% of the distribution lies.

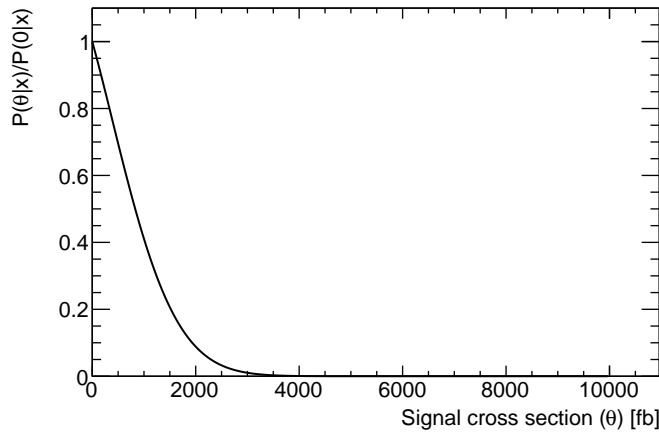


Figure 5.22: Normalized posterior probability scan in signal cross section (θ).

A distribution of expected 95% CL upper exclusion limits is formed for each mass point. The median is taken as the expected upper exclusion limit and $\pm 1\sigma$ and $\pm 2\sigma$ values cover respectively 68% and 95% of the pseudo-experiments.

In this way, the signal hypothesis is rejected directly from the data. Given a Higgs mass, the θ^{UEL} computed from the data represents the lower bound for the Higgs production cross section. All values of $\theta > \theta^{UEL}$ are regarded as excluded at 95% CL.

5.5.4 Discovery Significance

To establish a discovery, the usual procedure is the rejection of the null signal hypothesis. As already discussed in [88], one could reject the null signal hypothesis by the selection of a model with signal θ_1 against a model without it θ_0 . In principle this could be done by direct comparison of the posterior probabilities for both hypothesis. For example, if $\mathcal{P}(\theta_0|x)$ was considerably smaller than

$\mathcal{P}(\theta_1|x), \mathcal{P}(\theta_0|x) \ll \mathcal{P}(\theta_1|x)$, the model with signal θ_1 would be a better choice. However, as the posterior is proportional to the prior probability $\pi(\theta)$, the difficulty here would be to agree on a model to describe the non-existence of a new phenomenon, $\pi(\theta_0)$. This is the reason why we construct a quantity called the Bayes factor, which is usually employed in statistics to test the probability of a particular hypothesis relative to its complementary alternative hypothesis [89], because it is independent of the prior probability of the hypothesis. We define the posterior odds, as the probability of θ_1 over the probability of θ_0 :

$$\Omega_{10} = \frac{\mathcal{P}(\theta_1|x)}{\mathcal{P}(\theta_0|x)}$$

We define the prior odds as the prior probability for θ_1 over the prior probability for θ_0 :

$$\omega_{10} = \frac{\pi(\theta_1)}{\pi(\theta_0)}$$

The ratio of the posterior to prior odds is the Bayes factor, given by the following:

$$B_{10} = \frac{\Omega_{10}}{\omega_{10}} = \frac{\mathcal{P}(\theta_1|x)}{\pi(\theta_1)} \bigg/ \frac{\mathcal{P}(\theta_0|x)}{\pi(\theta_0)} \quad (5.11)$$

Taking into account equation (5.5), we obtain our definition for the Bayes Factor: The ratio of the maximized likelihood times the priors for the nuisance parameters at the expected cross-section to the maximized likelihood times the priors for the nuisance parameters at zero cross-section, like the following:

$$B_{10} = \frac{\mathcal{L}(\theta_1, \nu_1^{MLE}|x) \pi(\nu_1^{MLE})}{\mathcal{L}(\theta_0, \nu_0^{MLE}|x) \pi(\nu_0^{MLE})}$$

Taking the Bayes factor as a profile likelihood ratio, one can define a p -value [90] as:

$$p = \int_{B_{10}^{obs}}^{\infty} f(B_{10}) dB_{10} \quad (5.12)$$

where $f(B_{10})$ is the sampling distribution for the test statistic B_{10} . The p -value (5.12) represents the probability under certain hypothesis, of seeing data with equal or greater incompatibility, as measured by B_{10}^{obs} . In other words, if the data would yield an excess, the p -value computed from a statistic distribution under the null signal hypothesis, B_{10}^B , taking into account the statistic computed

for the data yielding an excess, B_{10}^{S+B} , we could quantify the probability that the observed data is a fluctuation of the null signal hypothesis, given by:

$$p = \int_{B_{10}^{S+B}}^{\infty} f(B_{10}^B) dB_{10}^B$$

Note that this technique is applicable when the signal cross section is small compared to the background cross section. In the event the signal cross section is large, the experimental distribution for B_{10}^{S+B} would never overlap any value of B_{10}^B and therefore, tend to the lower limit of zero. Figure 5.23 shows the distribution of B_{10}^{S+B} and B_{10}^B for small (left) and large (right) cross sections. Note that the non-overlapping of B_{10}^{S+B} and B_{10}^B in the right could be an effect of the lack of statistics. Thus, one could expect the distributions would overlap for some higher number of trials.

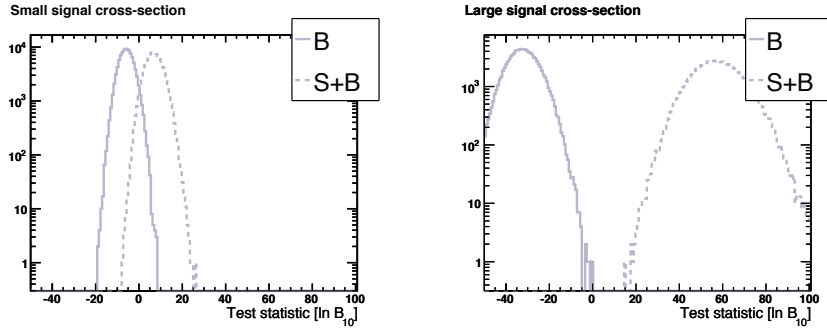


Figure 5.23: B_{01} test statistic distributions for background and signal plus background data for small and large signal cross sections.

The significance corresponding to a given p -value may then be defined as the number of standard deviations Z at which a Gaussian random variable of zero mean would give a one-sided tail area equal to p . That is, the significance Z is related to the p -value by the equation:

$$p = \frac{1}{\sqrt{2\pi}} \int_Z^{\infty} \exp(-x^2/2) dx = 1 - \Phi(Z)$$

where Φ is the cumulative distribution function for the standard Gaussian distribution (zero mean and unit variance). The standard normal cumulative distribution Φ may also be expressed in terms of the special error function erf

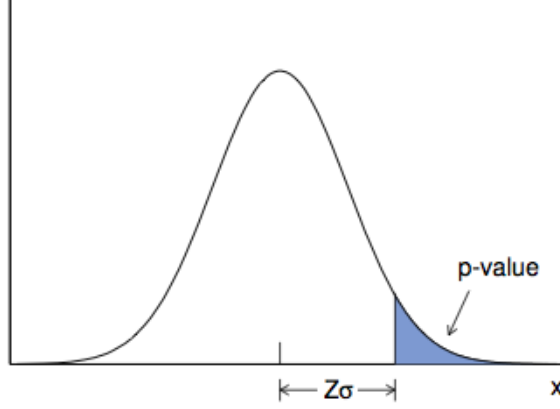


Figure 5.24: Correspondence between the significance Z and a p -value.

as:

$$\Phi(Z) = \frac{1}{2} \left[1 + \operatorname{erf} \left(\frac{Z}{\sqrt{2}} \right) \right]$$

Note that, equivalently, one has:

$$Z = \Phi^{-1}(1 - p)$$

where Φ^{-1} is the quantile of the standard Gaussian (inverse of the cumulative distribution). The relation between Z and p is shown in Figure 5.24. A significance of $Z = 5$ corresponds to $p = 2.87 \times 10^{-7}$. Note that for cases where the data would perfectly agree with the expected background one would obtain a p -value of 0.5 which corresponds to a significance $Z = 0$ as defined above. If the data fluctuate below the expected background Z would become negative.

To evaluate the expected significance of a discovery, we rely on pseudo-experimental data. For each $(m_A, \tan\beta)$ point, background only pseudo-experiments are used to obtain the B_{10}^B distribution and S+B pseudo-experiments are used to obtain the B_{10}^{S+B} distribution. The median of the B_{10}^{S+B} distribution is taken to describe the expected value of B_{10}^{S+B} . A p -value corresponding to the signal being a fluctuation of the background is computed for each $(m_A, \tan\beta)$ point, from which the corresponding significance of the signal is derived.

Look-Elsewhere-Effect

The significance calculated above is, though, dependent on the assumed value of the signal mass, included in the definition of the test statistic B_{10} . This way, the probability of rejecting the null-signal hypothesis is maximized if the signal is present at the specified mass. The search procedure is then carried out for all values of the signal mass (although, in practice, an interpolation may be applied between finite steps in mass). Note that the significance calculated this way can not be considered a proper measure of the significance of the excess as we have not allowed for the fact that such an excess could have occurred anywhere in the mass range (*look-elsewhere-effect*).

5.5.5 Software Implementation

The profiling algorithm (ProfileLikelihood) is implemented as an inheritance of a probability distribution function (PDF) which defines the way a minimization core (Minimizer) should treat it. The ProfileLikelihood holds data and template pointers to Container objects. It also takes Parameter objects to describe which parameters apply to which template and, if these should be variable and treated as Gaussian constraints or not.

The ProfileLikelihood computes the negative logarithm of the likelihood of the set of template histograms to the data. Thus the expression to minimize written in terms of the expected number of events per bin (μ_i), the observed number of events in each bin (x_i) and the nuisance parameters (ν_j) is given by:

$$-\log \mathcal{L} = \sum_{bins} \mu_i - x_i \log \mu_i + \log x_i! + \sum_{params} \frac{(\nu_j - \hat{\nu}_j)^2}{2\varepsilon(\nu_j)^2}$$

Nuisance parameters (ν_i) are identified by a boolean value. The way the templates and the parameters are used by the ProfileLikelihood is defined by an application matrix. The templates (t_{ij}) and the parameters (p_k) are separately set using an index. The application of a parameter to a shape is set by the parameter ID and the shape ID. It is possible to obtain any linear combination

of the shapes using the parameters, via the boolean coefficients (a_{jk}) given by:

$$\mu_i = \sum_j \sum_k a_{jk} t_{ij} p_k$$

Shift objects are defined to contain pointers to shifted templates and a morphing parameter ID. The morphing parameter itself is just another parameter. A morphing application is defined separately on each template by indicating the morphing parameter ID and the shifted template IDs. Template morphing is performed before the application of other parameters, as given by equation (5.6). The morphing parameter is just another nuisance parameter with a gaussian constraint. Thus its value is controlled by the minimization algorithm, and kept close to the nominal value due to the gaussian constraint.

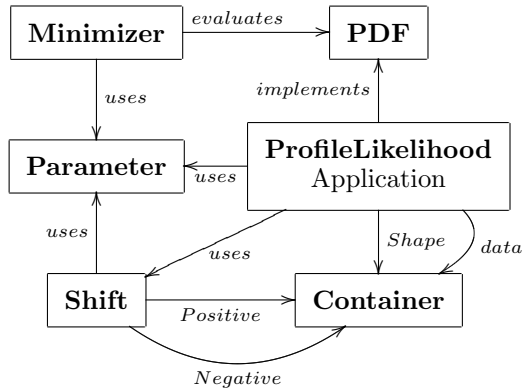


Figure 5.25: ProfileLikelihood implementation.

The Minimizer, which relies on the TMinuit implementation of the well known Minuit minimization package, is initialized with Parameters which represent the parameters of the ProfileLikelihood. It also needs the PDF to be set which can be the ProfileLikelihood. This way the possibility of adding other PDF descriptions is left open. Figure 5.25 shows a block diagram of the software package.

The election of the current implementation relies on the paradigm of separation of data from algorithms and conditions. This approach is common in other software packages such as the ATLAS offline software.

5.6 Results

Results for expected upper exclusion limits and discovery significances for the production of neutral MSSM Higgs bosons decaying into tau pairs are computed as explained in Section 5.5.3 and Section 5.5.4 from simulated data at $\sqrt{s} = 14$ TeV. Visible mass distributions explained in Section 5.1.5 are used as the observable. Signal datasets considered have values of $m_A = (150, 300, 450, 600)$ GeV, with different $\tan\beta$ values. The scaling of the signal to different cross sections, is performed by changing only the normalization, as explained in Section 5.2.1. Background datasets considered are $Z \rightarrow \tau^+\tau^-$, $t\bar{t}$ and W +jets (Table 5.7). Shifted distributions are computed to incorporate template morphing. Results with and without template morphing are compared. Systematic uncertainties considered are listed on Table 5.10.

Uncertainty	Type	Error
Luminosity	Normalization	10 %
$\sigma_{Z \rightarrow \ell\ell}$	Normalization	10 %
$\sigma_{t\bar{t}}$	Normalization	100 pb
$\sigma_{Wq \rightarrow \ell\nu}$	Normalization	10 %
Electron energy scale	Shape	1 %
Jet energy scale	Shape	10 %

Table 5.10: Uncertainty types and magnitudes used to compute expected results.

5.6.1 Expected Sensitivity for Exclusion

Distributions for 10^5 pseudo-experiments of upper exclusion limit cross section at 95% CL computed with and without template morphing, are shown in Figures 5.26 and 5.27 respectively. The median of the distribution is extracted as well as the $\pm 1\sigma$ and $\pm 2\sigma$ confidence intervals, which are listed in Table 5.11. Very little variation is observed between the two methods which indicates that the effect of the energy scale shift is small compared to the contribution of the rest of the uncertainties. Figure 5.28 shows the expected upper exclusion limit cross sections for 1 fb^{-1} for different values of m_A at 95% CL and the $\pm 1\sigma$ and $\pm 2\sigma$ probability bands. Limits using the morphing technique are slightly higher as expected due to the incorporation of more systematic uncertainties. A systematic effect is observed for $m_A = 600$ GeV.

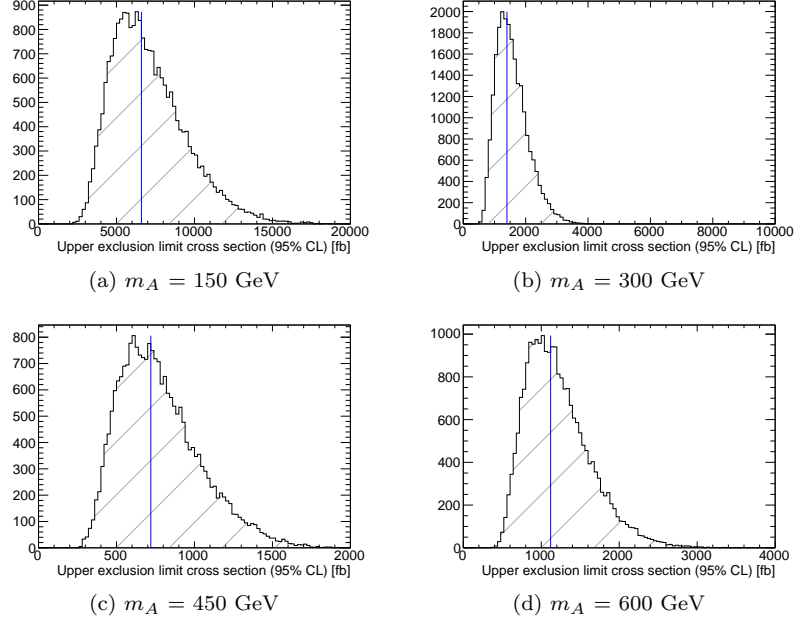


Figure 5.26: Upper exclusion limit cross section distributions for neutral MSSM Higgs bosons with morphing for 1 fb^{-1} at $\sqrt{s} = 14 \text{ TeV}$.

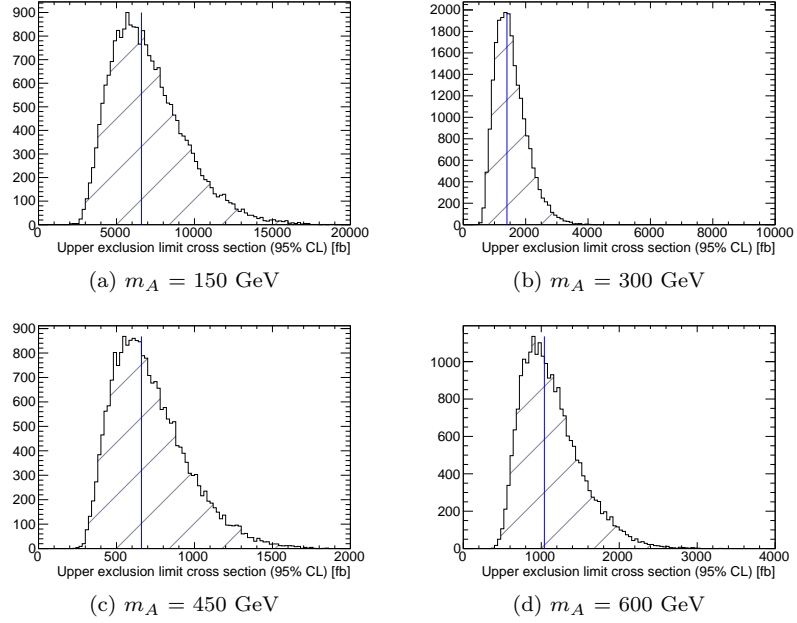


Figure 5.27: Upper exclusion limit cross section distributions for neutral MSSM Higgs bosons with no morphing for 1 fb^{-1} at $\sqrt{s} = 14 \text{ TeV}$.

m_A [GeV]	Morphing [pb]					No morphing [pb]				
	-2σ	-1σ	median	$+1\sigma$	$+2\sigma$	-2σ	-1σ	median	$+1\sigma$	$+2\sigma$
150	3.80	5.60	6.60	7.80	11.40	3.80	5.60	6.60	7.80	11.40
300	0.80	1.20	1.40	1.70	2.50	0.80	1.20	1.40	1.70	2.40
450	0.42	0.62	0.72	0.86	1.26	0.40	0.56	0.66	0.78	1.16
600	0.64	0.96	1.12	1.32	1.96	0.60	0.88	1.04	1.24	1.84

Table 5.11: Expected upper exclusion limit results for 1 fb^{-1} at $\sqrt{s} = 14 \text{ TeV}$.

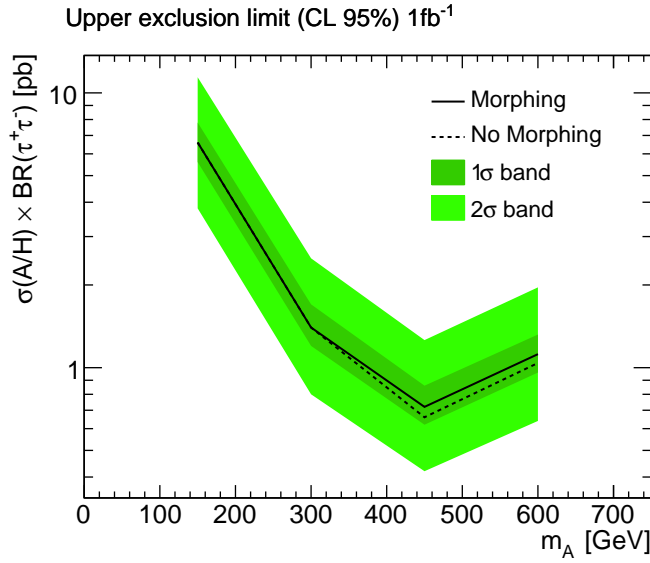


Figure 5.28: Expected upper exclusion limits cross section at 95% CL for neutral MSSM Higgs bosons decaying to tau pairs with and without morphing technique. for 1 fb^{-1} . Shaded areas are the $\pm 1\sigma$ and $\pm 2\sigma$ bands on the expected limit.

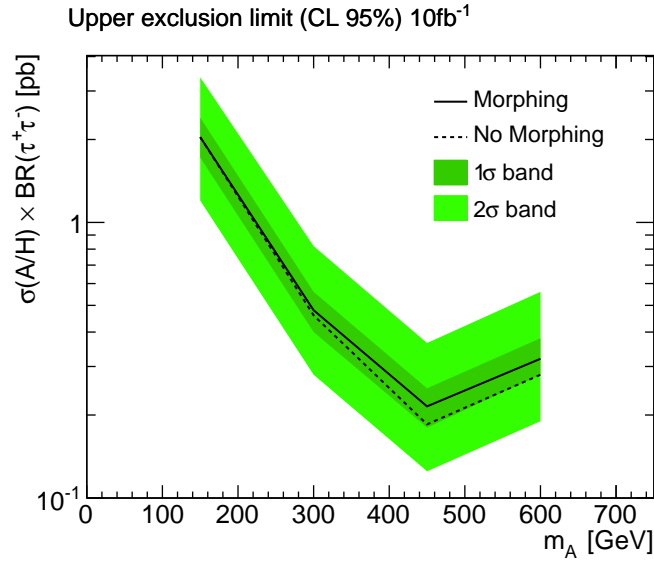
We present the same results for an integrated luminosity of 10 and 30 fb^{-1} which are listed in Tables 5.12 and 5.13. The expected upper exclusion limits for different values of m_A at 95% CL are shown in Figures 5.29 and 5.30 along with the $\pm 1\sigma$ and $\pm 2\sigma$ probability bands. Note this analysis is not addressed for these luminosities, where other event selection cuts would be foreseen such as b-tagging. However, the results provided improve the 1 fb^{-1} results as expected, and set an initial benchmark for ATLAS.

The interpretation of the limits in terms of the excluded region in the $(m_A, \tan\beta)$ plane for the three luminosities considered is shown in Figure 5.31 for the m_h -max scenario. This sets very promising expected results for the LHC.

m_A [GeV]	Morphing [pb]					No morphing [pb]				
	-2σ	-1σ	median	$+1\sigma$	$+2\sigma$	-2σ	-1σ	median	$+1\sigma$	$+2\sigma$
150	1.20	1.72	2.04	2.40	3.36	1.20	1.76	2.04	2.40	3.40
300	0.28	0.40	0.48	0.56	0.82	0.28	0.40	0.46	0.54	0.80
450	0.12	0.18	0.21	0.25	0.36	0.10	0.15	0.18	0.21	0.32
600	0.19	0.28	0.32	0.38	0.56	0.16	0.24	0.28	0.33	0.49

Table 5.12: Expected upper exclusion limit results for 10 fb^{-1} at $\sqrt{s} = 14 \text{ TeV}$.

m_A [GeV]	Morphing [pb]					No morphing [pb]				
	-2σ	-1σ	median	$+1\sigma$	$+2\sigma$	-2σ	-1σ	median	$+1\sigma$	$+2\sigma$
150	0.68	1.00	1.16	1.40	2.04	0.68	1.00	1.16	1.36	2.04
300	0.16	0.22	0.26	0.32	0.46	0.14	0.22	0.26	0.32	0.46
450	0.07	0.10	0.12	0.14	0.21	0.06	0.09	0.10	0.12	0.17
600	0.10	0.15	0.18	0.21	0.31	0.09	0.13	0.15	0.18	0.27

Table 5.13: Expected upper exclusion limit results for 30 fb^{-1} at $\sqrt{s} = 14 \text{ TeV}$.Figure 5.29: Expected upper exclusion limits cross section at 95% CL for neutral MSSM Higgs bosons decaying to tau pairs with and without morphing technique for 10 fb^{-1} . Shaded areas are the $\pm 1\sigma$ and $\pm 2\sigma$ bands on the expected limit.

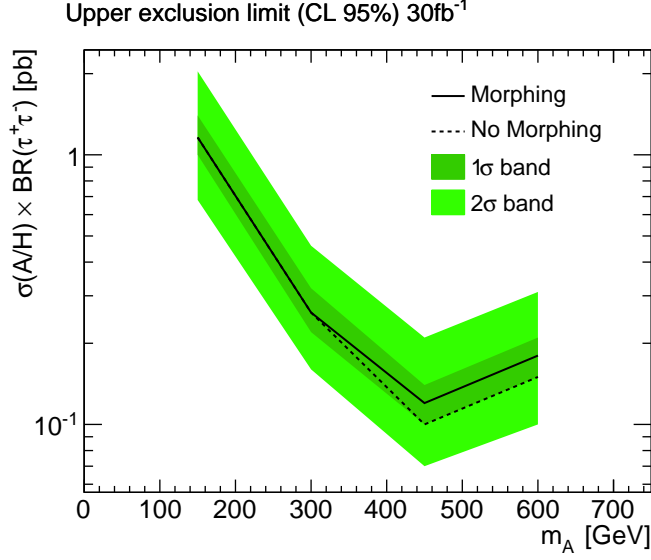


Figure 5.30: Expected upper exclusion limits cross section at 95% CL for neutral MSSM Higgs bosons decaying to tau pairs with and without morphing technique. for 30fb^{-1} . Shaded areas are the $\pm 1\sigma$ and $\pm 2\sigma$ bands on the expected limit.

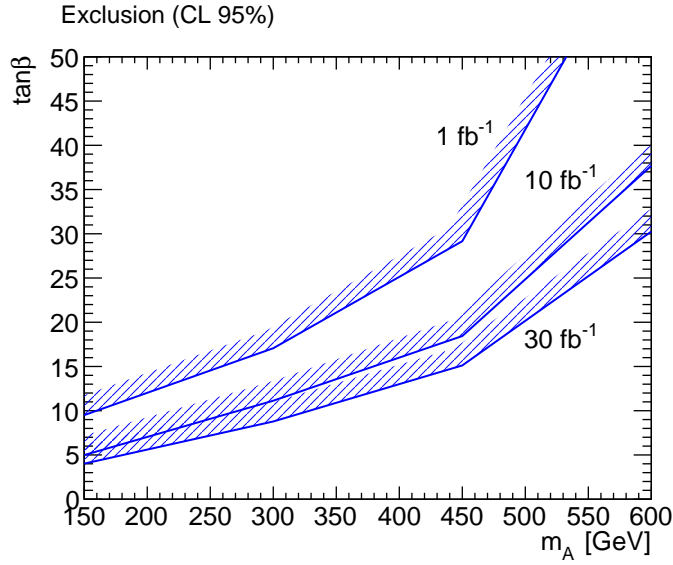


Figure 5.31: Expected exclusion region in the $(m_A, \tan\beta)$ plane at 95% CL for neutral MSSM Higgs bosons decaying to tau pairs for 1, 10 and 30fb^{-1} in the m_h -max scenario.

Limit Coverage

Frequentist confidence intervals [91] are constructed so as to include the true value of the parameter with a probability greater than or equal to a specified level, called the coverage probability. In other words, the coverage is the fraction of times that an interval constructed according to a given prescription from the data would contain the parameters value after many repetitions of the experiment.

In order to test the upper limit set by the Bayesian technique presented here, we generate S+B pseudo-experiments with a known contribution of the signal. This is done by adding the signal distribution to the B pseudo-experiment with a known cross-section. For a conservative limit we expect less than 5% of the S+B pseudo-experiment limits to lie below the true value of the cross-section for the signal. Figure 5.32 shows the limit distribution for 10^4 S+B pseudo-experiments with $m_A=300$ GeV and $\tan\beta=15$. Less than 1% of the events lie below the signal cross section for both methods. Hence the technique can be recalled as conservative.

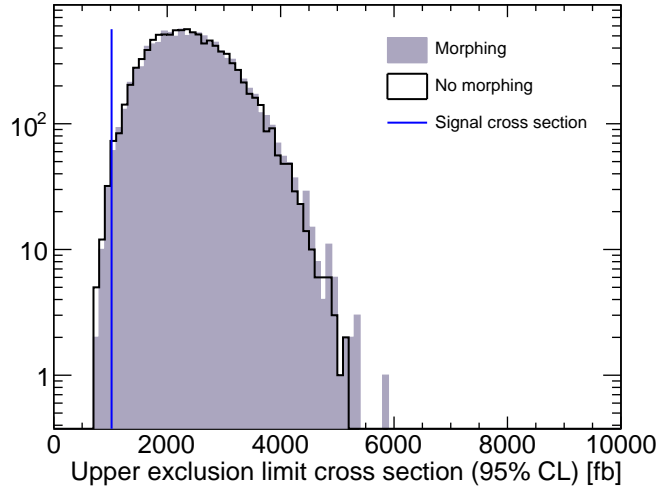


Figure 5.32: Cross section distributions with and without morphing at 95% for 10^4 S+B pseudo-experiments.

5.6.2 Expected Discovery Significance

The evaluation of the expected discovery significance is performed over the a wide $\tan\beta$ range for each value of m_A , in order to cover as much of the MSSM parameter space as possible.

Figure 5.33 shows the expected significance values at 95% CL for the discovery of neutral MSSM Higgs bosons based on 10^5 pseudo-experiments for different values of m_A and $\tan\beta$ computed with and without template morphing for 1 fb^{-1} . A Higgs boson with $m_A = 150 \text{ GeV}$ would be $5\text{-}\sigma$ significant already at $\tan\beta=15$, which makes this value of m_A a very promising scenario already for 1 fb^{-1} . Higher values of m_A are only significant at high $\tan\beta$ values. This is obviously caused by the smaller cross section as a function of m_A . The contribution of the morphing technique decreases the significance of the discovery as expected, due to the incorporation of more systematic uncertainties.

Similar results obtained for 10 and 30 fb^{-1} are shown in Figures 5.34 and 5.35 respectively. Previous results from studies conducted in the same channel for ATLAS fast simulation at 14 TeV [92] are shown in Figure 5.36 as $5\text{-}\sigma$ significance curves in the $\tan\beta$ vs m_A plane for 30 fb^{-1} . These results are compatible with the ones presented here at 30 fb^{-1} except for those at $m_A = 600 \text{ GeV}$, where our technique provides less sensitivity.

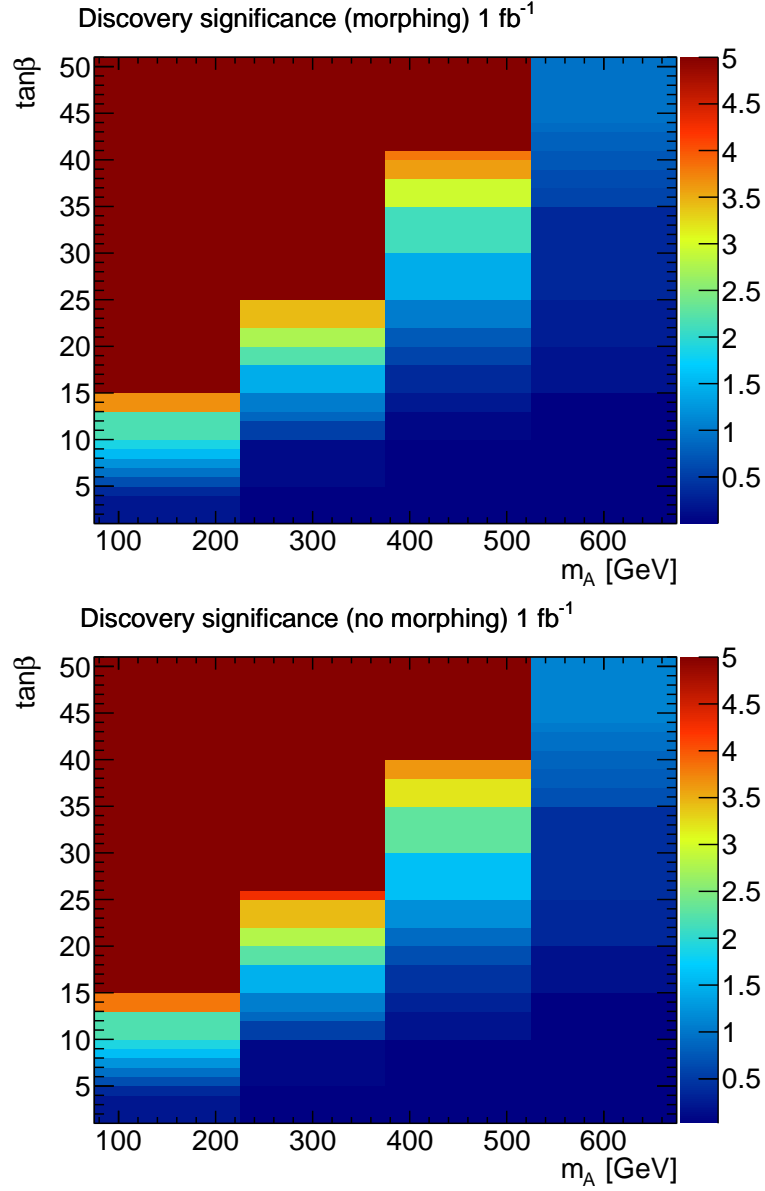


Figure 5.33: Expected significance values as a function of $\tan\beta$ and m_A for neutral MSSM Higgs bosons decaying into tau pairs with (top) and without (bottom) morphing technique for 1 fb⁻¹.

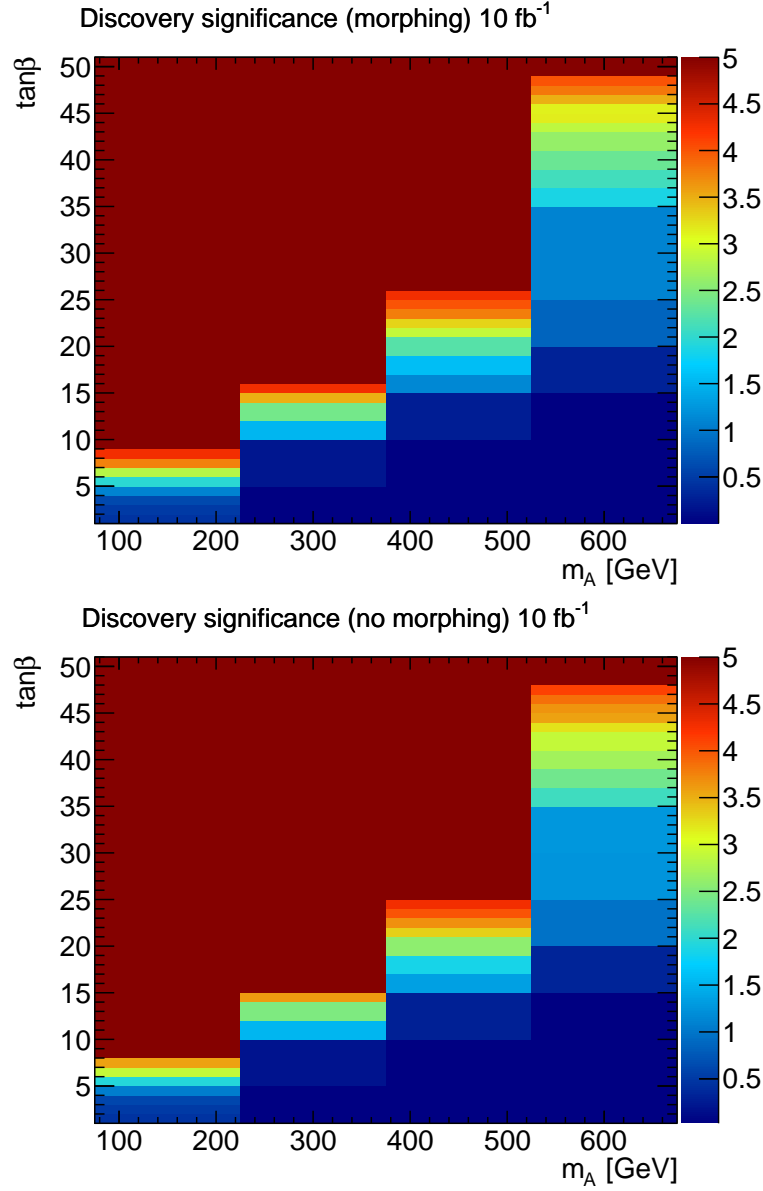


Figure 5.34: Expected significance values as a function of $\tan\beta$ and m_A for neutral MSSM Higgs bosons decaying into tau pairs with (top) and without (bottom) morphing technique for 10 fb^{-1} .

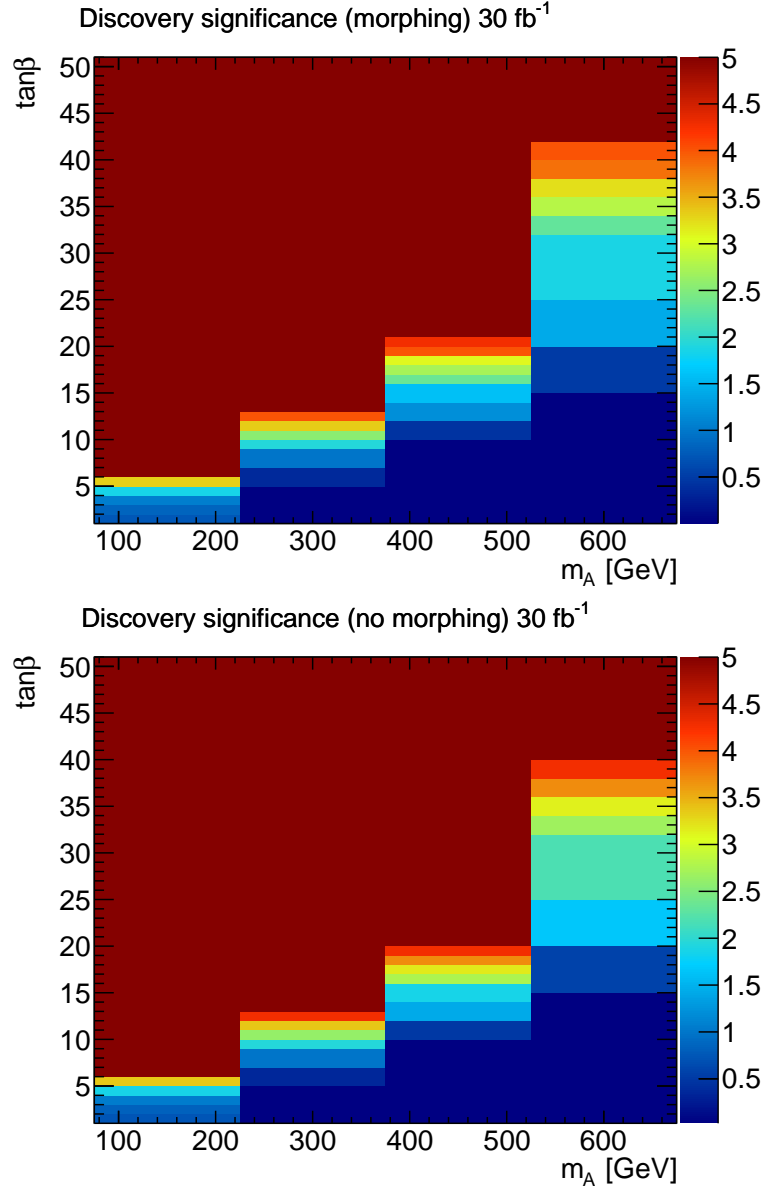


Figure 5.35: Expected significance values as a function of $\tan\beta$ and m_A for neutral MSSM Higgs bosons decaying into tau pairs with (top) and without (bottom) morphing technique for 30 fb^{-1} .

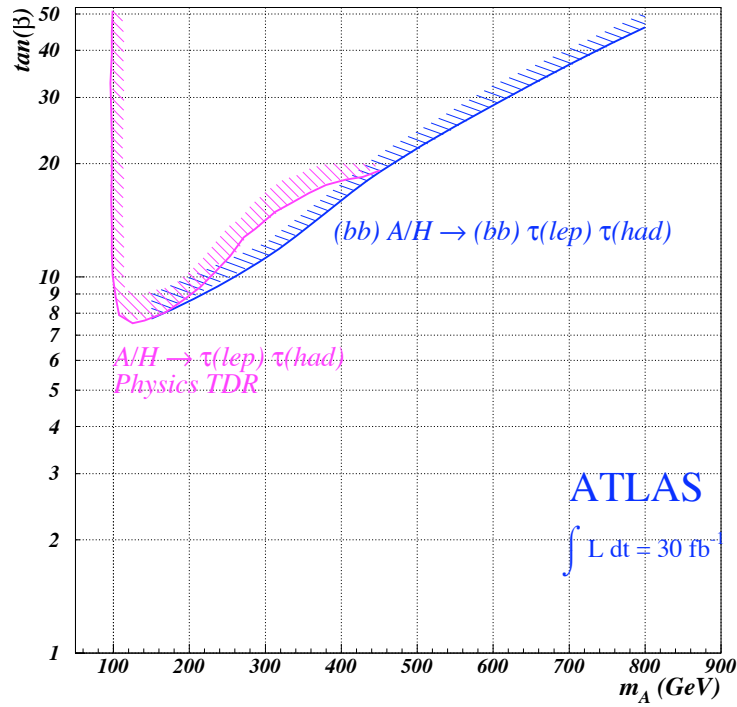


Figure 5.36: Contour plot for expected 5- σ discovery as a function of $\tan \beta$ and m_A for MSSM Higgs bosons decaying into tau pairs for 30 fb^{-1} [92].

5.7 Outlook

This Chapter is devoted to the search of neutral MSSM Higgs bosons decaying into tau pairs following the event selection criteria in [69], plus a cut on the transverse mass plane for the lepton + E_T^{miss} versus the hadron + E_T^{miss} .

The main background contribution comes from the Z boson production decaying to tau pairs, which mimics the signal process, and the W +jets production which remains of the same order of magnitude as the Z background after the event selection. Concerning the other background sources considered, $t\bar{t}$ production is significantly reduced by the event selection, and QCD di-jet background is neglected due to the high E_T^{miss} cut. Several Higgs masses are considered in a wide range from 150 to 600 GeV.

An alternative statistical method already used in CDF has been adopted to set upper exclusion limits to the Higgs cross section, and establish the significance of a potential discovery. Results have been obtained for a target luminosity of 1 fb^{-1} , and also for 10 and 30 fb^{-1} . These are promising already at 1 fb^{-1} for $m_A = 150\text{--}450 \text{ GeV}$, for which 95% CL exclusion limits and $5\text{-}\sigma$ discovery significances can be achieved for rather low $\tan\beta$ value. Discovery significance results obtained for 30 fb^{-1} are in agreement with recent published results [70], [92].

This analysis could be improved by the incorporation of QCD di-jet background, and proper handling of the signal distribution scaling. However, this analysis sets a guideline for the incorporation of other systematic uncertainties, such as trigger efficiencies or fake tau identification rates. Finally, the results prove that this method is worth considering for the analysis of the first ATLAS data.

Chapter 6

Conclusions

This Thesis is divided into two parts, the implementation of the ROD Crate DAQ software for the ATLAS Tile Calorimeter and a search for neutral MSSM Higgs Bosons decaying into tau pairs.

The ROD Crate DAQ for the ATLAS Tile Calorimeter has been implemented, on one hand, making use of sophisticated software techniques, and on the other hand, constantly testing and adequating its performance in a real data taking scenario since 2007. Enhanced DVS measurements provide fast and comprehensive diagnostics of the read-out, monitoring at all levels are implemented to assess the quality of the data, and the stopless recovery mechanism improves data taking efficiency which maximizes the physics output of the LHC luminosity.

The performance of the online signal reconstruction of the Tile Calorimeter is evaluated in terms of energy and time reconstruction. These show an excellent degree of agreement with the results of the signal reconstruction performed offline. Tile Calorimeter time calibration is evaluated in terms of a jet based signal selection criteria. Collision data from 2010 show time calibration in a very good shape for physics and below the Tile Calorimeter required precision. In conclusion, the ROD Crate DAQ for the Tile Calorimeter is ready to run at 75 kHz Level 1 Trigger rate.

The second part of the Thesis addresses the expected exclusion limit and discovery significance potential of neutral MSSM Higgs bosons decaying to tau

pairs, where one tau decays hadronically and the other one decays leptonically. The target for this analysis is to be applied on the first two years of data from the LHC, where the visible mass is used as observable as opposed to the invariant mass in order to gain sensitivity for the analysis.

This analysis incorporates an innovative statistical method in ATLAS (already used in CDF), which is based on the bayesian interpretation of probability, and provides a convenient way to incorporate systematic uncertainties on known parameters. Two types of uncertainties are considered, the first takes into account normalization errors, and the second takes into account shape variation errors due to energy scale uncertainties. In both cases, gaussian probability distributions are chosen to describe the (prior) probability on the (nuisance) parameters. A profiling technique is used to obtain the posterior probability on the parameter of interest, where the likelihood times the prior is maximized with respect to the nuisance parameters through an iterative procedure. Also a template morphing technique has been implemented to incorporate the effect of energy scale uncertainties on the observable distributions.

Monte Carlo simulation studies have been conducted at $\sqrt{s}=14$ TeV in the MSSM m_h -max scenario for 1, 10 and 30 fb^{-1} following ATLAS event selection criteria recommendations. Expected exclusion limits and discovery significances determined with this method are very promising in the low to moderate m_A region already for 1 fb^{-1} . Results are compatible with other searches that use a different approach and show that this method should be further pursuit with real data.

The statistical method presented in this Thesis has been validated in the ATLAS statistics forum and the results from the simulation studies have been presented in the ATLAS Higgs working group, where it was agreed that this method should be further explored.

Chapter 7

Resumen

7.1 El CERN, el LHC y el Experimento ATLAS

7.1.1 El CERN

El CERN, acrónimo de *Conseil Européen pour la Recherche Nucléaire*, es un laboratorio europeo de física de partículas situado entre la frontera Franco-Suiza, en el cantón suizo de Ginebra. El CERN fundado en 1954, está formado por 20 estados miembros, pero otros países también participan en el CERN. Numerosos descubrimientos han tenido lugar en el CERN, como el descubrimiento de los bosones W^\pm y Z .

7.1.2 El LHC

El LHC, acrónimo de *Large Hadron Collider*, es el acelerador de partículas más grande del mundo, donde dos haces de partículas collisionan frente a frente en el corazón de unos experimentos. El LHC está construido en antiguo túnel de LEP, de 27 km de largo, que estuvo operativo desde 1989 hasta 2000. Ha sido diseñado para alcanzar energías en centro de masas de 14 TeV y una luminosidad de $10^{34} \text{ cm}^{-2} \text{ s}^{-1}$ con una colisión cada 25 ns. Hay un total de siete experimentos construidos alrededor del anillo: ATLAS [2], CMS [3], LHCb [4], ALICE [5], TOTEM [6], LHCf [7], MoEDAL [8].

7.1.3 El Experimento ATLAS

El experimento ATLAS (A Toroidal LHC Apparatus) es un detector multi-propósito diseñado para explotar todo el potencial del LHC. Mide 45 m de largo y de 25 m de alto, y pesa más de 7000 toneladas. Está dividido en sub-detectores y construido con tecnologías altamente sofisticadas y materiales especializados. Tras un intenso periodo de puesta a punto, el experimento está actualmente operativo y se están llevando a cabo los primeros análisis de física.

El sistema de imanes está optimizado para desviar las trayectorias de las partículas cargadas minimizando los efectos de dispersión múltiple. El sistema magnético está compuesto de un solenoide central para el detector interno, con un campo axial de 2 T, un toroide de barril y dos toroides de tapa que generan un campo magnético tangencial de 0.5 T y 1 T respectivamente.

El sistema de muones cubre el rango $|\eta| < 3$, y hacer un uso eficiente del poder de separación de los imanes. Consta de cuatro sub-detectores en función de las necesidades de resolución espacial y temporal: MDT, CSC, RPC y TGC.

El detector interno está diseñado para reconstruir trazas y vertices primarios de desintegración con alta eficiencia. Consta de tres subdetectores: Pixels, SCT y TRT.

El sistema de calorímetros mide la posición y energía depositada por los chorros de partículas (jets), en el rango $|\eta| < 4.9$, utilizando una amplia variedad de técnicas. Un calorímetro electromagnético (EM) cubre la región $|\eta| < 3.2$, un calorímetro hadrónico de tejas (TileCal) cubre el rango $|\eta| < 1.7$, dos tapas hadrónicas (HEC) cubren el rango $1.4 < |\eta| < 3.2$, y dos calorímetros electromagnéticos y hadrónicos muy proyectivos (FCAL) cubren el rango $3.2 < |\eta| < 4.8$.

7.1.4 The Sistema de Trigger y Adquisición de Datos

El sistema de Trigger y adquisición de datos (TDAQ) de ATLAS [1] está dividido en dos partes altamente relacionadas: El sistema de Trigger y el sistema de adquisición de datos (DAQ). El sistema de Trigger selecciona eventos en tres niveles diferentes de la adquisición de datos: Nivel 1, Nivel 2 y *Event Filter*. Esta estrategia permite al Trigger de ATLAS seleccionar eventos interesantes del gran fondo de eventos de QCD producidos por el LHC. Siendo capaz de reducir la frecuencia de eventos desde 10^9 Hz hasta 10^2 Hz.

El Nivel 1 de Trigger está basado en electrónica hecha a medida, mientras que el Nivel 2 y el *Event Filter* están implementadas utilizando componentes informáticos de consumo. El DAQ es responsable del flujo de datos desde el detector hasta el Nivel 2 y desde éste hasta el *Event Filter*.

7.2 El ROD Crate DAQ del TileCal

Las partículas producidas en el punto de interacción atraviesan el TileCal produciendo luz mientras depositan su energía. La luz se torna azul mediante fibras que varían la longitud de onda y se guía hacia tubos fotomultiplicadores (PMTs). Los PMTs generan una señal analógica que tras un proceso de amplificación y modelado del pulso, se suman en grupos de cinco. Las sumas analógicas se envían al Nivel 1 de Trigger mediante señales analógicas diferenciales. Los pulsos analógicos también son recibidos en los *digitizers* donde la señal se convierte a muestras digitales cada 25 ns que finalmente se almacenan en las DMUs (*Data Management Units*). El CTP (Procesador Central de Trigger) del Nivel 1 procesa la información de Trigger y selecciona los eventos que merece la pena analizar con una frecuencia media de 75 kHz. El CTP envía una petición a la electrónica de *front-end* mediante una señal de L1A (*Level 1 Accept*) que se transmite utilizando el sistema de TTC (*Trigger Timing and Control*).

La electrónica de *back-end* del detector está separada en cuatro replicas independientes, cada una de ellas con su propia *crate* de TTC y lectura de datos, recibe las señales de TTC del CTP via el LTP (*Local Trigger Processor*) y las distribuye al *front-end* mediante fibras ópticas. Las señales dentro de los *super-drawers* se distribuyen hasta las DMUs, que a la recepción de un L1A, envían las muestras digitales a la *interface board*, que construye un fragmento de datos que contiene las muestras digitales de todos los PMTs de un *super-drawer* y los transfiere a la electrónica de *back-end* mediante fibras ópticas.

La frecuencia del flujo de datos se regula automáticamente mediante el feedback de *busy* que se genera en la lectura de datos y se combina en el módulo RODBusy y se transfiere al CTP via el LTP. Éste mecanismo introduce tiempo muerto durante el cual el CTP no puede solicitar nuevos eventos.

El ROD

El ROD (*Read-Out Driver*) es el elemento central de la electrónica de *back-end*. Tiene un diseño específico para cada sub-detector pero tiene un interfaz común con el ROS (*Read-Out System*) mediante el protocolo S-Link. Las funciones del ROD son: lectura de datos del *front-end*, cálculo de la energía, tiempo y factor de calidad, empaquetado y transmisión de los datos, recepción de señales de TTC y comparación de valores con los contenidos en los datos, generación de *busy* cuando el buffer del ROD está medio lleno, monitorización de cantidades sencillas sobre todos los datos recibidos.

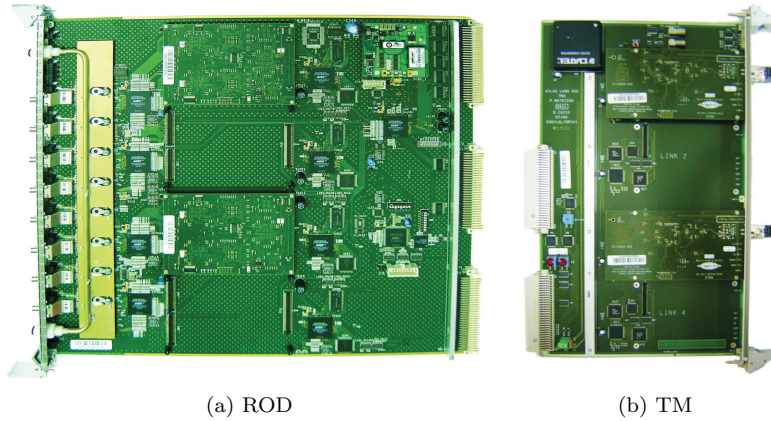


Figure 7.1: Imagen del ROD y el TM del TileCal.

El ROD está equipado con dos unidades de procesamiento (PUs) con dos DSPs cada una, para la reconstrucción de la señal. El TM (*Transition Module*) se conecta por detrás de cada ROD y proporciona dos ROLs (*Read-Out Links*) con el ROS. Una imagen del ROD y el TM se muestran en la Figura 7.1.

El algoritmo de Filtrado Óptimo (OF) reconstruye la amplitud, la fase y el factor de calidad de la señal mediante una combinación lineal de las muestras digitales utilizando unos pesos calculados a partir del método de multiplicadores de Lagrange [24]. La energía depositada en el detector es proporcional a la amplitud reconstruida y se calcula mediante constantes de calibración por PMT. Los pesos y las constantes de calibración se almacenan en la base de datos de condiciones [26].

7.2.1 El software online de TileCal

El ROD Crate DAQ

El ROD Crate DAQ (RCD) es el software para el control de la electrónica de *back-end* hecha a medida del detector. Está basado en un núcleo multihilos [29] que carga plug-ins específicos en tiempo de ejecución para adaptar su comportamiento a las necesidades de la adquisición de datos. Existen diferentes plug-ins para diferentes propósitos: Configuración, Trigger, Módulo y Salida.

El plug-in de configuración específico de TileCal es el TileConfig que se usa para obtener la configuración de los *super-drawers*. El resto de configuración se obtiene utilizando un plug-in de configuración genérico. Los plug-ins de trigger son el TileTTCprTriggerIn, que hace uso del hardware específico TTCpr [13], y el TileTBMTriggerIn que hace uso del TBM [14]. Los plug-ins de módulo son el TileDigiTTCModule, TileVMEReadoutModule, TileCal_RODModule, TileOfc-ShameModule, TileShaftModule y el TileLaserModule. No hay un plug-in de salida específico de TileCal.

La base de datos de configuración que utiliza el paradigma de objetos para almacenar la información, guarda la configuración del RCD utilizando las clases específicas del TileCal.

Stopless Recovery

El *Stopless Recovery* es el mecanismo de deshabilitación y reconfiguración de un elemento de la toma de datos sin necesidad de detener la mismo. La necesidad de detener la toma de datos para reconfigurar parte del sistema fue uno de los principales problemas durante 2008, e introdujo una considerable pérdida de tiempo de toma de datos. El TileCal tiene implementado el *Stopless Recovery* con granularidad de un ROL, lo que representa 4 *super-drawers* consecutivos en (η, ϕ) que cubre un rango $\Delta\eta \times \Delta\phi = 0.7 \times 0.4$. El registro de la actividad del *Stopless Recovery* se efectúa en la base de datos de condiciones. Si un ROL se pone en *busy*, el RCD deshabilita el hardware problemático. El hardware se puede resincronizar mediante un comando al RCD. La electrónica de *front-end* también se puede reconfigurar en el supuesto evento de que se pierda la configuración por un corte del suministro eléctrico.

Los tests de DVS

Los tests de DVS (*Detector Verification System*) son una parte importante del software online. Existen tests de DVS de gran precisión para el TileCal. En estos tests, los datos se leen por VME y se almacenan en la memoria. Los datos se decodifican y analizan y los resultados se devuelven al usuario. Los tipos de tests disponibles son los siguientes: funcionalidad del ROD, respuesta del *front-end* a la inyección de una carga conocida, medida del ruido electrónico en el *front-end*, estrés del sistema de lectura de datos, y comprobación del estado de la memoria de las DMUs del *front-end*.

Comunicación DAQ/DCS

El DCS (*Detector Control System*) es la parte del TDAQ responsable del control de los sub-detectores y la infraestructura compartida del CERN y el LHC (refrigeración, suministro eléctrico, etc). El intercambio de información entre DAQ y DCS proporciona mejor entendimiento de ambos sistemas mirando solo a uno de ellos. Por ejemplo, el estado del suministro eléctrico a los super-drawers controlado por DCS es relevante para el proceso de lectura de datos controlado por DAQ [31].

7.2.2 Operación del TileCal

El LHC ha comenzado a operar en 2010 a $\sqrt{s} = 7$ TeV. La Figura 7.2 muestra la luminosidad integrada medida en ATLAS en función del tiempo para los primeros meses de 2010. Durante este tiempo, el TileCal ha estado integrado en ATLAS, y ha proporcionado datos con 100% de calidad, tal y como muestra la Tabla 7.1.

Tiempos de transición

Uno de los factores que afectan directamente la eficiencia de toma de datos es el tiempo dedicado para realizar una transición de estados. La estructura de árbol para el control del run está organizada en sub-detectores para simplificar la tarea de incluir o excluir a los mismos de la toma de datos. El TileCal es uno de los sub-detectores más rápidos en el cambio de estados tal y como se

Periodo	Pixel	SCT	TRT	LAr	Tile	MDT	RPC	TGC	CSC
a	80.9	86.2	100	99.0	100	87.4	88.6	84.4	
b	88.8	92.8	100	100	100	94.0	94.6	92.2	
c	97.5	98.3	100	92.2	100	97.1	98.4	98.2	98.4
d	91.9	98.2	100	91.9	100	97.8	97.9	97.4	97.8
e	95.0	99.6	100	96.6	100	99.6	99.6	97.7	100

Table 7.1: Fracción relativa del tiempo de funcionamiento del detector y calidad de los datos pesada por la luminosidad durante los periodos de toma de datos con haz de 2009 y 2010. a) Haces estables 2009, b) Hasta 12/12/2009, c) 30/03/2010 - 17/05/10 d) 18/05/2010 - 27/05/2010 e) Desde 01/06/2010 (preliminar).

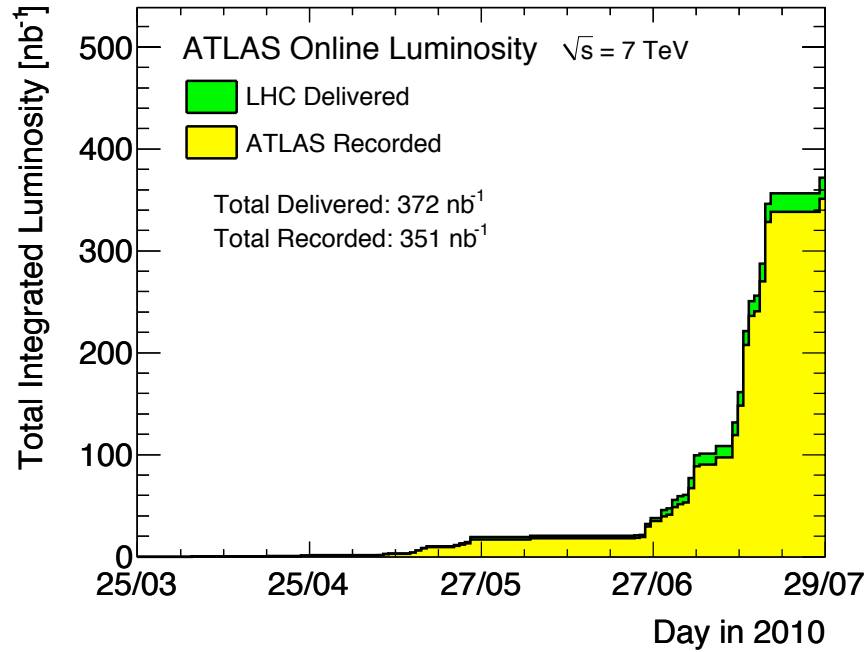


Figure 7.2: Luminosidad integrada medida en ATLAS en función del tiempo.

muestra en la Figura 7.3. El TileCal y LAr son los más lentos en la transición “prepare-for-run”. Esto es debido a que ambos acceden a la base de datos de configuraciones para obtener los pesos para la reconstrucción de la señal.

7.2.3 Calidad de los Datos Online

La infraestructura de monitorización o *monitoring* online de ATLAS llamada GNAM, permite la monitorización de datos en todos los niveles de la adquisición de datos. Todos los niveles de *monitoring* implementados en TileCal resumidos

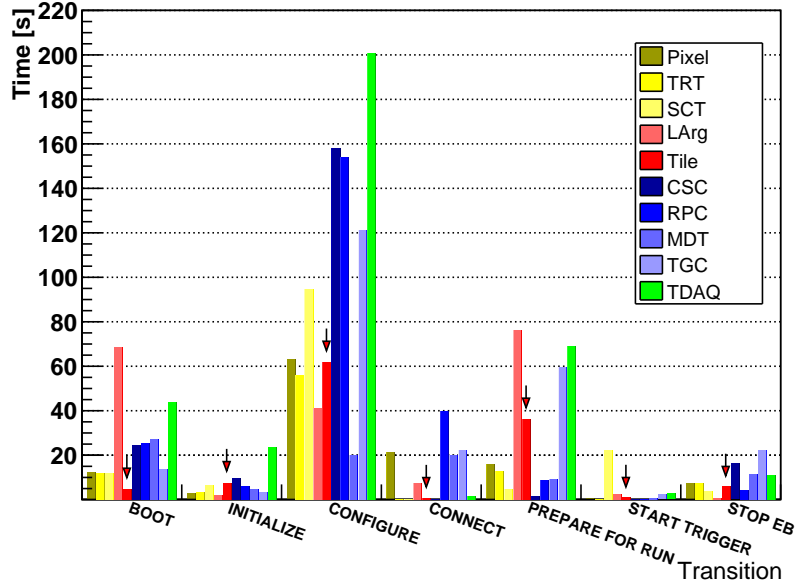


Figure 7.3: Media de los tiempos de transición por detector para las transiciones más importantes. Las flechas indican el TileCal.

en la Figura 7.4.

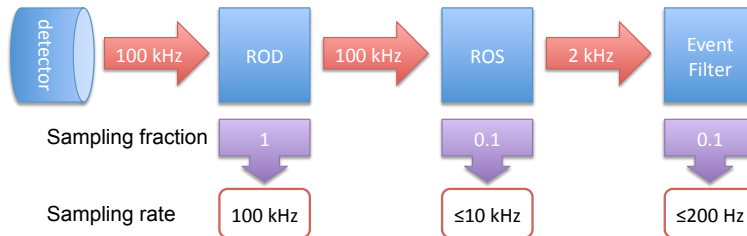


Figure 7.4: Resumen de los diferentes niveles de monitorización y frecuencias de muestreo.

Monitoring a nivel del ROD

El *monitoring* a nivel del ROD es una monitorización a nivel del hardware que muestrea cada uno de los eventos del Nivel 1 de Trigger. Existen dos tipos de resultados, contadores simples e histogramas. Los contadores proporcionan el estado de los registros del ROD y los histogramas información sobre el proceso de reconstrucción que tiene lugar en la DSP.

El RITMO (*ROD Information for Tile Monitoring*) es una selección de con-

tadores de la DSP que proporcionan información sobre el proceso de lectura de los datos.

Monitoring a nivel del ROS

El *monitoring* a nivel del ROS tiene por objetivo comprobar el estado de los *super-drawers* mediante histogramas con información por PMT, *super-drawer* y errores digitales.

Monitoring a nivel del Event Filter

El *monitoring* a nivel del *Event Filter* es un proceso complejo que tiene lugar sobre toda la información de un evento para lo que se emplea el software offline de ATLAS para el análisis de los datos. Es posible reconstruir la señal de nuevo con el OF y compararla con la reconstrucción que ha tenido lugar en la DSP. La Figura 7.5 muestra la diferencia del tiempo reconstruido online y offline por el *monitoring* del *Event Filter* para las cuatro particiones del TileCal para datos de colisiones a $\sqrt{s} = 7$ TeV. Las líneas rojas indican el margen de error máximo para que el test sea positivo. Por lo general, las magnitudes reconstruidas online y offline son iguales salvo errores de precisión.

7.3 Rendimiento de la Reconstrucción de la Señal

7.3.1 Filtrado Óptimo Online y Offline

El Filtrado Óptimo (OF) online está implementado en las DSPs del ROD utilizando una aritmética de coma fija. Las magnitudes de computan utilizando una lógica de 32-bit y luego se empaquetan de acuerdo con el formato de datos de TileCal. La energía se calcula en unidades de ADC y luego se escala por una constante de calibración que también tiene una precisión dada. La precisión de la energía es función de la precisión de la escala y el número de bits disponibles para empaquetar el resultado. La reconstrucción del tiempo está limitada por el valor de un bit, que corresponde con 0.0625 ns, y cubre un rango de -64 ns a 64 ns. Si el valor excede los límites, se devuelve el valor saturado.

El OF utilizado offline es el llamado OF iterativo, donde la fase de la señal se obtiene mediante la ejecución iterativa del algoritmo hasta tres veces. El

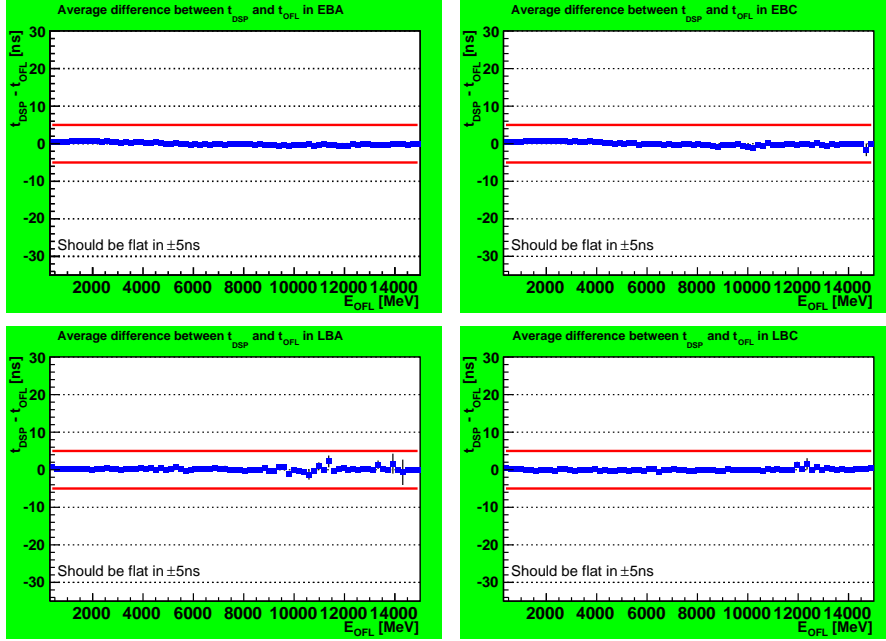


Figure 7.5: Diferencia de tiempo reconstruido entre online y offline en las cuatro particiones del TileCal para datos de colisiones a $\sqrt{s} = 7$ TeV.

tiempo calculado en la iteración previa se utiliza como tiempo esperado de la siguiente para seleccionar los pesos correspondientes, empezando de un tiempo esperado igual a cero. El OF iterativo se ha utilizado durante el periodo de *commissioning* del detector [32] con excelentes resultados. Una versión del OF iterativo se puede ejecutar en la DSP con menor precisión [33].

7.3.2 Estrategia Computacional

Existen diferentes formatos de datos para ATLAS: Raw, ESD, AOD y DPD. Para el presente análisis se hace uso de ESDs, seleccionando sucesos del Nivel 1 de Trigger con señales depositadas en los calorímetros. Los datos se analizan en el Grid y se obtienen archivos de resultados en formato ROOT [35].

Seleccionamos datos de colisiones de 2010 con $\sqrt{s} = 7$ TeV. Para seleccionar eventos del punto de interacción se establece un corte de tiempo por evento. Se exige que la diferencia absoluta menor de 10 ns entre la media de tiempos del lado A y C de las celdas de MBTS (*Minimum Bias Trigger Scintillator*). Además se requiere que el tiempo absoluto de cada lado sea menor de 10 ns.

7.3.3 Calibración del Tiempo

El objetivo de la calibración del tiempo es obtener un tiempo reconstruido por la DSP igual a cero. Para ello se pueden ajustar el tiempo del hardware en pasos gruesos de 25 ns y pasos finos de 104 ps, que se almacenan en la base datos de configuraciones. El residuo que no se puede ajustar, medido con precisión, se almacena en la base de datos de condiciones y supone el tiempo esperado de la señal.

Presentamos un procedimiento para obtener la calibración del tiempo a partir de datos de colisiones utilizando el tiempo reconstruido offline. La Figura 7.6 muestra las distribuciones de tiempo reconstruido online y offline para un datos de colisiones a $\sqrt{s} = 7$ TeV, donde se han suprimido los canales con energía inferior a 300 MeV. Ambas distribuciones son muy parecidas. El máximo de tiempo reconstruido por la DSP es 65 ns, como era de esperar. La diferencia abrupta en 25 ns es consecuencia de la imprecisión de la DSP por no hacer iteraciones.

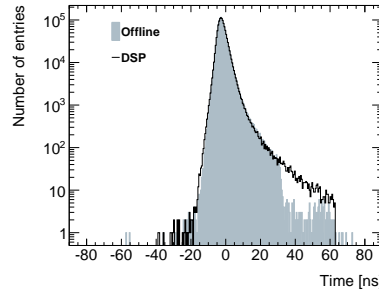


Figure 7.6: Distribución de tiempos por PMT reconstruidos mediante el algoritmo de OF online sin iteraciones (DSP) y OF offline con iteraciones (Offline) para datos de colisiones a $\sqrt{s} = 7$ TeV.

Las celdas del TileCal se leen por ambos lados mediante un PMT. La energía de la celda es la suma de la energía depositada en ambos PMTs y el tiempo de celda la media del tiempo de los mismos.

$$E_{cell} = E_{PMT1} + E_{PMT2}$$

$$T_{cell} = \frac{T_{PMT1} + T_{PMT2}}{2}$$

El uso de jets, reconstruidos a partir de trazas por evento utilizando el algoritmo anti- k_t [36] (algoritmo por defecto en ATLAS), proporciona la ventaja de la proyección desde el punto de interacción. El tiempo del jet es la media ponderada por el cuadrado de la energía del tiempo de las celdas que componen el jet.

$$T_{jet} = \frac{\sum_{cells}^{jet} T_{cell} E_{cell}^2}{\sum_{cells}^{jet} E_{cell}^2}$$

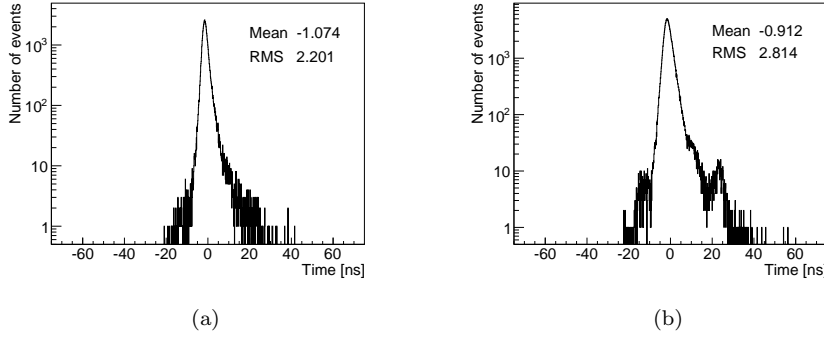


Figure 7.7: (a) Distribución del tiempo del jet para celdas del TileCal y (b) distribución del tiempo de las celdas dentro de un jet para sucesos de *stream* de L1Calo para datos de colisiones a $\sqrt{s} = 7$ TeV.

La distribución del tiempo de los jets para celdas de TileCal dentro de cada jet se muestra en la Figura 7.7(a). La notación T_{OFF-I} y E_{OFF-I} denotan el tiempo y la energía reconstruidas offline con OF iterativo. La mayoría de las celdas contribuyen al pico central. Un abultamiento se observa en -12.5 ns y un pequeño pico en 25 ns claramente indica que algunas celdas están fuera de tiempo, para las cuales el tiempo esperado de la señal debería volverse a calcular. En cualquier caso, el tiempo medio de los jets está dentro de la resolución temporal requerida para TileCal. La Figura 7.7(b) muestra la distribución del tiempo de las celdas que están contenidas dentro de un jet. En este caso, las celdas que están fuera de tiempo son más fáciles de identificar. Uno de los resultados más relevantes de este apartado el desarrollo de una técnica que permite la identificación de señales fuera de tiempo.

7.3.4 Rendimiento de la Reconstrucción de la Señal

Evaluación del Algoritmo Sin Iteraciones

La Figura 7.8 muestra la diferencia relativa de energía entre OF online sin iteraciones (E_{DSP}) y OF offline sin iteraciones (E_{OFF-NI}) en función de E_{OFF-NI} para ambas ganancias. La Figura 7.9 muestra la diferencia relativa de tiempo entre online (T_{DSP}) y offline (T_{OFF-NI}) en función de E_{OFF-NI} para ambas ganancias. Se han utilizado datos de colisiones con selección de eventos mencionada antes y un corte de 500 MeV por celda para eliminar el ruido.

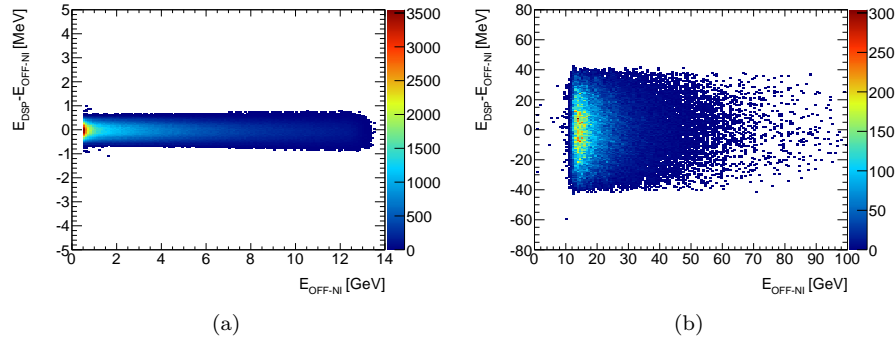


Figure 7.8: Diferencia relativa de energía online y offline reconstruida por el algoritmo de OF sin iteraciones en función de la energía offline para alta (a) y baja (b) ganancia para datos de colisiones a $\sqrt{s} = 7$ TeV.

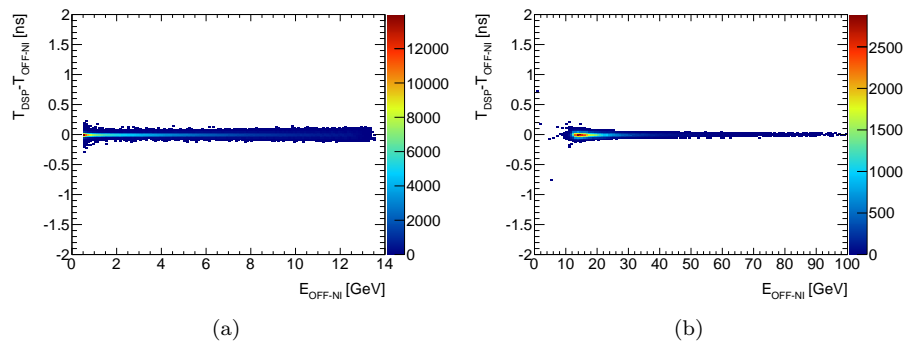


Figure 7.9: Diferencia relativa de tiempo online y offline reconstruida por el algoritmo de OF sin iteraciones en función de la energía offline para alta (a) y baja (b) ganancia para datos de colisiones a $\sqrt{s} = 7$ TeV.

Ambos resultados muestran que la implementación en la DSP del OF sin iteraciones es compatible con la implementación offline. La máxima diferencia

en la energía debida a la precisión es 1 MeV en alta ganancia y 40 MeV en baja ganancia, que está por debajo del corte de ruido de 500 MeV. La máxima diferencia en el tiempo debida a la precisión es inferior a 0.5 ns, por debajo de la resolución esperada de TileCal.

Rendimiento del Método No Iterativo

El rendimiento del método no iterativo se evalúa con la correlación entre el tiempo offline en función del online como se muestra en la Figura 7.10(a). La reconstrucción está correlacionada para fases entre ± 10 ns. La energía reconstruida por la DSP está afectada por la diferencia entre el tiempo de la señal esperado y recibido. La diferencia se puede parametrizar parabólicamente para fases entre ± 10 ns como se muestra en la Figura 7.10(b).

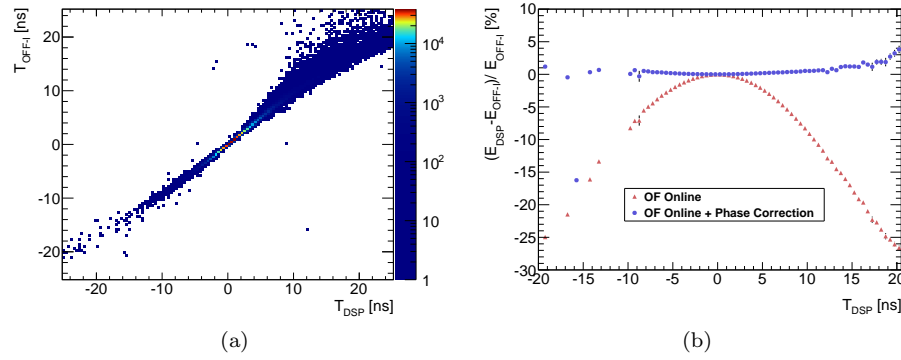


Figure 7.10: (a) Tiempo reconstruido offline en función de online y (b) desviación de la energía reconstruida online en función de la diferencia de tiempo para datos de colisiones a $\sqrt{s} = 7$ TeV.

La corrección parabólica mejora la reconstrucción de la DSP, tal y como se muestra en la Figura 7.11. Esta afecta sobretodo a señales de baja energía, de donde se infiere que las señales energéticas están calibradas en tiempo.

7.4 Motivación Teórica

7.4.1 El Modelo Estándar

El Modelo Estándar de las partículas elementales y sus interacciones, es la teoría cuántica de campos mas precisa que unifica tres de las cuatro fuerzas de la naturaleza, electromagnética, nuclear fuerte y nuclear débil, en una sola. Describe

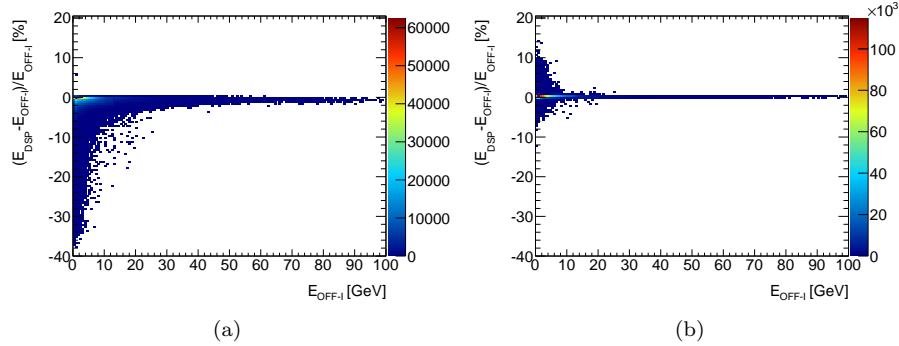


Figure 7.11: Diferencia relativa en la reconstrucción de la energía online en función de la energía offline sin (a) y con (b) corrección parabólica para datos de colisiones a $\sqrt{s} = 7$ TeV data

la interacción de fermiones puntuales de spin $\frac{1}{2}$ que obedecen el principio de exclusión de Pauli mediante bosones intermediarios de spin 1. Los fermiones se clasifican entre los que sienten la interacción fuerte, los quarks, y los que no, los leptones.

Existen seis leptones agrupados en tres generaciones (con las mismas propiedades salvo la masa): el electrón (e), el muón (μ) y el tau (τ), con la misma carga eléctrica igual a la del electrón, y sus compañeros neutros, el neutrino electrónico (ν_e), el neutrino muónico (ν_μ) y el neutrino tauónico (ν_τ). Los quarks también están agrupados en dobletes como los leptones, sus nombres son *up* y *down* (u, d), *charm* y *strange* (c, s) y *top* y *bottom* (t, b). Tienen carga eléctrica fraccionaria con respecto a la del electrón, $+\frac{2}{3}$ para los quarks de tipo *up* (u, c, t) y $-\frac{1}{3}$ para los quarks de tipo *down* (d, s, b). Los quarks también tienen carga de color, lo que hace que estén perpetuamente unidos unos a otros en partículas neutras de color conocidas como hadrones. Las tres generaciones de quarks están mezcladas. Es decir, los autoestados de masa no se corresponden a los autoestados de interacción. Esta mezcla está parametrizada por la matriz de Cabibbo-Kobayashi-Maskawa (CKM). Los bosones surgen como una manifestación del grupo de simetría de la teoría, siendo este $SU(3) \times SU(2) \times U(1)$ para el Modelo Estándar, tras la aplicación de una invariancia gauge local a los campos fermionicos.

La Electrodinámica Cuántica (QED) describe la interacción de las partículas

cargadas en términos del grupo de simetría $U(1)$ dando lugar a los fotones intermediarios. La Cromodinámica Cuántica (QCD) describe la interacción de las partículas con carga de color (los quarks) en términos del grupo de simetría $SU(3)$ dando lugar a 8 gluones intermediarios. La interacción Electrodébil (EW) describe la interacción de leptones cargados en términos del grupo de simetría $SU(2) \times U(1)$ dando lugar a cuatro bosones intermediarios. Estos representan a las partículas W^\pm , Z^0 y el fotón sin masa.

El Bosón de Higgs

La simetría del Lagrangiano de la interacción Electrodébil se rompe espontáneamente con la introducción de un nuevo campo escalar, llamado el bosón de Higgs (postulado), cuyo estado más bajo de energía no es simétrico bajo transformaciones. El campo de Higgs toma un valor esperado distinto de cero, y proporciona terminos de masa para todos los fermiones y bosones intermediarios, salvo el fotón. En consecuencia, la simetría que ya no está patente en el Lagrangiano, se dice que está oculta por la elección del valor esperado del campo de Higgs. Las secciones eficaces de producción del bosón de Higgs en el Modelo Estándar para colisiones pp a $\sqrt{s} = 14$ TeV se conocen a *next-to-next-to-leading order* (NNLO) para $gg \rightarrow H + X$ y *next-to-leading order* (NLO) para $t\bar{t}H$.

A pesar de los éxitos del Modelo Estándar, no es una teoría elegante. Un mínimo de 19 parámetros se necesitan por la teoría que no pueden ser medidos directamente por los experimentos, entre ellos las masas de los quarks y leptones, parámetros de mezcla de la matriz CKM y constantes de acoplamiento. Por ello, existe un creciente interés en explorar otros modelos debido a sus limitaciones.

7.4.2 El Modelo MSSM

La supersimetría (SUSY) [57] [58] es una simetría que transforma bosones en fermiones y viceversa, mediante operadores de spin $\frac{1}{2}$ y de la cual no hay evidencia experimental todavía. Sin embargo, es la única teoría actual que ofrece un mecanismo para la incorporación de la gravedad y una explicación a las divergencias que afectan a la masa del Higgs en el Modelo Estándar. Modelos supersimétricos postulan la existencia de partículas supersimétricas para todas las partículas conocidas del Modelo Estándar: squarks y sleptones son bosones

supersimétricos de los fermiones del Modelo Estándar y gluinos y gauginos son fermiones supersimétricos de los bosones del Modelo Estándar.

El MSSM (*Minimal Supersymmetric extension of the Standard Model*) [60] es la extensión supersimétrica más simple del Modelo Estándar. En ella el sector de Higgs está formado por dos dobletes (H_u y H_d), que generan masa para los quarks y leptones de tipo *up* y *down*, que dan lugar a cinco estados físicos: dos Higgs cargados (H^\pm), un pseudoescalar neutro (A), y dos escalares neutros (H y h). Los parámetros fundamentales del MSSM son la masa del pseudoescalar neutro (m_A) y la tangente de la relación de valores esperados entre los dos campos de Higgs ($\tan\beta$).

Estudios en búsqueda de bosones de Higgs neutros en el modelo MSSM, han tenido lugar en LEP y Tevatron [63,64], Las perspectivas de descubrimiento del bosón de Higgs MSSM están resumidas en [66], donde uno de los canales más prometedores es $H/A \rightarrow \tau^+\tau^-$ que es el objeto del presente estudio.

7.5 Búsqueda de Bosones de Higgs MSSM decayendo a pares de Taus

7.5.1 Introducción

Este análisis tiene por objetivo la búsqueda de bosones de Higgs MSSM neutros decayendo a pares de taus, y finalmente a pares leptón-hadrón, que ha sido objeto de análisis similares en Tevatron [67]. La constante de acoplamiento del Higgs a fermiones de tipo *down* como el quark b y el lepton tau están favorecidos un factor $\tan\beta$ relativo al Modelo Estándar. El presente análisis explora la viabilidad de un potencial descubrimiento con 1 fb^{-1} , para lo cual se ha llevado a cabo con simulaciones para el escenario $m_h - \text{max}$ de MSSM a $\sqrt{s}=14\text{ TeV}$.

Producción de Bosones de Higgs MSSM

La Figura 7.12 muestra los diagramas de Feynman de los principales procesos de producción de bosones de Higgs MSSM neutros en el LHC.

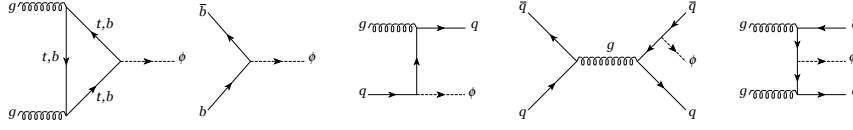


Figure 7.12: Diagramas de Feynman para la producción de bosones de Higgs MSSM neutros (A, h, H).

7.5.2 Datos de Monte Carlo

En este análisis se hace uso de datos simulados con Monte Carlo a $\sqrt{s} = 14$ TeV, haciendo uso del software offline de ATLAS [76].

Los datos se señalan han sido generados con PYTHIA [77], utilizando el proceso $gg, q\bar{q} \rightarrow b\bar{b}h$. Los fondos considerados en este análisis son : $Z/\gamma \rightarrow \tau^+\tau^-$, $t\bar{t} \rightarrow bW^\pm \rightarrow \tau^\pm\nu$ y $W \rightarrow \ell\nu$. El fondo de QCD no se considera.

7.5.3 Selección de Eventos

A continuación se detalla el criterio de selección de eventos.

- Se requiere un candidato de leptón, con $p_T > 25$ GeV para electrones y $p_T > 20$ GeV para muones y se lleva a cabo una preselección de sucesos con leptones.
- Se requiere un candidato a tau (hadrónico) utilizando un criterio de preselección basado en las variables de la reconstrucción.
- Se requiere un corte en $E_T^{miss} > 30$ GeV para eliminar el fondo de QCD.
- Se requieren cargas opuestas entre el candidato a electrón/muón y el candidato a tau.
- Se requiere un corte en el momento transversal del tau (hadrónico), $p_T^\tau > 30$ GeV, para eliminar falsos positivos en la reconstrucción de taus.
- Se requiere un corte en el número de jets por suceso menor a dos para eliminar el fondo de $t\bar{t}$.
- Finalmente se requiere un corte de anticorrelación en el plano de masa transversal del leptón más E_T^{miss} en función del hadrón más E_T^{miss} , para eliminar el fondo de W +jets. Donde se define la masa transversal como:

$$M_T^2 = 2E_{T1}E_{T2}(1 - \cos\Delta\phi_{12}))$$

7.5. BÚSQUEDA DE BOSONES DE HIGGS MSSM DECAYENDO A PARES DE TAUS

Las Tablas 7.2 and 7.3 muestran la contribución de cada set de datos en fb después de cada corte para señal y fondo.

Cut [fb]	A150	A300	A450	A600
Total	67041	1020	269	176
Lepton ID	34745	489	142	95
Tau ID	8684	122	31	18
$MET > 20GeV$	4181	89	26	16
Charge=0	4121	85	25	15
$E_T^\tau > 40GeV$	3227	77	23	15
$\#jets < 2$	2880	67	20	12
M_T cut	2389	48	13	8

Table 7.2: Número de eventos después de cada corte en seña.

Cut [fb]	$t\bar{t}$	$Wq \rightarrow e\nu$	$Wq \rightarrow \mu\nu$	$Wq \rightarrow \tau\nu$	$Z \rightarrow \tau\tau$
Total	461000	12420856	12416754	1374170	451440
Lepton ID	233573	7188633	8097155	485075	66622
Tau ID	6284	19493	21876	2203	8633
$MET > 20GeV$	5696	15755	18159	1630	2817
Charge=0	4514	11576	12794	1203	2518
$E_T^\tau > 40GeV$	3025	7143	7623	870	1227
$\#jets < 2$	817	6646	6922	790	984
M_T cut	67	383	371	208	663

Table 7.3: Número de eventos después de cada corte en fondos.

Distribuciones de Masa Visible

Utilizamos la masa visible como nuestro observable, definida como:

$$M_{vis} = |P_\ell^\alpha + P_h^\alpha + P_{Miss}^\alpha|$$

donde:

$$P_{Miss}^\alpha = \{p_{xMiss}, p_{yMiss}, 0, \sqrt{p_{xMiss}^2 + p_{yMiss}^2}\}$$

Las distribuciones obtenidas de masa visible M_{vis} , se muestran en la Figura 7.13, como una superposición de distribuciones de los procesos que contribuyen al fondo y la señal normalizada a $\tan\beta = 15$, para diferentes masas del Higgs.

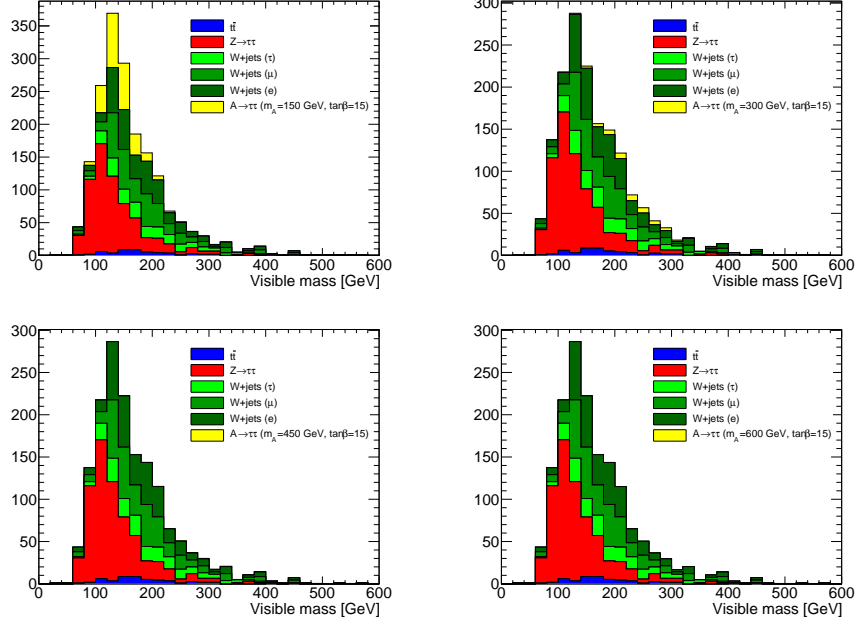


Figure 7.13: Distribuciones típicas de M_{vis} para señal y fondo para $\tan\beta = 15$ para diferentes valores de m_A .

Datos Pseudo-experimentales

Datos pseudo-experimentales generados a partir de las distribuciones M_{vis} son utilizados para evaluar los resultados esperados. Estos son una fluctuación de poisson del número esperado de cuentas en cada bin. Un ejemplo de un pseudo-experimento se muestra en la Figura 7.14, representado como un punto en cada bin.

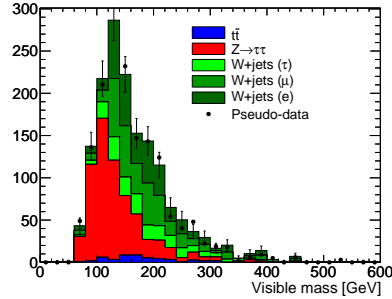


Figure 7.14: Datos pseudo-experimentales generados a partir de las distribuciones de M_{vis} que contribuyen al fondo.

7.5.4 Análisis Estadístico

Según el teorema de Bayes, la probabilidad condicional de una hipótesis dados los datos, es proporcional a la verosimilitud (likelihood) de los datos cuando la hipótesis es correcta por la probabilidad a priori de que la hipótesis sea correcta.

$$\mathcal{P}(\theta, \nu|x) = \frac{\mathcal{L}(\theta, \nu|x) \pi(\theta, \nu)}{\pi(x)} \quad (7.1)$$

donde x representa a los datos, (θ, ν) los parámetros de la hipótesis, $\mathcal{L}(\theta, \nu|x)$ la función likelihood y $\pi(\theta, \nu)$ la probabilidad a priori (el prior) de los parámetros.

En lo siguiente asumiremos que el prior es factorizable en un producto de priores:

$$\pi(\theta, \nu) = \pi(\theta) \times \pi(\nu)$$

Consideramos que el prior de nuestro parámetro de interés, θ , es no-informativo y no favorece ningún valor en particular del parámetro.

$$\pi(\theta) = \text{constant}; \theta \in [0, \Lambda_{\text{cutoff}}]$$

Y que el prior de los parámetros sin interés (nuisance) se parametriza como una función de probabilidad gaussiana, con un valor medio y una desviación estándar conocidas.

$$\pi(\nu) = G(\nu, \hat{\nu}, \varepsilon(\nu)) = \frac{1}{\sqrt{2\pi\varepsilon(\nu)^2}} \exp\left(-\frac{(\nu - \hat{\nu})^2}{2\varepsilon(\nu)^2}\right)$$

Profiling

Una función likelihood convencionalmente aceptada es la función de poisson. Consideramos un likelihood binado:

$$\mathcal{L}(\theta, \nu|x) = \prod_{ij} \frac{\mu_{ij}^{x_{ij}} \exp(-\mu_{ij})}{x_{ij}!}$$

donde los datos x_{ij} corresponden al número de eventos observados en el bin i para el canal j (donde $j = 1$ corresponde al canal eh y $j = 2$ al canal μh), μ_{ij} es el número de eventos esperados en el bin correspondiente, que podemos expresar de forma general en función de la luminosidad (L), la sección eficaz del

proceso (σ) y la eficiencia por bin y canal (ϵ_{ij}):

$$\mu_{ij} = s_{ij} + \sum_k b_{kij} = L\sigma_s \epsilon_{ij} + \sum_k L\sigma_k \epsilon_{kij}$$

El método convencional para obtener el posterior es integrando en la ecuación (7.1) sobre todo el espacio de parámetros (marginalización). En este caso proponemos maximizar la ecuación (7.1) en función de los parámetros. Este método se llama *profiling*.

$$\mathcal{P}(\theta|x) = \mathcal{C} \mathcal{L}(\theta, \nu_{MLE}|x) \pi(\nu_{MLE})$$

donde \mathcal{C} es un parámetro de normalización.

Template Morphing

Los errores sistemáticos en la escala de energía se tratan con el método de *template morphing* [86] utilizada anteriormente en CDF. La matriz de eficiencias teniendo en cuenta multiples errores sistemáticos en la escala de energía viene dada por:

$$\epsilon'_{ij} = \epsilon_{ij} + \sum_m f_m \frac{\epsilon_{ij}^{m+} - \epsilon_{ij}^{m-}}{2}$$

donde ϵ_{ij}^{m+} y ϵ_{ij}^{m-} corresponden a nuestro observable teniendo en cuenta una corrección de valor $+1\alpha$ and -1α en la escala de energía, ϵ_{ij} es el valor nominal y f_m es parámetro de *morphing* que controla la variación en la escala de energía m .

Límites de Exclusión

Establecemos un límite de exclusión, σ^{UEL} , integrando el posterior [87] en el parámetro de interés hasta la probabilidad deseada con un nivel de confianza (CL) $1 - \alpha$. Para ello normalizamos el posterior arbitrariamente al valor del posterior para valor cero del parámetro de interés:

$$1 - \alpha = \int_0^{\theta^{UEL}} \frac{\mathcal{P}(\theta|x)}{\mathcal{P}(0|x)} d\theta = \int_0^{\theta^{UEL}} \frac{\mathcal{L}(\theta, \nu_{MLE}|x) \pi(\nu_{MLE})}{\mathcal{L}(0, \nu_{MLE}|x) \pi(\nu_{MLE})} d\theta$$

Significancia de Discovery

Para establecer la significancia de descubrimiento, hacemos uso del *Bayes factor* [89], definido como la razón entre la razón de posteriores y la razón de priores para dos hipótesis alternativas:

$$B_{10} = \frac{\mathcal{L}(\theta_1, \nu_1^{MLE}|x) \pi(\nu_1^{MLE})}{\mathcal{L}(\theta_0, \nu_0^{MLE}|x) \pi(\nu_0^{MLE})}$$

Definimos el p -value [90] de observar B_{10} para datos con señal (B_{10}^{S+B}), como una fluctuación de B_{10} para datos sin señal (B_{10}^B):

$$p = \int_{B_{10}^{S+B}}^{\infty} f(B_{10}^B) dB_{10}^B$$

La significancia se obtiene del p -value a partir de la *inverse of the cumulative distribution*:

$$Z = \Phi^{-1}(1 - p)$$

7.5.5 Resultados

Resultados esperados para la exclusión y significancia de descubrimiento para la producción de bosones de Higgs MSSM neutros se han obtenido para datos simulados a $\sqrt{s} = 14$ TeV. Se han considerado diferentes $m_A = (150, 300, 450, 600)$ GeV, con valores diferentes de $\tan\beta$. Se han considerado errores sistemáticos de normalización y escala de energía.

Sensibilidad Esperada para Límites de Exclusión

Resultados esperados para el límite de la sección eficaz para la exclusión para diferentes masas del bosón de Higgs al 95% CL para 1, 10 y 30 fb⁻¹ se muestran en las Figura 7.15. Éste análisis no está optimizado luminosidades superiores a 1 fb⁻¹, donde vemos que el valor del límite de exclusión disminuye en función de la luminosidad tal y como se espera. La interpretación de estos límites en el espacio de parámetros se puede ver en la Figura 7.16 para 1, 10 y 30 fb⁻¹. Estos resultados establecen una primer punto de referencia para ATLAS.

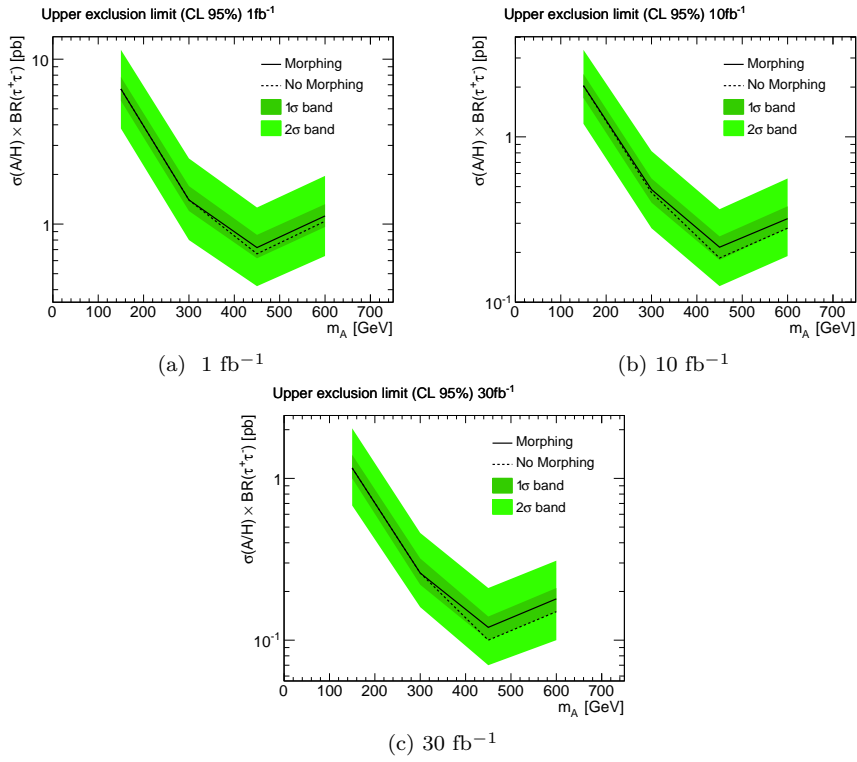


Figure 7.15: Límite de exclusión esperado al 95% CL de la sección eficaz de producción de bosones de Higgs MSSM neutros decayendo a pares de taus con y sin la técnica de morphing para 1, 10 y 30 fb⁻¹.

7.5. BÚSQUEDA DE BOSONES DE HIGGS MSSM DECAYENDO A PARES DE TAUS

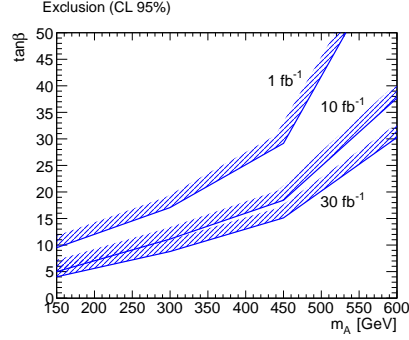


Figure 7.16: Región de exclusión esperada al 95% CL en el espacio de parámetros $(m_A, \tan \beta)$ para la producción de bosones de Higgs MSSM neutros decayendo a pares de taus para 1, 10 y 30 fb^{-1} .

Significancia Esperada de Descubrimiento

Resultados esperados para la significancia de descubrimiento para diferentes masas del bosón de Higgs al 95% CL para 1, 10 y 30 fb^{-1} se muestran en las Figuras 7.17, 7.18 y 7.19. Éste análisis no está optimizado luminosidades superiores a 1 fb^{-1} , donde vemos que el valor de $\tan \beta$ para el que la significancia es 5- σ , disminuye con la luminosidad tal y como se espera. Estos resultados establecen una primer punto de referencia para ATLAS.

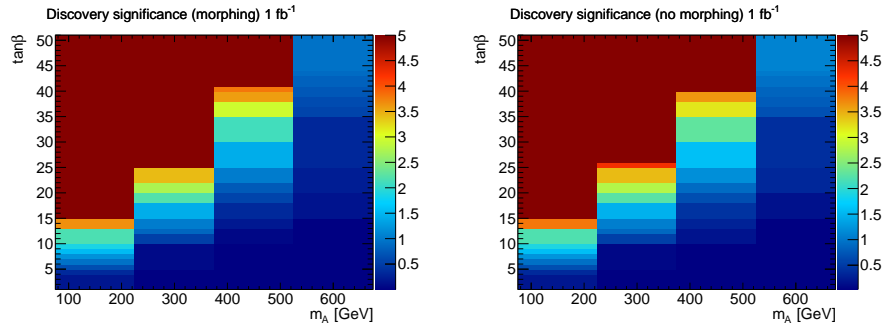


Figure 7.17: Significancia esperada de descubrimiento de bosones de Higgs MSSM neutros decayendo a pares de taus en función de $\tan \beta$ y m_A , con y sin la técnica de morphing para 1 fb^{-1} .

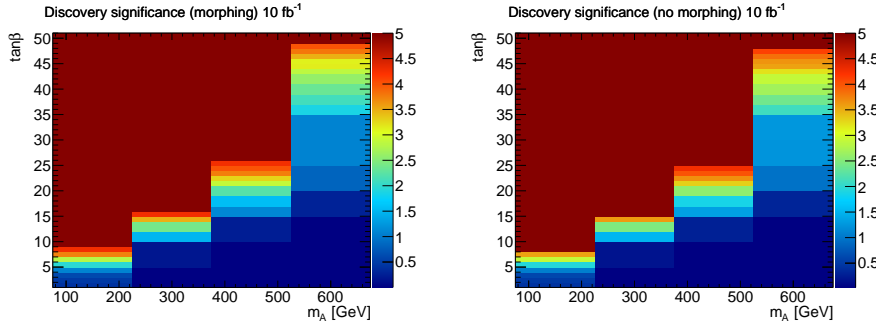


Figure 7.18: Significancia esperada de descubrimiento de bosones de Higgs MSSM neutros decayendo a pares de taus en función de $\tan\beta$ y m_A , con y sin la técnica de morphing para 10 fb^{-1} .

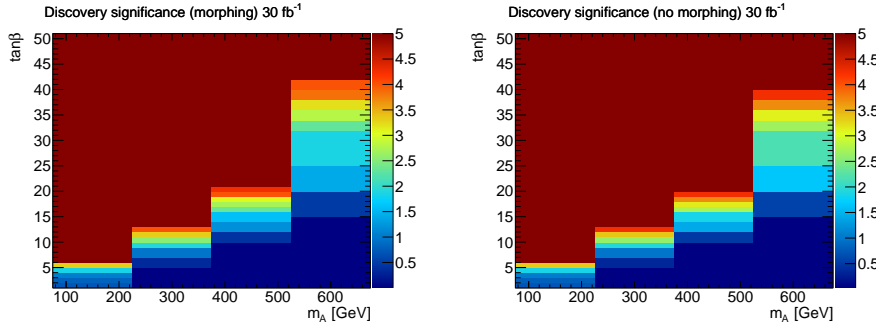


Figure 7.19: Significancia esperada de descubrimiento de bosones de Higgs MSSM neutros decayendo a pares de taus en función de $\tan\beta$ y m_A , con y sin la técnica de morphing para 30 fb^{-1} .

7.6 Conclusiones

Esta tesis está dividida en dos partes, la implementación del software del ROD Crate DAQ para el TileCal y una búsqueda de bosones de Higgs MSSM neutros decayendo a pares de taus.

El ROD Crate DAQ para el TileCal ha sido implementado, por un lado, haciendo uso de sofisticadas técnicas de software, y por el otro lado, comprobando y adecuando constantemente su rendimiento en un entorno de toma de datos real desde 2007. Los tests DVS proporcionan un diagnóstico rápido y en detalle del sistema de lectura de datos, *monitoring* a todos los niveles permiten evaluar la calidad de los datos, y el mecanismo de *stopless recovery* mejora la eficiencia de toma de datos maximizando la producción de física del LHC.

El rendimiento de la reconstrucción online de la señal del TileCal se evalua

en terminos de reconstrucción de energía y tiempo. Estos muestran un grado de acuerdo excelente con los resultados de la reconstrucción offline. La calibración del tiempo del TileCal se evalúa mediante un criterio de selección de señales basado en jets. Datos de colisiones de 2010 indican que la calibración del tiempo está lista para la física del LHC y por debajo de la resolución temporal requerida para TileCal.

La segunda parte de la Tesis evalúa el límite esperado de exclusión y potencial significancia de descubrimiento de bosones de Higgs MSSM neutros decayendo a pares de taus, donde un tau decae leptónicamente y el otro decae hadrónicamente. El objetivo de este análisis es ser aplicado sobre los dos primeros años de datos de LHC, donde la masa visible se emplea como observable en lugar de la masa invariante para ganar sensibilidad en el análisis.

Este análisis incorpora un método estadístico innovador en ATLAS, basado en la interpretación bayesiana de la probabilidad, y proporciona una manera conveniente de incorporar errores sistemáticos en los parámetros. Dos tipos de errores se consideran, el primero tiene en cuenta errores de normalización, y el segundo tiene en cuenta errores de variación de la forma debido a la imprecisión en la escala de energía. En ambos casos, distribuciones de probabilidad gaussiana se asumen en los parámetros. Una técnica de *profiling* se emplea para obtener la probabilidad posterior en el parámetro de interés, donde se maximiza la función de verosimilitud multiplicada por el prior de los parámetros en función de los parámetros mediante un procedimiento iterativo. Una técnica de *template morphing* se ha implementado para incorporar el efecto de la incertidumbre en la escala de energía en las distribuciones del observable.

Estudios de simulación de Monte Carlo se han realizado a $\sqrt{s}=14$ TeV en el escenario m_h -max del MSSM para 1, 10 and 30 fb^{-1} siguiendo los criterios de selección de eventos recomendados por ATLAS. Límites esperados de exclusión y significancias de descubrimiento calculadas con este método son muy prometedoras para valores bajos o medios de m_A para 1 fb^{-1} . Los resultados son compatibles con los obtenidos con otros métodos y muestras que este método debería ser considerado con datos reales.

El método estadístico presentado en esta Tesis ha sido validado en el fórum de estadística de ATLAS y los resultados de los estudios de simulación presentados

en una reunión del grupo de Higgs de ATLAS donde se acordó que este método debería seguir siendo explorado.

List of ATLAS and Tile Calorimeter Acronyms

ADC	Analogue to Digital Converter.
ATLAS	A Toroidal LHC AparatuS.
AOD	Analysis Object Data.
BCID	Bunch Crossing IDentifier.
CERN	Centre Europeen pour la Recherche Nucleaire.
CIS	Charge Injection System.
CMT	Configuration Management Tool.
CPU	Central Processing Unit.
CTP	Central Trigger Processor.
COOL	LCG Conditions Database Project.
CRC	Cyclic Redundancy Check.
DAC	Digital to Analog Converter.
DAL	Data Access Library.
DAQ	Data AcQuisition.
DCS	Detector Control System.
DDC	DCS DAQ Communication.
DVS	Detector Verification System.
DSP	Digital Signal Processor.
DPD	Derived Physics Data.
EB	Event Builder.
EBA	Extended Barrel A side.
EBC	Extended Barrel C side.

LIST OF ACRONYMS

EF	Event Filter.
ESD	Event Summary Data.
FEB	Front End Board.
FIFO	First In First Out.
FPGA	Field Programmable Gate Array.
FSM	Finite State Machine.
L1A	Level 1 trigger Accept.
LBA	Long Barrel A side.
LBC	Long Barrel C side.
LHC	Large Hadron Collider.
LTP	Local Trigger Processor.
LTPI	Local Trigger Processor Interface.
MSSM	Minimal Supersymmetric extension of the Standard Model.
OC	Output Controller.
OF	Optimal Filtering.
OFC	Optimal Filtering Constants.
OMB	Optical Mutiplexer Board.
PMT	PhotoMulTiplier.
PU	Processing Unit.
QCD	Quantum ChromoDynamics.
QED	Quantum ElectroDynamics.
RCD	ROD Crate DAQ.
RITMO	ROD Information for Tile MOnitoring.
ROB	Read-Out Buffer.
ROD	Read-Out Driver.
ROI	Region Of Interest.
ROIB	Region Of Interest Builder.
ROL	Read-Out Link.
ROS	Read-Out System.
SM	Standard Model.
SSB	Spontaneous Symmetry Breaking.
TBM	Trigger and Busy Module.
TIER	Grid Computing Site.

TDAQ	Trigger and Data AcQuisition.
TM	Transition Module.
TTC	Timing, Trigger and Control.
TTCEX	Timing, Trigger and Control Encoder Transmitter.
TTCVI	Timing, Trigger and Control VME Interface.
TTYPE	Trigger type.
UEL	Upper Exclusion Limit.
VME	Virtual Machine Environment.

LIST OF ACRONYMS

Bibliography

- [1] ATLAS Collaboration. *ATLAS high-level trigger, data-acquisition and controls: Technical Design Report*. CERN, Geneva, 2003. ATLAS-TDR-016; CERN-LHCC-2003-022.
- [2] ATLAS Collaboration. *ATLAS Technical Proposal for a General-Purpose pp experiment at the Large Hadron Collider at CERN*. CERN, Geneva, 1994. CERN-LHC-94-43.
- [3] CMS Collaboration. *Technical Proposal*. CERN, Geneva, 1994. CERN-LHCC-94-38 ; LHCC-P-1.
- [4] LHCb Collaboration. *LHCb: Technical Proposal*. CERN, Geneva, 1998. CERN-LHCC-98-004; LHCC-P-4.
- [5] ALICE Collaboration. *ALICE : Technical proposal for a Large Ion collider Experiment at the CERN LHC*. CERN, Geneva, 1995. CERN-LHCC-95-71; LHCC-P-3.
- [6] TOTEM Collaboration. *TOTEM, Total Cross Section, Elastic Scattering and Diffraction Dissociation at the LHC : Technical Proposal*. CERN, Geneva, 1999. CERN-LHCC-99-007 ; LHCC-P-5.
- [7] LHCf Collaboration. *LHCf experiment: Technical Design Report*. Technical Design Report LHCf. CERN, Geneva, 2006. LHCF-TDR-001; CERN-LHCC-2006-004.
- [8] MoEDAL Collaboration. Technical Design Report of the MoEDAL Experiment. Technical Report CERN-LHCC-2009-006. MoEDAL-TDR-001, CERN, Geneva, Jun 2009.

BIBLIOGRAPHY

- [9] A. Kugel, B. Gorini, B. Green, M. Joos, G. Kieft, R. Männer, M. Müller, J. Petersen, and M. Yu. A Robin Prototype for a PCI-Bus based ATLAS Readout-System. Technical Report ATL-COM-DAQ-2004-001, CERN, Geneva, Oct 2003.
- [10] K. Anderson et al. Design of the front-end analog electronics for the ATLAS Tile Calorimeter. *Nucl. Instrum. Meth.*, A(551):469476, 2005.
- [11] K. Anderson et al. ATLAS Tile Calorimeter interface. In *8th Workshop on Electronics for LHC Experiments*, Colmar, France, September 2002.
- [12] Technical Reference Manual for VP110/01X VME Pentium III-M Single Board Computer.
- [13] J.W. Dawson, D.J. Francis, W.N Haberichter, and J.L. Schlereth. TTCPR: a PMC receiver for TTC. In *Proceedings of the 7th Workshop on Electronics for LHC Experiments*, pages 215–216, Stockholm, Sweden, September 2001. CERN. CDS record: 529413.
- [14] P. Matricon. The Trigger and Busy Module of the ATLAS LARG ROD System. ATLAS EDMS document ATL-AL-EN-0054.
- [15] A. Ruiz Garcia. HOLA specification, 2001. ATLAS EDMS document 330901.
- [16] P. Matricon. A 9U Transition Module for the ROD Demonstrator. ATLAS EDMS document ATL-AL-EN-0053.
- [17] V. Gonzalez, E. Sanchis, J. Soret, J. Torres, J. Castelo, C. Cuenca V. Castillo, A. Ferrer, E. Fullana, E. Higon, J. Poveda, B. Salvachua A. Ruiz-Martinez, C. Solans, J. A. Valls, A. Munar, C. Iglesias, and A. Valero. Development of the Optical Multiplexer Board Prototype for Data Acquisition in the TileCal System. *Nuclear Science, IEEE Transactions on*, 53(4):2131–2138, August 2006.
- [18] C. Solans. ATLAS TDAQ Software for TileCal Commissioning. Master’s thesis, Universitat de València, Facultat de Física, July 2005.
- [19] Texas Instruments. *TMS320C6000 CPU and instruction set reference guide*, 2000. SPRU189F.

- [20] E. Fullana, J. Castelo, V. Castillo, C. Cuenca, A. Ferrer, E. Higon, C. Iglesias, A. Munar, J. Poveda, A. Ruiz-Martinez, B. Salvachua, R. Teuscher C. Solans, and J.A. Valls. Digital Signal Reconstruction in the ATLAS Hadronic Tile Calorimeter. *Nuclear Science, IEEE Transactions on*, 53(4):2139–2143, August 2006.
- [21] B. Salvachua, J. Abdallah, J. Castelo, V. Castillo, C. Cuenca, E. Fullana A. Ferrer, V. Gonzalez, E. Higon, A. Munar, J. Poveda, E. Sanchis A. Ruiz-Martinez, C. Solans, J. Soret, J. Torres, A. Valero, and J.A. Valls. Algorithms for the ROD DSP of the ATLAS Hadronic Tile Calorimeter. *Journal of Instrumentation*, 2(T02001), February 2007.
- [22] A. Valero, J. Abdallah, V. Castillo, C. Cuenca, A. Ferrer, V. Gonzalez E. Fullana, E. Higon, J. Poveda, A. Ruiz-Martinez, B. Salvachua, C. Solans E. Sanchis, J. Torres, and J.A. Valls. DSP Online algorithms for the ATLAS TileCal Read-Out Drivers. *Nuclear Science, IEEE Transactions on*, 55(1):158–164, February 2008.
- [23] A. Valero, J. Abdallah, V. Castillo, C. Cuenca, A. Ferrer, V. Gonzalez E. Fullana, E. Higon, J. Poveda, A. Ruiz-Martinez, M.A. Saez, E. Sanchis B. Salvachua, C. Solans, J. Torres, and J.A. Valls. ATLAS TileCal Read Out Driver Production. *Journal of Instrumentation*, 2(P05003), May 2007.
- [24] E. Fullana, J. Castelo, V. Castillo, C. Cuenca, A. Ferrer, E. Higon, C. Iglesias, J. Poveda A. Munar, A. Ruiz-Martinez, B. Salvachua, C. Solans, R. Teuscher, and J. Valls. Optimal Filtering in the ATLAS Hadronic Tile Calorimeter. ATL-TILECAL-2005-001, 2005.
- [25] E. Fullana. *Energy reconstruction algorithms for the ATLAS Hadronic Tile Calorimeter and their effect on extra dimensions signatures*. PhD thesis, Departamento de Física Atómica Molecular y Nuclear, Universitat de València - CSIC, 2007.
- [26] ATLAS Tile Calorimeter Group. Tile conditions cool layout. <https://twiki.cern.ch/twiki/bin/view/Atlas/TileConditionsCoolLayout>.

BIBLIOGRAPHY

- [27] H. Burckhart et al. and ATLAS TDAQ/DCS Global Issues Working Group. Partitioning. Technical report, CERN, 2003. ATLAS Internal Note, ATL-DAQ-2003-025.
- [28] ATLAS Collaboration. *ATLAS Level-1 Trigger Technical Design Report*. CERN, Geneva, 1998. CERN-LHC-98-014.
- [29] G. Crone, S. Gameiro, B. Gorini, M. Joos, E. Pasqualucci, and J. Petersen. ROD Crate DAQ User's Guide. ATL-DQ-EN-0020.
- [30] G. Lehmann Miotto. Operations at Different Activity Stages. Technical Report ATLAS-TDAQ-CONTROLS-2005-001, CERN, Geneva, 2005.
- [31] C Solans, A Abdallah, G Arabidze, B Carneiro Ferreira, and B Sotomaior Peralva. TileCal TDAQ/DCS communication. Technical Report ATL-TILECAL-PUB-2007-006. ATL-COM-TILECAL-2007-016, CERN, Geneva, Oct 2007.
- [32] ATLAS Collaboration. Readiness of the ATLAS Tile Calorimeter for LHC collisions. Technical Report ATL-COM-TILECAL-2010-005, CERN, Geneva, April 2010.
- [33] B.M. Salvachua. *Real Time Energy Reconstruction in the ATLAS Hadronic Tile Calorimeter and ATLAS sensitivity to Extra Dimension Models*. PhD thesis, Departamento de Física Atómica Molecular y Nuclear, CSIC - Universitat de València, 2007.
- [34] ATLAS Collaboration. ATLAS analysis model. *Journal of Physics: Conference Series*, 119(4):042012, 2008.
- [35] R. Brun et al. ROOT Home Page. URL: <http://root.cern.ch>.
- [36] M. Cacciari, G.P. Salam, and G. Soyez. The anti-kt jet clustering algorithm. *Journal of High Energy Physics*, 2008(04):063, 2008.
- [37] R.P. Feynman. Mathematical Formulation of the Quantum Theory of Electromagnetic Interaction. *Phys. Rev.*, 80(3):440–457, November 1950.
- [38] E. Noether and M. A. Tavel. Invariant Variation Problems. *Transport Theory and Statistical Physics*, 1(3):183–207, 1971.

- [39] J.C. Maxwell. A dynamical theory of the electromagnetic field. *Philosophical Transactions of the Royal Society of London*, 155:459–513, 1865.
- [40] T. Levi-Civita and M.M.G. Ricci. Méthodes de calcul différentiel absolu et leurs applications. *Mathematische Annalen*, 54:125 – 201, March 1900.
- [41] M. Gell-Mann. Symmetries of Baryons and Mesons. *Physical Review*, 125(3):1067–1084, February 1962.
- [42] M. Gell-Mann. A schematic model of baryons and mesons. *Physics Letters*, 8:214–215, February 1964.
- [43] G. Zweig. An SU_3 model for strong interaction symmetry and its breaking; Part I. Technical Report CERN-TH-401, CERN, January 1964.
- [44] G. Zweig. An SU_3 model for strong interaction symmetry and its breaking; Part II. Technical Report CERN-TH-412, CERN, February 1964.
- [45] M.Y. Han and Y. Nambu. Three-Triplet Model with Double $SU(3)$ Symmetry. *Physical Review*, 139(4B):B1006–B1010, August 1965.
- [46] R.K. Ellis, W.J. Stirling, and B.R. Webber. QCD and collider physics. *Camb. Monogr. Part. Phys. Nucl. Phys. Cosmol.*, 8:1–435, 1996.
- [47] C.N. Yang and R.L. Mills. Conservation of Isotopic Spin and Isotopic Gauge Invariance. *Phys. Rev.*, 96(1):191–195, October 1954.
- [48] J. Chadwick. Possible Existence of a Neutron. *Nature*, 129(3252):312–312, February 1932.
- [49] S.L. Glashow. Partial-symmetries of weak interactions. *Nuclear Physics*, 22(4):579–588, 1961.
- [50] S. Weinberg. A Model of Leptons. *Phys. Rev. Lett.*, 19(21):1264–1266, November 1967.
- [51] A. Salam. in *Elementary Particle Theory*. N. Svartholm Almquist and Wiksell, Stockholm, 1968.
- [52] G. Arnison et al. Experimental observation of lepton pairs of invariant mass around 95 GeV/c² at the CERN SPS collider. *Physics Letters B*, 126(5):398–410, 1983.

BIBLIOGRAPHY

- [53] P.W. Higgs, Phys. Rev. Lett. 12, 132 (1964),
P.W. Higgs, Phys. Rev. 145, 1156 (1966),
F. Englert and R. Brout, Phys. Rev. Lett. 13, 321 (1964),
G.S. Guralnik, C.R. Hagen, and T.W. Kibble, Phys. Rev. Lett. 13, 585 (1964).
- [54] N. Cabibbo, L. Maiani, G. Parisi, and R. Petronzio. Bounds on the fermions and Higgs boson masses in grand unified theories. *Nuclear Physics B*, 158(2-3):295 – 305, 1979.
- [55] U. Aglietti et al. Tevatron-for-LHC Report: Higgs, 2007. arXiv: arXiv:hep-ph/0612172.
- [56] C. Amsler et al. *Particle Data Group*, volume 1. URL: <http://pdg.lbl.gov>, 2008. PL B667.
- [57] H.P. Nilles. Supersymmetry, Supergravity and Particle Physics. *Physics Reports*, 110:1–162, 1984.
- [58] S.P. Martin. A supersymmetry primer, 1997. arXiv: hep-ph/9709356.
- [59] R.N. Hill and E.H. Kerner. Unique Canonical Representation of the Inhomogeneous Lorentz Group in Relativistic Particle Dynamics. *Physics Review Letters*, 17(22):1156–1158, November 1966.
- [60] H.E. Haber and G.L. Kane. The Search for Supersymmetry: Probing Physics beyond the Standard Model. *Physics Reports*, 117:75–263, 1985.
- [61] L.J. Hall and M.B. Wise. Flavor changing Higgs boson couplings. *Nuclear Physics B*, 187(3):397–408, 1981.
- [62] C. Wagner M. Carena, S. Heinemeyer and G. Weiglein. Suggestions for Benchmark Scenarios for MSSM Higgs Boson Searches at Hadron Colliders. *Eur. Phys. J. C*, 26, 2003. hep-ph/0202167.
- [63] CDF Collaboration. Search for Neutral MSSM Higgs Bosons Decaying to Tau Pairs with 1.8 fb⁻¹ of Data. Technical Report CDF Note 9071, FNAL, October 2007.

-
- [64] DØ Collaboration. Search for Neutral Higgs Boson Production in the Decay $h \rightarrow \tau_\mu \tau$ with the DØ Detector at $\sqrt{s}=1.96$ TeV. Technical Report DØ Note 5331-CONF, FNAL, February 2007.
- [65] M. Schumacher. Investigation of the discovery potential for Higgs bosons of the minimal supersymmetric extension of the standard model (MSSM) with ATLAS, 2004. arXiv: hep-ph/0410112.
- [66] V. Buscher and K. Jakobs. Higgs boson searches at hadron colliders. *International Journal of Modern Physics A*, 20:2523–2602, 2005.
- [67] CDF Collaboration. Search for Higgs Bosons Predicted in Two-Higgs-Doublet Models via Decays to Tau Lepton Pairs in 1.96 TeV $p\bar{p}$ Collisions. *Physics Review Letters*, 103(201801), November 2009. CDF Note 9622.
- [68] A. Ruiz Martinez. *Studies with Muons in ATLAS: TileCal Level-2 Trigger and MSSM Higgs Discovery Reach*. PhD thesis, Departament de Física Atòmica Molecular i Nuclear, Universitat de València, 2009.
- [69] C. Anders et al. Discovery Potential of $A/H \rightarrow \tau^+ \tau^- \rightarrow \ell h$ in ATLAS. Technical report, CERN, 2010. ATL-PHYS-INT-2010-036.
- [70] ATLAS Collaboration. Search of the Higgs boson decaying into tau-leptons at ATLAS. *Nuclear Physics B*, 189:299–304, 2009. Proceedings of the Tenth International Workshop on Tau Lepton Physics.
- [71] S. Heinemeyer, W.F.L. Hollik, and G. Weiglein. FeynHiggs: a program for the calculation of the masses of the neutral CP -even Higgs bosons in the MSSM. *Computet Physics Communications*, 124(hep-ph/9812320. CERN-TH-98-389. DESY-98-193. KA-TP-98-16):76–89, December 1998.
- [72] M. Spira. HIGLU and HDECAY: Programs for Higgs Boson Production at the LHC and Higgs Boson Decay Widths. Technical Report hep-ph/9610350. CERN-TH-96-285, CERN, Oct 1996.
- [73] H/A tau tau CSC Note web page:
<https://twiki.cern.ch/twiki/bin/view/AtlasProtected/CSCHAtautauNote>.

BIBLIOGRAPHY

- [74] A. Anastassov, J. Conway, C. Cuenca, D. Jang, and A. Lath. Search for Neutral MSSM Higgs Boson(s) in the $\tau\tau$ Decay Channel. Technical Report CDF/PHYS/EXOTIC/CDFR/8972, FNAL, September 2007.
- [75] ATLAS Collaboration. *Expected performance of the ATLAS experiment: detector, trigger and physics*. CERN, Geneva, 2009.
- [76] ATLAS Collaboration. *ATLAS computing: Technical Design Report*. Number ATLAS-TDR-017, CERN-LHCC-2005-022 in Technical Design Report ATLAS. CERN, Geneva, 2005.
- [77] Pythia web site: <http://home.thep.lu.se/~torbjorn/pythia.html>.
- [78] Electron/Photon trigger in ATLAS web page: <https://twiki.cern.ch/twiki/bin/view/Atlas/TrigEgammaOverview>.
- [79] S. Hassani, L. Chevalier, E. Lançon, J.F. Laporte, R. Nicolaidou, and A. Ouraou. A muon identification and combined reconstruction procedure for the ATLAS detector at the LHC using the (MUONBOY, STACO, Mu-Tag) reconstruction packages. *Nuclear Instruments and Methods in Physics Research Section A*, 572(1):77–79, 2007. Frontier Detectors for Frontier Physics - Proceedings of the 10th Pisa Meeting on Advanced Detectors.
- [80] D Froidevaux, P Nevski, and E Richter-Was. Energy flow studies with hadronic tau-decays using DC1 data samples. Technical Report ATL-COM-PHYS-2005-024, CERN, Geneva, May 2005.
- [81] A. Kaczmarska, E. Richter-Was, M. Wolter, and L. Janyst. Performance of the tau1p3p algorithm for hadronic tau decays identification with release 12.0.6. Technical Report ATL-PHYS-INT-2008-004. ATL-COM-PHYS-2007-039, CERN, Geneva, June 2007.
- [82] W. Lampl, S. Laplace, D. Lelas, P. Loch, H. Ma, S. Menke, S. Rajagopalan, D. Rousseau, D. Snyder, and G. Unal. Calorimeter Clustering Algorithms: Description and Performance. Technical Report ATL-LARG-PUB-2008-002. ATL-COM-LARG-2008-003, CERN, Geneva, April 2008.
- [83] Y.Q. Fang, L.R. Flores-Castillo, B. Mellado, S. Padhi, and S.L. Wu. Object-Based Approach for the Reconstruction of Missing Transverse Momentum

- with the ATLAS Detector. Technical Report ATL-COM-CAL-2006-002, CERN, Geneva, July 2006.
- [84] Overlap removal web page:
<https://twiki.cern.ch/twiki/bin/view/AtlasProtected/RemoveOverlap>.
- [85] S. Eidelman et al. Pdg. 38 kinematics. *Physics Letters B*, 1(592), 2004.
<http://pdg.lbl.gov/>.
- [86] A. Anastassov, J. Conway, C. Cuenca, D. Jang, and A. Lath. Search for Neutral MSSM Higgs Boson(s) in the $\tau\tau$ Decay Channel. Technical Report CDF/PHYS/EXOTIC/CDFR/8639, FNAL, January 2007.
- [87] C. Amsler et al. Pdg. 32 statistics. *Physics Letters B*, 1(667), 2008.
<http://pdg.lbl.gov/>.
- [88] G. Cowan. Bayesian methods for the ATLAS Higgs Search. DRAFT 4 September 2007.
- [89] R.E. Kass and A.E. Raftery. Bayes Factors. *Journal of the American Statistical Association*, 90(430):773, 1995.
- [90] I.J. Good. The Bayes/Non-Bayes Compromise: A Brief Review. *Journal of the American Statistical Association*, 87(419):597, 1992.
- [91] J. Neyman. Outline of a Theory of Statistical Estimation Based on the Classical Theory of Probability. *Phil. Trans. R. Soc. Lond. A*, 236(doi:10.1098/rsta.1937.0005):333–380, August 1937.
- [92] D. Cavalli and G. Negri. Extension of the Study of A/H to tau-tau to lepton-hadron in the high m_A region. Technical Report ATL-PHYS-2003-009, CERN, Geneva, May 2003.

BIBLIOGRAPHY

List of Figures

1.1	The Globe of Science and Innovation at CERN.	2
1.2	Operational CERN accelerators.	3
1.3	Diagram showing the cross-section of an LHC dipole magnet. . .	4
1.4	Proton-proton cross section as a function of center of mass energy for a hadron collider [1].	6
1.5	Representation of the LHC ring with its detectors.	7
1.6	The four main LHC experiments.	8
1.7	The ATLAS experiment.	9
1.8	First candidate for an event with a W boson decaying to electron + neutrino seen in 7 TeV collision data.	9
1.9	Picture of the toroid magnet.	11
1.10	The ATLAS muon spectrometer in the rz (left) and xy view (right). 12	
1.11	The Inner detector.	15
1.12	Layout of the ATLAS calorimeters.	17
1.13	Cumulative amount of material, in units of interaction length, as a function of absolute pseudorapidity, in front of the calorimeters and across them.	18
1.14	Diagram of a LAr EM calorimeter barrel module. It is shown the longitudinal segmentation, cell size is shown and the accordion structure.	20
1.15	TileCal module components and structure.	21
1.16	Scheme of the TileCal cell distribution for half of a long barrel module (on the left) and a extended barrel module (on the right) with lines that show the pseudorapidity projective distribution. .	22

LIST OF FIGURES

1.17	ATLAS data acquisition system and trigger levels.	24
1.18	Block diagram of the Level 1 Trigger.	25
1.19	Block diagram of the DAQ HLT architecture.	27
1.20	Block diagram of Tile Calorimeter electronics.	29
1.21	Scheme of a TileCal PMT block.	31
1.22	Block diagram of the digitizer system.	33
1.23	Block diagram of the Interface board.	33
1.24	Picture of the back-end electronic crates.	35
1.25	Pictures of the front (a) and rear (b) views of the ROD crate. . .	38
1.26	TileCal ROD motherboard picture.	38
1.27	TileCal Optical Multiplexer Board picture.	40
2.1	Schematic diagram of the TTC distribution and Read-out of a super-drawer.	43
2.2	Tile Calorimeter ROD module data flow.	44
2.3	TileCal ROD motherboard and Transition Module pictures. . . .	45
2.4	Tile Calorimeter Processing Unit daughter board picture.	45
2.5	Optimal Filtering magnitudes.	47
2.6	ROD Crate DAQ schematic diagram.	52
2.7	Overview of the RCD schema classes and their inheritance. . . .	54
2.8	Crate sub-panel in the Tile IGUI panel.	55
2.9	TTC sub-panel in the Tile IGUI panel.	57
2.10	Schematic view of the ROD crate operation in S-link read-out mode. Commands are issued by the user to the ROD Crate Con- troller (RCC), and monitoring quantities are returned from it. The configuration and control of the boards is done through the VME bus. Monitoring quantities are read-out from the boards. Data is trasmitted to the Read-out System through S-Link. . . .	57
2.11	Globals sub-panel in the Tile IGUI panel.	58
2.12	Bunch structure of an LHC fill.	59
2.13	Shaft sub-panel in the Tile IGUI panel.	61
2.14	Laser sub-panel in the Tile IGUI panel.	62

2.15	VME read-out mode of the ROD crate. Commands and results are issued by the user to the ROD Crate Controller (RCC). The configuration and control of the boards and the read-out of the data is done through the VME bus.	64
2.16	DVS application view.	65
2.17	High gain Charge Injection System DVS test results.	65
2.18	DAQ to DCS display in the Tile Calorimeter specific IGUI panel for one Tile Calorimeter partition (LBA). Each partition is divided into 64 modules.	67
2.19	Screenshot of the Igui for ATLAS partition in state running. . .	68
2.20	Integrated Luminosity as a function of days.	69
2.21	Data taking efficiency during stable beams in 2010.	69
2.22	Mean values of longest transition times per sub-detector. The arrows indicate the Tile Calorimeter.	71
2.23	Mean values of Tile interesting transition times in the Tile Calorimeter.	72
2.24	Mean values of Tile interesting transition times in LBC TTC partition.	72
2.25	Summary of the different Tile Calorimeter monitoring levels and rates.	73
2.26	Distribution of the RMS of the pedestal for LBA02 (left) and distribution of the fraction of events with digital errors as a function of super-module and DMU (right) as seen by the ROS monitoring for beam data at $\sqrt{s} = 7$ TeV.	76
2.27	Time difference between online and offline reconstruction versus offline reconstructed time as seen by the Event Filter monitoring in the four TTC partitions for beam data at $\sqrt{s} = 7$ TeV. . . .	78
2.28	Position (ϕ vs η) of cells with depositions above 300 MeV for any physics triggered event as seen by the Event Filter monitoring for beam data at $\sqrt{s} = 7$ TeV. Masked channels are left blank. . . .	78
3.1	Relative difference between $1/A$ and the corresponding value in the look-up-table (LUT) of the DSP implementation as a function of the amplitude.	84

LIST OF FIGURES

3.2	Iterative Optimal Filtering magnitudes.	85
3.3	ATLAS Event Data Model representation. The square areas are proportional to the event size.	87
3.4	Mean value of time for side A MBTS cells versus mean value of time for side C MBTS cells from $\sqrt{s} = 7$ TeV data.	88
3.5	Mean value of time for side A MBTS cells versus mean value of time for side C MBTS cells from $\sqrt{s} = 7$ TeV data.	89
3.6	Channel time distributions computed by the Optimal Filtering online with no iterations (DSP) and Optimal Filtering offline with iterations (Offline) from $\sqrt{s} = 7$ TeV data.	90
3.7	Time distribution for Tile Calorimeter cells with energy deposit above 300 MeV per channel for Level 1 Calorimeter Trigger stream from $\sqrt{s} = 7$ TeV data.	92
3.8	Topological cluster time for Tile Calorimeter cells for Level 1 Calorimeter Trigger stream from $\sqrt{s} = 7$ TeV data.	93
3.9	Time distribution for Tile Calorimeter cells within a topological cluster for Level 1 Calorimeter Trigger stream from $\sqrt{s} = 7$ TeV data.	93
3.10	Jet time distribution for Tile Calorimeter cells for Level 1 Calorimeter Trigger stream from $\sqrt{s} = 7$ TeV data.	95
3.11	Time distribution for Tile Calorimeter cells within a jet for Level 1 Calorimeter Trigger stream from $\sqrt{s} = 7$ TeV data.	95
3.12	Relative energy difference between online and offline Optimal Filtering without iterations (E_{DSP} , E_{OFF-NI}) as a function of the E_{OFF-NI} for high (top) and low (bottom) gains for collision data at $\sqrt{s} = 7$ TeV.	97
3.13	Relative time difference between online and offline Optimal Filtering without iterations (T_{DSP} , T_{OFF-NI}) as a function of the energy of the offline Optimal Filtering without iterations (E_{OFF-NI}) for high (top) and low (bottom) gains for collision data at $\sqrt{s} = 7$ TeV.	98

3.14	Reconstructed time of the offline Optimal Filtering with iterations (T_{OFF-I}) as a function of the time of the online Optimal Filtering without iterations (T_{DSP}) from collision data at $\sqrt{s} = 7$ TeV.	99
3.15	Relative difference of the energy of the online Optimal Filtering without iterations (E_{DSP}) with respect to the offline Optimal Filtering with iterations (E_{OFF-I}) as a function of the time of the online Optimal Filtering without iterations (T_{DSP}) with and without parabolic correction from collision data at $\sqrt{s} = 7$ TeV.	100
3.16	Relative difference of the energy of the online Optimal Filtering without iterations (E_{DSP}) with respect to the offline Optimal Filtering with iterations (E_{OFF-I}) as a function of E_{OFF-I} without (top) and with (bottom) parabolic correction from collision data at $\sqrt{s} = 7$ TeV.	101
4.1	The Standard Model.	105
4.2	Diagram of a low energy electron beam colliding against a double slit.	105
4.3	Feynman diagram of the $e^+e^- \rightarrow$ hadrons mediated by a photon (γ) or a Z boson.	108
4.4	Gell-Man's matrix representation of the infinitesimal generators of the SU(3) symmetry group.	111
4.5	Pauli's matrix representation of the infinitesimal generators of the SU(2) symmetry group.	113
4.6	Spontaneous symmetry breaking potentials.	116
4.7	Gauge invariant potential in terms of real and imaginary fields.	118
4.8	Feynman diagrams for the SM Higgs production mechanisms at the LHC.	121
4.9	SM Higgs boson production cross-section for $\sqrt{s}=14$ TeV at the LHC as a function of the Higgs boson mass [55].	122
4.10	SM Higgs branching ratios $\sqrt{s}=14$ TeV at the LHC as a function of the Higgs boson mass [56].	122
4.11	Masses of the Higgs bosons in the MSSM m_h -max scenario as a function of m_A for two values of $\tan\beta$	127

LIST OF FIGURES

4.12	Neutral MSSM Higgs bosons production cross sections [fb] at the LHC, $\sqrt{s}=14$ TeV, for the most relevant production mechanisms as a function of the Higgs boson mass for $\tan\beta = 5, 40$ in the m_h -max and no mixing scenarios [55].	131
4.13	The MSSM exclusion contours at 95%C.L. (light-green) and 99.7%CL (dark-green) in the $\tan\beta$ - m_A plane, obtained by LEP for the CP conserving m_h -max benchmark scenario, with $m_t = 174.3$ GeV [56].	132
4.14	The 95% C.L. MSSM exclusion contours obtained by CDF and $D\bar{D}$ in the $H \rightarrow \tau^+\tau^-$ searches in the no-mixing benchmark scenario with $\mu=200$ GeV, projected on to the $(m_A, \tan\beta)$ plane. The Tevatron limits for the m_h -max scenario are nearly the same as in the no-mixing scenario. Also shown are the regions excluded by LEP searches, separately for the m_h -max scenario (darker shading) and the no-mixing scenario, (lighter shading). The LEP limits are shown for a top quark mass of 174.3 GeV (the Tevatron results are not sensitive to the precise value of the top mass) [56].	133
4.15	Discovery potential for light CP-even Higgs boson in the m_h -max CP-conserving scenario after collecting 30 fb^{-1} (left) and 300 fb^{-1} (right) from the ATLAS TDR physics performance. The cross hatched area is excluded by LEP at 95% C.L. from [65]. . .	134
5.1	Feynman diagrams contributing to the MSSM Higgs boson production.	139
5.2	Total MSSM Higgs bosons production cross section times branching ratios as a function of m_A for different values of $\tan\beta$ calculated with FeynHiggs at $\sqrt{s} = 14$ TeV.	140
5.3	Tree level Feynman diagram for the Drell-Yan Z/γ production decaying into tau pairs.	142
5.4	Tree level Feynman diagram for the production of W^\pm associated with jets.	142
5.5	Tree level Feynman diagram for the top quark production with two W^\pm and two b quark jets in the final state.	143
5.6	Feynman diagrams for QCD background processes.	144

5.7	Delta ϕ distributions for signal and background data.	146
5.8	M_{vis} and M_{inv} distributions for $m_A = 150$ GeV and $\tan\beta = 45$	147
5.9	Electron identification efficiency as a function of transverse momentum, p_T	150
5.10	Muon identification efficiency as a function of transverse momentum, p_T	151
5.11	Tau signal cone and isolation annulus for tracks and pions. The inner cone contains the hadronic tau track.	152
5.12	Tau identification efficiency as a function of transverse momentum, p_T	155
5.13	Rate of fake tau identification as a function of P_T for a set of tight and loose cuts.	156
5.14	Jet multiplicity per event in Signal (top) and Background (bottom) samples.	158
5.15	Missing transverse energy distributions for signal (top) and background (bottom) samples.	159
5.16	Lepton versus Hadron Transverse mass distributions for signal (top) and background (bottom) samples normalized to unity.	162
5.17	Typical M_{vis} distribution of the background and signal processes at $\tan\beta = 15$ for different values of m_A (150, 300, 450 and 600 GeV from top to bottom) for 1 fb^{-1}	164
5.18	Typical M_{vis} distribution of the background and signal processes at $\tan\beta = 45$ for different values of m_A (150, 300, 450 and 600 GeV from top to bottom) for 1 fb^{-1}	165
5.19	Pseudo-experimental data generated from M_{vis} distribution of the background.	166
5.20	Nominal and shifted p_T (top) and M_{vis} (bottom) distributions for $Z \rightarrow \tau^+\tau^-$ dataset with jet energy scale shift.	173
5.21	Difference between positive and negative shifted p_T (top) and M_{vis} (bottom) distributions for $Z \rightarrow \tau^+\tau^-$ dataset with jet energy scale shift.	174
5.22	Normalized posterior probability scan in signal cross section (θ).	176

LIST OF FIGURES

5.23	B_{01} test statistic distributions for background and signal plus background data for small and large signal cross sections.	178
5.24	Correspondence between the significance Z and a p -value.	179
5.25	ProfileLikelihood implementation.	181
5.26	Upper exclusion limit cross section distributions for neutral MSSM Higgs bosons with morphing for 1 fb^{-1} at $\sqrt{s} = 14 \text{ TeV}$	183
5.27	Upper exclusion limit cross section distributions for neutral MSSM Higgs bosons with no morphing for 1 fb^{-1} at $\sqrt{s} = 14 \text{ TeV}$	183
5.28	Expected upper exclusion limits cross section at 95% CL for neutral MSSM Higgs bosons decaying to tau pairs with and without morphing technique. for 1 fb^{-1} . Shaded areas are the $\pm 1\sigma$ and $\pm 2\sigma$ bands on the expected limit.	184
5.29	Expected upper exclusion limits cross section at 95% CL for neutral MSSM Higgs bosons decaying to tau pairs with and without morphing technique for 10 fb^{-1} . Shaded areas are the $\pm 1\sigma$ and $\pm 2\sigma$ bands on the expected limit.	185
5.30	Expected upper exclusion limits cross section at 95% CL for neutral MSSM Higgs bosons decaying to tau pairs with and without morphing technique. for 30 fb^{-1} . Shaded areas are the $\pm 1\sigma$ and $\pm 2\sigma$ bands on the expected limit.	186
5.31	Expected exclusion region in the $(m_A, \tan \beta)$ plane at 95% CL for neutral MSSM Higgs bosons decaying to tau pairs for 1, 10 and 30 fb^{-1} in the m_h -max scenario.	186
5.32	Cross section distributions with and without morphing at 95% for 10^4 S+B pseudo-experiments.	187
5.33	Expected significance values as a function of $\tan \beta$ and m_A for neutral MSSM Higgs bosons decaying into tau pairs with (top) and without (bottom) morphing technique for 1 fb^{-1}	189
5.34	Expected significance values as a function of $\tan \beta$ and m_A for neutral MSSM Higgs bosons decaying into tau pairs with (top) and without (bottom) morphing technique for 10 fb^{-1}	190

5.35	Expected significance values as a function of $\tan\beta$ and m_A for neutral MSSM Higgs bosons decaying into tau pairs with (top) and without (bottom) morphing technique for 30 fb^{-1}	191
5.36	Contour plot for expected $5\text{-}\sigma$ discovery as a function of $\tan\beta$ and m_A for MSSM Higgs bosons decaying into tau pairs for 30 fb^{-1} [92].	192
7.1	Imagen del ROD y el TM del TileCal.	200
7.2	Luminosidad integrada medida en ATLAS en función del tiempo.	203
7.3	Media de los tiempos de transición por detector para las transiciones más importantes. Las flechas indican el TileCal.	204
7.4	Resumen de los diferentes niveles de monitorización y frecuencias de muestreo.	204
7.5	Diferencia de tiempo reconstruido entre online y offline en las cuatro particiones del TileCal para datos de colisiones a $\sqrt{s} = 7 \text{ TeV}$	206
7.6	Distribución de tiempos por PMT reconstruidos mediante el algoritmo de OF online sin iteraciones (DSP) y OF offline con iteraciones (Offline) para datos de colisiones a $\sqrt{s} = 7 \text{ TeV}$	207
7.7	(a) Distribución del tiempo del jet para celdas del TileCal y (b) distribución del tiempo de las celdas dentro de un jet para sucesos del <i>stream</i> de L1Calo para datos de colisiones a $\sqrt{s} = 7 \text{ TeV}$	208
7.8	Diferencia relativa de energía online y offline reconstruida por el algoritmo de OF sin iteraciones en función de la energía offline para alta (a) y baja (b) ganancia para datos de colisiones a $\sqrt{s} = 7 \text{ TeV}$	209
7.9	Diferencia relativa de tiempo online y offline reconstruida por el algoritmo de OF sin iteraciones en función de la energía offline para alta (a) y baja (b) ganancia para datos de colisiones a $\sqrt{s} = 7 \text{ TeV}$	209
7.10	(a) Tiempo reconstruido offline en función de online y (b) desviación de la energía reconstruida online en función de la diferencia de tiempo para datos de colisiones a $\sqrt{s} = 7 \text{ TeV}$	210

LIST OF FIGURES

7.11	Diferencia relativa en la reconstrucción de la energ�a online en funci�n de la energ�a offline sin (a) y con (b) correcci�n parab�lica para datos de colisiones a $\sqrt{s} = 7$ TeV data	211
7.12	Diagramas de Feynman para la producci�n de bosones de Higgs MSSM neutros (A, h, H).	214
7.13	Distribuciones t�picas de M_{vis} para se�al y fondo para $\tan \beta = 15$ para diferentes valores de m_A	216
7.14	Datos pseudo-experimentales generados a partir de las distribuciones de M_{vis} que contribuyen al fondo.	216
7.15	L�mite de exclusi�n esperado al 95% CL de la secci�n eficaz de producci�n de bosones de Higgs MSSM neutros decayendo a pares de taus con y sin la t�cnica de morphing para 1, 10 y 30 fb ⁻¹	220
7.16	Regi�n de exclusi�n esperada al 95% CL en el espacio de par�metros ($m_A, \tan \beta$) para la producci�n de bosones de Higgs MSSM neutros decayendo a pares de taus para 1, 10 y 30 fb ⁻¹	221
7.17	Significancia esperada de descubrimiento de bosones de Higgs MSSM neutros decayendo a pares de taus en funci�n de $\tan \beta$ y m_A , con y sin la t�cnica de morphing para 1 fb ⁻¹	221
7.18	Significancia esperada de descubrimiento de bosones de Higgs MSSM neutros decayendo a pares de taus en funci�n de $\tan \beta$ y m_A , con y sin la t�cnica de morphing para 10 fb ⁻¹	222
7.19	Significancia esperada de descubrimiento de bosones de Higgs MSSM neutros decayendo a pares de taus en funci�n de $\tan \beta$ y m_A , con y sin la t�cnica de morphing para 30 fb ⁻¹	222

List of Tables

1.1	LHC beam parameters.	4
1.2	. General performance goals of the ATLAS detector.	10
1.3	Overview of the magnet system paramters.	11
1.4	Muon sytem parameters.	13
1.5	Parameters of the Inner Detector.	16
1.6	Main parameters of the ATLAS calorimeters.	19
2.1	Details of the ROD Crate DAQ configuration. The RCD are a subset of the Tile which includes other applications for monitoring.	53
2.2	Luminosity weighted relative fraction of detector uptime and good quality data during 2009 and 2010 beam periods a) All sta- ble beams 2009, b) Until 12/12/2009, c) 30/03/2010 - 17/05/10 d) 18/05/2010 - 27/05/2010 e) From 01/06/2010 (preliminary).	68
3.1	Data format of the reconstruction word for a read-out channel in the Tile Calorimeter.	82
3.2	Online reconstruction range and precision of the energy for the different energy units in low gain	83
3.3	Online reconstruction range and precision of the energy for the different energy units in high gain.	83
3.4	Table of the different data streams as of 2010.	86
4.1	List of quarks in the Standard Model.	109

LIST OF TABLES

4.2	Listing of Standard Model Leptons and their quantum numbers relevant for the Electroweak interaction. Helicity (H), Charge (Q), Weak Isospin (I) and Weak Hypercharge ($Y=2(Q-I_3)$). . . .	112
4.3	MSSM particle listing.	124
4.4	MSSM parameters for the m_h -max and no mixing benchmark scenarios.	130
5.1	Listing of mass of Higgs bosons and direct and associated production cross sections in the m_h -max scenario for $\tan\beta = 20$. . .	139
5.2	Branching ratios for MSSM Higgs Bosons to tau and muon pairs in the m_h -max scenario for $\tan\beta = 20$	140
5.3	Branching ratios of single tau decay modes for $\tan\beta = 20$	141
5.4	Branching ratios of tau pair decay modes.	141
5.5	Cross section values for background processes as recommended by ATLAS. Values are quoted for one lepton family.	141
5.6	Signal datasets.	148
5.7	Background datasets.	149
5.8	Cut flow in fb for signal datasets.	163
5.9	Cut flow in fb for background datasets.	163
5.10	Uncertainty types and magnitudes used to compute expected results.	182
5.11	Expected upper exclusion limit results for 1 fb^{-1} at $\sqrt{s} = 14 \text{ TeV}$. 184	
5.12	Expected upper exclusion limit results for 10 fb^{-1} at $\sqrt{s} = 14 \text{ TeV}$.185	
5.13	Expected upper exclusion limit results for 30 fb^{-1} at $\sqrt{s} = 14 \text{ TeV}$.185	
7.1	Fración relativa del tiempo de funcionamiento del detector y calidad de los datos pesada por la luminosidad durante los periodos de toma de datos con haz de 2009 y 2010. a) Haces estables 2009, b) Hasta 12/12/2009, c) 30/03/2010 - 17/05/10 d) 18/05/2010 - 27/05/2010 e) Desde 01/06/2010 (preliminar).	203
7.2	Número de eventos después de cada corte en señal.	215
7.3	Número de eventos después de cada corte en fondos.	215